Meltwater delivery from the tidewater glacier Kronebreen to Kongsfjorden, Svalbard; insights from *in situ* and remote-sensing analyses of sediment plumes

by

Eleanor Darlington

A Doctoral Thesis

Submitted in partial fulfilment
of the requirements for the award of

Doctor of Philosophy
of
Loughborough University

1st November 2015

Acknowledgements

Sat in my grandfather's front room as a child, I was entranced by a slide show of life at a research station in Antarctica. My passion for science was ignited and a burning desire to work at the Poles set in. This PhD research has been a journey, from Pole to Pole. It would not have been possible without invaluable supervisory support from Richard Hodgkins; thank you for your continued guidance, patience and confidence in my decision making. Embarking on Arctic oceanography was prompted by Adrian Jenkin's enthusiasm and subsequent supervision, for which I'm sincerely grateful for. Dave Graham, Dave Ryves, and Jo Bullard have provided guidance and new perspectives which have shaped this thesis.

My studies were funded by a Loughborough University Postgraduate studentship and the data collected for this work were funded by the Arctic Field Grant Project number 1787. Thanks to Jack Kohler, Tore Nordstad and the support staff at Sverdrup Station, for field guidance and assistance. Other financial contributions which supported my studies have been gratefully received from: Loughborough University Geography Department and the Polar and Alpine Research Centre, Loughborough Graduate School, the Challenger Society, and the Royal Geographical Society. This PhD was initially funded because of logistical support from Extreme World Races, for Antarctic fieldwork. This granted me the most wonderful white Christmas; I'd like to thank Gary, Monica, and Kenny for their friendship and joviality, particularly on our days snowed in! Arctic Trucks kept us moving and provided technical support with the automatic weather stations.

The geography department has provided a wealth of support and opportunities, with particular thanks to Paul Wood and Sue Clarke. Colleagues at the British Antarctic Survey, the UK Polar Network and the Association of Polar Early Career Scientists have provided fruitful conversations, research opportunities and valued friendship whilst I've been a student. Lunch breaks, tea escapes and payday beers offered a welcome distraction, thanks to Stacey, Catherine, Annie, Sophie, Matt, and Tom, et al. Outdoor shenanigans and mountain bikes adventures were fuelled by some super friends: Vian, Kate, and Huw and the SUCC community, for which I'm really grateful for.

My family have provided extensive support, listened to my Polar ramblings, and always kept in touch when I've been away. Mum and Dad, thank you for believing in me, and encouraging me to pursue the Antarctic dream. Chris, you're a patient man, your support has been invaluable; thank you for everything.

Abstract

Tidewater glaciers form a significant drainage catchment of glacierised areas, directly transporting meltwater from the terrestrial to the marine environment. Surface melt of glaciers in the Arctic is increasing in response to warmer atmospheric temperatures, whilst tidewater glaciers are also exposed to warmer ocean temperatures, stimulating submarine melt. Increased freshwater discharge not only freshens fjord waters, but also plays a key role in glacimarine sedimentary processes, transporting sediment to glacial fjords. Despite this, the temporal evolution of meltwater production, storage and release from tidewater glacier systems at seasonal and interannual time scales is poorly understood. This leaves large uncertainties in the predictions for future sea level rise, ocean circulation and the impacts on the marine ecosystem.

This study focuses on Kronebreen, a tidewater glacier which flows into the head of Kongsfjorden, north west Svalbard. Surface melt produces freshwater runoff, which is discharged from the grounding line as a buoyant, sediment laden plume, which spreads laterally across the surface water. This supraglacial melt is the dominant freshwater source, contributing an order of magnitude more freshwater to Kongsfjorden, than direct submarine melting of the ice face.

Calibration of MODIS band 1 satellite imagery with *in situ* measurements of Total Suspended Solids and spectral reflectance, provides a method to quantify meltwater and sediment discharge. Plume extent has been determined for each cloud free day, from June to September, 2002 – 2013. Analysis of plume extent with atmospheric temperature and modelled surface runoff, gives a source to sea insight to meltwater production, storage and discharge. The extent of the plume changes in response to meltwater; larger plumes form when discharge increases. These results reveal that meltwater discharge into Kongsfjorden lags atmospheric temperature, the primary driver of meltwater production, by over a week during June and July. This is reduced to only 1 – 2 days in August and September, indicating a decline in meltwater storage as the ablation season progresses, and the development of more efficient glacial drainage.

Sediment plumes respond to meltwater production, making them a valuable tool for quantifying meltwater discharge from a tidewater glacier. Insights to glacier hydrology can also be obtained when surface processes are also considered. This furthers the understanding of tidewater glacier hydrology, which is valuable for improving the accuracy of sea level rise predictions.

Contents

List of Figures

List of Tables

Acronyms and Abbreviations

ADCP	Accousic doppler current profiler
AO	Arctic Oscillation
ArW	Arctic water
AVHRR	Advanced very high resolution radiometer
AW	Atlantic water
AWS	Automatic weather station
CMB	Climatic mass balance
CTD	Condutivity, temperature and depth
DJFM	December, January, February and March
ELA	Equilibrium Line Altitude
FMAM	February, March, April and May
GiFW	Glacial freshwater melt
GPS	Global positioning system
IPCC	Intergovernmental panel on climate change
IW	Intermediate water
JJAS	June, July, August and September
KBF	Kronebreen face
LW	Local water
M	Mean
MODIS	Moderate resolution imaging spectroradiometer
NAO	North Atlantic Oscillation
NASA	National aeronautics and space administration
ONDJ	October, November, December and January

PDD	Positive degree days
PFA	Perennial firn aquifer
PSU	Practical salinity unit
ROI	Region of interest
SD	Standard deviation
SgFW	Subglacial freshwater discharge
SLR	Sea level rise
SMB	Surface mass balance
SST	Sea surface temperature
SW	Surface water
TAW	Transformed Atlantic water
TSS	Total suspended solids
UK	United Kingdom
USGS	United States geological survey
WCW	Winter cooled water
WRF	Weather research forecasting
WSC	West Spitsbergen current

Variables

α	Specific volume
ρ_f	Density of freshwater
ρ	Density
ρ_w	Density of water
H	Depth
θ_f	Freezing temperature
θ_i^*	Effective ice temperature
θ_i	Temperature of ice
θ	Potential temperature
c_i	Heat capacity of ice
c_p	Heat capacity of seawater
F_w	Rate of melted ice
f	Fraction of a specific volume of water
F	Coriolis parameter
g'	Reduced gravity
$GiFW$	Glacial ice freshwater
G_s	Subsurface conductive heat flux
LHF	Latent heat flux
L	Latent heat of fusion
LW	Longwave radiation
M	Mass
ME	Melt energy
obs	Observed characteristic
P	Pressure
r_i	Rossby radius
R_{net}	Net radiation
S	Salinity
$SgFW$	Subglacial freshwater
SHF	Sensible heat flux
SW	Shortwave radiation
t	Time
T	Temperature
v	Velocity
V	Volume of seawater
WT	Water type
x	Horizontal axis

Chapter 1

Introduction

1.1 Rationale for research

The Randolph Glacier Inventory (Arendt et al., 2012; Pfeffer et al., 2014) highlights that 39% of the total global glacierised area (726,800 ± 34,000 km^2) drains via tidewater glaciers, directly into the ocean. Only 3% of glaciers monitored globally are tidewater, resulting in under representation in the estimates of mass balance of the world's glaciers and ice caps (Sharp, 2014). The recent rapid retreat of some tidewater glaciers (e.g. Sund et al., 2011; Straneo and Heimbach, 2013) merits further investigation into the processes leading to their mass loss. Several mechanisms contribute to the retreat of tidewater glaciers, given their connectivity with both the atmosphere and ocean. Increased surface melt, driven by atmospheric processes, enhances glacier thinning and can lead to flotation. Subsequently, increased surface melt can lead to fracturing and calving at the glacier terminus. Despite this, how meltwater reaches the ocean, and the duration of transit remains poorly understood.

Climate forecasts predict that the polar amplification will persist, causing large areas of the Arctic to receive near-surface temperature increases greater than the global average; results from climate models (IPCC, 2013) and observations (Chylek et al., 2009) support this. Further glacier retreat is forecast as surface melt becomes enhanced and the summer melt season is prolonged, in response to these warming trends (Oerlemans, 2005; Nuth et al., 2010; IPCC, 2013). Freshwater runoff from Arctic glaciers and the Greenland ice sheet has a direct impact on sea level rise (SLR) (Church et al., 2013). Understanding glacier hydrology, which can control the rate and timing of runoff, is imperative to forecast accurate sea level rise predictions (Chu, 2014).

Submarine melting of the termini of tidewater glaciers is a contributing factor to reducing glacier mass (Motyka et al., 2003), which enforces the need to understand both atmospheric and oceanic processes (Figure 1.1; Straneo et al., 2013). The temperature of the warm, northerly flow, of Atlantic water is increasing, transporting more heat to the Arctic basin (Pavlov et al., 2013), whilst a decrease in sea ice formation can reduce the buttressing support at the glacier terminus (Vieli and Nick, 2011). This can make tidewater termini more susceptible to submarine melting, as has been found in Greenland (Rignot et al., 2010; Sutherland and Straneo, 2012; Straneo and Heimbach, 2013). Convective driven melt is another consideration, with buoyant freshwater plumes emerging subglacially into the marine environment, causing further melt of the ice face (Jenkins, 2011). As the plumes rise, they entrain ambient seawater, increasing heat transfer; greater discharge produces a faster plume which increases turbulent mixing at the ice - ocean interface (Kimura et al., 2014). Several, smaller plumes across the ice face will create greater melt, compared to just one submarine outlet source (Slater et al., 2015).

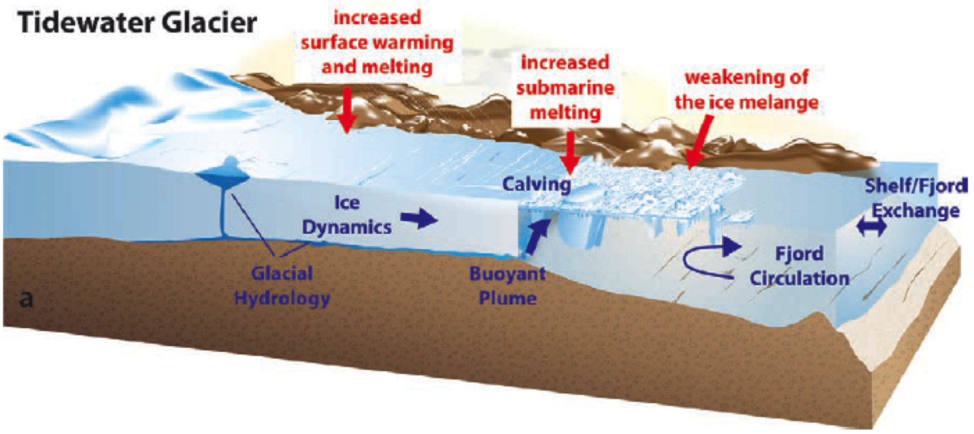

Figure 1.1: Schematic detailing the mechanisms of retreat for tidewater glaciers. Key processes that require further research are highlighted in blue text (Straneo et al., 2013).

Increased freshwater supply to the marine environment has numerous implications: i) it alters ocean circulation (e.g. Straneo et al., 2011; Mortensen et al., 2013; 2014) ii) can enhance the submarine melting (Jenkins, 2011; Motyka et al., 2013), iii) leads to increased iceberg calving (Benn et al., 2007; Bartholomaus et al., 2013), iv) affects the marine biogeochemistry (Bhatia et al., 2013; Hawkings et al., 2014) and v) alters the biological composition (Hop et al., 2002; Lydersen et al., 2014). Freshwater inputs to the marine environment as a result of the interactions between glaciers, atmosphere and ocean, needs to be better constrained to enable greater accuracy in the forecasting of global sea level rise (Hanna et al., 2013; Chu, 2014).

However, despite the impacts of freshwater entering the marine system, the ice - ocean interface of tidewater glaciers remains poorly understood, largely due to their inaccessibility. This exemplifies the value of oceanographic observations in the ice proximal zone (Cottier et al., 2010). There are only a few studies which address the seasonal and interannual variability of meltwater discharge, and the impacts this has on fjord circulation (Cottier et al., 2005; Mortensen et al., 2013; 2014). Increased accuracy, which this study promotes, is required when quantifying the volume of melt, from where it originates, and the timing of delivery. There are also differences between the amount of melt produced at the glacier surface, and how much is discharged into the fjords (Harper et al., 2012). This places importance not only on quantifying meltwater production and delivery, but also upon understanding glacial hydrological processes of tidewater glaciers, and how these affect ice dynamics (Straneo et al., 2013). Increased meltwater discharge can cause the terminus to become unstable, causing calving (Bartholomaus et al., 2013), in addition to freshening the surface water, implicating fjord circulation (Figure 1.1) (Cottier et al., 2005; Salcedo-Castro et al., 2011; Sciascia et al., 2013). To study the processes taking place at the glacier-ocean interface, a fjord which is free of ice melange would be ideal.

1.2 Study site

1.2.1 Kongsfjorden

This study focuses on the delivery of meltwater entering at the head of Kongsfjorden, from the tidewater glacier system of Kronbreen and Kongsvegen (Figure 1.2). Located at 79°N, 11°E on the west coast of Spitsbergen, Kongsfjorden forms one of the main regions of tidewater drainage together with with Krossfjord, Hornsund and Van Keulenfjord (Nuth et al., 2013). It is part of a two armed glacially eroded fjord system with Krossfjorden (Figure 1.2). Krossfjorden is orientated from north to south, whilst Kongsfjorden is orientated from southeast to northwest. The two meet at the mouth of the fjord, forming a deep glacial basin, Kongsfjordrenna, in which a shallow sill is present. Its bathymetry is complex and variable, ranging from <60 m at the head of the fjord, to 400 m, creating a system of distinctive basins. Kronebreen is a polythermal glacier, which is frozen to the bed rock at the margins, but has a wet bed in the upper region of the glacier. It forms the majority of the ice front, with Kongsvegen adjoining to the south. There are three other tidewater glaciers in Kongsfjorden: Blomstrandbreen, Conwaybreen and Kongsbreen. Meltwater discharge from Kronebreen and Kongsvegen is sediment laden, forming a distinctive surface plume (Figure 1.3). Unlike Greenlandic fjords, Kongsfjorden has relatively few icebergs and lacks ice melange. As such, it is possible to remotely observe the ice-ocean interactions directly in front of the ice face which has not been possible in other studies (Tedstone and Arnold, 2012).

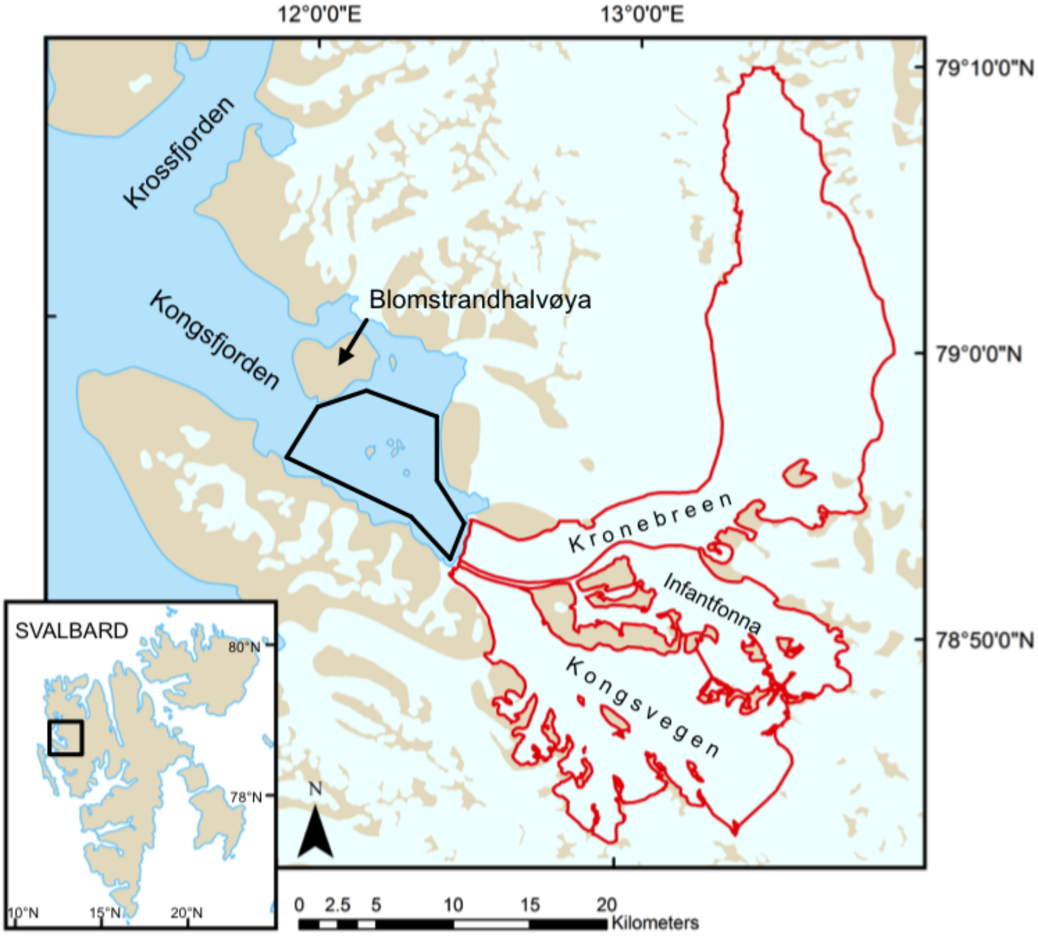

Figure 1.2: Regional map of Kongsfjorden, with Kronebreen, Kongsvegen and Infontanna glaciers detailed. The area of interest extends to the island of Blomstrandhalvøya.

Kongsfjorden is a climatically sensitive region of Svalbard. Strongly influenced by the west Spitsbergen current (WSC), atmospheric temperatures and changes to the cryosphere, it provides a natural laboratory for studying the ice - ocean interactions of tidewater glaciers. Within the fjord, there is a balance between Atlantic water (AW) and freshwater inputs, which both change spatially, on seasonal and interannual time scales. Kongsfjorden is sea ice free during the summer months, and increasingly more so during winter. No ice melange is present in the fjord, allowing for access directly in front of Kronebreen's marine terminus. Freshwater

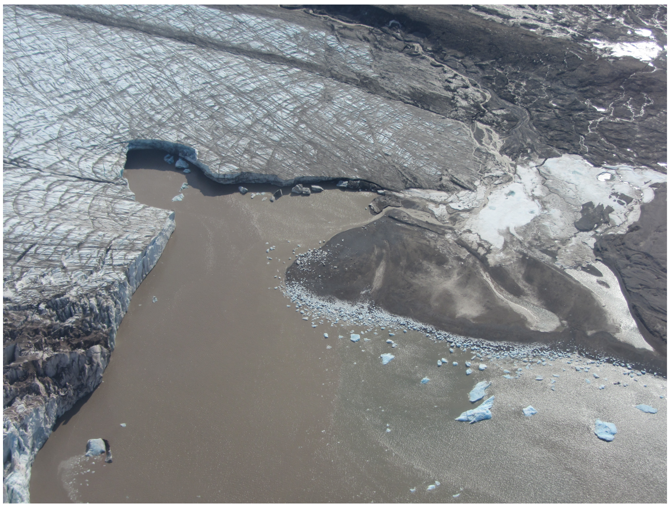

Figure 1.3: Aerial photo of the terminus of Kongsvegen, highlighting the strong presence of sediment in the surface water, visible as a distinctive brown colour (Storvold, 2012).

discharge, and active glacier calving at the head of the fjord, is a measure of mass loss from Kronebreen and Kongsvegen. The meltwater discharge transports glacial sediment to the fjord, influencing bathymetry, glacier stability and it also impacts the marine ecosystem. The meltwater plumes rise to the surface of Kongsfjorden, given depths of <100 m in front of Kronebreen's terminus. The geology underlying Kronebreen, allows the lateral spread of sediment laden meltwater across the fjord surface, to be easily identified as a distinctive plume. Therefore, Kongsfjorden is an ideal location to build upon previous sediment plume studies, forming a deeper understanding of the ice - ocean interactions of a fast moving, tidewater glacier, at seasonal and interannual time scales.

1.2.2 Kronebreen and Kongsvegen glacier complex

Kronebreen is a grounded polythermal glacier with an area of $\sim$390 km^2 (Figure 1.2). Kongsvegen is a smaller glacier (165 km^2), joining Kronebreen 5 km from the terminus, creating a confluent glacier with Infantfonna (85 km^2). The boundary between Kronebreen and Kongsvegen is defined by a medial moraine. The drainage area encompasses the ice fields of Dovrebreen, Holtedahlfonna and parts of Isachsenfonna, through a relatively narrow channel at its calving face (Nuth et al., 2012). Melt produced supraglacially is transported through the englacial system and discharged at the calving face, directly into Kongsfjorden. Meltwater transports sediment produced by basal erosion to the head of Kongsfjorden, which is visible as buoyant sediment plumes in the ice proximal zone (Figure 1.4).

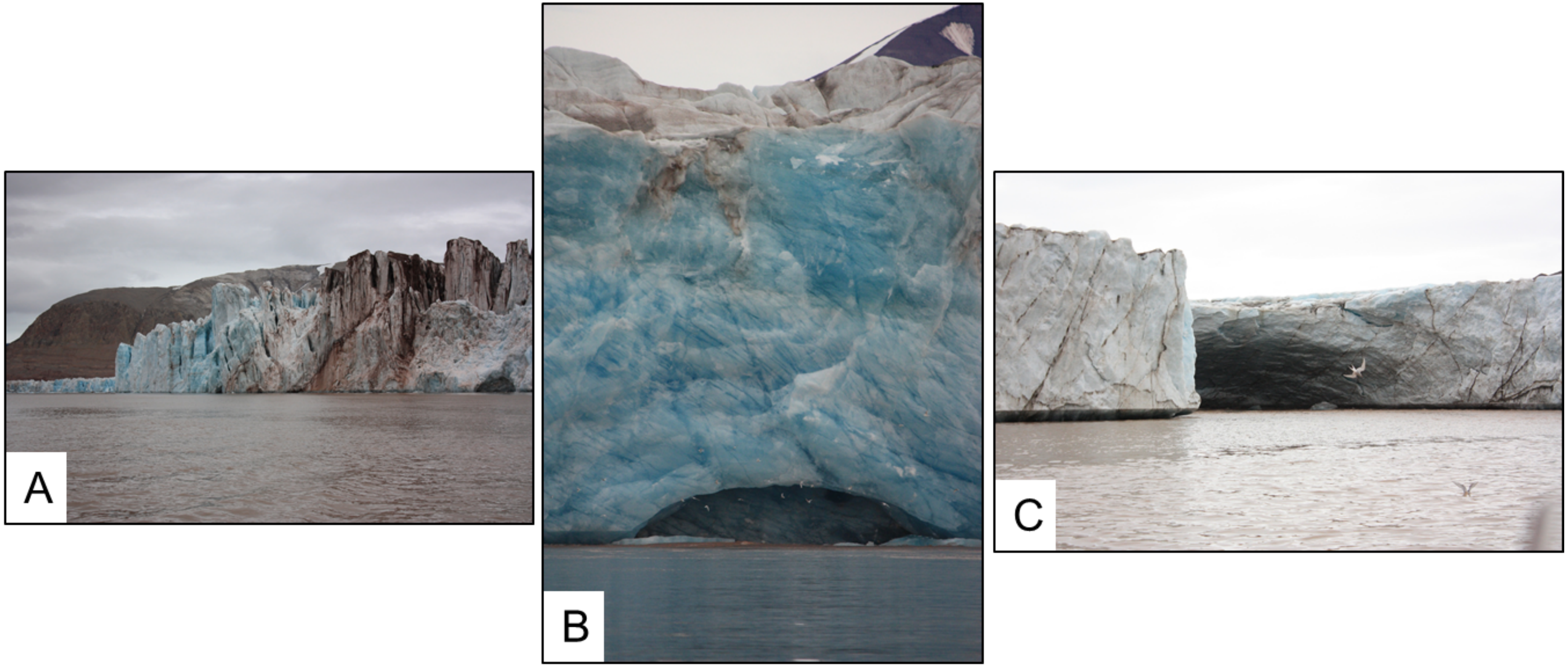

Figure 1.4: Photographs of Kronebreen glacier calving face: (A) Looking to the north, glacier is formed of pinnacles heavily laden with sediment (B) The centre of the glacier has the highest elevation. Here, and ice cave formed. The sediment rich water makes a popular location for marine birds (C) Southern extent at Kongsvegen. Another undercut channel in the ice.

Kronebreen terminates with an ice cliff directly into Kongsfjorden (Figure 1.4). The ice cliff measures 3.2 km wide (Błaszczyk et al., 2009) and extends 5 – 60 m vertically above the fjord surface in August (Chapuis, 2011). It is shared with Kongsvegen and Infantfonna, however, Kronebreen currently occupies approximately 70% of the width (Sund et al., 2011). Kongsvegen's calving front is small, with the majority of the glacier terminating on land.

Kronebreen (including its associate ice field catchments) is approximately 50 km long, with an elevation range of 0 – 1400 m (Nuth et al., 2012). The surface elevation at the glacier centre line is steepest near the calving front, increasing from 0 – 700 m, within 20 km distance of the calving front (Figure 1.5; Solbø and Storvold, 2013). It has a mean thickness of 289 m and a maximum thickness of 434 m (Bamber, 1989). Digital terrain models indicate that there are two prominent longitudinal ridges on Kronebreen, with the glacier surface reflecting bed topography. One is located at the northern margin and the other in the centre (Sund et al., 2011). These are separated by an overdeepening in the bed, approximately 80 m below sea level (Sund et al., 2011).

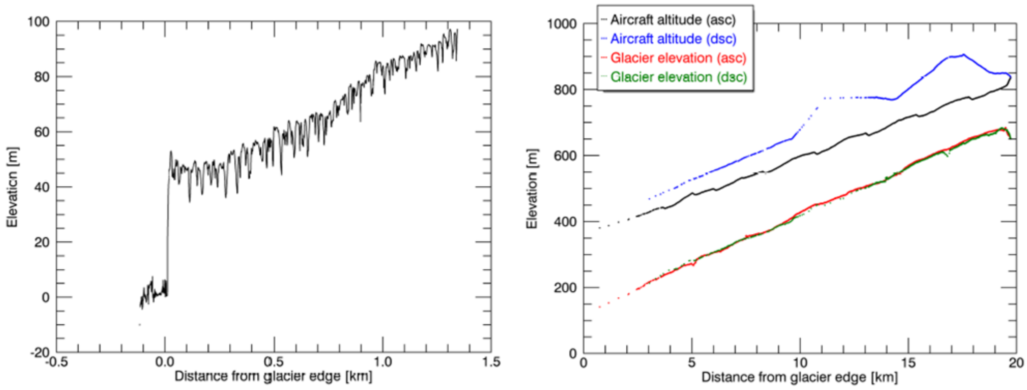

Figure 1.5: Elevation profiles measured using the Cryowing UAS: (left) displaying the glacier front and the heavily crevassed region behind the calving front (right) elevation profile along the centre line of Kongsvegen (Solbø and Storvold, 2013).

Typical surface velocities of tidewater glaciers in Svalbard are in the region of $\sim$ 100 m yr^{-1}, whilst Kronebreen exhibits velocities of 300 – 800 m yr $^{-1}$ at its calving face (Błaszczyk et al., 2009). This makes it Svalbard's fastest measured glacier due to its large drainage area and narrow outlet channel, exhibiting a mean annual velocity of 2 m d^{-1} (Hagen et al., 2003a; Błaszczyk et al., 2009), whilst summer velocities range from 1 – 3.5 m d^{-1} (Kääb et al., 2005; Rolstad and Norland, 2009). The fast flow of Kronebreen is persistent, with measurements taken in 1964 (Voigt, 1966), 1986 (Lefauconnier et al., 1994) and 2000–02 (Kääb et al., 2005) all presenting similar velocities.

Intra-seasonal velocity change of Kronebreen has been captured by photogrammetric techniques, indicating that summer a speed up commences around mid-June, peaking in mid-July (Svanem, 2011). August and September typically exhibit slower velocities (Svanem, 2011). Kronebreen's velocity is greatest within 4.5 km of the calving front, as identified by remote sensing using synthetic aperture radar feature tracking (Schellenberger et al., 2014). The *in situ* samples for this study were taken between 14 – 18th July 2012, during the seasonal peak in velocity of ~3 m d^{-1} at Kronebreen's calving front (Figure 1.6; Schellenberger et al., 2014).

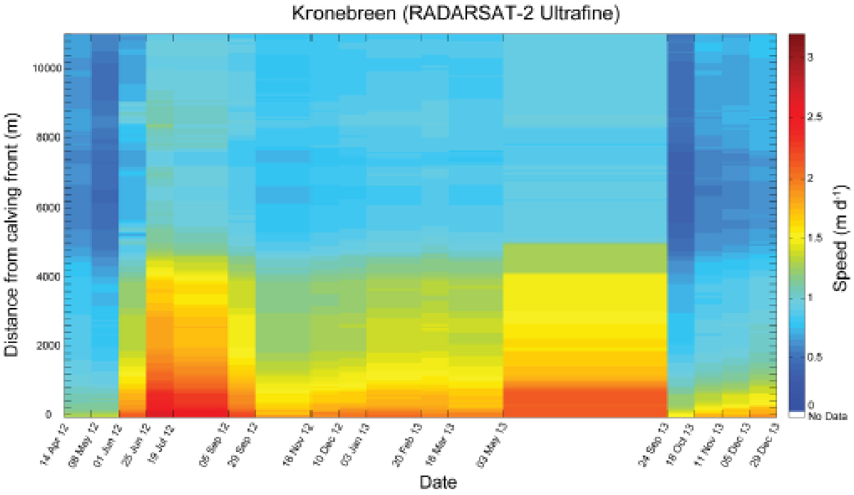

Figure 1.6: Time series of seasonal speed of Kronebreen's velocity, with distance from the calving from, taken at the centre line between 14th April 2012 – 29th December 2013 using RADARSAT-2 Ultrafine data (Schellenberger et al., 2014).

Kongsvegen covers an area of 102 km^2 and is 26 km in length, with a north-westerly flow direction from an ice divide at 800 m a.s.l (Figure 1.2). It terminates at Kongsfjorden, where the majority is on land, but a small part actively calves alongside Kronebreen. It has the been studied annually since 1987, when the first mass balance stakes were put in place by the Norwegian Polar Institute. The longevity of measurements makes it an ideal location for glacier mass balance studies. The changes in altitude of Kongsvegen are reflective of the net glacier mass balance, because it does not calve at the same rate of Kronebreen (Hagen et al., 2003b).

Its flow rate contrasts Kronebreen's in that it's only <4 m yr^{-1} (Melvold and Hagen, 1998), reflecting its quiescent phase. Glaciers of Svalbard experience the quiescent phase for 50 – 100 yeasr, while surges last for only 3 – 10 years (Dowdeswell et al., 1991). From 1987 – 1994 Kongsvegen exhibited a weak but positive net balance of 0.09 m w. eq (Melvold and Hagen, 1998). However, from 1965 – 2005 Kongsvegen underwent a net mass loss of -1.8 m w. eq, which is small in comparison to the neighbouring glaciers of Midre Lovénbreen (-1.17 m w. eq) and Austre Brøggerbreen (-18.8 m w. eq)(Karner et al., 2013). The initial mass gain has been attributed to a dynamic response to the last surge event in 1948 (Hagen et al., 2003a).

1.2.3 Historical change of the tidewater termini

The Kronebreen - Kongsvegen tidewater glacier complex was at its maximum Holocene extent during the Little Ice Age (Liestøl, 1988). It has since been in retreat, interrupted by advance through surging, three times in historical documentation. Liestøl (1988) notes the earliest advance took place around 1800, with two more taking place in 1869 (Lamont, 1876) and 1948 (Bennett et al., 1999). Prior to the 1948 surge, the width of Kongsvegen and Infantfonna at the ice cliff was near equal, where together they occupied 25% of the ice cliff, which was dominated by Kronebreen. The surge of 1948 saw Kongsvegen push north, as determined by the medial moraine. This was reversed by 1964, as Kongsvegen was pushed south, and the Infantfonna ice stream no longer reached the ice cliff; Kronebreen then occupied 65% of the ice cliff (Voigt, 1967).

Between 1975 and 1983 sediment contributions to Kongsfjorden built a delta in front of Kongsvegen spanning 180 m out from the glacier, with an estimated volume of 4.5 x 10^6 m^3 (Lefauconnier, 1987). The summer flux being discharged from the glacier complex at the time was 0.25 x 10^6 m^3 (Elverhøi et al., 1980). The shared glacier complex terminus has fluctuated with time, having retreated 11 km since its maximum in 1869 (Liestøl, 1988); 6 km of this has occurred since its surge in 1948 (Trusel et al., 2010). However, calving was responsible for 97.5% of Kronebreen's geodetic volume change between 1960 – 1995 and decreased to 75% from 1995 – 2007 (Nuth et al., 2012).

During the latter part of the 20th century, Kronebreen exhibited a maximum ice velocity of 785 m yr^{-1} (Melvold, 1992) and an average retreat of 50 m yr^{-1}; this contrasts Kongsvegen which was largely stationary (Lefauconnier et al., 1994). Since 1990, the Kronebreen - Kongsvegen glacier front has been mobile, but stable (Figure 1.7). Its position has fluctuated, yet exhibits a trend of retreat. A large retreat of 850 m occurred in 2011, causing a loss of area totalling 2.8 km^2 (Schellenberger et al., 2014).

Another retreat took place in 2013; Kronebreen's terminus retreated 500 – 750 m from its 2011 location. Most noticeably, Kongsvegen retreated dramatically in 2013 compared to the rest of the glacier complex (Figure 1.7), contrasting its previous relatively static state (Lefauconnier et al., 1994).

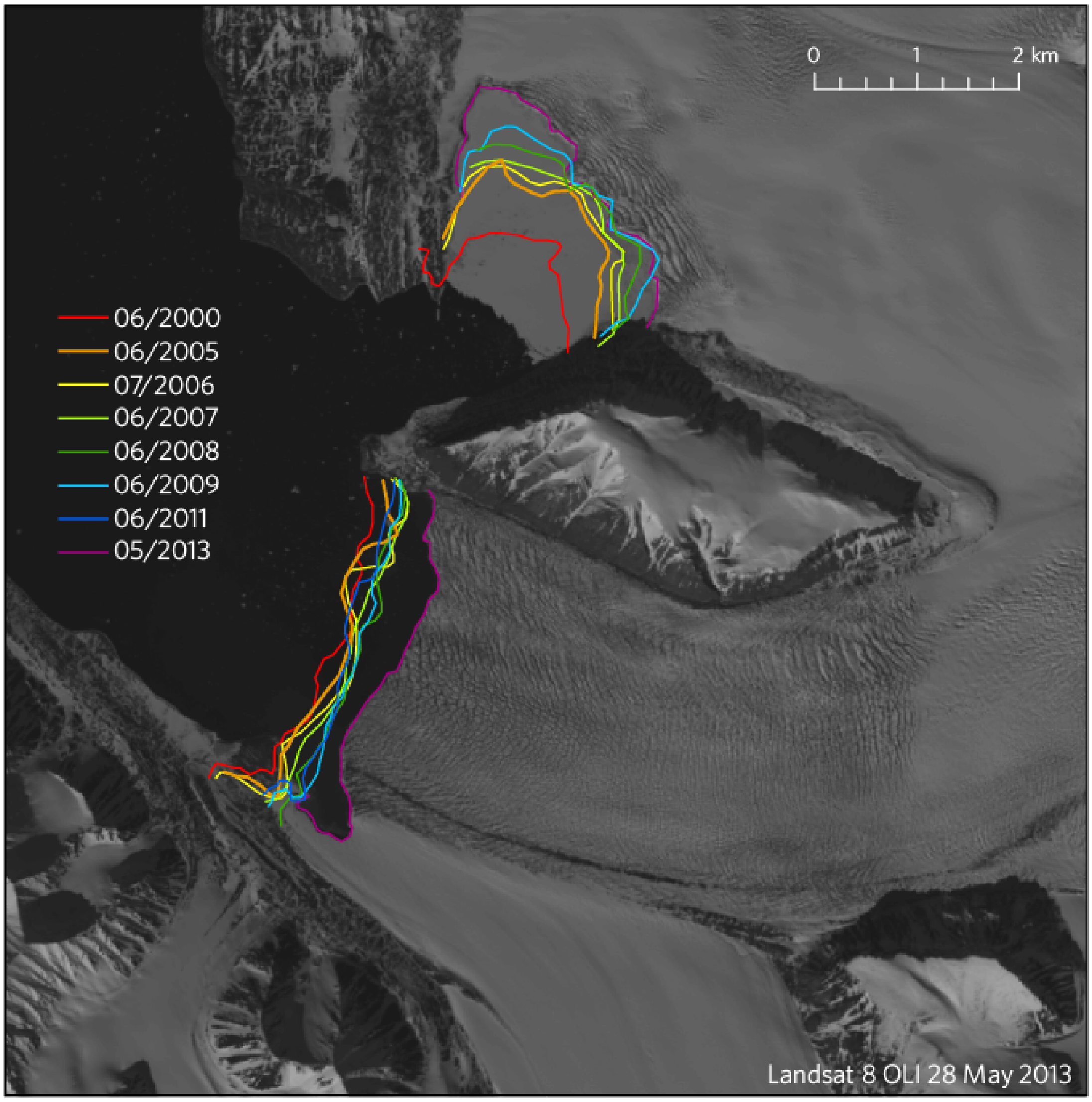

Figure 1.7: The location of the glacier front of Kronebreen - Kongsvegen from 2000 - 2013 (Trusel 2014, pers.comms)

1.2.4 Geological and geomorphological setting

Devonian sandstones and siltstones dominate the upper reaches of Kronebreen south, whilst the lower extent is situated upon Permo-Carboniferous limestone and chert (Harland, 1997). Central and northern Kronebreen lies upon metamorphic rocks formed of marble, schist and psammite dated to the Middle Proterozoic (Svendsen et al., 2002).

The geomorphological regime of Kongsfjorden is dictated by glacial activity. The bathymetry and fjord topography has been sculpted by periods of glacial advance and retreat. Moraine assemblages formed on the southwest side of Kongsfjorden as a result of the advances in 1869 and 1948 (Whittington et al., 1997; Bennett et al., 1999). During phases of retreat, glacier sliding and abrasion of bedrock contributes sediment to the fjord, reducing the water depth (Powell, 1991). Approximately 10 m of sediment has been deposited on top of the ice-scoured bedrock in central and outer Kongsfjorden, which was last exposed during the glacial re-advance of the Little Ice Age (Howe et al., 2003). Kongsfjorden continues to be shaped by contemporary glaciomarine sedimentary processes. Subglacial sediment is entrained in meltwater, and enters the fjord from the base of the glacier in two locations: 1) at the centre of the glacier, via a subglacial stream and 2) at the southern margin of Kongsvegen via an ice-marginal stream (Trusel et al., 2010). The location of the central subglacial stream has undergone change; between 1987 and 2001 it was located in the centre of the ice front, but it moved north by 400 – 500 m in 2002 (Kehrl et al., 2011). The grounding line fan at the location of the previous subglacial stream is being degraded in contrast to the new location which is observed to have a sedimentation rate between 0.06 m a^{-1} (Trusel et al., 2010) and 1 m a^{-1} (Kehrl et al., 2011).

1.3 Research aims and thesis structure

This overarching aim of this thesis is to quantify meltwater inputs from the tidewater glacier Kronebreen, into Kongsfjorden, Svalbard, and to bolster understanding regarding meltwater production, transport and delivery into the fjord environment. This is achieved using a multi-method approach, utilising *in situ* hydrographic measurements, spectral reflectance and total suspend solids (TSS), from a field campaign in July 2012, together with remotely sensed data. The methods employed offer a means to progress knowledge regarding the interactions and feedback mechanisms of tidewater glaciers with the atmosphere and ocean, which has been highlighted as a research priority (IPCC, 2013). Better constraints on meltwater contributions from glacier marine margins is important to accurately forecast sea level rise, which poses large societal impacts. The following interdisciplinary research encompasses the atmosphere, cryosphere, ocean and glacimarine sedimentary processes. To further understand the links between these processes, the research aims of this study are to:

i Determine the origin of freshwater inputs and to quantify the amount being delivered to the marine environment at the head of Kongsfjorden.

ii Calibrate MODIS satellite imagery with *in situ* measurements to determine the daily to interannual variability of freshwater and TSS from 2002 – 2013.

iii Understand the meteorological and cryospheric controls on meltwater production, storage and delivery from Kronebreen - Kongsvegen to Kongsfjorden.

iv Determine the external forcing factors affecting the spatial plume extent and TSS, once discharged to the fjord.

A detailed evaluation of oceanographic, climatic and glacier controls on meltwater production, along with a description of the environments of Kronebreen and Kongsfjorden is given in Chapter 2. Chapter 3 presents the hydrographic properties at the head of Kongsfjorden, together with identifying the source of the freshwater contributions and subsequent impacts on fjord circulation. Chapter 4 details the method of quantifying TSS and sediment plume area by calibrating MODIS satellite imagery with *in situ* spectral reflectance and TSS measurements. An assessment is made as to the effectiveness of this method. Chapter 5 uses meteorological and modelled runoff data together with the plume size and TSS, as determined in Chapter 5, to ascertain the drivers and temporal variability of seasonal and interannual meltwater production. Focus is placed on the spatial distribution of TSS and the influencing factors in Chapter 6. The final discussion, conclusions and prospects for future research are presented in Chapter 7.

Chapter 2

Tidewater glaciers in the ocean - climate system

Tidewater glaciers form a dynamic part of the cryosphere; influenced by both the climate and the oceans, each element needs to be investigated to fully understand the impacts to the glacier system. Yet obtaining high-resolution data sets of both the cryospheric and oceanic elements of marine terminating glaciers is impeded by logistical constraints: access to glacier termini is difficult owing to ice melange in fjords, active iceberg calving and the high costs associated with extensive field campaigns. Remote monitoring of sediment plumes, discharged from the grounding line of tidewater glaciers, holds potential to determine meltwater discharge over prolonged periods of time. To this end, this chapter aims to explore and discuss the following key areas required to form a solid understanding of both the environment and remote detection methods:

i Local oceanographic properties and fjord circulation

ii Climatic controls on supraglacial meltwater production and glacier hydrology

iii Subglacial and glacimarine sedimentary processes

iv Methods of remote detection of sediment plumes

2.1 Oceanographic influences

2.1.1 Regional coastal currents

The northward flow of the WSC is a principal pathway of heat and volume transportation to the Arctic from lower latitudes (Figure 2.1; Aagaard and Greisman, 1975). The AW in the WSC is topographically steered along the continental shelf

(Jónsson et al., 1992; Woodgate et al., 1998), flowing northwards, with maximum temperature, salinity and velocity centred at its core (Saloranta and Haugan, 2004). A barrier between the WSC and the west Spitsbergen fjords is formed of cooler, less saline, Arctic water (ArW), which also flows northwards (Figure 2.2) (Saloranta and Svendsen, 2001). Upwelling in the WSC is caused by northerly winds, resulting in Ekman drift; when the horizontal density gradient is changed, exchange takes place between the WSC and ArW (Svendsen et al., 2002; Cottier et al., 2007). Transformed Atlantic water (TAW) is clearly distinguishable from the WSC, and is formed when AW crosses the shelf, mixing with ArW (Cottier et al., 2005).

The exchange between northerly flowing coastal currents and fjord waters is variable, dependant on the geostrophic coastal flow at the mouth of the fjord (Klinck et al., 1981). When meanders and eddies form in the WSC, heat is transported across the shelf and towards the west coast fjords (Nilsen et al., 2006; Teigen et al., 2010). The direction of the wind influences this cross-shelf exchange, due to Ekman drift. Southerly winds initiate downwelling, with the geostrophic gradient promoting a greater build up of water at the coast. The reverse is true under the influence of northerly winds, where export away from the coast occurs. The volume of AW transported into the fjords is dictated by eddy formation, as demonstrated by numerical modelling of cross shelf exchange at Kongsfjorden (Tverberg and Nøst, 2009). As such, the water mass classification from Cottier et al. (2005) reflects water masses from the adjacent shelf, and within Kongsfjorden.

Heat and volume transport to the Arctic is interannually variable, resulting in significant changes to the Arctic heat budget (Aagaard and Greisman, 1975). Increased volume transport of AW intensified between 1995 and 2007 (Walczowski and Piechura, 2007), leading to warmer temperatures in the WSC from the early 2000s (Figure 2.3; Schauer et al., 2008). Warm anomalies in AW have been advected north through the Fram Strait by the west WSC, since the late 1990s (Schauer et al., 2004). From 1997 – 2005, the temperature of AW south of Spitsbergen, rose by approximately 1°C and salinity increased by 0.06 PSU; maximum temperatures were observed in 2001 and 2005 (Walczowski and Piechura, 2007). Lateral mixing, particularly in the subsurface water of the column (below 50 – 100 m), acts as a heat exchange between WSC and ArW; greater lateral spread of heat promotes heat exchange with the atmosphere and sea ice (Saloranta and Haugan, 2004). The influence of this has been measurable in fjords located on the west coast of Spitsbergen, with approximately a 2°C rise in temperature between 1912 – 2009 (Pavlov et al., 2013). Temperatures in the WSC core intensified during the 2000s (Walczowski and Piechura, 2007; Schauer et al., 2008), promoting stronger 21st century warming in Spitsbergen's west coast fjords (>1°C), comparable to

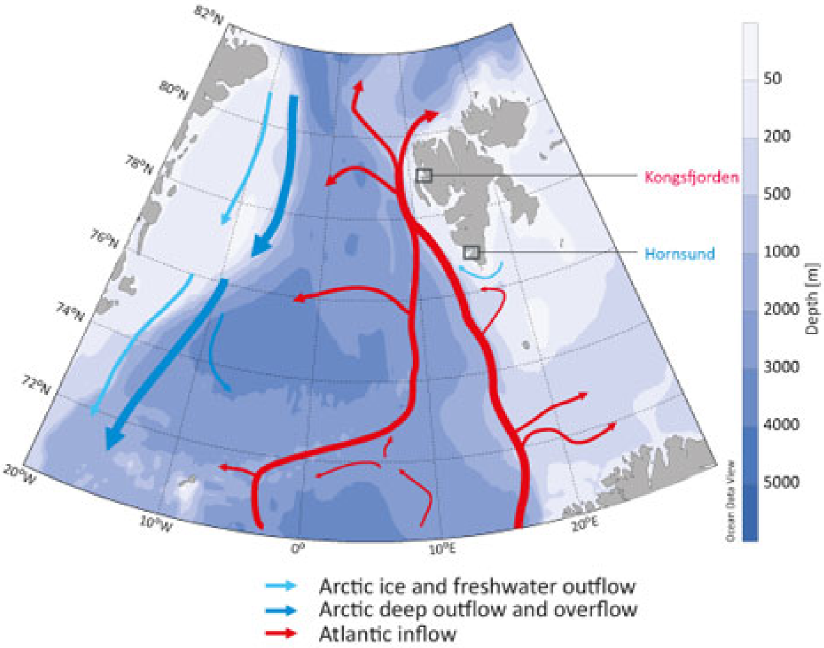

Figure 2.1: Schematic displaying the northerly AW inflow passing the west coast of Svalbard, contrasting the southerly flow of Arctic freshwater outflow (Weslawski et al., 2015)

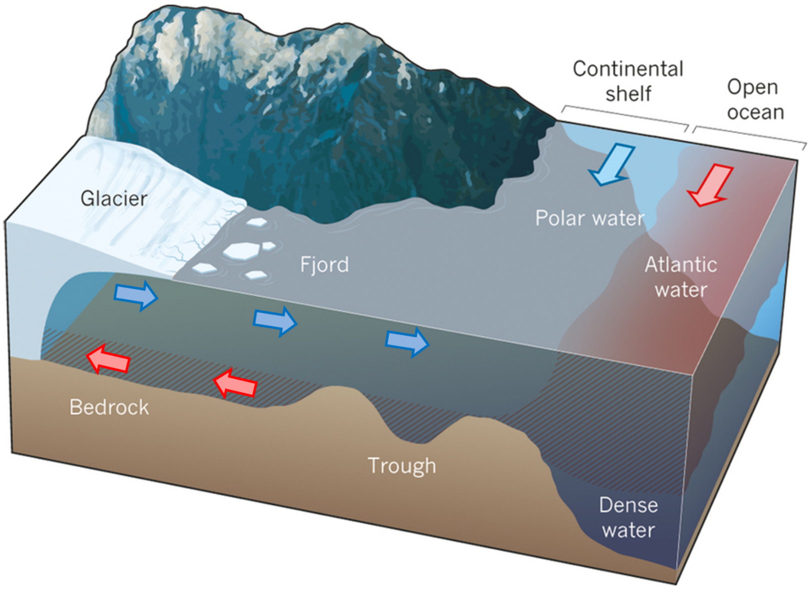

Figure 2.2: Diagram illustrating coastal currents and fjord circulation. Warm, saline AW is transported by the WSC. Polar water (ArW) provides a cold buffer between AW and the fjord itself. AW flows into fjords at depth, with a freshwater surface outflow driven by glacier meltwater. Modified from Straneo and Heimbach (2013).

historical records for the 20th century (Pavlov et al., 2013). Warm TAW was again prominent in the summer of 2011 (Nilsen, 2011).

Unlike many Arctic fjords the Kongsfjorden - Krossfjorden system doesn't have a defined sill, which enables easier transport of shelf waters into the fjord (Svendsen et al., 2002). The amount of heat that reaches the surface of the water column, plays a role in determining if sea ice will form in fjords (Tverberg and Nøst, 2009; Nilsen, 2011). As a result, the region west of Kongsfjorden remains largely sea ice free due to heat transport from the WSC, which ranges from 28 – 45 TW (Schauer et al., 2004), 42 TW (Cisewski et al., 2003), up to 70 TW (Walczowski et al., 2005).

The inner part of Kongsfjorden contrasts that of the mouth, with considerable contributions of freshwater from the five tidewater glaciers. An estimated 1.4 ± 0.42 km^3 of freshwater flows into Kongsfjorden annually, from glacier and snow melt, precipitation and surface runoff (Svendsen et al., 2002). The freshwater contribution accounts for approximately 5% of the water mass in the fjord (Cottier et al., 2005), substantially greater than the average of 1% found in Spitsbergen's fjords (Cottier et al., 2010). Whilst climatically sensitive, the freshwater contributions are an important element to accurately quantify. Glacial melt forms surface water (SW) at the head of the fjord, which decreases with distance from the glacier (Svendsen et al., 2002; Cottier et al., 2005). The runoff from some catchments

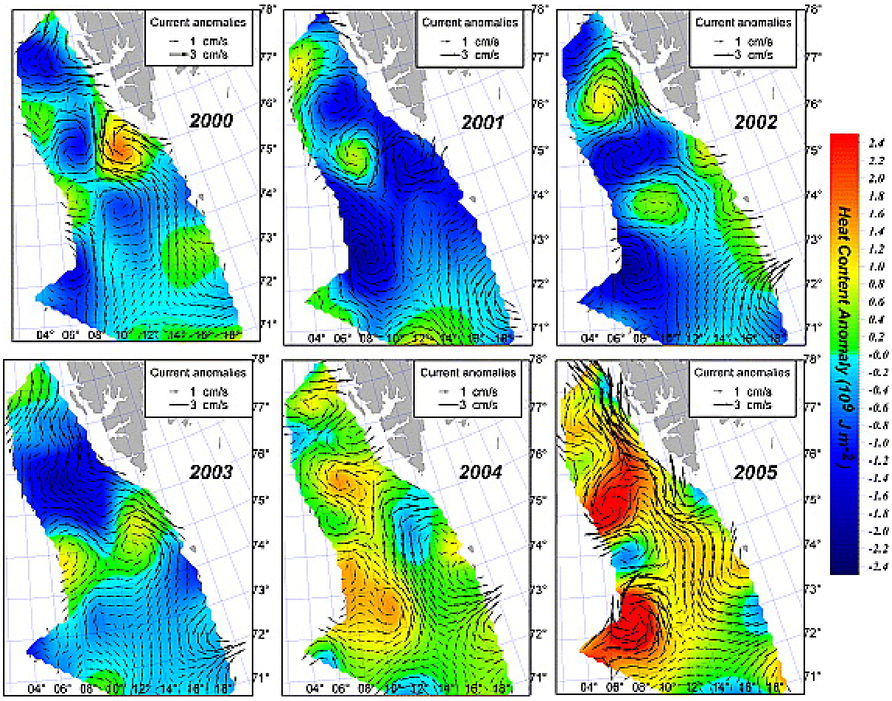

Figure 2.3: Anomalies in AW heat content and baroclinic currents, at 100 m depth. Anomalies calculated from the differences from the July mean, 2000 – 2005 (Schauer et al., 2008).

which enter closer to the mouth of Kongsfjorden, such as Bayelva, terminate terrestrially allowing freshwater discharge to be quantified by runoff gauging stations (Killingtveit et al., 2003). However, owing to the tidewater nature of the terminus of the Kronebreen - Kongsvegen system, such meltwater discharge is not possible with current methods. This causes large uncertainties when quantifying glacial meltwater inputs to the marine system, affecting the accuracy of SLR forecasts (Church et al., 2013). Intermediate water (IW) forms when SW mixes with AW and TAW.

Tides propagate along the west Spitsbergen coast as Kelvin waves (Gjevik and Straume, 1989). The tidal amplitude outside of Kongsfjorden is 0.5 m, which propagates into the fjord. The average tidal range at Ny-Ålesund is 1.8 m and the maximum is 2.3 m. Tides in Kongsfjorden are predominantly semi-diurnal lunar (M_2), with a solar component (S_2) of approximately 50% of the M_2 component (Svendsen et al., 2002).

2.1.2 Circulation of glacial fjords

Freshwater plays a key role in the circulation of Arctic fjords, and it has two potential origins: i) submarine glacial melt, caused by either the ocean directly melting the ice face (e.g. Holland et al., 2008; Sutherland and Straneo, 2012; Straneo et al.,

2013) or convection driven melt (Jenkins, 2011) and ii) freshwater runoff, driven by surface ablation (e.g. Hodgkins, 1997; Karner et al., 2013). Increased volumes of supraglacially produced runoff discharged at depth, can initiate further submarine melting of the ice face (Kimura et al., 2014), forming a positive feedback mechanism which enhances submarine melting. This freshwater flux plays a key role in the circulation of glacial fjords (Figure 1.1).

Fjords typically exhibit a two layer circulation, with the upper layer largely influenced by wind stress, and the bottom layer dominated by coastal inflow (Klinck et al., 1981). Glacial fjords have an additional forcing mechanism affecting the physical dynamics: the freshwater flux from glacier melt (Cowan, 1992; Ingvaldsen et al., 2001). The fjords on the west coast of Spitsbergen are the most sensitive to the northward flow of warm, saline AW (Figure 2.1). Melt contributions to glacial fjords freshens the surface layer, and supplies fine grained sediment to the fjord. Biological productivity is already low, and is sensitive to changes in the freshwater balance (Cui et al., 2006), whilst sediment at the fjord surface could impose light limitations on the surface layer.

2.1.3 Seasonal water mass modification and circulation processes

Arctic fjords undergo seasonal changes in circulation and stratification, responding to meltwater inputs, temperature changes and sea ice formation (Figure 2.4) (Matthews, 1981; Cottier et al., 2010). Spring and summer are governed by thermal processes, and autumn and winter by salinity driven processes (Cottier et al., 2007). This not only governs the water masses, but vertical overturning circulation in the fjord (Figure 2.4). Glacial meltwater entering the fjord at depth during summer, creates upwelling and vertical mixing. The effect of meltwater on water column stratification decreases with increasing distance from the source, as a result of dilution and mixing (Cottier et al., 2005). Brine rejection in the winter months forms the reverse processes, with dense water being produced at the surface, initiating convective over turning of the full water column (Cottier et al., 2010).

A three water mass structure is present, formed of: SW, IW and old winter water (Cottier et al., 2010). The very surface of the SW can be capped with a freshwater lens from meltwater inputs (Rysgaard et al., 1999b). The SW temperature can reach >5°C, due to atmospheric heat gain and the insolating effect of suspended sediment, transported to the fjord by glacial melt (Rysgaard et al., 1999b; Cottier et al., 2005; Nilsen et al., 2008). Downward mixing of meltwater produces a brackish layer, which evolves with the seasonal development and deep-

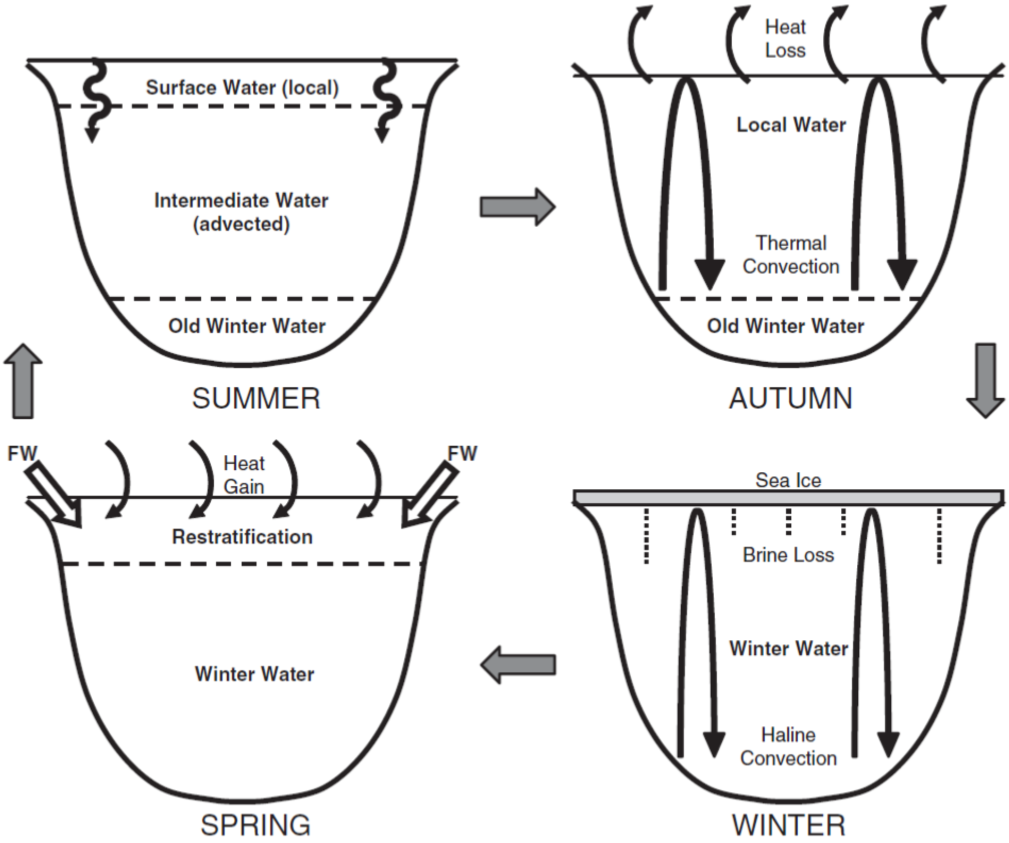

Figure 2.4: Illustration of the seasonal development of stratification and mixing in a shallow (<300 m) glacial fjord, typical of Svalbard (Cottier et al., 2010).

ening of a pycnocline (Figure 2.5), responding to seasonal change in freshwater transport (Matthews, 1981). This mixing leads to the modification of IW, which becomes warmer and less saline during the summer (Skogseth et al., 2005b). Two layer circulation is typical in summer, with the inflow of AW and IW at depth, and the outflow of the fresh SW (Figure 2.2).

Rapid sensible heat removal from the water column occurs during autumn, driven by colder atmospheric temperatures and intensified wind strength (Cottier et al., 2007). Cooling of the SW drives thermal convection, producing a well mixed water column, which overlies old winter water. Winter cooling brings fjord waters to freezing point, generally between November and December in Svalbard (Gerland and Renner, 2007), which prompts sea ice formation. Brine rejection increases the salinity and density of the upper water column, which forms Winter Cooled Water (WCW; Svendsen et al., 2002; Nilsen et al., 2008). The increased salinity in the upper water column drives haline convection. This results in a fully mixed water column, which enables the bottom waters in the fjord to be re-oxygentated (Nilsen et al., 2008). It is the sea ice production that governs the formation of WCW, but in some fjords, thick winter sea ice does not form (Cottier et al., 2007; Gerland

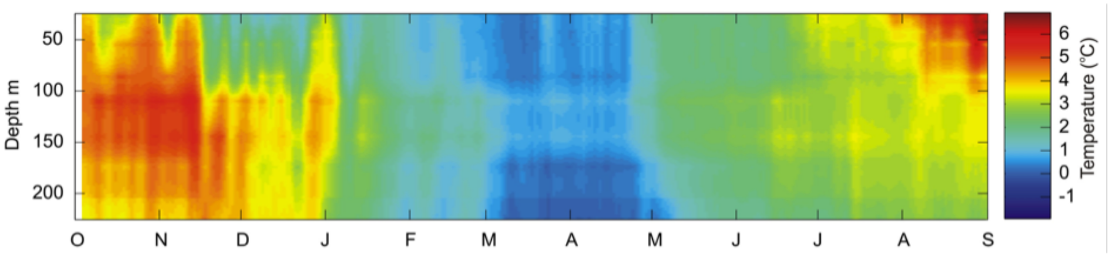

Figure 2.5: Temperature plot displaying seasonal variation from moored observations between 4th of October 2012 and 1st of September 2013 in Kongsfjorden (Nahrgang et al., 2014).

and Renner, 2007), leading to fresher winter water. The presence of sea ice during winter prevents wind mixing, but makes the effects of tidal mixing more prominent (Fer and Widell, 2007).

2.1.4 Effect of the Earth's rotation

Some fjords are affected by the Coriolis effect; however, this is dependant on the fjord width and the depth of stratification (Cushman-Roisin et al., 1994). The Rossby radius of deformation provides a means of determining the importance of both stratification and rotation. It is the ratio of the speed of a baroclinic (internal) wave to the Coriolis parameter. Measuring 20 km in length and 4 – 10 km wide, Kongsfjorden is deemed a "board fjord". The effects of Coriolis are felt in Kongsfjorden during the summer months, due to a Rossby radius of deformation of approximately 4 km (Svendsen et al., 2002; Cottier et al., 2005). However, given the seasonality associated with Arctic fjord stratification, the effect of rotation will depend on the season.

The definition of the internal Rossby radius (r_i), in a two layer model is given by:

$$r_i = \frac{c_i}{f} \tag{2.1}$$

where

$$c_i^2 = \frac{g' H_1 H_2}{H} \tag{2.2}$$

is the phase speed of the baroclinic wave and

$$g' = g\frac{\rho_1 - \rho_2}{\rho_2} \tag{2.3}$$

is the reduced gravity, and ρ_1, ρ_2, and H_1, H_2, are the upper and lower densities and depths, respectively, H is the total water depth and f is the Coriolis parameter. Under summer, stratified conditions, r_i is approximately 3.5 – 6 km; this is less than the typical outer Arctic fjord width of 10 km. Therefore many high-latitude fjords, such as Kongsfjorden, are affected by rotational dynamics, despite r_i decreasing with increasing latitude. As such, high latitude fjords exhibit circulation patterns which are more complex than the two layer estuarine system; this has been reported for numerous Arctic fjords (Cushman-Roisin et al., 1994; Ingvaldsen et al., 2001; Svendsen et al., 2002; Cottier et al., 2005; Skogseth et al., 2005a; Skarhamar and Svendsen, 2010).

As a result of rotational circulation, inflowing water masses typically hug the right hand side of the fjord. The distribution of freshwater across the fjord surface is also altered. Hydrographic observations reveal that meltwater contributions are deflected to the right of the direction of outflow (Ingvaldsen et al., 2001; Svendsen et al., 2002; Skogseth et al., 2005b). This creates a horizontal gradient in surface temperature over the width of fjords, that are influence by Coriolis (Aliani et al., 2004).

2.1.5 Sea ice

The WSC keeps the west coast of Svalbard largely ice free (Vinje, 1982), however sea ice in Kongsfjorden is present during winter, generally between December and March (Svendsen et al., 2002). However, the warming of the WSC has been attributed to the reduction in winter sea ice extent around Svalbard, particularly in the north (Onarheim et al., 2014).

Between 1981 – 1986 sea ice in Kongsfjorden was recorded to break up between April and July (Mehlum, 1991; Lydersen and Gjertz, 1986). The period of break up was reduced between 2003 – 2005, in which sea ice at the head of Kongsfjorden broke up between 28th May and 11th June (Figure 2.6 Gerland and Renner, 2007). The maximum thickness of sea ice between 2003 – 2005 was between 0.83 – 1.03 m, which declined to 0.63 m in 2005 due to a milder season (Gerland and Renner, 2007). In 2006 Kongsfjorden was completely ice free by 10th May which coincided with high air temperatures on Svalbard in winter and spring (Gerland and Renner, 2007). In general Arctic sea ice has continued to decline (Cavalieri and Parkinson, 2012) and thin (Lindsay and Schweiger, 2015). The maximum winter sea ice extent, determined in March, only reached the northern extent of Svalbard, and the west coast remained predominantly ice free (Figure 2.7) (Perovich et al., 2013).

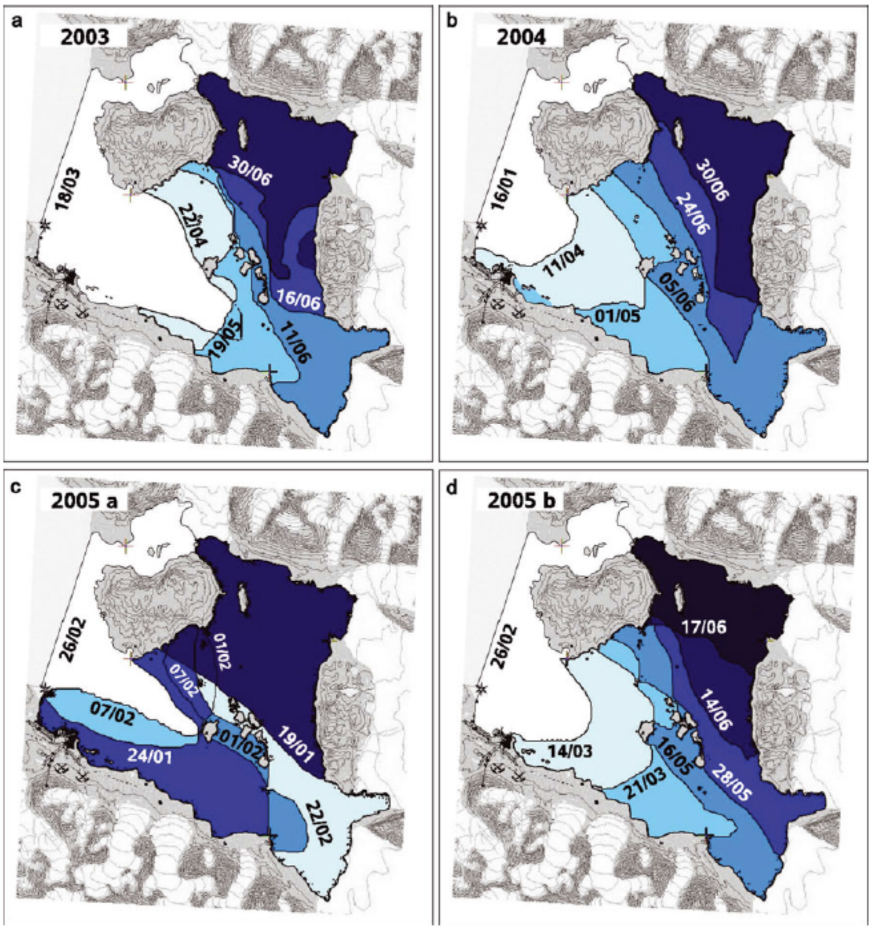

Figure 2.6: Timing and extent of fast sea ice extent at the head of Kongsfjorden from 2003 – 2005. It should be noted that Kongsfjorden was sea ice free in 2006 (Gerland and Renner, 2007).

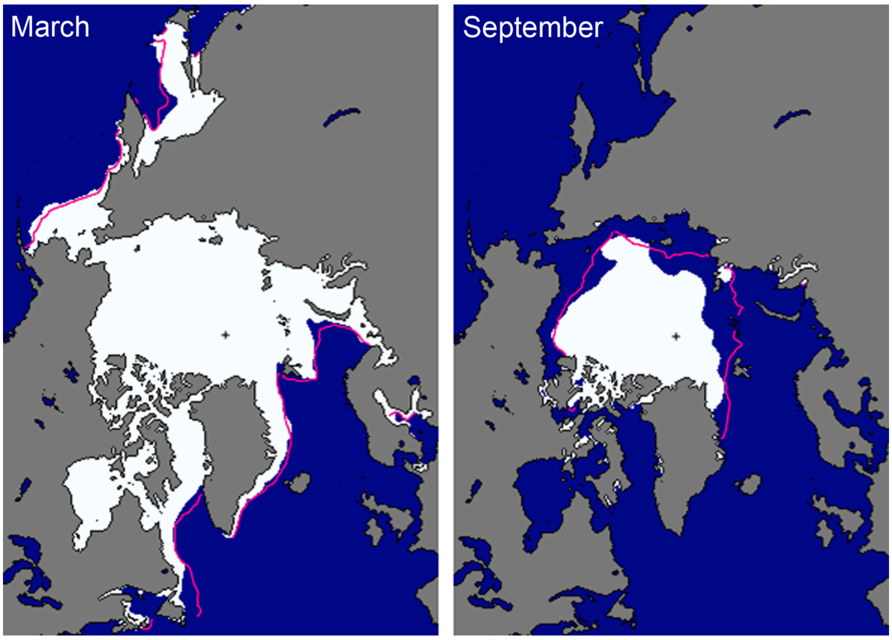

Figure 2.7: Winter maximum (March) and summer minimum (September) sea ice extents for 2013. The magenta line indicates the median sea ice extent during the period 1981 – 2010 (Perovich et al., 2013).

2.2 Meteorological influences on the west coast of Svalbard

Arctic warming has been observed over the past 35 years, but Svalbard, unlike Greenland, has not displayed accelerated melting (Lang et al., 2015). Whilst Greenland has exhibited record melt in the last 10 years (Fettweis et al., 2013), the surface mass balance (SMB) of Svalbard has remained closer to balance since 2004 (Moholdt et al., 2010). This implies that the ice cap of Svalbard appears to be less sensitive to the recent Arctic warming (Serreze et al., 2009). Such stability has been attributed to the change in atmospheric circulation which sees Svalbard receive north-westerly atmospheric flows (Lang et al., 2015). Despite this, the Svalbard's west coast glaciers have been losing mass; Kongsvegen and Kronebreen underwent increased melt during the 1990s (Kohler et al., 2007; Nuth et al., 2012) and Kronebreen's tidewater terminus has retreated (Figure 1.7).

2.2.1 Seasonal patterns

Air temperatures in Kongsfjorden are strongly seasonal; solar radiation becomes positive in mid February, and remains positive until the end of October (Figure 2.8. Winter temperatures typically reach -15°C and rise to 6°C by mid summer (eKlima, 2014). Winter temperatures are more variable, owing to the larger temperature difference between air masses originating from the Arctic and the Atlantic (Hanssen-Bauer et al., 1990; Førland et al., 1997). The advection of mild maritime air over cold land surfaces is greatest during the summer months, producing Arctic sea fog and over cast days. Cloud free days are most frequent in winter (5 – 8 days/month), contrasting the summer months (June-September), which have the lowest number of clear days annually, approximately 1 day/month (Førland et al., 1997). Seasonal snow cover changes the surface albedo of the region, with typically 94 snow free days in the summer (Winther et al., 2002). Radiation produces the energy to melt the snow (Boike et al., 2003), which is subsequently transported to Kongsfjorden (Svendsen et al., 2002). Wind forcing is topographically steered from the head to the mouth of Kongsfjorden (Hanssen-Bauer et al., 1990; Førland et al., 1997), driven by the land-sea breeze (Esau and Repina, 2012). The winter months typically have faster wind speeds than the summer months. The wind forcing in Kongsfjorden plays a key role in moving SW, but cannot penetrate beneath the strong pycnocline in the summer months. During the autumn and winter, the wind plays a larger role in driving the over turning circulation in Kongsfjorden (Cottier et al., 2010).

2.2.2 Interannual variability

The Icelandic low pressure and the Greenland high pressure, forces warm humid air towards Svalbard, which dictates the large scale atmospheric circulation of the region (Svendsen et al., 2002). Typically, the Icelandic low pressure sits between east Greenland and Iceland, driving cyclonic circulation between Europe and Greenland. This generally results in northerly winds being channelled down the west coast of Spitsbergen, which is partly why the SMB of Svalbard is in relative stability (Lang et al., 2015). Increased cyclone activity occurs in the Fram Strait, with anomalously high pressures over Scandinavia, resulting in milder winters for Spitsbergen (Rogers et al., 2005). However, cyclone activity focussed in the Barents sea results in colder winters (Rogers et al., 2005). Positive phases of the North Atlantic oscillation (NAO) result in cyclone events being twice as common, compared to the negative extreme (Serreze et al., 1997). This was exemplified in January 2006, when the Icelandic low moved east of Iceland, and a large, high pressure system was located over Russia and the Eastern Arctic. Cyclone activity in the Fram Strait intensified to the extent that the wind direction along the west coast of Spitsbergen reversed, from northerly to southerly (Figure 2.9). This led to anomalously warm temperatures in January (Walker, 2006). By February, this pattern reversed and northerly winds prevailed once again. The reversal of the winds promoted cross-shelf exchange of AW; fjords on the west coast of Svalbard

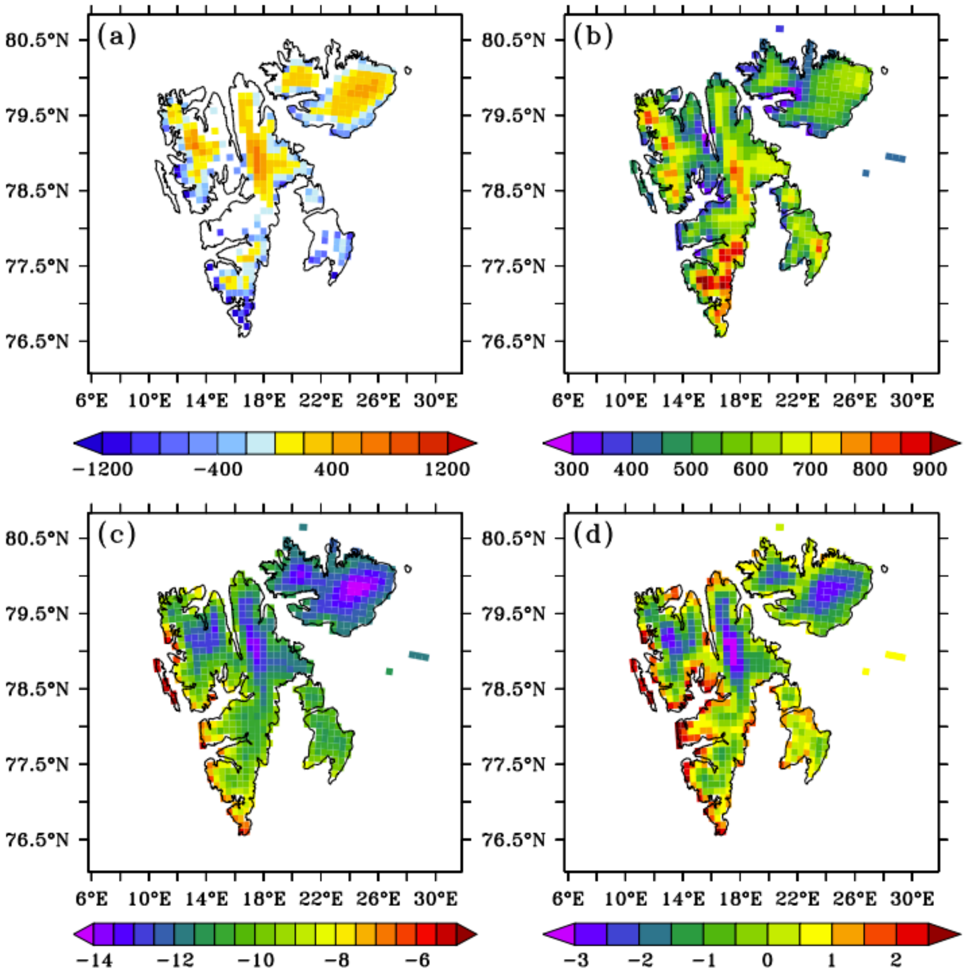

Figure 2.8: Mean annual properties averaged over 1979 – 2013 for (A) SMB (mm w.e.yr^{-1}), (B) annual precipitation (mm w.e. yr^{-1}), (C) mean annual near-surface temperature (°C), and (D) mean summer near-surface temperature (June, July and August; °C; Lang et al., 2015).

were observed to receive greater volumes of AW, bringing the water column back to pre-winter temperatures (Cottier et al., 2007).

2.3 Glacier system

2.3.1 Surface meltwater production

Glacier surface ablation is driven by the net flux of energy from the atmosphere, which is transferred to the surface of the glacier, resulting in temporal and spatial variability of SMB across a glacier. Meltwater is produced where ablation is greater than accumulation during the length of a season (Figure 2.10). At higher altitudes, greater temperatures are required to cause melt. The average equilibrium line

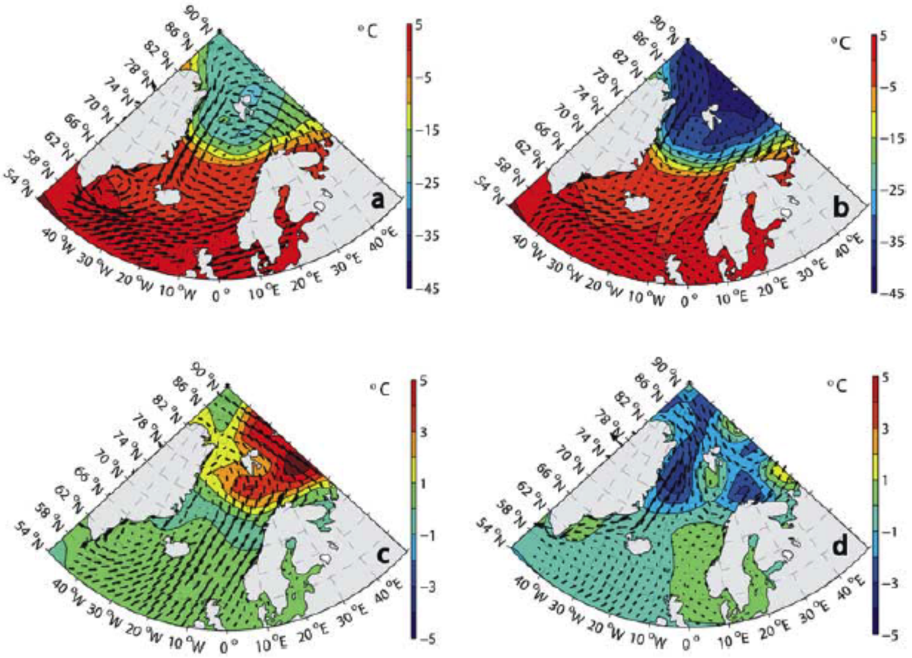

Figure 2.9: Mean surface air temperature and wind stress fields for the years 1995 – 2005 in (A) January and (B) February. Anomalous patterns occurred in 2006, illustrated by the mean surface air temperature and wind stress anomaly, compared to the 1995 – 2006 mean for (C) January and (D) February (Cottier et al., 2007).

altitude (ELA), indicating the zone where accumulation is equal to ablation at Kronebreen was located at ~700 m a.s.l from 1996 – 2006 (Baumberger, 2007). Below this altitude, net ablation occurs.

The surface energy balance dictates the rate of melt at the glacier surface, as given by Equation 2.4, in which ME is melt energy ($ME = 0$ if surface temperature is <273.15 K), $SW\downarrow$ and $SW\uparrow$ are downward and upward shortwave radiation, $LW\downarrow$ and $LW\uparrow$ are downward and upward longwave radiation, SHF is the sensible heat flux LHF is the latent heat flux and G_s is subsurface conductive heat flux and the net radiation is R_{net} (Broeke et al., 2008). Under conditions where ME is positive, the glacier surface will heat up, causing melting. The reverse is true of negative values.

Normally R_{net} are the dominant components of the energy balance. However, in maritime environments, turbulent heat fluxes, in which an upward positive transfer of energy occurs, play a much greater role (Paterson, 2001). Large diurnal and seasonal variation in R_{net} occurs, due to the cyclical variations in global radiation. Early in the ablation season, R_{net} can be negative as a result of low $SW\downarrow$ due to high surface albedo, and low $LW\downarrow$, due to cooler air temperatures (Oerlemans, 2001). Ablation is greatest during the summer, when ME is highest. The

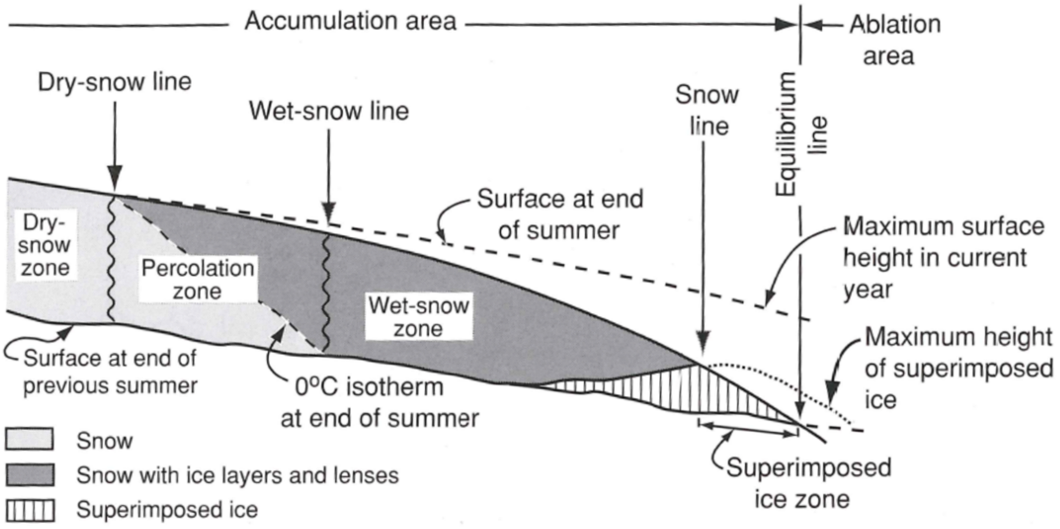

Figure 2.10: Upper glacier zonation, illustrating the relative locations of the dry zone, the percolation zone and the wet zone. The ELA represents the elevation where accumulation and ablation are in equilibrium (Hooke, 2005). Below this is the ablation area, which is not depicted.

cumulative sum of positive temperatures, positive degree days (PDD), provides a measure of how much energy is being transmitted to a glacial environment. An empirical relationship can be formed between PDD and melt rates, which can be used for temperature index modelling (Hock, 2003). Temperature data across glacier surfaces are more prevalent than full energy budgets, which is why temperature index modelling is widely used in studies of glacier mass balance (Hock, 2005).

$$\begin{aligned} ME &= SW \downarrow + SW \uparrow + LW \uparrow + SHF + LHF + G_s \\ ME &= SW_{net} + LW_{net} + SHF + LHF + G_s \\ ME &= R_{net} + SHF + LHF + G_s \end{aligned} \tag{2.4}$$

Albedo affects glacier melt, with the ratio between upward and downward shortwave radiation altering the surface energy balance. Variable both temporally and spatially, albedo is measured between 1 and 0. Fresh snow exhibits a high reflectivity, and therefore high albedo, close to 1.0, firn typically exhibits values of 0.5 – 0.6, whilst dirty glacier ice has a much reduced albedo of approximately 0.1 (Cuffey and Paterson, 2010). Glacier albedo varies seasonally, depending on snow cover. In Svalbard, snow fall begins in mid-September, increasing surface albedo. As snow melts, from mid- June, the grain size of snow increases, decreasing surface albedo, therefore increasing the amount of solar energy absorbed, promoting further melt. Short term variability in albedo (hourly) is caused by changes in snow cover, whereas day to day changes are as a result of seasonal weathering of the surface crust (Jonsell et al., 2003). At a seasonal scale, surface albedo is least variable in winter and summer, but the changing snow conditions of autumn and spring prompts large albedo changes (Winther et al., 2002).

The zonation of glacier surfaces is representative of the melt energy and meltwater fluxes in the region (Broeke et al., 2008). Three distinctive zones are present at the surface of glaciers, depending on elevation and melt processes: the dry zone, the percolation zone and the wet zone (Figure 2.10) (Benson, 1961; Müller, 1962). Typically, no melting takes place in the dry zone. The boundary between this, and the percolation zone is the dry-snow line, located near to the elevation where summer temperatures do not rise above -6°C (Benson, 1961). When surface temperatures increase above 0°C in the summer months (Nghiem et al., 2012), dry zones become smaller. In the percolation zone, meltwater percolates into snow and firn, where it can refreeze. At the lowest elevations, summer melting is sufficient to wet the entire snow pack, by melting all snow from previous season, and is therefore known as the wet zone. Refreezing of surface snow in the wet zone forms a porous layer. Saturation of the bottom layers of the snow pack occurs further down the glacier. This refreezes to form superimposed ice, if the underlying ice is cold (Hooke, 2005). Slush pools can form in this region of superimposed ice; the slush limit represents the highest point at which mass is removed from the glacier as flowing water (Chu, 2014). Regions of accumulation and ablation, at the end of the melt season, are separated by the equilibrium line ELA. Beneath this elevation, the glacier has undergone net mass loss, during the melt season.

2.3.2 Glacier mass balance

The mass balance of glaciers depends on the balance between accumulation, as a result of snowfall, and ablation, as result of surface melt and terminal calving (Braithwaite, 2002). Glacier mass balance is typically determined annually, achieved by taking direct measurements, or numerical modelling, to determine changes in volume (Barry, 2006). Svalbard's glaciers are in a state of negative mass balance, having experienced a 7% loss in ice mass over the last 30 years (Nuth et al., 2013). This loss of ice volume amounts to -9.71 ± 0.53 km^3 yr^{-1}, which equates to 0.026 mm yr^{-1} sea level equivalent (Nuth et al., 2010). Estimates of global SLR contributions over the last 40 years vary between +0.01 and +0.38 mm yr^{-1} (Hagen et al., 2003a;b), which accelerated to 0.8 – 10. mm yr^{-1} from 2001 – 2004 (Kaser et al., 2006). This amounts to 4% of the total global contribution, originating from smaller glaciers and ice caps (Nuth et al., 2010).

Svalbard's annual volume loss is equivalent to 40% of the total for the Canadian Arctic from 1995 – 2001 (Abdalati et al., 2004), yet twice as much as the loss from the Russian Arctic between 1952 – 2001 (Glazovsky et al., 2006; Meier et al., 2007). The geodetic mass balance of Svalbard is twice as negative as the Canadian Arctic and four times as negative as the Russian Arctic when glacier area is considered (Nuth et al., 2010). Tidewater glaciers cover an area of 14,900 km^2 in Svalbard (Figure 2.11), almost 50% of the total glacerised area, 34,000 km^2 (Gardner et al., 2013), which is proportionally greater than both Alaska (13%) and Greenland (35%) (Pfeffer et al., 2014). Approximately 42% of the freshwater budget for Svalbard's shelf waters is sourced from glacial discharge, driven by mass loss from the glaciers (Beszczynska-Moller et al., 1997). Specifically, the SMB of the Kronebreen system has become more negative since 1995. From 1960 – 1995 the system was in relative balance, -0.02 ± 0.06 m w. eq. yr^{-1} (metres water equivalent per year), mass loss increased to -0.18 ± 0.03 m w. eq. yr^{-1} during 1995 – 2007 from enhanced summer melt (Nuth et al., 2012). The resultant freshwater enters the ocean through two outlets: marine terminating outlets account for 68% of meltwater discharge, whilst the remainder exits at land terminating outlets as runoff (Nuth et al., 2013). Addressing the recent accelerated thinning of Svalbard's west coast glaciers (Kohler et al., 2007), a better understanding of processes leading to glacier retreat deserves attention from both the cryospheric and oceanographic research communities (Straneo et al., 2013). To enable accurate quantification of meltwater delivery to the ocean, a deeper understanding of glacier hydrology is required (Chu, 2014).

2.4 Glacier hydrology

The hydrology of glaciers modulates meltwater storage, transport and discharge of meltwater produced supraglacially. Surface melt is transported through the glacial system, and is discharged from the glacier terminus (Figure 2.12). The mechanisms by which englacial drainage develops in polythermal glaciers is of interest because meltwater that reaches the subglacial system, can modulate the basal motion of glaciers (Zwally et al., 2002; Boon and Sharp, 2003; Copland et al., 2003). Increased contributions to subglacial channels can lead to glacier speed up (Zwally et al., 2002), calving (Rignot et al., 2010), and drive submarine melt (Kimura et al., 2014). Another point of interest lies in how much surface melt reaches the ocean, and the time taken for this englacial transport. Being able to quantify this is important, and would enable increased accuracy when forecasting SLR (Church et al., 2013). Current uncertainties remain regarding the quantity of melt stored, rather than being discharged; this has been attributed to cause

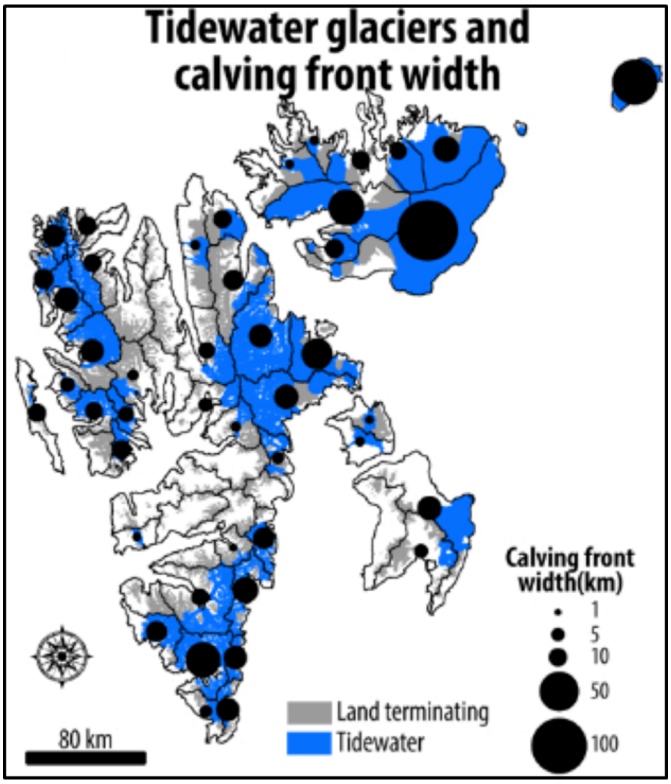

Figure 2.11: Map of Svalbard displaying tidewater glaciers in blue and terrestrially terminating glaciers in grey. The width of the caving front is indicated by the size of the black circles (Nuth et al., 2013).

errors in SLR predictions (Harper et al., 2012; Rennermalm et al., 2013).

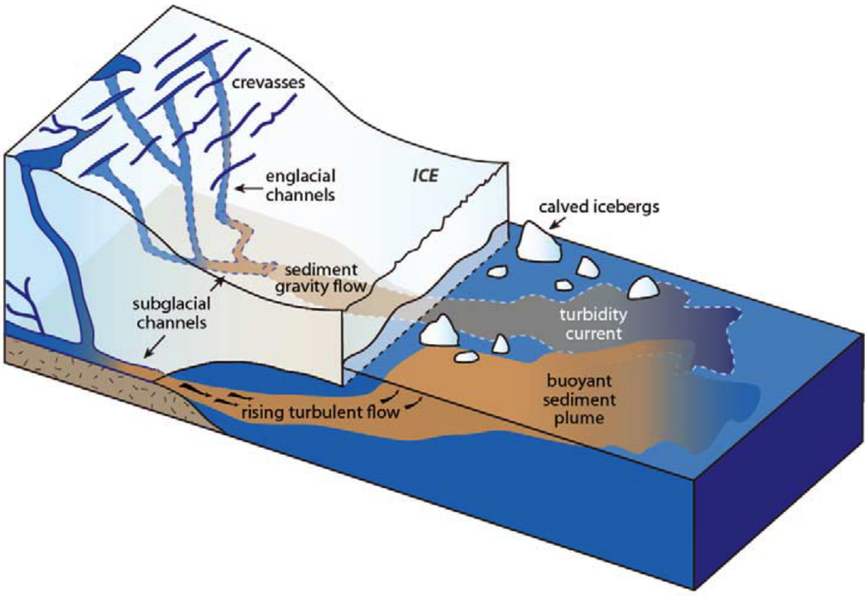

Figure 2.12: Glacier hydrology of a marine terminating glacier, illustrating supraglacial, englacial and subglacial processes. Buoyant plumes of sediment laden freshwater enter directly to the marine environment. Figure modified from Chu (2014).

2.4.1 Glacier storage

Glaciers themselves are a storage mechanism for water as ice, which is released once melted. As Jansson et al. (2003) describes, there are three time scales for glacier storage: long term (years to centuries), intermediate (days to years), and short term (hours to days). Long term storage depends on the volume of the glacier itself, and provide storage in the form of ice and snow.

Intermediate storage

Storage of meltwater occurs within a glacier when the melt production exceeds the rate of glacial discharge, which is largely dependant on the drainage system of the glacier (Jansson et al., 2003). Seasonal snow cover provides intermediate term storage, as does water retention in firn. Generally, >80% of annual discharge of runoff occurs in the summer months, June - August (Jansson et al., 2003). Runoff is delayed by about a month when the area of exposed ice is 0 – 7% of the glacier, decreasing to ∼2 weeks when the exposed glacier area increases from 50 – 100% (Fountain and Tangborn, 1985).

Runoff is significantly delayed due to storage in firn (Schneider, 2000). Perennial firn aquifers (PFAs) form in the percolation zone; winter snowfall provides the meltwater reservoir, as the porous space in snow. Melt infiltrates porous firn until it reaches the underlain ice, which can refreeze the meltwater. Aquifer formation in this porous region will develop (e.g. Fountain, 1989; Fountain and Walder, 1998; Schneider, 1999), unless accumulation was too low, or summer melting too high. Continued supply leads to saturation, which increases with depth (Koenig et al., 2014; Christianson et al., 2015) of the firn. PFAs found on Kronebreen are 10 – 20 m thick (Christianson et al., 2015), whereas the firn aquifers on the Alpine glaciers, Storglaciären and Aletschgletscher, are 5 m and 7 m thick, respectively (Jansson et al., 2003). PFAs have recently been found to provide a buffer mechanism, storing meltwater in the Greenland ice sheet, preventing it from reaching the ocean (Harper et al., 2012; Forster et al., 2014; Koenig et al., 2014). The underlain ice can be melted by stored summer meltwater (Humphrey et al., 2012). At high elevations, once firn is saturated, a gravity driven flow transports meltwater towards the glacier terminus, along the base of the firn (Christianson et al., 2015). At lower elevations, thin firn layers can become saturated to form slush, which leads to meltwater ponds.

Meltwater ponds typically form in topographic depressions, forming surface meltwater storage (Liestøl et al., 1980). Once formed, ponds lower the surface albedo, driving a positive melt feedback, increasing radiation driven melt (Lüthje et al., 2005). Ponds evolve over time, increasing in size and volume (Sneed and Hamilton, 2007). Surface pond evolution on Kongsvegen has been enhanced by superimposed ice, which covers u pto 35% of the glacier surface, equivalent to the area of exposed glacier (Obleitner and Lehning, 2004; König et al., 2002). Multi-year accumulation of superimposed ice started between 1956 and 1966, when crevasses would have closed (Brandt et al., 2008). Over the following ∼42 years the annual accumulation of superimposed ice is 0.16 ±0.06 m w. eq. yr^{-1}, corresponding to ∼5 – 10% of the total winter mass balance (Brandt et al., 2008).

Supraglacial streams are fed by meltwater ponds, forming an arborescent drainage network across the glacier surface. Meltwater is transported to lower elevations, with increasing drainage efficiency throughout the season as the channels enlarge (Cuffey and Paterson, 2010). Meanders develop in streams as a result of high, early season discharge (Ferguson, 1973). Streams which have survived a winter, can be regenerated by renewed discharge, but less supply is required than for the formation of a new stream (Hambrey, 1977). Meltwater streams feed crevasses and moulins that they intersect with, forming surface storage (Figure 2.13); should these become full, meltwater overflows, feeding into the stream network (Marston, 1983; Boon and Sharp, 2003). Surface melt storage feeds englacial glacier drainage network, connecting the supraglacial melt with subglacial.

At the end of the melt season, melt contributions can exceed the transport

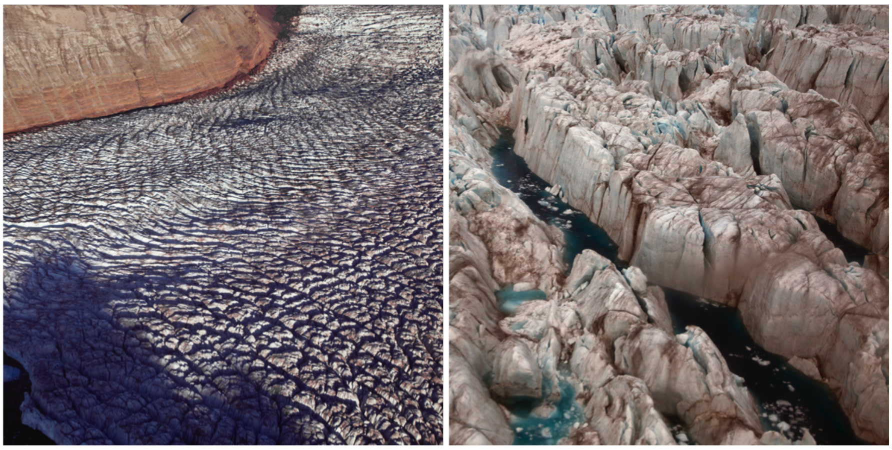

Figure 2.13: Heavily crevassed lower region of Kronebreen expresses meltwater storage in the crevasse openings (Burko, 2015).

drainage capabilities, causing melt to be frozen in channels and stored during winter (Hodgkins, 1997; Hodgkins et al., 1998). For water to be discharged from a glacier, a high water pressure within the glacier needs to be obtained. Meltwater stored from the previous ablation season can provide this pressure, priming for early subglacial discharge (Hodson et al., 2005a). Discharge of the stored meltwater from the previous ablation season presents a distinctive geochemical signature, allowing it to be distinguished from first year melt (Hodson et al., 2005b).

2.4.2 Glacier drainage

The idea of tubular conduits as a key mechanism of melt transport through glaciers, is based upon studies at the margin of glaciers (Shreve, 1972; Röthlisberger, 1972). This is not possible at the termini of tidewater glaciers, owing to logistical constraints of surveying their termini. However, subsequent studies have indicated that englacial hydraulics are not likely to be dominated by these tubular conduits (Hock et al., 1999). Instead, incised englacial conduits (Gulley et al., 2009) or engalcial fracture networks (Fountain et al., 2005), are more probable, especially in polythermal glaciers such as Kronebreen.

Surface melt can feed supraglacial streams, which incise the glacier surface, transporting melt down the glacier. Smaller melt streams can join, feeding into a larger supraglacial stream network. Discharge and stream slope are responsible for the rate of stream incision (Fountain and Walder, 1998). When the rate of channel incision is greater than ablation, englacial conduits can form (Gulley et al., 2009). This process occurs in the upper reaches of polythermal glaciers, where the drainage area is large enough to sustain high rates of discharge (Figure 2.14).

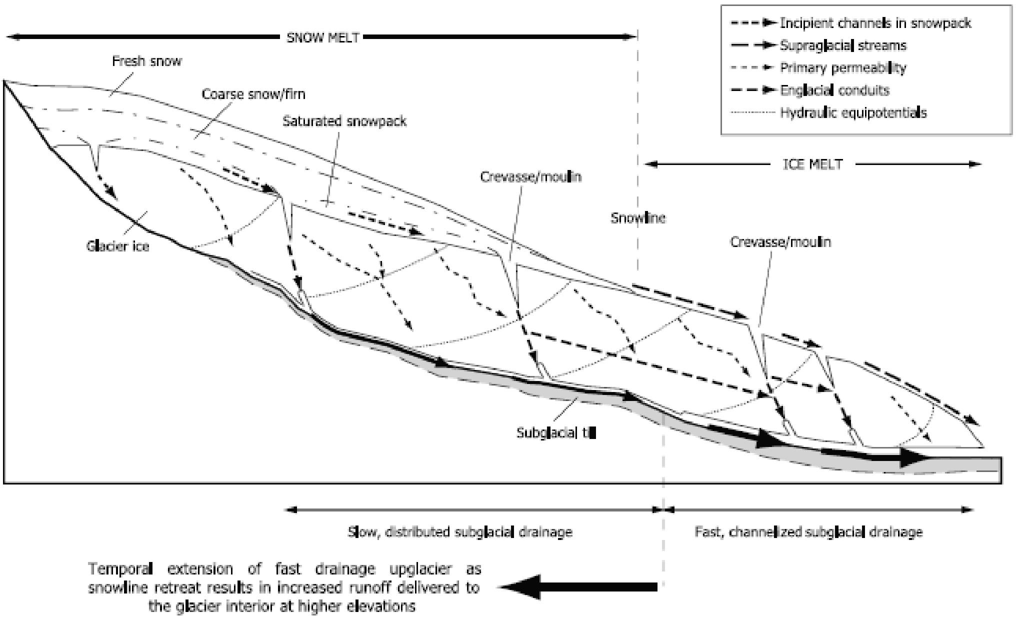

Figure 2.14: Schematic of glacier hydrological routing (Irvine-Fynn et al., 2011).

The region cannot be crevassed, else the streams feed into the crevasses (Boon and Sharp, 2003). The englacial conduits evolve in time and space; internally ponded water can refreeze during the winter months, providing a storage mechanism (Gulley et al., 2009). These near surface conduits can link together areas of different hydraulic potential (Gulley and Benn, 2007). Integrated, hydraulically connected networks form between cavities filled with water (Fountain et al., 2005). These take the form of fractures, which have been found to extend almost to the glacier bed, as well as throughout the glacial system. These develop both seasonally and interannually; continuous pathways can be formed when new fractures intersect with older, water filled ones (Fountain et al., 2005).

Crevasses open and propagate through the ice, as a result of glacier speeds and basal topography (Benn et al., 2007). Surface meltwater can flow into crevasses, forming ponds (Fountain and Walder, 1998), which increases the hydrostatic pressure. This can enable water to propagate to the bottom of the glacier (Van der Veen, 1998). Hydrofracturing has been proposed as the mechanism driving melt through the glacier, forcing crevasses deeper through the ice (Benn et al., 2009). Should they intersect with a subglacial channel, a connection with the basal environment is formed, providing an outlet for rapid surface to bed meltwater drainage.

An icefall, 12 km from Kronebreen's terminus marks the start of the crevassed zone. This region is 500 m a.s.l and is dominated by simple, transverse crevasses (Sund et al., 2011). Between 6 – 9 km from the terminus, a more complex crevasse pattern is apparent, and from 6 km additional transverse crevasses form.

Prints of chevron and longitudinal crevasses are imprinted on the transverse crevasses advected down glacier, forming a complex system of fractures, ice blocks and seracs (Sund et al., 2011). This crevassed zone forms a region of weakness, with calving events occurring when the glacier ice can no longer support its own weight. Kronebreen's ice front actively calves during the summer months, producing numerous small icebergs, <10 m wide (Dowdeswell and Dowdeswell, 1989; Dowdeswell and Forsberg, 1992), which total an estimated loss of 0.23 $\mathrm{km}^3\ \mathrm{yr}^{-1}$ (Błaszczyk et al., 2009).

In contrast, Kongsvegen's surface is smooth and largely uncrevassed, owing to its slow velocity. The glacier is polythermal, frozen to the mountainsides in the ablation area (Björnsson et al., 1996). The upper layer, which is between 50 and 130 m thick, exhibits sub-freezing temperatures. Large supraglacial channels form in the ablation area draining meltwater to Kongsfjorden (Melvold and Hagen, 1998).

2.4.3 Subglacial and sedimentary processes

Glacier sliding occurs when the base of glacier is at the pressure melting point, producing fine grained sediment as a product of erosional processes. The supply of meltwater to the subglacial environment plays a role in determining glacier velocity (Iken and Truffer, 1997; Copland et al., 2003; Bartholomew et al., 2012). This has an impact on basal erosion, which is dependant on glacier velocity (Koppes and Hallet, 2002). Whilst the physical processes dictating glacier movement are fairly well constrained, the englacial and subglacial drainage which supplies meltwater to the base of the glacier is difficult to evaluate. The speed of glacier sliding is dependant on the effective water pressure at the bed and the basal drag. The supply of surface melt plays a key role in seasonal speed-up of glacier motion (Sole et al., 2011). Therefore, the efficiency of the englacial drainage modulates the rate of supraglacial melt to the glacier bed (Bartholomew et al., 2010), influencing the effective pressure. Pressurised subglacial water decreases the effective pressure at the bed, inducing glacier sliding. Borehole measurements have revealed how variable subglacial water pressure is across the Greenland ice sheet, both spatially and temporally (Andrews et al., 2014).

Evolving throughout the melt season, distributed subglacial drainage can develop into a channelised system. Early in the ablation season, subglacial water pressures are high, corresponding to higher glacier velocities (Iken and Truffer, 1997; Bartholomew et al., 2012). Drainage efficiency improves as subglacial channels develop creating easier passage for meltwater to be expelled from the glacier terminus (Bartholomew et al., 2010). An efficient drainage system slows the rate of glacier flow (Cowton et al., 2013). This seasonal reorganisation of subglacial drainage has been found in alpine glaciers (Hubbard et al., 1995; Gordon et al., 1998; Mair et al., 2003) as well as in the Greenland ice sheet (Chandler et al., 2013; Andrews et al., 2014). Sediment produced by erosion is dispelled from the glacier front into the fjord, mobilised by meltwater availability (Powell and Molnia, 1989; Cowan and Powell, 1990; Swift et al., 2002).

The relationship between sediment production and meltwater release has enabled the thermal regime of glaciers in numerous locations to be reconstructed in palaeoclimate studies (e.g. Elverhøi et al., 1983; Shevenell et al., 1996; Cowan and Powell, 2004). Arctic fjords act as natural sediment traps for glacially eroded sediment, producing a well preserved record detailing glacier fluctuations, the rate of erosion, and the associated climate conditions at the time (Elverhøi et al., 1983; Syvitski, 1989; Cowan et al., 2010). Meltwater transports glacially derived sediments to the fjord environment (Figure 2.15), which is a well studied process in Kongsfjorden (Elverhøi et al., 1983; Trusel et al., 2010; Kehrl et al., 2011) as well as in Alaskan fjords (e.g. Hoskin and Burrell, 1972; Cowan and Powell, 1990; Hallet et al., 1996).

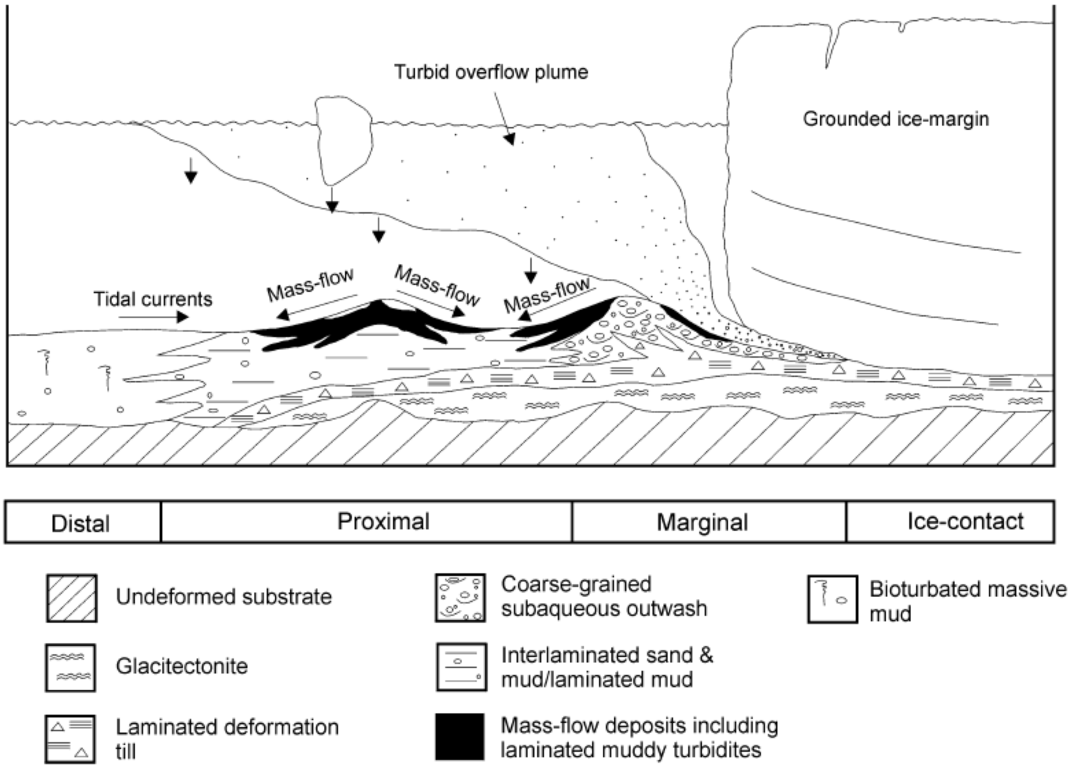

Figure 2.15: Schematic of buoyant sediment plume emerging from a tidewater glacier. Glacimarine sedimentation is driven by sediment fall out (vertical black arrows), forming sedimentary layering at the base of the glacier (Ó Cofaigh and Dowdeswell, 2001).

The calving front of Kronebreen is grounded approximately 60 m below sea level, with bed topography playing a pivotal role on retreat, by which increased water depths increase retreat (Sund et al., 2011). Buoyancy driven plumes rise from the grounding line of the glacier, mixing with ambient sea water to transport the sediment to the fjord surface (Figure 2.15) (Syvitski, 1989). This leads to sedimentation in the ice proximal zone, which decreases with distance from the glacier (Cowan and Powell, 1990; 1991). The build up of sediment at the grounding line of temperate glaciers can be in the order of tens of metres per year (Powell and Alley, 1997). In Kongsfjorden, 90% of the sediment input from Kongsvegen is deposited close (<0.5 km) to the glacier front (Elverhøi et al., 1983). As such, the rate of infill of the Kongsfjorden basin is expected to increase with the increasing length of the glacial ablation season, and the subsequent influx of sediment (Trusel et al., 2010). This may lead to the stabilisation of Kronebreen through the formation of submarine landforms, and potentially allow it to re-advance in the future (Trusel et al., 2010). Therefore, the seasonal variability of glacimarine and oceanographic processes in Kongsfjorden requires further understanding (Aliani et al., 2004).

2.5 Detecting plumes by spectral reflectance

Sediment plumes are visually present in the surface waters of fjord environments as a result of erosional processes (Hallet et al., 1996) and meltwater delivery (Hubbard and Nienow, 1997). Influenced by rates of meltwater discharge, bathymetry, winds and tides, they vary temporall and spatially, making them complex to study with *in situ* measurements alone (Purkis and Klemas, 2011). Satellite remote sensing has been used, together with *in situ* measurements, to address the limitations associated with *in situ* sampling (Klemas, 2011). Ocean colour, turbidity, temperature, and chlorophyll are all features of plumes, allowing plumes to be distinguished from the surrounding seawater. Some coastal plumes, such as the Amazon River Plume, can extend hundreds of kilometres, making remote sensing the only viable method of monitoring (Jo et al., 2005). Buoyancy driven surface sediment plumes have been used as a tool to monitor the variability of river discharge in coastal waters for many years (Walker, 1996; Ruhl et al., 2001; Brodie et al., 2010), as well as a method for monitoring cliff erosion (Curran et al., 1987) and marine pollution (Clark, 1993). Whilst plume detection is well established in the lower latitudes, it is only recently that such methods have been applied in a high latitude, glacial setting (Chu et al., 2009; McGrath et al., 2010; Chu et al., 2012; Tedstone and Arnold, 2012).

2.5.1 Multispectral remote sensing

Multispectral sensors can be found on several satellites, providing varying repeat times and at different spatial resolutions. Passive observation of the Earth's surface is achieved by simultaneous measurements of reflected electromagnetic radiation, with multiple wavebands. Images are recorded in the visible: near infrared, shortwave infrared and thermal infrared wavelengths (Campbell, 2006). Spectral response depends on the surface; snow and clouds have a high reflectance, whereas open ocean has a low reflectance. This has enabled maps of specific land surfaces, such as snow, to be mapped (Hall et al., 1995). True colour images can be easily formed with a combination of bands, making multispectral images very user friendly. This has led to their extensive use in environmental monitoring. Different bands can be used to determine spectral reflectance from different surfaces. The high correlation between TSS and spectral reflectance has proved to be a valuable tool to detect sediment plumes remotely (Curran and Novo, 1988).

There are several different multispectral sensors; emphasis here is placed on Advanced Very High Resolution Radiometer (AVHRR), Moderate Resolution Imaging Spectroradiometer (MODIS), and Landsat, as they have each been used in sediment plume studies (e.g. Stumpf and Tyler, 1988; Chu et al., 2009; Kim et al., 2014). All multispectral sensors are hindered by cloud cover, meaning that usable data is only available during cloud free comditions. The first AVHRR sensor was launched in 1978, and has a maximum spatial resolution of 1.1 x 1.1 km. So far, there have been 15 sensors launched, providing continuous, daily, global data from 1981 - present. It has six bands ranging from 580 – 1250 nm (NOAA, 2015). The Landsat programme, which was launched in 1978, has become the dominant multispectral imager for Earth observation, and continues to present (Loveland and Dwyer, 2012). The latest addition to the programme is Landsat 8, which offers a spectral range of 430 – 1380 nm, over 9 spectral bands. Bands 10 and 11 are thermal. It boasts a fine spatial resolution of 30 m (previous Landsat sensors provided 15 – 90 m), but this comes at the expense of a 16 day revisit cycle (USGS, 2015). MODIS is found on two NASA satellites, Terra, launched in 1999, and Aqua, launched in 2002, and are both still in operation. With 36 bands, MODIS offers a larger spectral range from 405 – 14385 nm, in addition to a finer spatial resolution, with a maximum of 250 x 250 m (NASA, 2012a). The MODIS sensors are in a daily orbit, meaning that with both Terra and Aqua, twice daily, global coverage is achieved.

There are numerous considerations when choosing the right multispectral sensor for a study. These include: spatial resolution, temporal resolution, spectral resolution/band wave lengths, cost and ease of access to data, length of data archive and the availability of pre-processed products. There is no optimal sensor for all studies, forcing users to trade-off between sensor specifications, to achieve the best possible outcomes.

2.5.2 Sediment plume detection

Low latitudes

Early studies monitoring *in situ* buoyant plume dynamics took place in the Mississippi River (Wright and Coleman, 1971) and the Fraser River in British Columbia (Stronach, 1981). These detailed the spatial and temporal challenges which need to be overcome when monitoring sediment plumes: *in situ* sampling becomes expensive, time consuming and often inaccurate due to the unknown representativeness of spot samples to the wider environment (Curran and Novo, 1988). The visibility of TSS in coastal waters, and its relationship with reflectance has enabled TSS to be quantified remotely (Curran and Novo, 1988). Higher TSS results in greater reflectance, whilst lower concentrations have lower reflectivity (Figure 2.16). Higher TSS responds better at higher wavelengths, with 600 – 700 nm providing an optimal range to encompass both high and low TSS concentrations (Moore, 1977). *In situ* measurements must be well spaced, representing the range of the variable which is to be detected remotely, in order to provide suitable calibration data (Schofield et al., 2004).

Turbid estuarine plumes have been detected using AVHRR, which were calibrated with *in situ* measurements to determine chlorophyll and sediment concentrations (Stumpf and Tyler, 1988). An early review highlights some of the challenges associated with determining TSS with remote sensing (Curran and Novo, 1988). Suggestions were made to increase the accuracy of TSS estimation from spectral reflectance, which involve: take simultaneous measurements of TSS and spectral reflectance, correct for environmental influences, and to derive an empirical relationship between TSS and spectral reflectance. This paved the way for a wealth of marine and hydrological research, which utilises the differences in ocean colour, to enable remote environmental monitoring. More recently, Klemas (2011) highlighted the need for representative *in situ* samples of the full range of measurements in the environment of interest, to ensure the best calibration possible, when studying coastal plumes.

Further work detailed the complex forcing factors that affect plume velocity and size. Both winds and tides have the ability to extend the plume further from the source, with wind stress remaining in the surface waters, increasing plume velocity (Stumpf et al., 1993). Changes in river discharge, and therefore plume size, has been detected using AVHRR, despite the influence of wind and tides

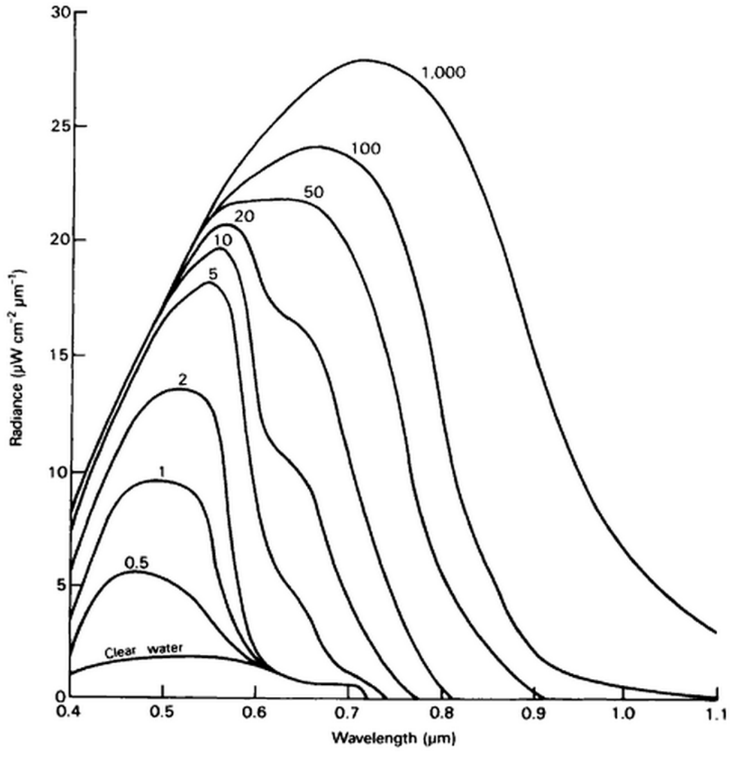

Figure 2.16: Effect of TSS (μmg l^{-1}) on radiance at different wavelengths (Curran and Novo, 1988).

(Walker, 1996). This allowed for the seasonal and interannual variability of river discharge to be determined by variability in sediment plume size, in the Mississippi River (Walker, 1996).

With the launch of MODIS, this work has been expanded, but the finer resolution has enabled greater detail to be observed. Mapping TSS using MODIS band 1 revealed the complex dynamics of coastal waters in the Northern Gulf of Mexico (Miller and McKee, 2004). The twice daily global coverage provided by MODIS is a valuable attribute, supporting numerous studies of the temporal and spatial change of TSS (e.g. Ruhl et al., 2001; Warrick et al., 2004; Chen et al., 2015). Although Landsat has a finer resolution, its 16 day repeat time restrains it from being used in temporal monitoring studies; TSS mapping using MODIS remaining the preferable platform for monitoring coastal and riverine environments (Chen et al., 2015). Both sensors are affected by cloud, but there is greater probability of retrieving several viable images from MODIS during a season.

High latitudes

Remote sensing of TSS in the high latitude and glacial environments is in the early stages of development. However, there is a wealth of potential since quantifying freshwater discharge from glaciers is of global importance (IPCC, 2013). Access to make regular, *in situ* measurements, is difficult due to the remoteness of the Polar Regions. Sampling in close proximity to tidewater glaciers induces additional complexities: ice melange at the calving face and iceberg calving restricts access for *in situ* sampling in the ice proximal zone. To determine temporal and spatial variability of submarine meltwater release from field measurements alone would be extremely timely and expensive, harbouring efforts to understand the key processes affecting tidewater glaciers.

Sediment entrained in glacier meltwater discharge forms visible plumes in Arctic fjords. The glacimarine sedimentary processes have been explored, but using the sediment plumes to quantify discharge has only been recently achieved. Owing to the high temporal repeat times and a reasonable resolution of 250 x 250 m when using bands 1 and 2, MODIS has been the optical sensor of choice. It provides a means to remotely detect sediment plumes, intra-seasonally, as has been achieved at the lower latitudes (Figure 2.17).

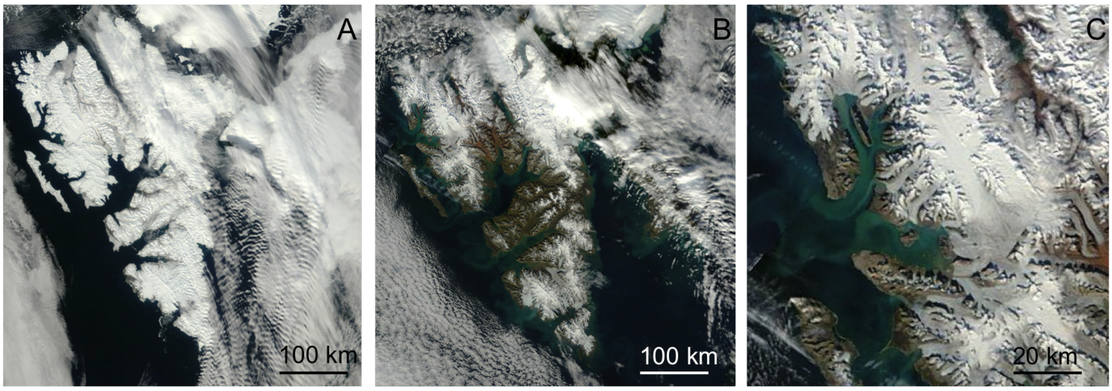

Figure 2.17: MODIS satellite images of Svalbard (A) 6th June 2012, displaying snow cover (B) 29th September 2012, at the end of the ablation season (C) same previous images but focussed on Kongsfjorden as in Figure 2, displaying high suspended sediment loads (NASA, 2012b).

Initially, the extent of sediment plumes was determined by spectral reflectance alone (McGrath et al., 2010), revealing that plume extent provided a suitable proxy for runoff. Large plume extents correspond with high runoff, which was measured at a gauging station. Further to this, *in situ* TSS samples were collected, together with spectral reflectance measurements, forming an empirical relationship which was used to calibrate with MODIS band 1. This illustrated the evolution of glacial melt inputs to Kangerlussuaq fjord, Greenland, from 2000 – 2007; including capturing large lake drainage events (Chu et al., 2009). The technique was upscaled, around the coast of Greenland, giving a synoptic scale insight to meltwater discharge from the Greenland ice sheet. At interannual scales, high TSS corresponds with high Positive Degree Days (PDD), and plume extent again, correlates with runoff (Chu et al., 2012). These studies demonstrated that plume extent can be useful for determining melt entering the ocean, from land terminating glaciers.

Tedstone and Arnold (2012) progressed the field by analysing the effectiveness of plume extent as a runoff proxy, at both land and marine terminating glaciers in Greenland. Automated detection of sediment plumes in 36 outlet glaciers, both land and marine terminating, along the length of Greenland's west coast, illustrated that MODIS is a suitable form of remote sensing to monitor glacial meltwater delivery. The method was most effective in long, wide (>2 km), fjords, with runoff from land terminating outlets. Although it is possible to determine plume extent in marine terminating outlets, ice melange and sea ice can be a problem. Intra-seasonal variability was difficult to determine, particularly melt onset, because of the limited availability of suitable MODIS images. As such, (Tedstone and Arnold, 2012) recommended that remote detection of sediment plumes is best placed for detecting interannual variability.

Again focussing on land terminating glaciers, (Hudson et al., 2014) has improved the detection method by using both band 1 and 2 of MODIS. This is offers detection of a wider loading of TSS in synoptic scales studies. One the caveats of (Chu et al., 2009), was that high TSS was not always detected; high TSS is common in riverine discharge. Plume extent was again found to be a better indicator of runoff, because annual TSS and river volume discharge did not correlate (Hudson et al., 2014). Numerous processes take place in glacio-fluvial fjord systems, making it increasingly complex to understand meltwater discharge at a synoptic scale (Hudson et al., 2014). Despite this, sediment plume detection has been suggested as means to further understand glacier hydrology, and remains a relatively unexplored tool (Chu et al., 2012). A detailed study, capturing the seasonal and interannual variability of meltwater discharge, from a tidewater glacier, has not been undertaken. This leaves an area for further investigation, which could allow for meltwater delivery to be quantified remotely, overcoming many logistical problems associated with *in situ* sampling near tidewater glaciers.

2.6 Summary

Significant uncertainties remain regarding the stability of tidewater glaciers, and how this will change in the Arctic as both the ocean and atmosphere warm. Observational studies are limited owing to logistical, time and funding constraints. Therefore, novel methods of remote monitoring need to be explored to enhance process based understanding. To this end, oceanographic and spectral reflectance measurements taken during a field campaign in July 2012 are presented. These reveal the hydrographic structure at the head of Kongsfjorden, in addition to providing a time series of meltwater discharge, illustrating its seasonal and inter-annual variability, achieved by the remote detection of sediment plume extents.

Chapter 3

Freshwater contributions and circulation at the head of Kongsfjorden

3.1 Introduction

Kongsfjorden is a relatively well studied fjord however, oceanographic measurements at the head of the fjord, in the vicinity of Kronebreen's calving front, are limited. This is despite other studies which have focussed on the glacimarine processes (e.g. Elverhøi et al., 1980; Kehrl et al., 2011). This chapter uses hydrographic sections from the ice proximal zone of Kronebreen, to expand the understanding of the hydrographic processes taking place in front of a fast flowing, tidewater glacier. This study aims to quantify the freshwater inputs and understand how they affect fjord circulation. This has been achieved by the following objectives:

i Provide a detailed description of water masses and their relative locations, directly in front of Kronebreen.

ii Illustrate the circulation and mixing processes within the ice proximal zone.

iii Quantify the volume of freshwater entering at the head of Kongsfjorden, and determine the contributions from subglacially discharged runoff, and direct submarine melt of the ice face.

Owing to the impacts of freshwater inputs to Arctic fjords (Section 2.1.2), oceanographic observations are highly valued to further the understanding of glacier - ocean interactions (Cottier et al., 2010). Hydrographic measurements enable the relative quantities of freshwater to be diagnosed, revealing whether meltwater is predominantly submarine melt or surface runoff (Jenkins, 1999; Motyka et al., 2003; Mortensen et al., 2013). Unlike terrestrially terminating glaciers, it is not possible to quantify discharge from tidewater glaciers with a gauging station. To address this, hydrographic sections can be used to calculate water column velocity, and the volume of additional inputs to the system, where geostrophic circulation permits (Jenkins and Jacobs, 2008). Such methods would assist in forming better quantifications of meltwater discharge from tidewater glaciers, since these remain poorly constrained. This is despite glacier melt being marked as a major contributor to eustatic sea level rise in the 21^{st} century (Meier et al., 2007; Church et al., 2013).

Meltwater contributions to Arctic fjords, not only contribute to sea level rise but also cause a freshening of the water column, which has impacts for the marine ecosystem (Zajaczkowski and Legezynska, 2001). Subglacially derived meltwater also transports sediments, which affects primary productivity in the SW. Therefore, a better understanding of meltwater contributions and their origins, is not only important to improve estimations of sea level rise and fjord circulation (Straneo et al., 2013), but also to assess the impacts on marine biodiversity (Lydersen et al., 2014).

3.2 Methodology

3.2.1 Hydrographic Data

Hydrographic data were collected from 15 – 18^{th} July 2012 at the head of Kongsfjorden, in the ice proximal zone of Kronebreen (Figure 3.1). Temperature and salinity profiles were measured using a YSI Castaway CTD (conductivity, temperature, depth; Table 3.1). The instrument was deployed by hand from the front of a small boat. It was stabilised at 5 m depth, for approximately 5 minutes. It was then steadily lowered to either the sea bed, as determined by the feeling the line of the CTD go slack, or to the full extent of the 80 m line, which ever was deepest. When the CTD reached the seabed, a basic bathymetry was obtained.

Two sections were sampled, comprising of 25 stations in total. Each section was repeated, with 3 – 4 days between sampling. Stations were located 200 m apart for the north - south section, at a distance of approximately 250 m from the ice face. The stations forming the east - west section were 200 m apart up to 1400 m from the start of the section, closest to the ice. Beyond this they were 300 m apart until the end of the section (Figure 3.1). The spacing between stations was determined by using a hand held GPS. However, the actual location of the start and end of the CTD cast was measured and recorded by the YSI Castaway; the station location was determined as the mid-point between start and end locations.

The data were processed using YSI Castaway software to calculate values for depth, salinity, sound velocity and density. These were binned into 0.3 decibar intervals, starting at 1.5 decibars. This resulted in 30 cm depth resolution. The CTD reached the seabed enabling water depth to be established for all but two of the stations. The two furthest from Kronebreen were deeper than the line on the CTD. These temperature and salinity measurements have been used to identify the water masses in Kongsfjorden (Table 3.2).

	Range	Resolution	Accuracy
Conductivity	0 - 100,000 μS/cm	1 μS/cm	0.25% ± μS/cm
GPS		10m	
Pressure	0 - 100 dBar	0.01 dBar	0.25% of FS
Salinity (derived)	Up to 42 (PSS-78)	0.01 (PSS-78)	0.1 (PSS-78)
Temperature	-5 to + 45 °C	0.01 °C	0.05 °C

Table 3.1: YSI Castaway CTD specifications

Water mass	Abbreviation	T (°C)	S (PSU)
External Atlantic water	AW	>3.0	>34.65
Arctic water	ArW	-1.5 to 1.0	34.30 to 34.80
Internal Winter-cooled water	WCW	<-0.5	34.40 to 35.00
Local water	LW	-0.5 to 1.0	34.30 to 34.85
Surface water	SW	>1.0	<34.00
Mixed Transformed Atlantic water	TAW	1.0 to 3.0	>34.65
Intermediate water	IW	>1.0	34.00 to 34.65

Table 3.2: Water masses found in Kongsfjorden and the adjacent shelf, defined by (Cottier et al., 2005)

3.2.2 Meltwater fractions from Temperature - Salinity analysis

In the marine environment ice will melt when the ambient ocean water has a temperature above the *in situ* freezing point, leading to changes in temperature (T) and salinity (S) as a result of heat loss and freshening. The opposite effects take place with freezing. Considerable energy is required to melt glacial ice; seawater contributes heat to bring the glacier ice to the freezing point of fjord water as well as supplying the latent heat of fusion. The mixing of freshwater with ambient seawater is apparent as a straight line in T-S space, with 2.5 °C slope per salinity unit, beneath floating ice (Gade, 1979). The resultant changes in T-S space

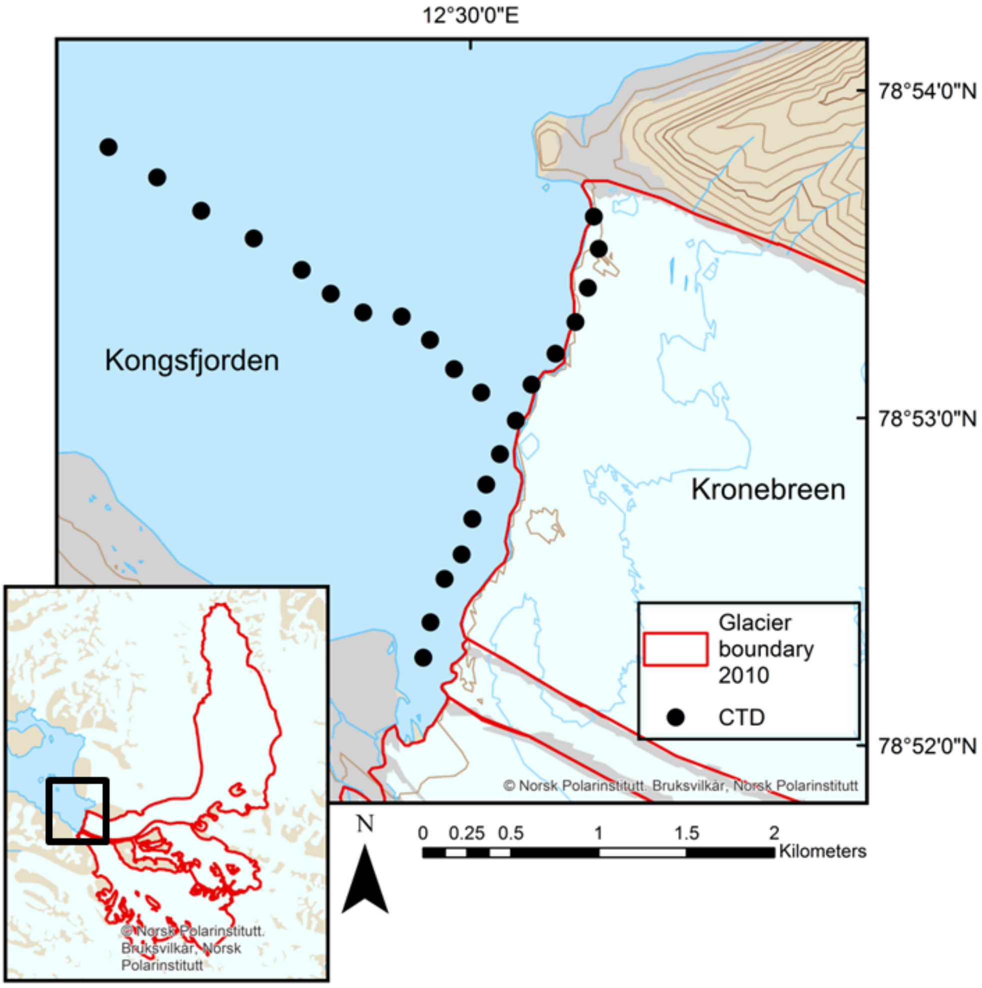

Figure 3.1: Map displaying occupied CTD stations in front of Kronebreen's ice face and those extending through the plume. These stations were each occupied twice during July 2012. Note, Kronebreen's terminus has retreated since the base map was produced, in 2010.

have been used to understand glacier-ocean interactions and processes in fjord environments (e.g. Rignot and Steffen, 2008). Water masses have been identified, including quantifying the relative proportion of freshwater, by the characteristic changes in T-S space (Figure 3.2; Mortensen et al., 2013). Another method to identify and quantify mixed water masses is to use the thermodynamic relationship between glacier melt and seawater, which has been successfully applied near a floating ice shelf in the Amundsen Sea (Jenkins, 1999). Addressing the origin of freshwater reveals the dominant production process, enabling better forecasts of freshwater entering the marine system (Mortensen et al., 2014). This study quantifies subglacial freshwater (SgFW), which comprises of surface melt, that has been discharged as a buoyant plume from the grounding line of Kronebreen, and glacial melt (GiFW), which is formed of submarine melt, resultant of direct melting of the ice face. This is achieved using a method analogous to the thermodynamic model and characteristic changes in T-S space (Mortensen et al., 2013).

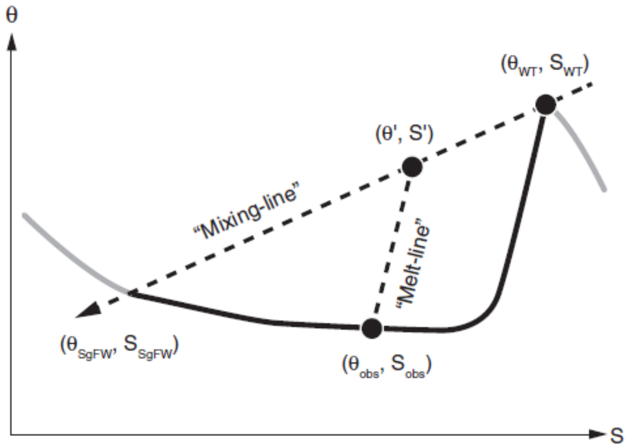

Figure 3.2: Schematic illustrating the thermodynamic and mixing processes associated with melting ice in a θ-S diagram. The observed potential temperature and salinity characteristic (θ_{obs}, S_{obs}) is a result of mixing water source type (θ_{WT}, S_{WT}) with SgFW (θ_{SgFW}, S_{SgFW}) leading to a mixing ratio determined by (θ', S'), proceeded by thermodynamic changes due to the melting of ice, illustrated by the dotted "melt-line" (Mortensen et al., 2013).

To quantify the relative fractions of subglacial meltwater and glacial melt in a water mass, a volume of seawater (V) is considered. It has a potential temperature (θ) above the freezing temperature (θ_f) in contact with ice, and density (ρ_w). This therefore gives the local heat balance:

$$V\rho_w c_p \frac{\partial \theta}{\partial t} = -L\rho_f F_w + c_i \rho_f F_w \left(\theta_i - \theta_f\right) + c_p \rho_w F_w \left(\theta_f - \theta\right) \tag{3.1}$$

Where L is the latent heat of fusion, F_w is the rate of melted ice in water equivalents, ρ_f is the freshwater density, c_p and c_i are the heat capacities of seawater and ice, respectively, θ_i is the temperature of the ice, and t is time. This assumes that the local heat balance is not affected by other sources, such as solar insolation. The equivalent balance for local salinity is specified as

$$V\frac{\partial S}{\partial t} = -F_w S \tag{3.2}$$

Equation 3.3 illustrates the straight line formed in T-S space as a result of changes in temperature and salinity from the processes of melting and freezing; these steep lines are referred to as “melt lines” as illustrated in Figure 3.2.

$$\frac{\partial \theta}{\partial S} = \frac{1}{S}\left(\frac{L}{c_p}\right) - \left(\frac{c_i}{c_p}\left(\theta_i - \theta_f\right) - \left(\theta_f - \theta\right)\right) \tag{3.3}$$

The melt line defined by Equation 3.3 passes through (θ, S) and (θ_i^*, S_i). Since $S_i = 0$, we get equation 3.4. This results in an effective temperature as given in (Jenkins, 1999; Equation 3.5).

$$(\theta - \theta_i^*) = \left(\frac{L}{c_p} - \left(\frac{c_i}{c_p}\left(\theta_i - \theta_f\right) - \left(\theta_f - \theta\right)\right)\right) \tag{3.4}$$

$$\theta_i^* = \theta_f - \frac{L}{c_p} + \frac{c_i}{c_p}\left(\theta_i - \theta_f\right) \tag{3.5}$$

3.2.3 Freshwater fraction model

To quantify the freshwater fractions (f) of a specific volume (Equation 3.6), the individual components must be evaluated: ambient water type (f_{WT}), glacial melt (f_{GiFW}), and subglacial freshwater (f_{SgFW}). In this instance f_{GiFW} is the product of ocean water directly melting the ice face, where as f_{SgFW} is the product of subglacial discharge entering at the grounding line. Presented here is a three water mass mixing model to quantify the relative fractions of f_{WT}, f_{GiFW} and f_{SgFW} (Tomczak, 1981). This method has been applied using oxygen isotopes rather than temperature as a secondary tracer (Meredith et al., 2008). Because oxygen isotope data are not available for this study, the approach of quantifying water masses by temperature and salinity characteristics has been adopted instead (Jenkins, 1999; Jenkins and Jacobs, 2008; Jacobs et al., 2011). Applying this approach to the three water mass mixing model has been shown to be synonymous to Jenkins (1999) in determining water masses in the Amundsen Sea (Nakayama et al., 2013). The characteristics of salinity (Equation 3.7) and temperature (Equation 3.8) for each of the water masses is resolved, enabling the relative fractions of f_{WT}, f_{GiFW} and f_{SgFW} to be established (Equation 3.6). A matrix equation has been formulated to solve for the three previous simultaneous equations (Equation 3.9).

$$f_{WT} + f_{GiFW} + f_{SgFW} = 1 \tag{3.6}$$

$$f_{WT}S_{WT} + f_{GiFW}S_{GiFW} + f_{SgFW}S_{SgFW} = S_{obs} \tag{3.7}$$

$$f_{WT}\theta_{WT} + f_{GiFW}\theta^{*} + f_{SgFW}\theta_{SgFW} = \theta_{obs} \tag{3.8}$$

$$\begin{pmatrix} 1 & 1 & 1 \\ S_{WT} & S_i & S_{SgFW} \\ \theta_{WT} & \theta_i^{*} & \theta_{SgFW} \end{pmatrix} \begin{pmatrix} f_{WT} \\ f_i \\ f_{SgFW} \end{pmatrix} = \begin{pmatrix} 1 \\ S_{obs} \\ \theta_{obs} \end{pmatrix} \tag{3.9}$$

With increasing distance from Kronebreen, the potential temperature and salinity properties ($\theta_{obs}S_{obs}$) will be resultant of mixing between the ambient water, f_{WT}, and the two freshwater fractions, f_{GiFW} and f_{SgFW}. It must be noted that this method cannot distinguish between glacial melt from the glacier terminus, or that of melting icebergs in the fjord.

A combined freshwater fraction can be defined since $S_i = 0$ and $S_{SgFW} = 0$ (Equation 3.10). Using the salinity signal allows the overall water mass to be split into two fractions: freshwater (f_{FW}) and ambient water (f_{WT}; Equation 3.10). This leads to a solution for S_{obs} (Equation 3.7). The total f_{WT} is determined using equation 3.12 enabling the f_{FW} to also be solved (Equation 3.13).

$$f_{GiFW} + f_{SgFW} = f_{FW}f_{WT} + f_{FW} = 1 \tag{3.10}$$

$$f_{WT}S_{WT} = S_{obs} \tag{3.11}$$

$$f_{WT} = \frac{S_{obs}}{S_{WT}} \tag{3.12}$$

$$f_{FW} = 1 - \frac{S_{obs}}{S_{WT}} \tag{3.13}$$

Utilising the salinity equation enabled f_{FW} to be separated from f_{WT}. To determine f_{SgFW} from f_{GiFW}, the effective temperature is used (Equation 3.8). The energy required to melt glacial ice is much greater than that of meltwater runoff entering the marine system as a liquid. Using the effective temperature permits f_{SgFW} to be quantified in the f_{FW} fraction (Equation 3.14). The f_{GiFW} is the remaining fraction of f_{FW} (Equation 3.15). This method is equivalent to that of Jenkins (1999) despite resolving for three water masses, rather than just the combined meltwater fraction. Additionally this method is equivalent to Mortensen et al. (2013), in which the freshwater fractions were diagnosed by a geometrical reconstruction of the T-S diagram (Figure 3.2). Equation 3.14, which quantifies f_{SgFW}, only differs from the methods of Mortensen et al. (2013) because the effective ice temperature (θ_i^*) is used, rather than the gradient of the "mixing-line" which passes through θ_{WT}, S_{WT} (Figure 3.3).

$$f_{SgFW} = \frac{(\theta_{obs} - \theta_i^*) - \frac{S_{obs}}{S_{WT}}(\theta_{WT} - \theta_i^*)}{(\theta_{SgFW} - \theta_i^*)} \tag{3.14}$$

$$f_i = f_{FW} - f_{SgFW} \tag{3.15}$$

3.2.4 Geostrophic current velocities

The width and stratification of a fjord dictate whether it will be influenced by the dynamic effect of the Earth's rotation, Coriolis (Cushman-Roisin et al., 1994). When the fjord is wider than the internal Rossby radius, cross-fjord variations in flow can be attributed to rotational dynamics. At 4 km wide Kongsfjorden is affected by Coriolis (Svendsen et al., 2002; Cottier et al., 2005). Since direct velocity measurements were not taken for this study, geostrophic circulation will be calculated to quantify the velocity and volume of freshwater exchange at the ice front of Kronebreen. The geostrophic velocity calculations, as described in Jenkins and Jacobs (2008), have been used. This method was applied to Pine Island Glacier, Antarctica, in which the results from the geostrophic methods were comparable to velocity measurements taken with an acoustic doppler current profiler (ADCP) in a later field campaign (Jacobs et al., 2011). The vertical pressure gradient is directly related to the density of the water. This estimate relies upon the calculation of density, under the assumption that flows are in hydrostatic and geostrophic balance (Equations 3.16).

$$F\frac{\partial v}{\partial P} = -\frac{\partial \alpha}{\partial x}|_P \tag{3.16}$$

In which F is the Coriolis parameter, v is the velocity perpendicular to the CTD section, P is pressure, α is specific volume, x is the horizontal axis, and the derivative is taken along the isobaric surface. The velocity can be calculated on any pressure surface relative to that at a reference pressure by integrating the equation with respect to pressure:

$$v(P) = v(P_{ref}) + \frac{1}{f}\frac{\partial}{\partial_\chi}\left(\int_P^{P_{ref}} \alpha\right)|_P \tag{3.17}$$

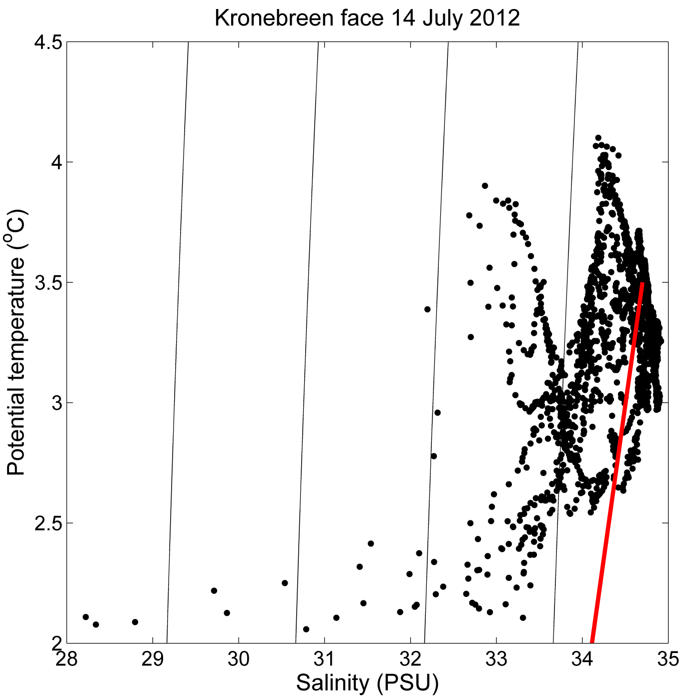

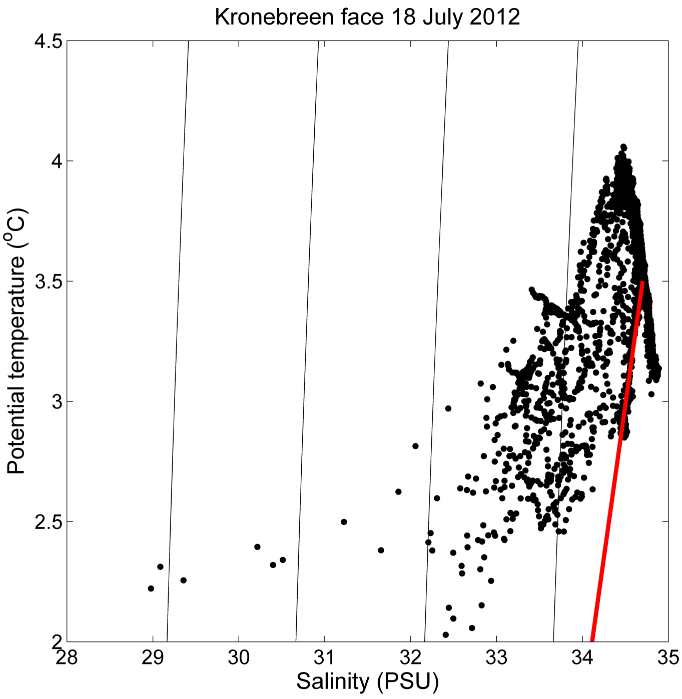

Figure 3.3: θ-S plots from CTD stations in front of Kronebreen on 14th and 18th July 2012. "Melt Line" is displayed as a solid red line representing the thermodynamic changes as a result of melting ice (Equation 3.3).

A reference velocity is required to vertically integrate flow velocities (Jenkins and Jacobs, 2008). In deep sea environments the level of no motion is placed where the vertical shear of currents is assumed to be zero, typically at a depth of 2000 m (Defant, 1961). The currents would then be integrated as a function of depth up to the sea surface and down to the sea bed. In this scenario, the depth at the head of Kongsfjorden ranges between 40 – 80 m. The freshwater fraction is expected to flow away from the ice front at the surface; as such, the level of zero motion has been set at the seabed and velocities have been integrated vertically up to the fjord surface (Equation 3.17).

In a closed system, with no additional inputs, the inflow and outflow across the section would be equal. The CTD section parallel to Kronebreen essentially closes the system. Therefore the transport across the section can be calculated with Equation 3.18, in which M is mass and the summation runs over n station pairs.

$$\sum_{j=1}^{n}(M_{out} - M_{in})_j) = M_{melt} \tag{3.18}$$

3.3 Results

3.3.1 Hydrographic sections

The hydrographic data presented in this chapter, detail the composition and spatial variability of water masses within the ice proximal zone at the head of Kongsfjorden, which have been previously undocumented. This has been achieved with hydrographic sections, taken ~300 m in front of Kronebreen's ice face, and through the buoyant meltwater plume, which extends down Kongsfjorden (Figure 3.1). These were taken in mid-July, when glacial meltwater discharge from Kronebreen to Kongsfjorden is expected to be high. Temperature and salinity profiles of the stations parallel to Kronebreen's ice front, covering the full depth of the water column, are shown in Figure 3.4, and stations through the plume are shown in Figure 3.5. A basic bathymetric profile has also been obtained, due to the CTD reaching the floor at each station, apart from the two furthest from the ice face.

At the ice front, temperature varies between 0.8 – 4.2 °C and salinity between 24.0 – 34.4 PSU (Figure 3.4). A bathymetric ridge is apparent 1.3 km south along the section (Figure 3.6). The temperature and salinity properties differ either side of this ridge. The south exhibits surface temperatures of 1.6 °C which increase to 4.1 °C at 15 m depth. The surface temperatures in the north range from 0.8 – 3.8 °C increasing to 2.4 – 3.4 °C at 14.0 m depth, where the thermocline is observed. This general temperature structure is similar on both 14th and 18th July however, the latter day has far less variability in temperature between the southern stations (Figure 3.4). The southern stations have the greatest range of salinity, from 24.0 – 34.4 PSU, compared to the northern stations which exhibit a range of 31.2 – 34.4 PSU. A fresh surface layer is revealed by surface salinities as low as 24.0 PSU in the upper 4.0 m of the water column. At 4.0 m depth the salinity has increased to 32.5 PSU and continues to increase to 34.2 PSU at 20 m depth. Between 4 – 20 m the northern stations exhibit lower salinities than the south by up to 1 PSU. From 20 m to the sea bed, the salinities of the north and south have converged and exhibit the same properties.

The temperature in the plume is not as low as at the ice front, with temperatures ranging from 2.6 – 4.4 °C (Figure 3.5). Between 4.0 – 20.0 m temperature increases rapidly from 3.1 – 4.1 °C, coinciding with a salinity increase from 33.4 – 34.9 PSU, forming the pycnocline layer. The pycnocline layer displays much greater temperature variability on the 15th July than on the 18th July (Figure 3.5). From 26.0 m temperature continues to decrease with depth, whilst there is only a small change in salinity. Below 62.0 m depth, the rate of temperature change increases; the temperature cools from 3.0 °C to 2.3 °C at 82.0 m.

Water masses

Three distinct water masses have been identified at the head of the Kongsfjorden: AW, IW, and SW. Sourced from the WSC, AW is the primary influx of heat and salt to Kongsfjorden (Svendsen et al., 2002). Large freshwater inputs are sourced from freshwater runoff (surface and submarine), direct submarine melt of Kronebreen and precipitation. These contribute to the formation of SW, which exhibits low salinity but is relatively warm due to solar heating in the summer months (T (°C) >1 and S (PSU)<34.00). When AW and SW mix, IW is formed (T (°C) >1 and S (PSU) 34.00 – 34.65).

The hydrographic structure at the ice front revealed differences in temperature and salinity properties between the north and the south of the section, either side of the bathymetric high (Figure 3.4). Here, the description of water mass occupation has been separated into north and south for the section in front of Kronebreen (Figure 3.6). The south comprises of SW from 0.0 – 8.9 m depth, IW from 9.0 – 34.9 m and the dense AW occupies from 35.0 m to the sea bed. The top 4.0 m of the SW has signals of fresh water, with salinities reaching as low as 24.0 PSU (Figure 3.7). The north displays the same vertical arrangement but in different proportions: 0.0 – 13.9 m SW, 14.0 – 45.0 m IW, and 45.0 m to the seabed is occupied by AW. Comparatively, the northern extent of the transect is cooler and fresher than the southern extent. Again, the top 4.0 m of the SW is fresh, with

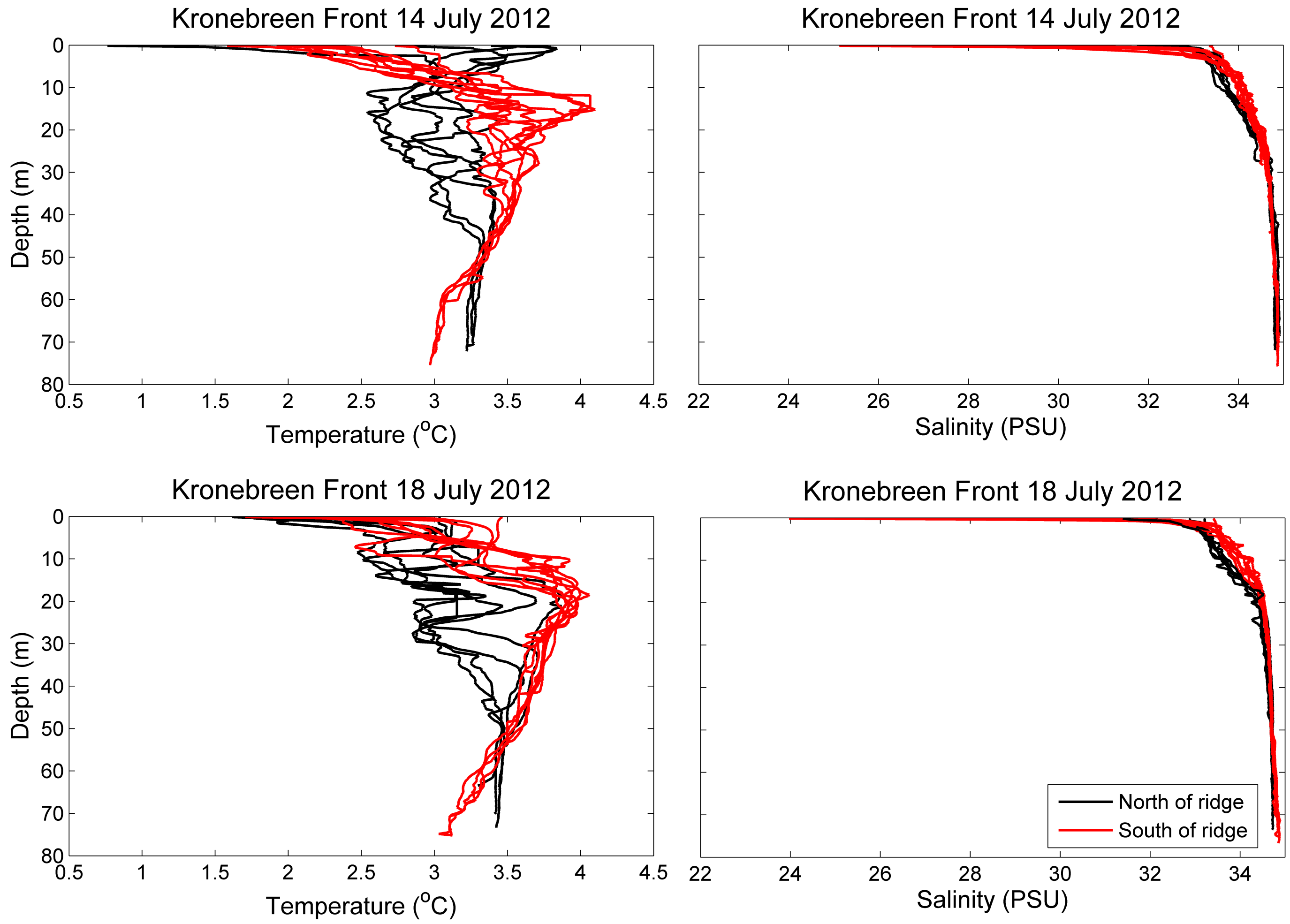

Figure 3.4: Depth profiles of temperature (°C) and salinity (PSU) from CTD stations occupied at the front of Kronebreen on 14th and 18th July 2012. The solid black lines represent the six CTD stations north of the bathymetric ridge and the solid red lines represent the eight CTD stations south of the ridge. The bathymetric ridge can be seen in the contour plots in Figure 3.6.

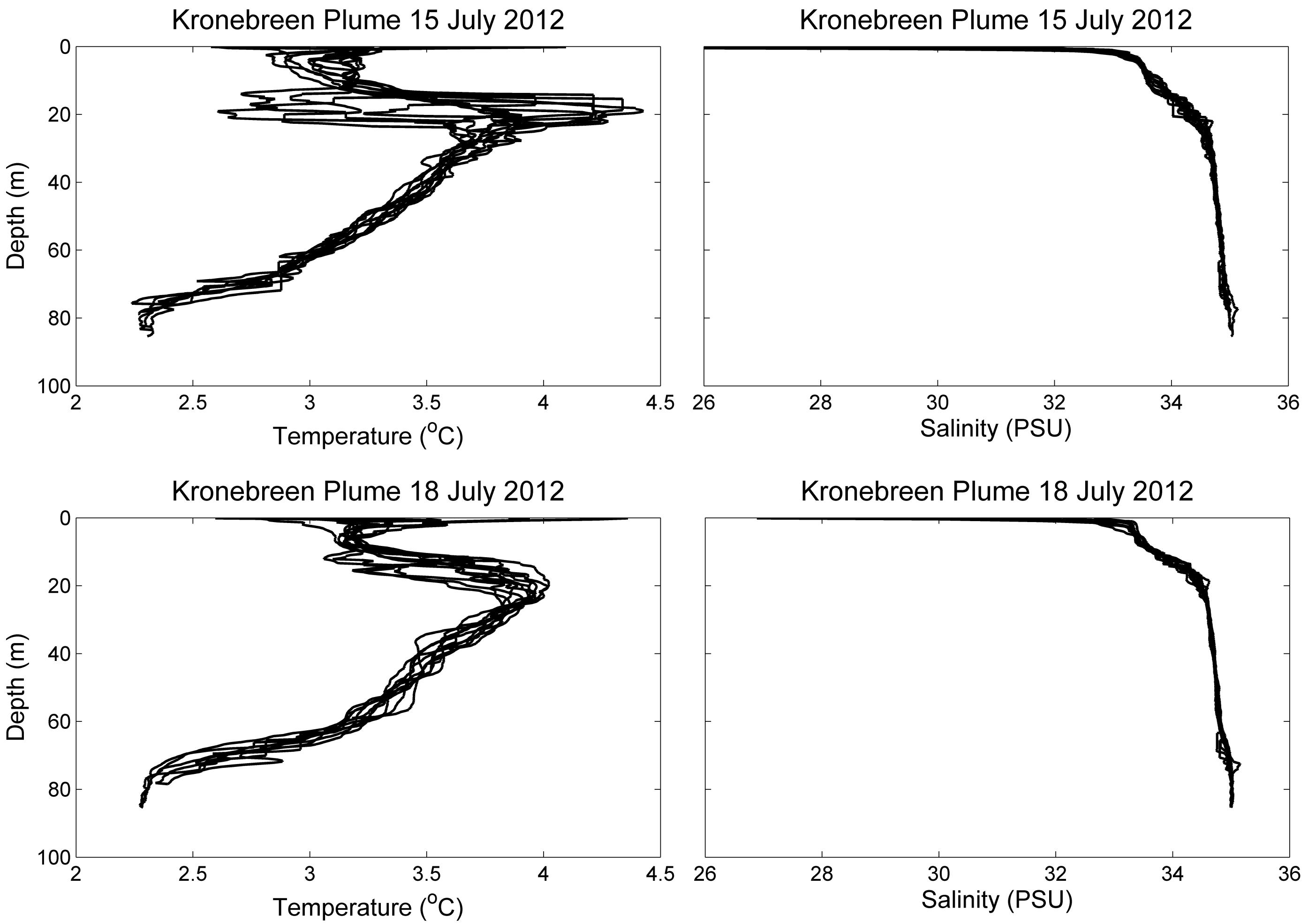

Figure 3.5: Depth profiles of temperature (°C) and salinity (PSU) from CTD stations occupied from the front of Kronebreen to 2.7 km away through the centre of the plume (Figure 3.1). Measurements were taken on the 15th and 18th July 2012. The CTD reached the floor each time, apart from the two stations furtherest from Kronebreen.

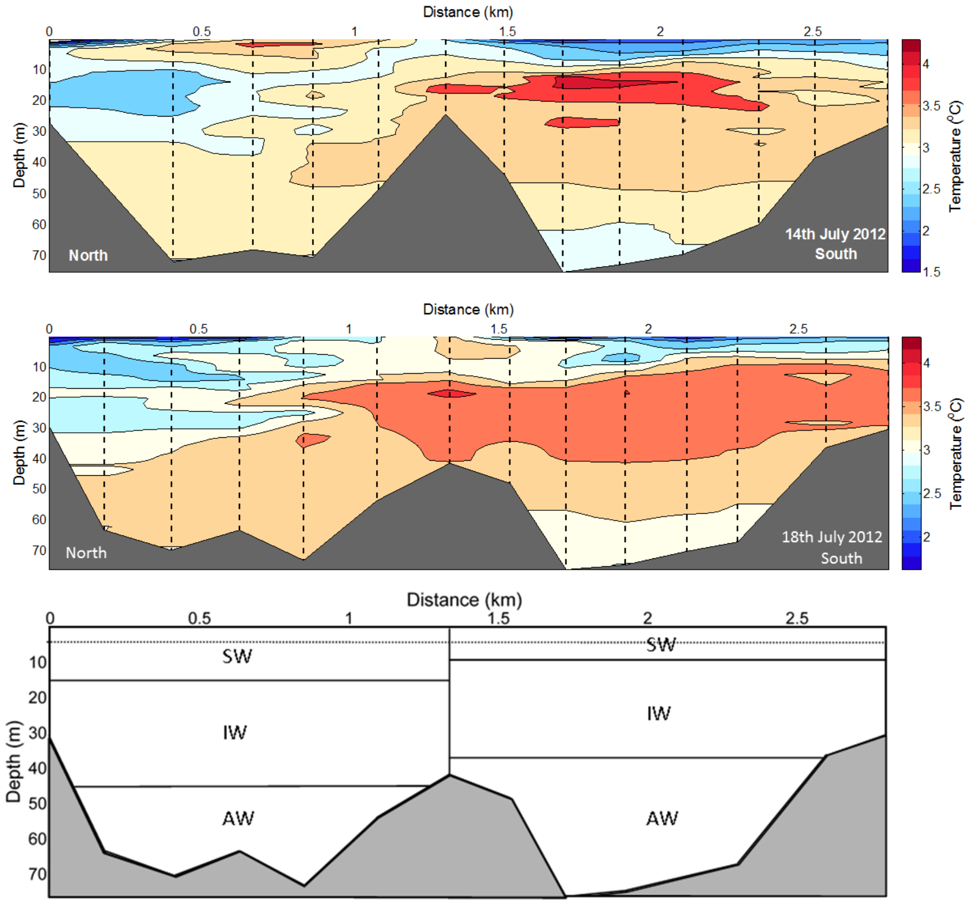

Figure 3.6: Depth contour plots of temperature (°C) in front of Kronebreen's calving face, as determined from CTD stations. Vertical black lines indicate locations of CTD measurements in front of Kronebreen on the 14th and 18th July 2012 (Figure 3.1). The CTD reached the floor each time, providing basic bathymetry for the fjord, shown as the blacked out region. The schematic details the location of water masses using the classifications as in Cottier et al. (2005). Dotted line indicates base of the freshest SW at 4.0 m depth.

salinities ranging from 31.0 to 33.0 PSU (Figure 3.7).

The along fjord CTD section depicts the water masses entering the fjord and those that leave from the ice face (Figure 3.8). The same three water masses are present at the ice face (AW, IW, SW), with the addition of TAW (T (°C) <3, S (PSU) >34.65). Closest to the glacier, the top 14.0 m of the water column is occupied by SW, 14.0 – 38.0 m occupied by IW and 38.0 – 64.0 m is AW. Surface salinities are lowest closest to Kronebreen (Figure 3.9). Beneath the AW lies TAW which extends to the sea bed. At the furthest extent of the transect, 2.5 km from the ice face, the oceanographic structure is the same. However, IW occupies less space, from 14.0 – 30.0 m, with AW replacing the difference. The TAW is the densest of the four water masses and therefore located at the bottom of the water

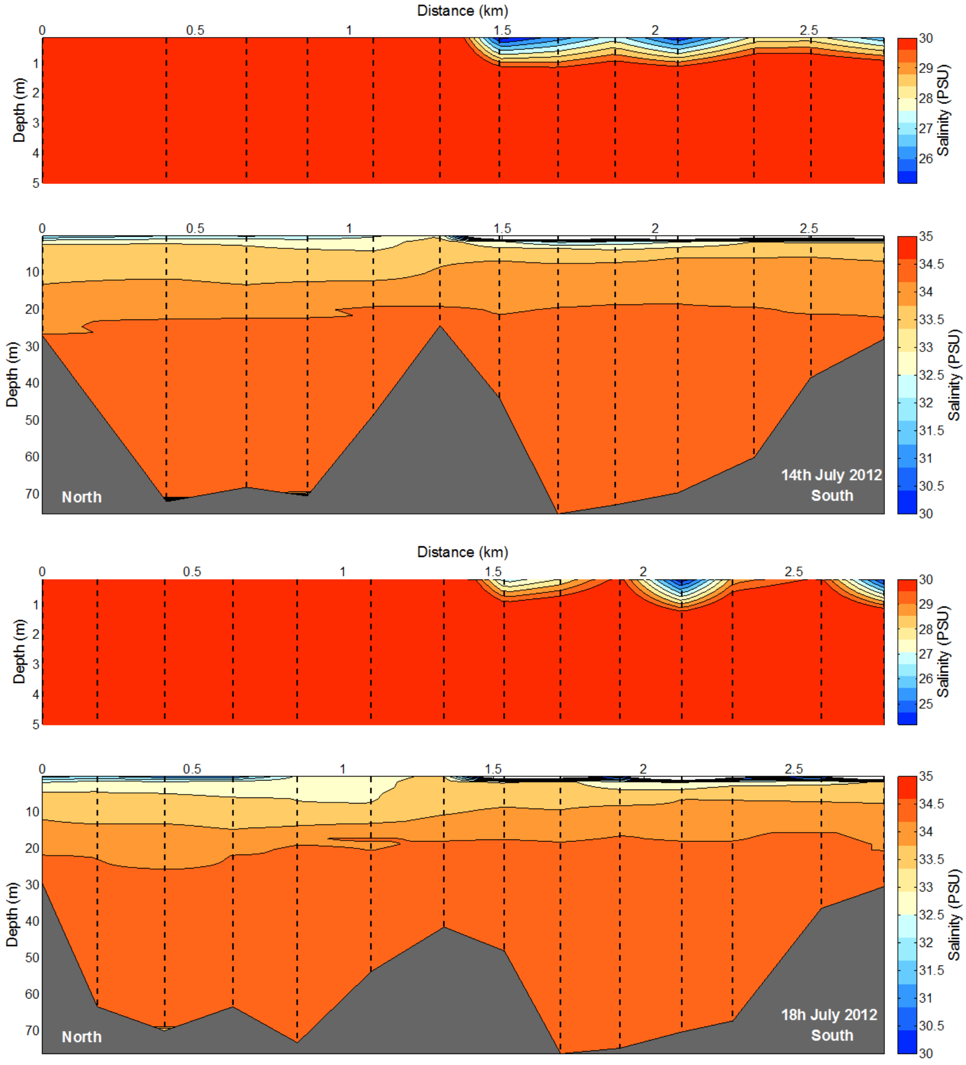

Figure 3.7: Depth contour plots of salinity (PSU) in front of Kronebreen's calving face, as determined from CTD stations. Vertical black lines indicate locations of CTD measurements in front of Kronebreen on the 14th and 18th July 2012 (Figure 3.1). The CTD reached the floor each time, providing basic bathymetry for the fjord, shown as the blacked out region. The upper plot focuses on the top 5 m of the water column, which has a lower salinity than the rest of the water column.

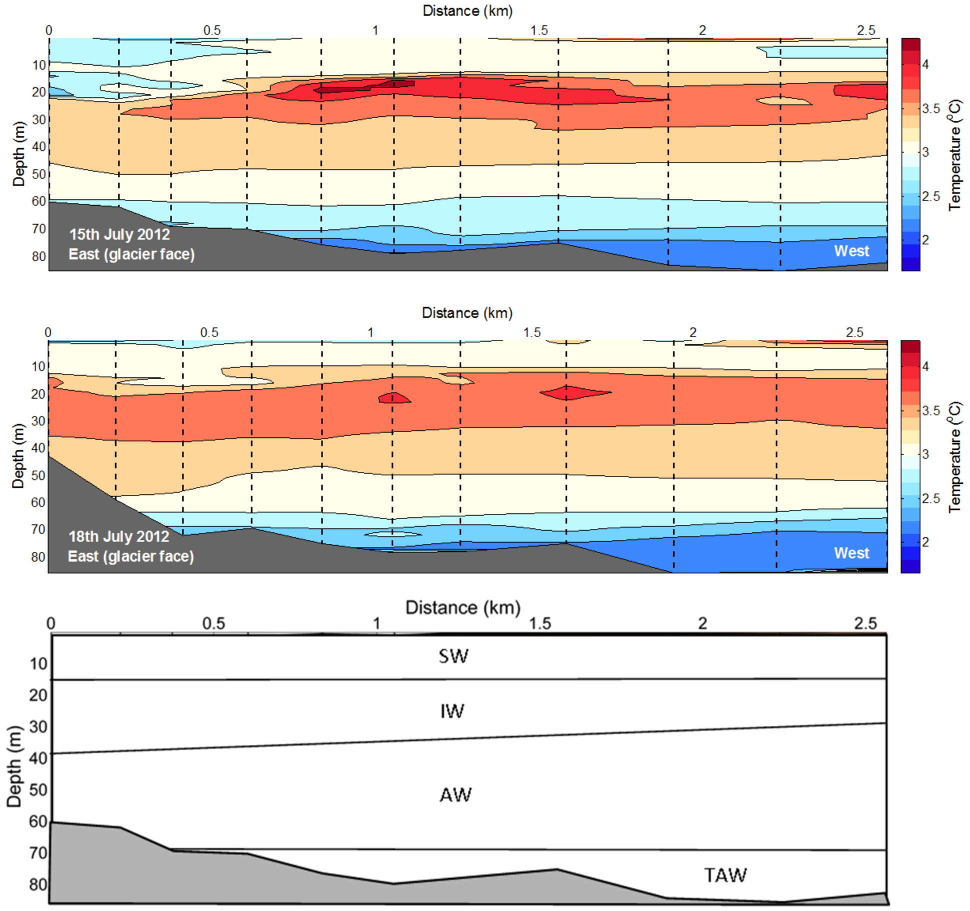

Figure 3.8: Depth contour plots of temperature (°C) through the plume, determined from CTD stations at the front of Kronebreen to a distance of 2.7 km away, through the centre of the plume (Figure 3.1). The vertical black lines indicate location of CTD measurements on the 15th and 18th July 2012. The CTD reached the floor each time, apart from the two stations furtherest from Kronebreen providing basic bathymetry for Kongsfjorden as displayed by the blacked out region. The schematic details the location of water masses using the classifications as in Cottier et al. (2005).

column. Its density prevents it from rising above the ridge created by sediment deposition and therefore it does not reach the glacier face (Figure 3.8).

Freshwater fractions

The fractions of ambient AW, GiFW and SgFW have been quantified using the three water mass mixing model (Equation 3.9). The proportion of freshwater in the water column has been quantified (Equation 3.13), in addition to quantifying the relative contributions from SgFW and GiFW. This has revealed that the dominant freshwater source entering the head of Kongsfjorden is SgFW, with GiFW only accountable for a small proportion of the freshwater present.

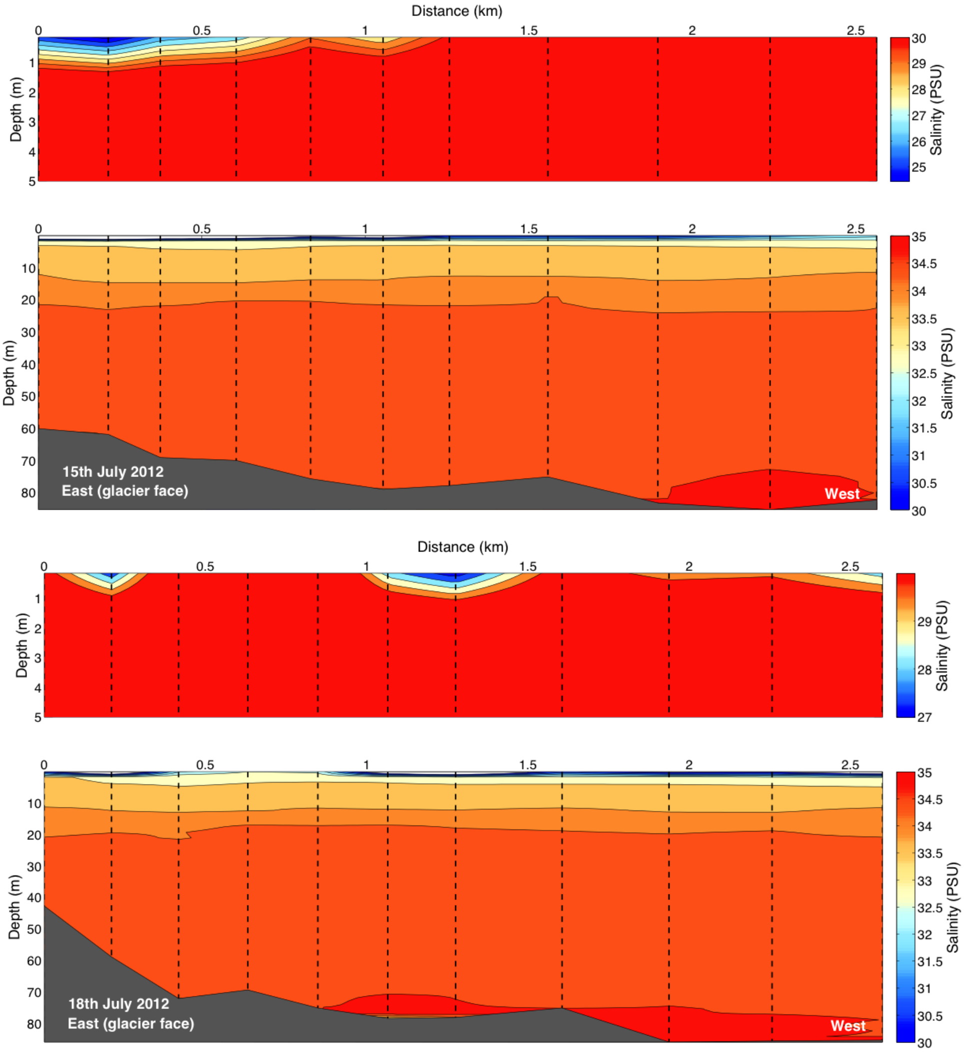

Figure 3.9: Depth contour plots of salinity (PSU) through the plume, determined from CTD stations. Vertical black lines indicate locations of CTD measurements in front of Kronebreen on the 14th and 18th July 2012 (Figure 3.1). The CTD reached the floor each time, providing basic bathymetry for the fjord, shown as the blacked out region. The upper plot focuses on the top 5 m of the water column, which has a lower salinity than the rest of the water column.

In the section in front of Kronebreen between 3 – 30% of the SW is composed of SgFW (Figure 3.10). The upper 45.0 cm of the water column has SgFW contributions up to 30%, and decreases with depth. From 0.5 m to 14.0 m depth SgFW declines to 3%. A spatial change in SgFW is present between the northern and southern sections of the transect. North of the central bathymetric high (Figure 3.10), 3 – 8% of the SW is formed of SgFW. The southern extent receives considerably more SgFW in the range of 12 – 30%. Although small, there are glacial melt contributions up to 3% (Figure 3.11); this varies across the ice front with the north receiving up to 1% more than the south. In contrast to SgFW, the glacial ice melt is not constrained to the surface layer. In the south, the GiFW is located at the surface within the upper 10.0 m of the water column, whilst in the north it can also be found at 10.0 – 20.0 m depth (Figure 3.11).

Extending through the plume down the fjord, SgFW remains the dominant freshwater fraction (Figure 3.13), with small a GiFW contribution (Figure 3.12). The top 45.0 cm is again dominated by SgFW with up to 3% penetrating to a depth of 10.0 m. GiFW is not found beyond 300 m of the glacier front; the small volume found close to Kronebreen is located at 15.0 – 20.0 m depth, in the IW (Figure 3.13). The same pattern of freshwater distribution, for both GiFW and SgFW is observed in both the sections, on two different days.

This surface freshwater signal extends beyond the 2.5 km transect on both days sampled (Figure 3.14). A strong ebb tide on the 15th July, exhibited a tidal range of 42.0 cm which has coincided with a steady decrease in SgFW with increasing distance from the ice front. SW closest to the ice front was formed of 30% SgFW at 15 cm depth, decreasing to 10% at 2.5 km along the section. At 45 cm depth, a SgFW fraction of 15% is found closest to the ice front, decreasing to 8% at 2.5 km distance (Figure 3.14). Three days later on 18th July the CTD stations were sampled during high to low tide, with a much reduced tidal range of 14.0 cm compared to the 15th July. The SgFW appears more variable with distance. It does not exhibit the same layer structure with greater SgFW at 15 cm than 45 cm depth as was found on the 15th July (Figure 3.14). The fraction of SgFW varies from 6 – 2 %, with greatest variability apparent at 15 cm depth.

3.3.2 Transport velocity and freshwater volume

Transport velocity of water masses and the volume of freshwater has been calculated using the geostrophic balance across the CTD stations (Jenkins and Jacobs, 2008; Jacobs et al., 2011). This has been applied to each of the two repeat CTD sections parallel to Kronebreen's ice front. This has enabled the velocities of inflow, towards the ice front, and outflow, away from the ice front at the glacier-ocean

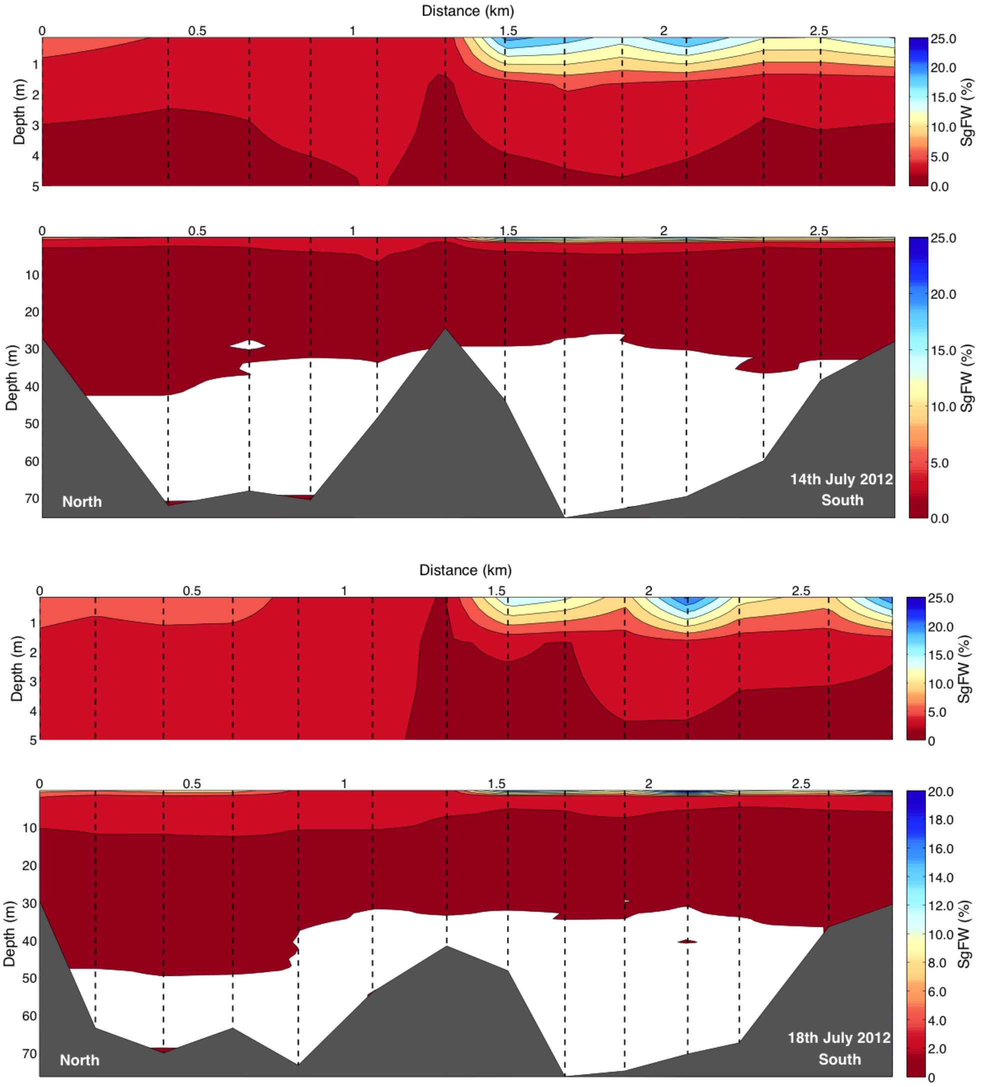

Figure 3.10: Depth contour plots of SgFW, determined from CTD measurements (black vertical lines) at the front of Kronebreen on 14th and 18th July 2012 as detailed in Figure 3.1. Sea floor bathymetry (blacked out region) was obtained by the CTD reaching the floor. The fraction of SgFW has been determined using Equation 3.14. The white region represents AW which has a salinity higher than that defined in the freshwater fraction model, and appears to the right of the melt line in Figure 3.3.

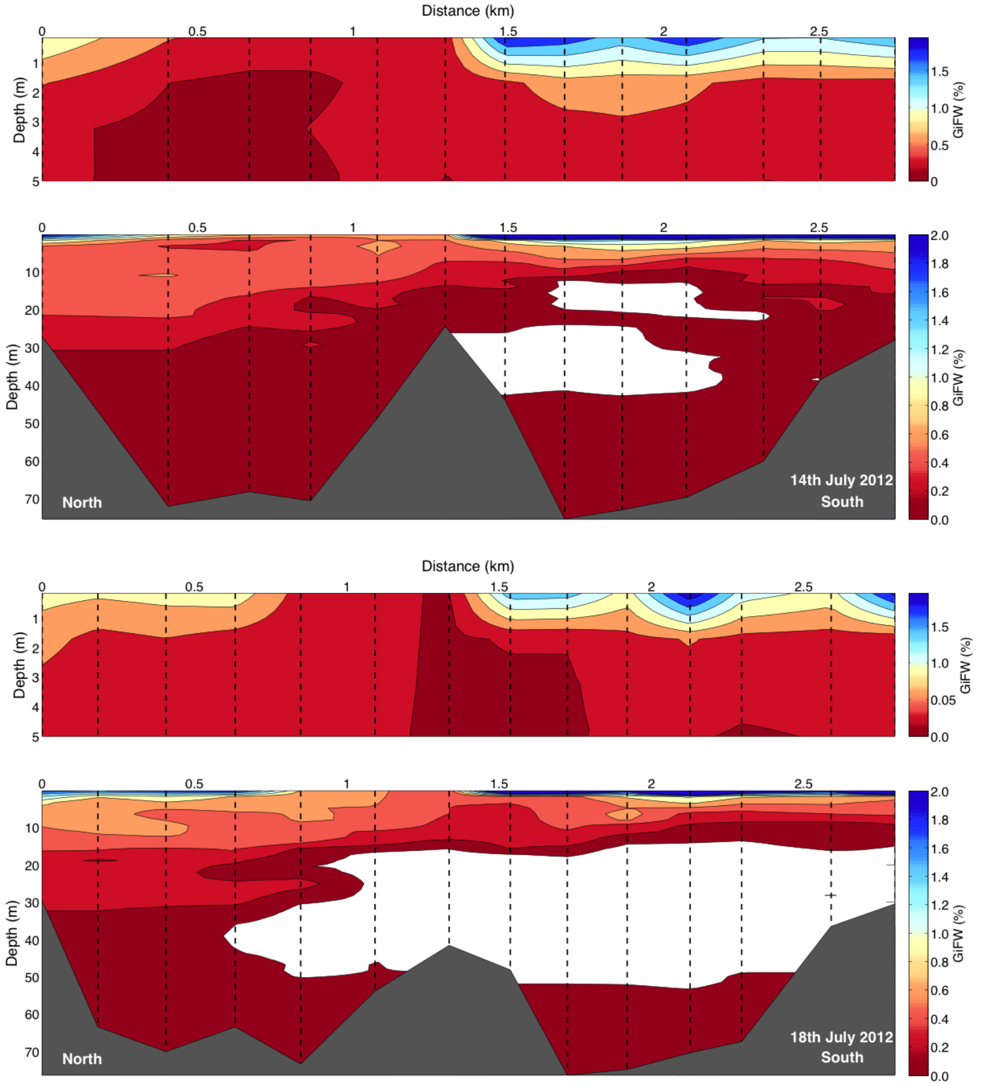

Figure 3.11: Depth contour plots of GiFW, determined from CTD measurements (black vertical lines) at the front of Kronebreen on 14th and 18th July 2012 as detailed in Figure 3.1. Sea floor bathymetry (blacked out region) was obtained by the CTD reaching the floor. The GiFW fractions have been determined using Equation 3.15. The white region represents AW which has a salinity higher than that defined in the freshwater fraction model, and appears to the right of the melt line in Figure 3.3.

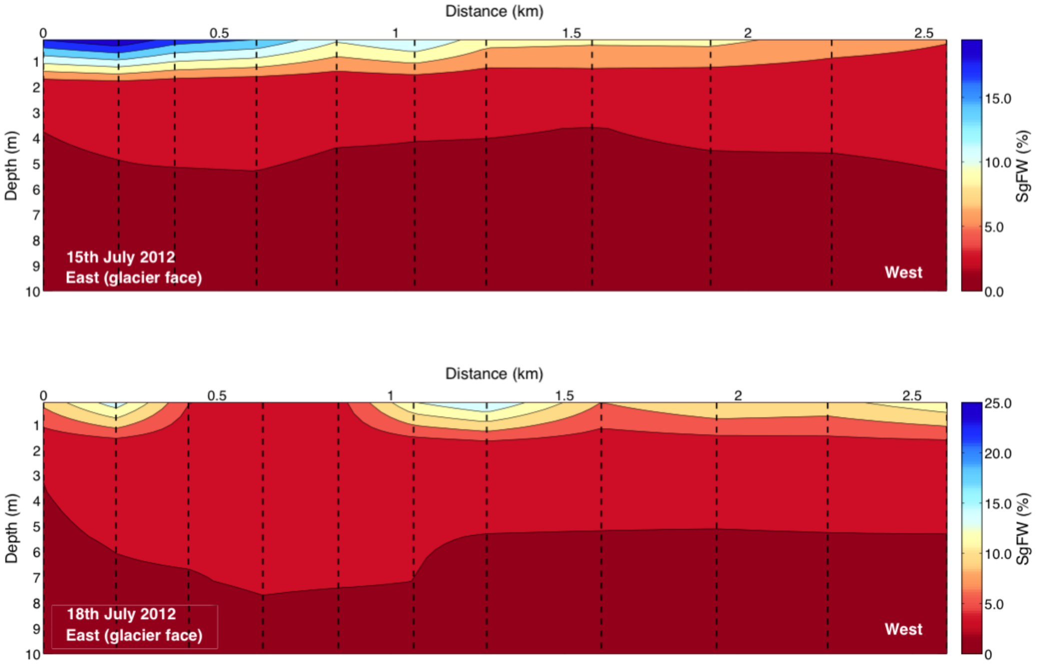

Figure 3.12: Depth contour plots of SgFW fractions determined from CTD measurements (black vertical lines), extending down Kongsfjornde away from Kronebreen, as illustrated in Figure 3.1. The fraction of SgFW has been determined using Equation 3.14. The white region represents AW which has a salinity higher than that defined in the freshwater fraction model. Freshwater is only located in the upper water column.

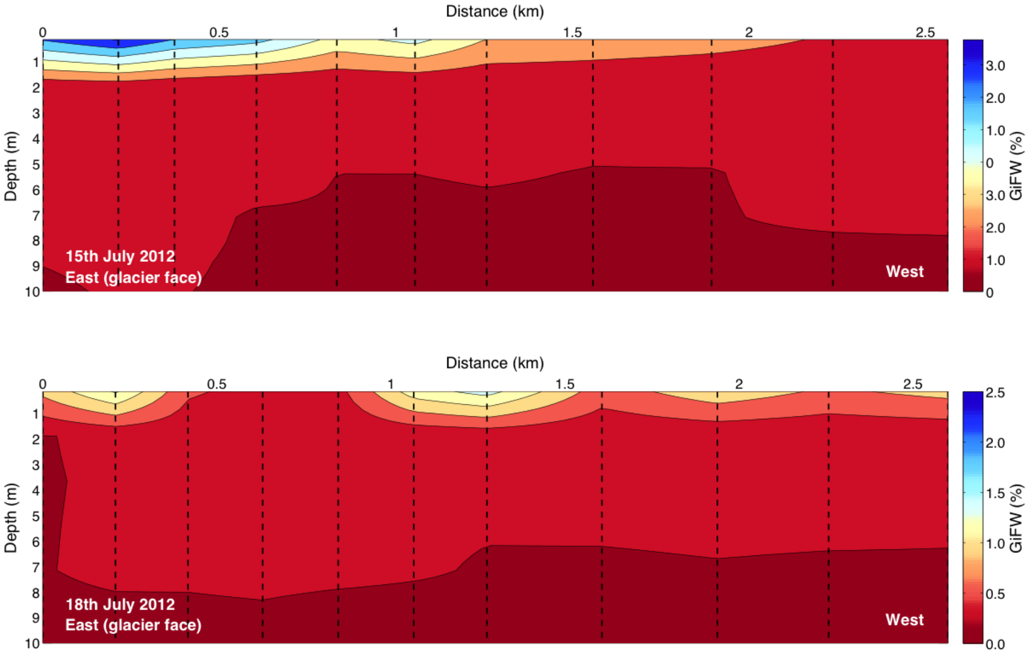

Figure 3.13: Depth contour plots of GiFW fractions determined from CTD measurements (black vertical lines), extending down Kongsfjornde away from Kronebreen, as illustrated in Figure 3.1. The fraction of GiFW has been determined using Equation 3.15. The white region represents AW which has a salinity higher than that defined in the freshwater fraction model, and appears to the right of the melt line in Figure 3.3. Freshwater is only located in the upper water column.

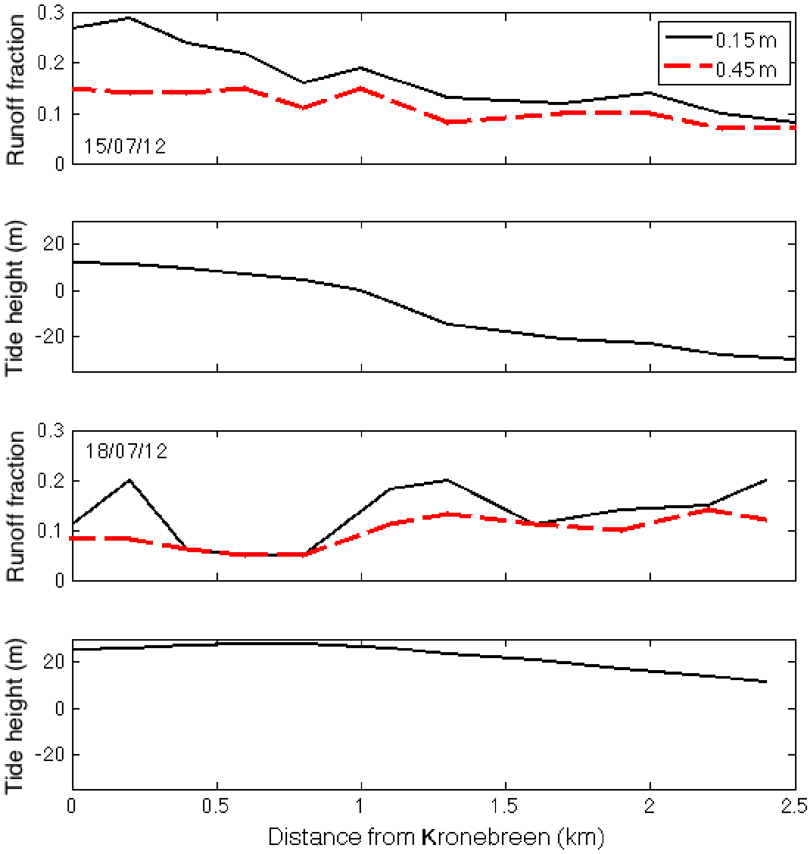

Figure 3.14: Changes in SgFW at 15 (black line) and 45 cm (red line) depth with distance from Kronebreen through the plume on the 15th and 18th July 2012. The tidal height has been determined from the corresponding time of CTD sampling. Tidal height data were obtained from the tide gauge located at Ny-Ålesund (Vannstand, 2014).

interface of Kronebreen, to be calculated. The balance between inflow and outflow of a closed system would be equal. Therefore if the outflow is greater than inflow, additional freshwater inputs are reaching the marine system, which can then be quantified.

A general trend of inflow at depth and outflow at the surface prevails, following the two layer circulation associated with Arctic fjords (Cottier et al., 2010). A greater inflow is found in the south, whilst the greatest outflow velocities are found in the north (Figure 3.15). Outflow velocity is greatest in the top 45.0 cm of the water column, 1.25 – 1.50 km along the transect from the north. Maximum velocities of 0.6 – 1.0 m s^{-1} are found in the SW, with velocity decreasing with depth (Figure 3.15). The velocities differed between days; the maximum transport of 1.0 m s^{-1} was calculated for 15th July, whilst three days later on the 18th July this maximum decreased to 0.6 m s^{-1} (Figure 3.15). Inflow velocities are slower, ranging from 0 – 0.4 m s^{-1}, but are more uniform across the ice front. The calculated outflow velocities lie in agreement with a drifter study which stated mean velocities of 0.36 – 0.8 m s^{-1} (Zajaczkowski and Legezynska, 2001). The vertical profile structure also agrees with Zajaczkowski and Legezynska (2001), in which the greatest velocities are found in the top 45 cm of the water column, and decrease with depth.

Comparison of inflow and outflow volumes, to and from the ice front, as determined by geostrophic velocities, reveals a net volume increase at the head of Kongsfjorden. An additional 3.6 x 10^6 m^3 entered the marine system on 14th July. This increased to 4.4 x 10^6 m^3 on the 18th July. By taking these two calculated results of freshwater input, annual freshwater input can be estimated. Based on a 121 day melt season, from June 1st to 30th September, an estimated 4.4 – 5.3 x 10^8 m^3 yr^{-1} of additional water entered the marine system during 2012. The rate of flow is found to be 50.94 m^3 s^{-1} on the 14th July, decreasing to 41.74 m^3 s^{-1}. These values are greater than the daily mean runoff for the Kronebreen - Kongsvegen system, established from the Weather Research and Forecasting model for Climatic Mass Balance (WRF-CMB). Modelled runoff was 26.35 and 22.21 m^3 s^{-1} for the 14th and 18th respectively (Aas, K 2015, pers. comm., 30 Jan).

Upscaling these daily measurements to a 121 day ablation season reveals the geostrophic velocities and runoff are of the same order of magnitude: geostrophic 4.3 – 5.3 x 10^8 m^3 yr^{-1}, and runoff 0.9 – 1.1 x 10^8 m^3 yr^{-1}. However, these measurements are substantially less than the total runoff for 2012 as produced by the WRF-CMB model, of 1.0 x 10^{10} m^3 yr^{-1} (Aas, K 2015, pers. comm., 30 Jan). The modelled runoff results indicates that upscaling annual runoff from only two days of the melt season, under represents the annual runoff.

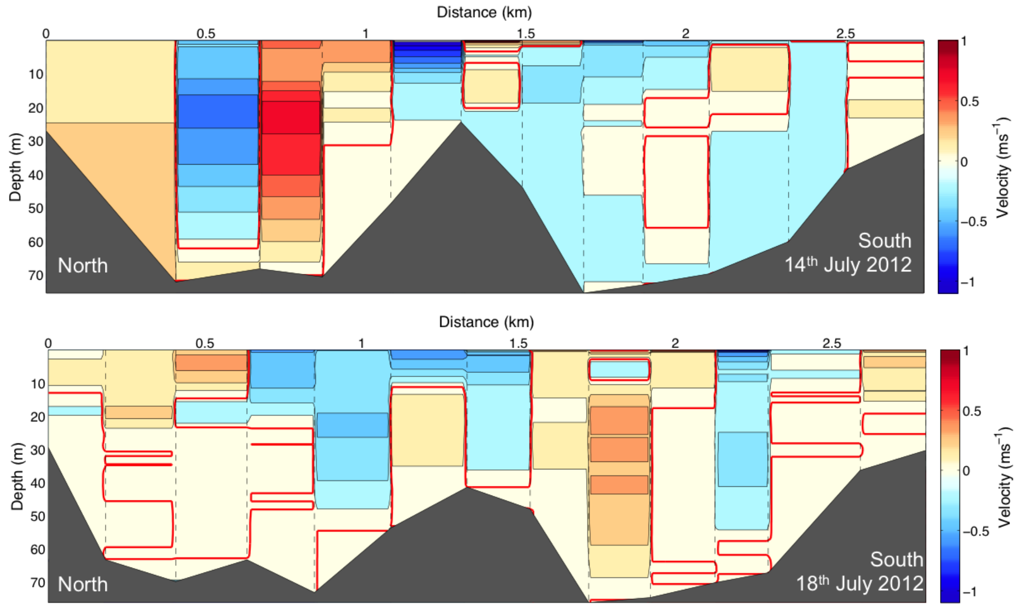

Figure 3.15: Adjusted geostrophic velocities from two repeat sections parallel to Kronebreen ice front, with CTD stations occupied on 14th and 18th July 2012. The sections are orientated looking towards Kronebreen's ice front, in which negative values denote flow away from Kronebreen, and positive denotes flow towards Kronebreen. The location of CTD stations is indicated by the vertical black lines. The red lines indicate no motion.

3.4 Discussion

Located at the head of Kongsfjorden, in the ice proximal zone of Kronebreen, there are three water masses present: SW, IW and AW, typical of summer water column structure in Arctic fjords (Cottier et al., 2005). SW is formed of freshwater contributions, formed of both SgFW and GiFW, and extends down Kongsfjorden, occupying the upper 15 m of the water column. It is downwelled, mixing with IW; with increasing distance from Kronebreen, the occupation of AW increases, as the depth of IW decreases. Across the ice face, AW occupied a greater proportion of the water column at the southern side, which corroborates with observations at the mouth of Kongsfjorden, indicating that AW inflow is concentrated on the right hand side of the fjord (Aliani et al., 2004). An uneven distribution of freshwater across the fjord surface has been observed (Figure 3.10), which exemplifies the role rotational forces upon the fjord. Although SgFW discharge occurs south of the centre line of Kronebreen (Trusel et al., 2010; Kehrl et al., 2011), the SW layer is 5 m deeper north of the bathymetric high at the ice front (Figure 3.10). The freshwater is deflected to the right of the outflow (Azetsu-Scott and Tan, 1997; Ingvaldsen et al., 2001; Svendsen et al., 2002; Skogseth et al., 2005b). Deeper mixing of freshwater in the north is assisted by downwelling, which occurs to the right of the wind (Svendsen, 1995; Cottier et al., 2005).

This study has discerned transport velocities throughout the water column, enabling the additional volume of freshwater entering at the head of Kongsfjorden to be quantified during mid summer in 2012. The method of determining water transport using geostrophic velocities has been previously applied to the cavities of ice shelves: George VI (Jenkins and Jacobs, 2008) and Pine Island (Jacobs et al., 2011) Glaciers, Antarctica. Using geostrophy provides an ideal alternative when *in situ* velocity measurements are not available (Jacobs et al., 2011). However, both of these Antarctic locations have water depths >1000 m, making the frictional effects of the atmosphere and seabed negligible (Defant, 1961). Kongsfjorden contrasts these studies as the deepest location is only 80 m; therefore the results are likely to have incorporated some frictional processes. Despite this, the results reveal that a two layer circulation is present in Kongsfjorden, as with many Arctic fjords (Svendsen et al., 2002; Cottier et al., 2005). At depth AW is present (Figure 3.10), flowing towards the ice front with velocities up to 0.4 m s^{-1}. Outflow velocity was greatest in the SW at the north of Kronebreen, with maximum velocities of 0.6 – 1.0 m s^{-1}, corroborating with (Zajaczkowski and Legezynska, 2001; Figure 3.15). SW velocities were not constant across the ice face, supporting the idea that fjord velocities close to the discharge site is set by the discharge velocity (Syvitski et al., 1990). This implies that the dominant buoyancy forcing at the head of Kongsfjorden is from subglacial discharge entering at depth from the grounding line, which agrees with both modelled and theoretic studies (Sciascia et al., 2013; Xu et al., 2012; Jenkins, 2011). Further down the fjord, the estuarine circulation sets the transport speed (Inall and Gillibrand, 2010). The topography of Kongsfjorden, as with other Arctic fjords, causes the strong and persistent katabatic winds to be steered, resulting in a bi-modal, up-fjord and down-fjord wind system, which effects the SW (Svendsen et al., 2002; Nilsen et al., 2008; Esau and Repina, 2012). Given that Kongsfjorden lacks a defined sill, allowing easy exchange with coastal waters, it is influenced by changes in WSC properties, which propagate through the fjord, altering the AW properties at varying timescales (Cottier et al., 2007).

The three water mass mixing model (Equation 3.9), which is synonymous to the methods of Mortensen et al. (2013), revealed SgFW as the dominant freshwater type at the head of Kongsfjorden. Up to 30% of the SW is formed of SgFW, which enters Kongsfjorden as subglacial discharge from the grounding line of Kronebreen. The GiFW fraction in the SW layer is an order of magnitude smaller, with inputs up to 3%. Production of GiFW by submarine glacier melt has been highlighted as a significant contributor to freshwater production in Greenlandic fjords (Rignot et al., 2010; Enderlin and Howat, 2013), whilst it appears to only play a small role at the ice - ocean interface of Kronebreen - Kongsfjorden during the summer (Figure 3.10). Driven by ablation, the production of SgFW is strongly seasonal (Bhatia et al., 2011; Sciascia et al., 2013). This study in Kongsfjorden has only analysed the summer freshwater regime, whilst the dominating process for freshwater production may be different during the winter months.

Extending down Kongsfjorden, the lateral spread of the freshwater plume has been revealed by the temperature and salinity profiles (Figure 3.8) in addition to determining the freshwater fractions (Figure 3.12). The dominant freshwater fraction through the plume is again SgFW, with GiFW exhibiting a minor signal. The lateral spread of freshwater differed on the two sampling days. On the 14th July a steady decrease in SgFW at 15 cm depth from 30% at 0 km to 10% at 2.5 km, and is estimated to extend a further 1.0 – 2.0 km away from the ice front under the influence of a strong ebb tide. However, on the 18th July under the influence of high tide, the SW is disrupted at the beginning of transect closest to the ice front. The reduced tidal amplitude in comparison to the previous section implies that the S_2 tide component, which causes the tidal amplitude to vary considerably within the fortnightly tidal cycle (Svendsen et al., 2002), affects the transport of SgFW down Kongsfjorden. As a result the transport of SgFW away from Kronebreen appears to be more effective under the influence of a strong ebb tide (Figure 3.14).

Kongsfjorden receives a net influx of freshwater at the head of the fjord, with observations ranging from 3.6 – 4.4 x 10^6 m^3 day^{-1} on the two days of CTD occupation, as determined by geostrophic velocities (Figure 3.15). The greater outflow of 4.4 x 10^6 m^3 day^{-1} occurred on the 14th July, with CTD stations sampled between 13:00 and 15:00 and under the influence of a strong ebb tide (Figure 3.14). Freshwater contributions determined here by geostrophic velocities are almost double the daily mean runoff produced by the WRF-CMB model, 7.6 – 9.1 x 10^5 m^3 day^{-1}, respectively (Aas, K 2015, pers. comm., 30 Jan). Some of the discrepancy between these results could be from the time of sampling; the data for the geostrophic calculations were collected during the early afternoon, whereas the WRF-CMB results are a daily mean. As such, the geostrophic calculations have not taken into account the diurnal variability of freshwater production, and instead represent a time of high flow.

Over the duration of the 2012 summer ablation season from 1st June to 30th September, the total additional freshwater entering the marine system, as determined by geostrophic velocities, was 4.3 – 5.3 x 10^8 m^3 yr^{-1}. This is substantially less than the seasonal total runoff for 2012 from the WRF-CMB model of 1.0 x 10^{10} m^3 yr^{-1} (Aas, K 2015, pers. comm., 30 Jan). The geostrophically derived daily value for freshwater input is almost 50% higher than the modelled runoff. There are two likely possibilities for the underestimation of meltwater delivery, the method and meltwater retention in the glacier hydrological system. Frictional processes could lead to an underestimation of geostrophic velocities, which in turn leads to reducing the calculated meltwater outflow. In addition, only two days were used to upscale the seasonal meltwater delivery. As such, these may not be wholly representative of the seasonal meltwater delivery to Kongsfjorden since freshwater production, and therefore delivery, has a seasonal evolution (Hodgkins, 2001; Kaser et al., 2010). This in turn creates seasonal fjord circulation patterns (Straneo et al., 2011). Repeat CTD sections would be required throughout the ablation season to be able to resolve the seasonal variability in freshwater inputs and the resultant circulation patterns, using this method. It is possible that all of the runoff produced during the ablation season is not discharged into Kongsfjorden, and that a proportion is retained and stored in the glacier, as has been found in Greenland (Humphrey et al., 2012; Rennermalm et al., 2013). Such firn aquifers have recently been identified at Kronebreen, highlighting that meltwater storage is an active process, which can potentially account for the meltwater delivery being less than surface runoff (Christianson et al., 2015).

During the summer months this study has found SgFW to be the dominant source of freshwater entering at the head of Kongsfjorden. However, composition of freshwater transport during the winter months cannot be determined. Studies in Greenland have revealed that the winter months contribute greater GiFW than SgFW (Sciascia et al., 2014). During the summer months SgFW is the dominant driving mechanism for producing GiFW by buoyancy driven convection (Jenkins, 2011), whereas winter melt is dependent on ambient water temperatures and velocities at the ice front (Sciascia et al., 2014). The current warming trend of AW entering the Arctic (Spielhagen et al., 2011; Steele et al., 2008) could see warmer AW entering west Spitsbergen fjords (Schauer et al., 2004). Given the findings of Sciascia et al. (2014), freshwater from GiFW could potentially increase during the winter due to the ambient ocean temperatures, whilst summer freshwater production relies upon mass balance changes of Kronebreen and Kongsvegen (Nuth et al., 2012).

The contribution of freshwater has only been determined for either SgFW or GiFW. Contributing to SgFW is the melt of Kronebreen, Kongsvegen and the Infontanna ice field (Figure 1.2). Results from the WRF-CMB model reveal the proportions of freshwater from each of the three terrestrial sources: Kronebreen = 44%, Kongsvegen = 43%, Infontanna = 13%. There are methods to further distinguish the origin of freshwater, such as oxygen isotopes (Meredith et al., 2008; Brown et al., 2014) and nutrient concentrations to determine routes of freshwater transport (Torres-Valdés et al., 2013).

The transport and mixing of SgFW and GiFW in Kongsfjorden also has implications for the ecosystem (Hop et al., 2002; Lydersen et al., 2014). The freshness of the SgFW at the fjord surface has direct implications for copepod mortality rates; salinities below 24 PSU reduce copepod survival rate to 1 hour, whilst most species are resilient to salinities above 24 (Zajaczkowski and Legezynska, 2001). The high copepod mortality in front of Kronebreen's ice cliff creates a scavenging zone for sea birds as a result of the freshwater contributions (Figure 1.4). In addition, suspended sediment is transported by the freshwater from subglacial channels, and rises to the surface in the buoyant plume. Previous studies (Rysgaard et al., 1999a; Cottier et al., 2005; Nilsen et al., 2008) have noted that summer insolation in addition to the high suspended sediment load in the SW can lead to temperatures >5 °C. The transects from this study did not display temperatures that warm, instead a maximum of 4 °C was observed. Encompassing the supraglacial and subglacial systems, SgFW is rich in nutrients (Hodson et al., 2008) supplying biogeochemical properties to Kongsfjorden, supporting the diverse marine ecosystem (Lydersen et al., 2014). Recent studies have highlighted the importance of bioavailable iron transported by SgFW as an importance mechanism for stimulating primary productivity (Hawkings et al., 2014; Bhatia et al., 2013), yet the fjords of Svalbard remain under studied in this domain.

3.5 Conclusions

Presented is this chapter are hydrographic data from the head of Kongsfjorden, which has direct contact with the ice front of Kronebreen, from July 2012. These data and analyses make an important contribution to determining the water mass structure, circulation and identify the sources of freshwater contributions, from the fast flowing tidewater glacier Kronebreen. The volume of freshwater discharged into the head of Kongsfjorden, during mid summer, has also been ascertained. Determining the water masses, together with the transport velocities, revealed strong SW outflow, to the right of discharge location. Inflow of AW was strongest on the right hand side of the fjord, complying with a geostrophically driven estuarine circulation, in the ice proximal zone.

The dominant freshwater is SgFW, sourced from subaerially produced meltwater runoff. Submarine melt, forming GiFW, is present, but inputs are an order of magnitude smaller than SgFW. The volume of additional water entering the marine system has been quantified by geostrophic velocities. When compared to runoff from the WRF-CMB model, geostrophic velocities produce a significantly higher amount of freshwater entering Kongsfjorden, as a daily comparison. However, when upscaled to the entire summer season, geostrophic velocities underestimate the amount of melt compared to the WRF-CMB model, but the results are within the same order of magnitude (Aas, K 2015, pers. comm., 30 Jan). The friction from the seabed may be the cause of the difference between the freshwater volume produced by geostrophy in this study, and those from the WRF-CMB model. In addition, the hydrographic measurements are a snapshot from the middle of July, and do not represent the variability of glacial meltwater discharge thoughout the season, which produces inaccuracies when upscaling.

To obtain a more precise estimate of meltwater discharge throughout a melt season, another method needs to be employed which captures the temporal variability of discharge magnitude. At Kronebreen, the dominant source of freshwater is SgFW, and is discharged from the subglacial environment transporting sediment to fjord surface. Therefore there is potential to be able to use the sediment as a tracer for freshwater as has been achieved with terrestrially discharged meltwater in Greenland (Chu et al., 2009; McGrath et al., 2010; Hudson et al., 2014).

Chapter 4

Detection of sediment plumes to quantify meltwater discharge

4.1 Introduction

The dominant source of freshewater entering the head of Kongsfjorden during the summer months is from subaerially produced runoff, which has been subsequent routed through Kronebreen and discharged at the grounding line (Chapter 3). *In-situ* measurements directly in front of the ice face are sparse, and lack temporal resolution. To address this need for better temporal quantification of freshwater inputs to the Arctic marine system, formulating a method to remotely detect meltwater discharge, from daily to interannual timescales, will enhance predictions of freshwater contributions. Building upon previous plume detection studies in the Arctic (e.g. Chu et al., 2009; McGrath et al., 2010; Tedstone and Arnold, 2012) this chapter aims to use *in situ* sampling of spectral reflectance and TSS measurements to calibrate satellite images from MODIS to determine the sediment plume area and concentration of TSS, to use as a proxy for freshwater discharge. This is achieved with the following objectives:

i Calibrate MODIS images with *in situ* measurements to formulate a method to remotely detect the spatial and temporal extent of plume area and TSS concentration from 2002 – 2013.

ii Determine if MODIS images are suitable for detecting seasonal and interannual change of Kronebreen's terminus.

iii Quantify the changes in meltwater and TSS delivery from daily to interannual time scales using sediment plume area.

Up to 30% of the surface water in front of Kronebreen is freshwater runoff, with a small contribution (up to 3%) of glacial melt (Chapter 3). This is discharged from the grounding line, transporting fine grained sediment to the fjord surface (Figure 1.3). At the head of Kongsfjorden it is approximately 80 m deep, therefore the freshwater, despite being sediment laden, forms a buoyant plume which spreads laterally across the fjord surface. As a result, high concentrations of suspended inorganic sediment are found 200 – 400 m from the termini of Kronebreen and Kongsvegen; these buoyant sediment laden plumes are strongly seasonal, dependent on freshwater inputs (Trusel et al., 2010).

As discussed in Section 2.5, it has been found that by calibrating MODIS with *in situ* TSS measurements, sediment plume extent can be used a proxy for meltwater runoff in Greenland (Chu et al., 2009; Hudson et al., 2014). Remote sensing has enabled remote monitoring of freshwater runoff from land terminating glaciers at seasonal to interannual time scales (Chu et al., 2009; McGrath et al., 2010). The method has also proved successful for quantifying runoff from marine terminating glaciers (Tedstone and Arnold, 2012; Chu et al., 2012). This study builds upon this research, providing the first long time series which addresses both the seasonal and interannual variability of meltwater discharge from a tidewater glacier. This will benefit sea level rise predictions, which are currently hindered by the lack of knowledge regarding the seasonal and interannual variability of meltwater discharge to the oceans (Rignot and Steffen, 2008).

4.2 Methodology

TSS in marine environments can be estimated using the high correlation between TSS and spectral reflectance (Curran and Novo, 1988). Here *in situ* sampling of TSS and spectral reflectance is utilised to calibrate spectral reflectance data from MODIS instruments on board the polar orbiting Terra and Aqua satellites. The temporal and spatial variability of TSS is too great to quantify from *in situ* measurements alone (Curran and Novo, 1988). By calibrating MODIS spectral reflectance with *in situ* measurements, the spatial and temporal context of TSS is better resolved (Robinson, 1995). This enables the quantification of plume area which serves as a proxy for meltwater delivery (Chu et al., 2009; Tedstone and Arnold, 2012).

4.2.1 Data collection

***In situ* sampling**

In situ measurements of TSS were taken at multiple locations at the head of Kongsfjorden, ensuring both high and low sediment concentrations were represented (Figure 4.1). The water samples were collected from 0 – 15 cm depth, in a plastic bottle. The TSS_{min} and TSS_{max} were used to define the region occupied by the sediment plume. Spectral reflectance was determined *in situ* using a hand held Analytical Spectral Devices Inc. FieldSpec spectroradiometer, which measures a wavelength range of 325 – 1075 nm (Figure 4.2). The instrument was fitted with a 25° field of view fore-optic which when held at a height of 50 cm above the water surface is the most appropriate set up for water surfaces (MacArthur et al., 2012). Before each surface reading a white reference was taken to calibrate the spectral reflectance data; these were acquired by the instrument as raw digital numbers and converted to absolute reflectance. Five repeat spectral reflectance measurements were taken at each sampling location to minimise the effects of water and boat motion on the measurements. The spectroradiometer was connected directly to a netbook, where the files were stored and later processed using ViewSpec Pro software. The *in situ* TSS and spectral reflectance measurements were sampled synonymously with the CTD sampling from Chapter 3.

MODIS satellite imagery

The MODIS instruments are onboard NASA's Terra and Aqua satellites and travel in sun-synchronous orbits. Remaining in the same location, relative to the sun, they orbit the earth once every 24 hours. The temporal and spatial resolution of spectral reflectance data from the MODIS instruments makes them ideal for studying sediment plumes in Kongsfjorden. There are at least two MODIS overpasses of Svalbard each day, measuring reflectance in visible to infrared (400 – 1440 nm) wavelengths, split into 36 bands. Band 1 (620 – 670 nm) and band 2 (841 – 876 nm) have a higher spatial resolution of 250 m compared with bands 3 – 7 (500 m) and 8 –19, 26 (1000 m) (NASA, 2012a). The high temporal resolution of the MODIS instruments outweighs the better spatial resolution of other products. For example, Landsat 8 offers up to 15 m resolution, but only a 16 day repeat. Therefore MODIS is preferential for this study owing to its frequent sampling and resolution up to 250 m, which is suitable for the detection of sediment plumes. The use of spectral remote sensing is constrained by availability of daylight; in the Arctic it is only possible to use the visible bands during the summer months, when there is daylight. For Svalbard, optimum images can be obtained between June and September. Beyond September, the onset of the Polar night curtails MODIS image retrieval until June the following year, when there is enough light. In addition, cloud free days are required for a suitable image to determine the extent of TSS.

This study has used the NASA level two products, MOD09GQ (Terra) and MYD09GQ (Aqua), which are daily gridded products in the sinusoidal projection.

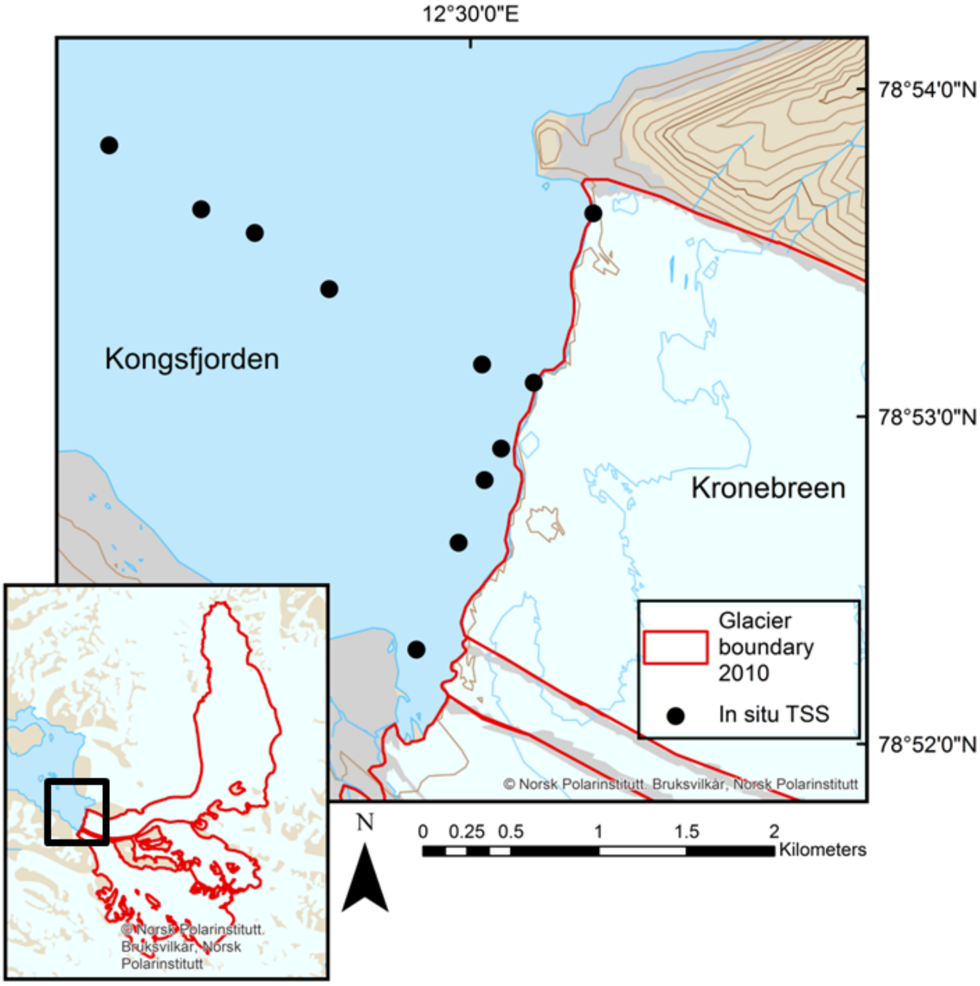

Figure 4.1: Map displaying locations of *in situ* TSS and spectral reflectance measurements. These were occupied between 14 – 18th July 2012. Fewer stations were sampled than for the CTD sampling (Figure 3.1) due to small, bergy bits of ice inhibiting the spectral reflectance measurements.

Figure 4.2: Left: A small boat was used to access the waters at the ice front of Kronebreen, Svalbard. Right: Hand held spectroradiometer was used to measure spectral reflectance of the surface water (Photo depicts same instrument and technique, but is located in Iceland).

These products have been corrected for atmospheric gases and aerosols, providing spectral reflectance data at 250 m resolution (Vermote et al., 2011). The Kongsfjorden system is available on plate h18v01.005, which can be identified using the NASA Reverb online search facilities (NASA, 2012c). Cloud free days between 1st June and 30th September from 2002 – 2013 were identified, following a three step process:

i Cloud free days visually identified in true colour images (NASA, 2012b)

ii Image of composite bands 3–6–7, which highlights cloud, was viewed in NASA's Earth Observing System (NASA, 2012b)

iii Quality control data from the file had to show cloud free, cloud free binary bit = 00

The cloud free images were downloaded from NASA Reverb (NASA, 2012c). MODIS Terra images were used in the first instance, with cloud free Aqua images used when Terra was unavailable. The preference to Terra was formed because it was launched two years earlier than Aqua, meaning that suitable data spans a greater amount of time. In addition, Terra typically allows for acquisition in the morning, when cloud cover is less. A total of 239 images were used, 189 from Terra and 50 from Aqua (Table 4.1). The year with fewest suitable images was in 2004, with only 9 available. In 2013, 28 images were used, providing the best yield of satellite data. On average, 20 images were available per year, representing 24% of the days between 1st June - 31st September.

Over the 12 year period, the 12th July (day 193) was the most frequent suitable image, with a total of six retrievals (Figure 4.3). Three days exhibited five retrievals: 22nd and 28th June, and 13th July. The longest period with no retrievals was three days, from the 27th – 29th July.

The downloaded hierarchical data format (hdf) files were imported into ERDAS Imagine software. The files contain five layers: two comprise of the spectral data of bands 1 and 2, and the additional three layers contain additional information on orbit and coverage, data quality and the number of observations. The layers containing bands 1 and 2 spectral reflectance data were converted from hdf to img files for processing in ArcGIS 10.1.

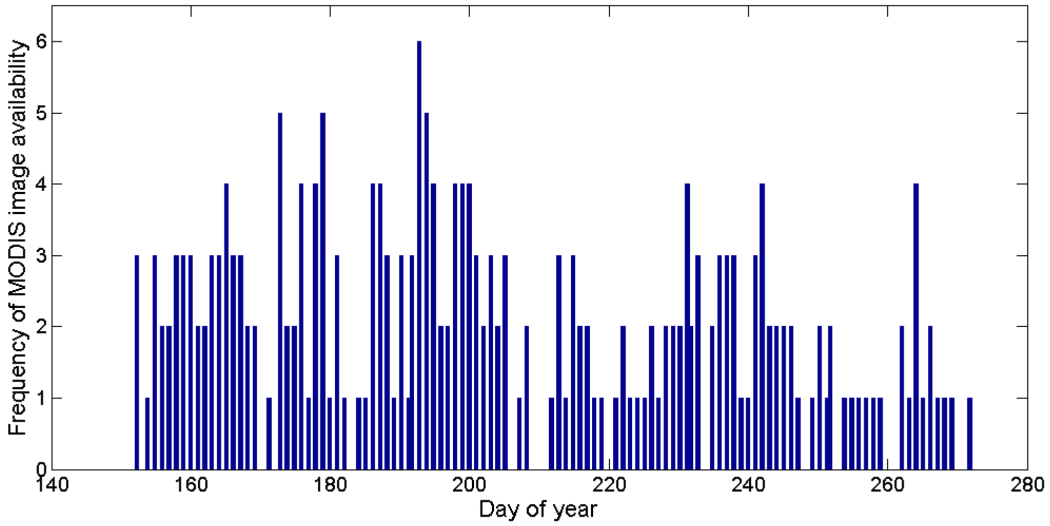

Figure 4.3: Histogram illustrating the frequency of images throughout the summer season.

4.2.2 Data processing

TSS concentration

The surface water samples were filtered through cellulose nitrate membrane filters to determine the weight of sediment for the volume of sample (mg l^{-1}) (Gray, 1973). The filters were pre-weighed on analytical balance (precision 1 x 10^{-3} g). A pore size of 0.45 μm meant that all material in suspension was captured on the filter. Samples were stirred, to ensure all sediment was in suspension. For the majority of the collected samples, 200 ml of the sediment laden water was filtered in the laboratory, using a hand pumped vacuum filtration system. All the filter papers were air dried, and transported to the UK for analysis. TSS has been determined by deducting the original weight of the filters, from the final filter weight.

	2002	2003	2004	2005	2006	2007	2008	2009	2010	2011	2012	2013
	173	*186*	179	155	152	152	155	169	171	156	155	152
	179	187	189	163	154	161	156	184	187	162	*158*	157
	181	*188*	193	164	*160*	162	157	185	*188*	*163*	*159*	158
	192	193	194	173	165	163	158	*186*	194	164	160	159
	193	199	226	176	167	*165*	159	187	*213*	165	161	176
	194	201	*227*	*178*	173	166	160	192	215	166	167	*178*
	195	202	230	179	*174*	167	164	193	222	173	*175*	193
	208	213	231	186	*176*	168	165	194	*231*	174	*181*	*194*
	217	214	232	187	199	169	*166*	195	*233*	175	182	195
	218	216	*233*	188	200	177	*168*	203	235	176	190	198
	223	219	264	203	201	*178*	173	205	236	190	*192*	199
	224	238		205	203	179	178	213	*247*	*196*	198	200
	226	239		215	204	190	*179*	229	254	*197*	202	*208*
	250	241		*216*	241	191	*180*	*233*	*257*	200	228	215
	252			225	242	193	181	*237*	*262*	201	*231*	222
	259			250	243	195	186	238		207	236	231
				267	251	196	198	240		*217*	237	*237*
				272	252	197	199	241		221	238	242
					255	198	200	246		229	263	243
						235	204			*230*	*264*	*246*
						236	205			232	266	*258*
						242	212			256		262
						244	*228*			264		264
						245	*242*					265
						249	244					266
							245					*268*
												269
Total	16	14	11	18	19	25	26	19	15	23	21	27

Table 4.1: Cloud free days from MODIS Terra and Aqua (italic) instruments 2002 – 2013.

Empirical relationship between *in situ* total suspended solids and spectral reflectance

The mean *in situ* spectral reflectance per location was calculated with reference to MODIS bands 1 – 4 (459 – 876 nm); this omits interference from wavelengths outside of the interest range. The mean spectral reflectance of the repeat samples was calculated for each location (Figure 4.4). Samples with a standard deviation greater than 0.04 from the mean were removed; at least three of the five repeat spectral reflectance measurements were used per locational mean (Figure 4.4). Some locations had multiple measurements omitted, whilst others had none. This process removed outlying measurements which were likely associated with changing light conditions. In addition, locations influenced by bergy bits in the water and by rain were omitted from the final calibration; this is due to the impacts these factors had on the water surface, altering the spectral reflectance (Figure 4.5). The meteorological and observational details came from field notes.

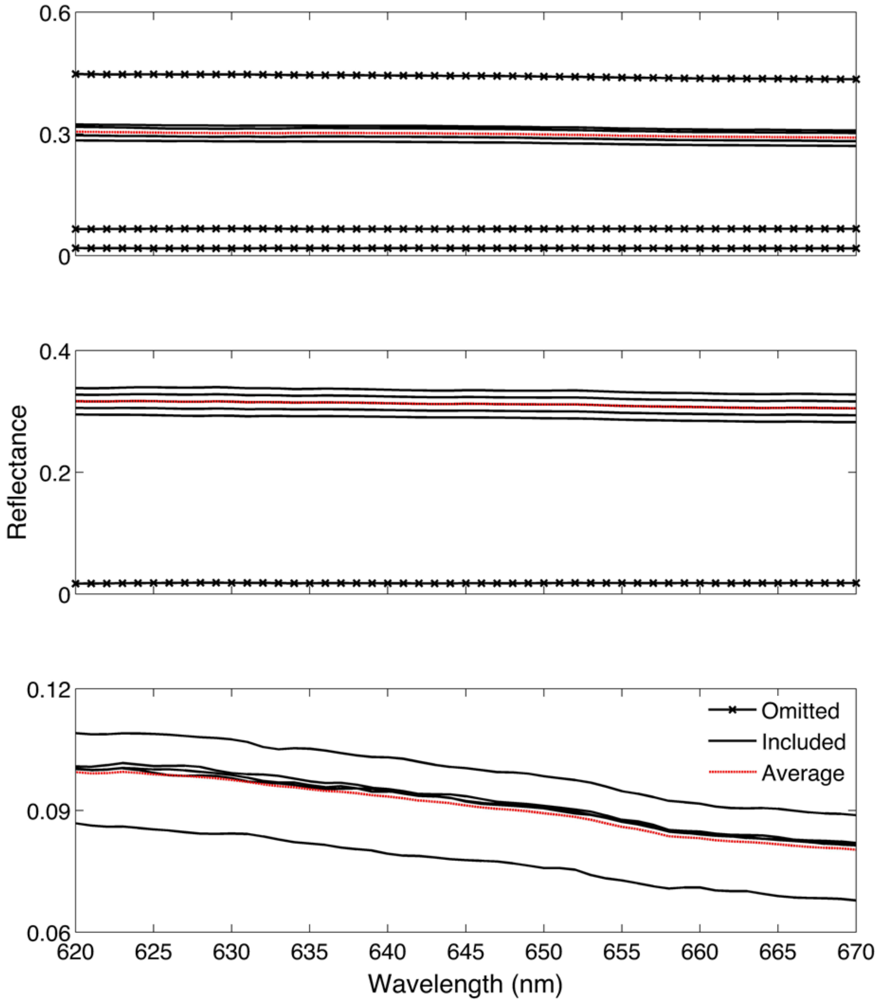

Figure 4.4: Examples of removing outlying spectrum measurements of *in situ* spectral reflectance with reference to MODIS band 1. Top: required several measurements omitted. Middle: one anomalous spectrum. Bottom: all the repeats are within the 0.04 nm threshold set and therefore none were removed. Note different scales for reflectance, which allow outliers to be highlighted.

Figure 4.5: Left: Visual comparison of ice covered and ice free water. Right: Some days exhibited more ice coverage than others.

The final mean spectra for each location was calibrated with TSS. The strength of this calibration against wavelength, indicates the wavelength that spectral reflectance is most sensitive to TSS. The corresponding wavelengths for MODIS band 1 (620 – 670 nm) and band 2 (841 – 876 nm) exhibit the higher correlations of $R^2 \geq 0.8$ (Figure 4.6). This indicates that MODIS bands 1 and 2 are likely to be the best bands to calibrate with TSS.

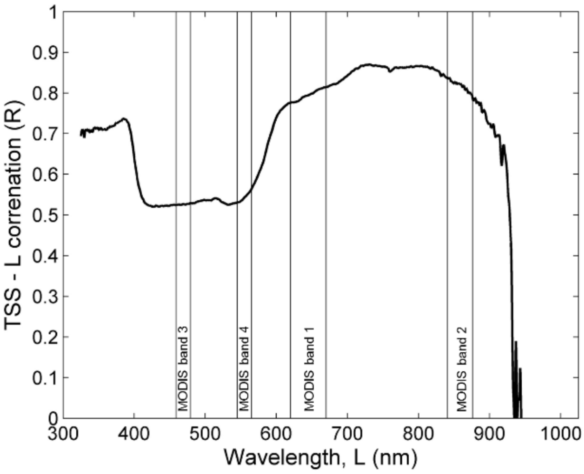

Figure 4.6: Strength of correlation between *in situ* TSS and spectral reflectance, against wavelength.

Calibrating MODIS to *in situ* measurements

The empirical relationship between TSS and *in situ* spectral reflectance was applied to form a correlation between MODIS bands 1 – 4, and the equivalent MODIS wavelengths of the *in situ* absolute reflectance data. The highest reflectance corresponds to the highest TSS, and the lowest TSS with the least reflectance (Figure 4.7). This concurs with Han and Rundquist (1994), in that the signature of TSS can be detected in spectral reflectance measurements. MODIS bands 1 and 2 exhibit the highest correlation between TSS and reflectance, r = 0.79 and 0.82 respectively (Table 4.2). This indicates that band 1 and 2 are much more effective at responding to TSS than bands 3 and 4, in which r = 0.53 and 0.58 respectively.

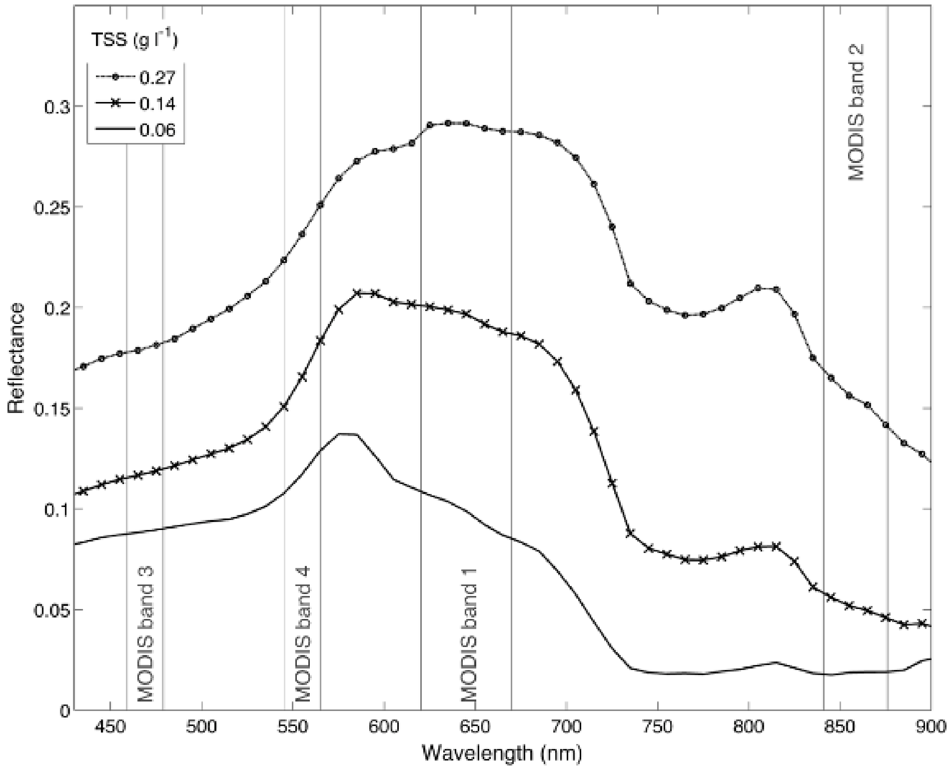

Figure 4.7: *In situ* spectral reflectance of high, medium and low TSS, with MODIS bands 1–4 highlighted.

Band	Wavelength (nm)	Resolution (m)	*R*
1	620 - 670	250	**0.79**
2	841 - 876	250	**0.82**
3	459 - 479	500	0.53
4	545 - 565	500	0.58

Table 4.2: Correlation between TSS and reflectance within different MODIS equivalent wavelengths.

The the empirical relationship of *in situ* TSS and spectral reflectance was used to calibrate the spectral data from MODIS bands one and two. The regression trendline was forced through zero, since the reflectance of clear water should be very low, due to high absorbency. In this instance, a linear relationship is apparent between TSS and spectral reflectance. Laboratory experiments have shown that a linear relationship is more likely with low TSS values, as exhibited here, and that higher TSS values are more likely to display a non-linear relationship (Han and Rundquist, 1994). However, non-linear relationships have been used in field studies in Greenland which exhibited similar TSS values (Chu et al., 2012).

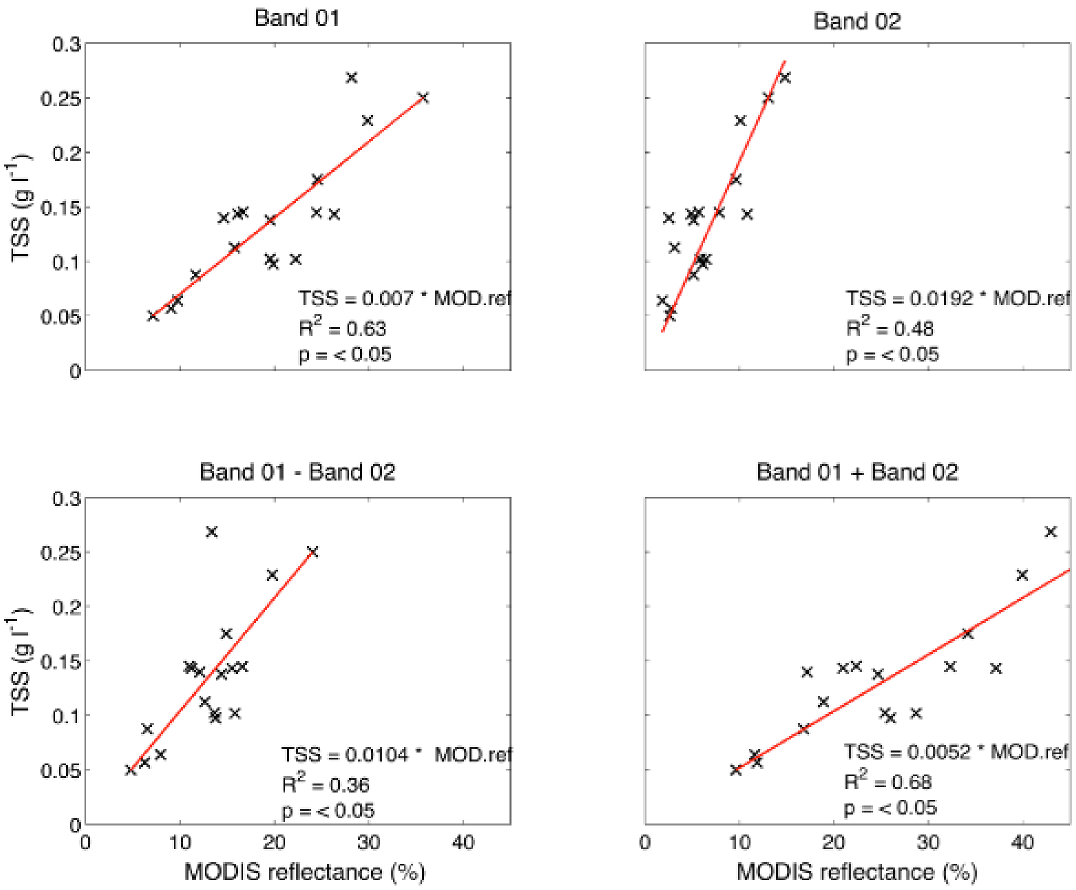

Figure 4.8: Regression between *in situ* TSS and equivalent wavelengths of MODIS bands

Following the calibration of MODIS reflectance with the *in situ* empirical relationship, MODIS band 1 exhibited the best regression coefficient, $R^2 = 0.63$ compared to $R^2 = 0.48$ with band 2 (Figure 4.8). Some studies e.g. Wang et al. (2010) have demonstrated the benefits of combining spectral bands to improve the detection of suspended sediments. Band 1 is focussed in the red spectrum, whilst band 2 is placed in the green, so both signals would be reflected in the results. A slightly higher regression coefficient of $R^2 = 0.68$ was produced through the addition of MODIS bands 1 and 2. Despite the addition of band one and two being the most responsive, the doubling of image processing and handling, as well as additional computing time, did not outweigh the benefits of pursuing such a combination. As such, using twice the amount of data was not deemed appropriate, since it gave only a modest 5% improvement, compared to using band 1 alone. To this end, multi-band processing was not pursued.

Selecting a region of interest

A 64.25 km^2 subset of the cloud free MOD09GQ and MYD09GQ images as detailed in Table 4.1, have been used in this analysis. The area of interest was selected to include the glacial calving front and fjord waters, out to a distance of 13.5 km from the glacier. This extends up to the island of Blomstrandhalvøya, at which point the glaciers of Conwaybreen and Kongsbreen meet Kongsfjorden. The area of the region of interest enables the TSS, which spreads laterally down the fjord, to be detected without picking up signals from other sources of freshwater. The majority of sedimentation occurs within the inner fjord of Kongsfjorden, with the most sediment laden waters located 200 – 400 m from the ice front (Trusel et al., 2010).

The terrestrial area around Kongsfjorden was masked out, together with the group of islands including Storholmen and Midholmen, which form one of the Kongsfjorden bird sanctuaries. Interference from sediment laden freshwater leaving Kongsbreen, another tidewater glacier in close proximity, has been minimised by masking the area in front of the glacier. This masking process ensures that the freshwater forming the plumes is attributed to melt from the Kronebreen - Kongsvegen system. Signals of TSS from other sources have the potential for the area of the plume to be over estimated; omitting such regions minimises this risk. The residence time of suspended sediment at such close proximity to the glacier front is about 1 day (Trusel et al., 2010). MODIS images are suitably placed to detect these sediment plumes due to their sub daily repeat overpass time. MODIS spectral reflectance was calibrated to TSS by applying the correlation between *in situ* TSS and spectral reflectance (Figure 4.8). This method offers a method to upscale *in situ* TSS measurements to the entire fjord system.

The spectral reflectance of ice and snow is much greater than that of water or land. Here, ice covered regions have been classified as areas which exhibit spectral reflectance grater than 30%, enabling the area of ice within the masked region to be quantified within each image.

4.2.3 Sediment plume detection model

By constructing a model to detect TSS automatically, all the data are treated in a consistent manner. This avoids human bias and enables the processing to take place without supervision. User defined inputs are required to determine the region of interest, threshold of ice, and the calibration coefficient between the *in situ* measurements and the MODIS satellite imagery. These were consistent for each image processed. The numerical results are collated into a table to be exported for analysis. This automated method of calculating TSS within the masked region of Kongsfjorden has enabled the identification of sediment plumes at 250 x 250 m resolution. The model was constructed in ArcGIS 10.0 and returns four automated result outputs for each MODIS image processed: map of TSS distribution, area of ice removal (km^2), sediment plume area (km^2), and statistics regarding TSS (maximum, minimum, mean, standard deviation; Figure 4.10). The ArcGIS distance measuring function was used to determine the length of the sediment plumes, with a reference line perpendicular to the ice front. This suite of results enable a thorough analysis of sediment plume dimensions and TSS concentrations on daily to inter-annual time scales.

Sediment plume classification

To be able to define the dimensions of the sediment plumes and TSS concentration, a criteria to classify what is "plume" must be applied. In this instance the following criteria have been applied to the calibrated MODIS data:

i TSS value must be between 0.05 and 0.27 g l^{-1}, as determined by the minimum and maximum *in situ* TSS values, obtained from the filtered water samples. Higher values were excluded as they could be misinterpreted icy regions e.g. bergy bits.

ii The plume must have contact with the glacier face.

iii Any periphery plumes not directly attached to the primary plume (which intersects with the glacier front), must be within 500 m from the primary plume. If periphery plumes are >500 m (two pixels) from the primary plume, they are excluded.

This method eliminates regions which meet the TSS criteria, but are not likely to have been produced by the freshwater outflow on the day of the image, given the 1 day residency time of suspended sediments (Trusel et al., 2010). The lower boundary of 0.05 g l^{-1} also represents the concentration of TSS which is detrimental to copepods (Arendt et al., 2011). The excluded periphery plumes could be sediment melting out from icebergs transported down the fjord (Dowdeswell and Dowdeswell, 1989; Syvitski et al., 1996). Regions occupied by icebergs or bergy bits are characterized by high spectral reflectance, and therefore have been excluded by the criteria of maximum TSS value.

Kronebreen's terminus retreated during the period of this study (Figure 1.7). The line feature marking the glacier terminus was moved back to reflect this for the years 2012 and 2013. Without this, the plume area would have been underestimated. These selection criteria have ensured the best representation of plume extent, and concerted effort has been made not to over or underestimate plume size.

4.3 Results

Calibrating MODIS images with *in situ* spectral reflectance and TSS has provided a method to quantify TSS and the area of plumes emerging from Kronebreen. Each of these is analysed here with respect to the seasonal evolution of meltwater delivery to Kongsfjorden.

4.3.1 Modelled spatial distribution of total suspended solids

Calibrating MODIS band 1 spectral reflectance with *in situ* TSS has enabled the temporal and spatial variability of TSS at the head of Kongsfjorden to be mapped and quantified. Instead of spot measurements, it is now possible to determine the distribution of TSS, and at what concentration, over an area of 65 km^2 at a spatial resolution of 250 x 250 m. A selection of TSS maps from 2012 are used to give an insight into seasonal evolution (Figure 4.11).

Early in the season, the plume area was small, with a low concentration as seen on 5th June (day 155). A week later on the 9th June (day 161), plume area increased as had the TSS concentration at the ice front. As the melt season progressed, plume area generally increased but remains variable. On the 15th August (day 228), a considerably sized plume formed. TSS throughout the plume was greater, and spanned a larger area, than earlier in the season. It also extended along the northern extent of Kongsfjorden, spreading alongside the islands Storholmen and Midholmen. This also occurred on 19th September (day 263), however it was not a constant pattern as the plume extended along the southern extent of the fjord on 25th August (day 238). The highest TSS was found at the ice front, decreasing with distance down Kongsfjorden (Figure 4.11). A plume core of higher TSS values was observed in the central plume.

In addition to the variability of the plume size and TSS, changes in area of ice at the front of Kronebreen were detected. The early season displays the glacier front extending across the region of interest at the fjord. This breaks up through the season, depending on the flow dynamics of Kronebreen. Substantial retreat of Kongsvegen at the southern part of the glacier terminus can be seen.

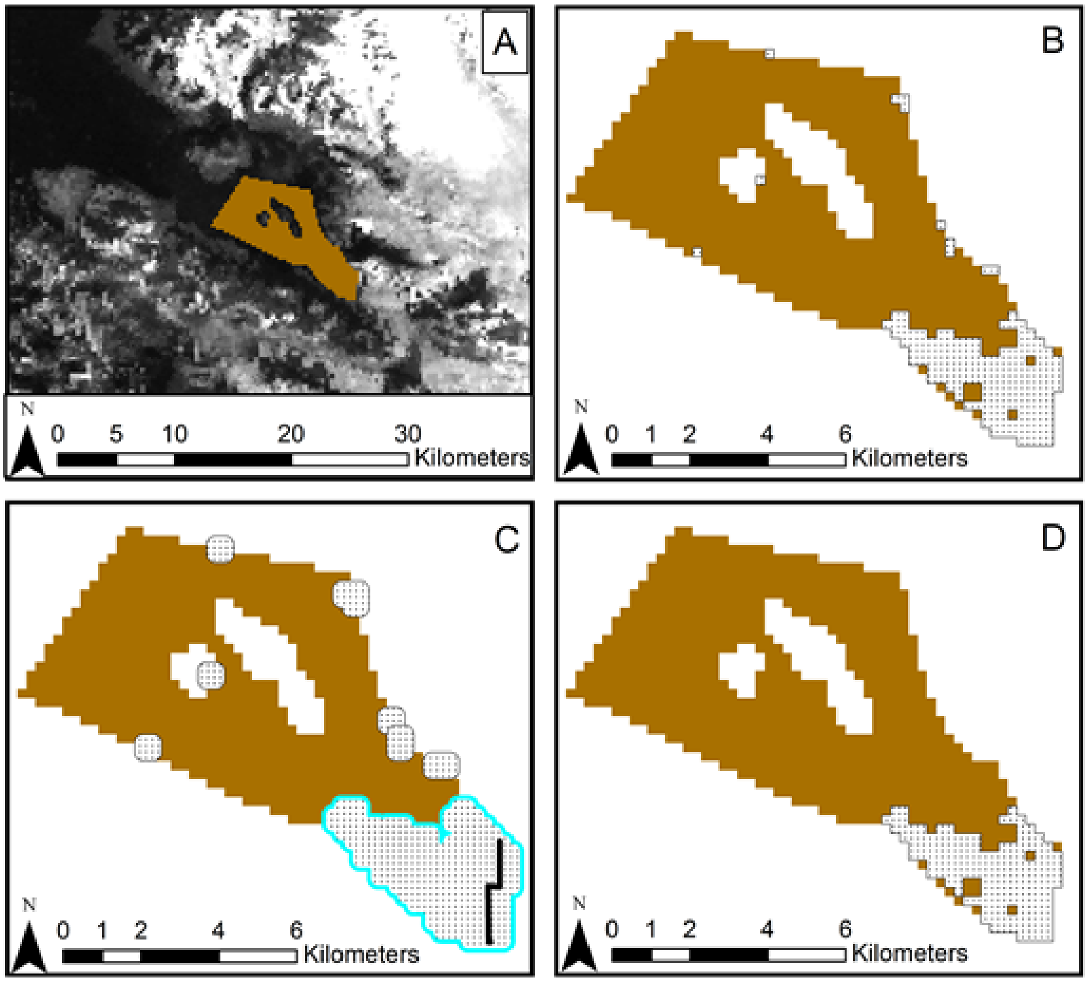

Figure 4.9: Sediment plumes were automatically detected by calibrating MODIS spectral reflectance with *in situ* TSS. (A) The area if interest is selected from the MODIS image, open water is shown in brown. (B) Calibration between TSS and spectral reflectance is applied. The region that meets the TSS criteria is selected (stippled white). (C) The primary sediment plume (encased by blue line), which intersects with the glacier face (solid black line) is highlighted, with peripheral plumes being excluded from this selection. (D) Peripheral plumes are removed, leaving only the primary plume (stippled white), which meets all the plume specification criteria.

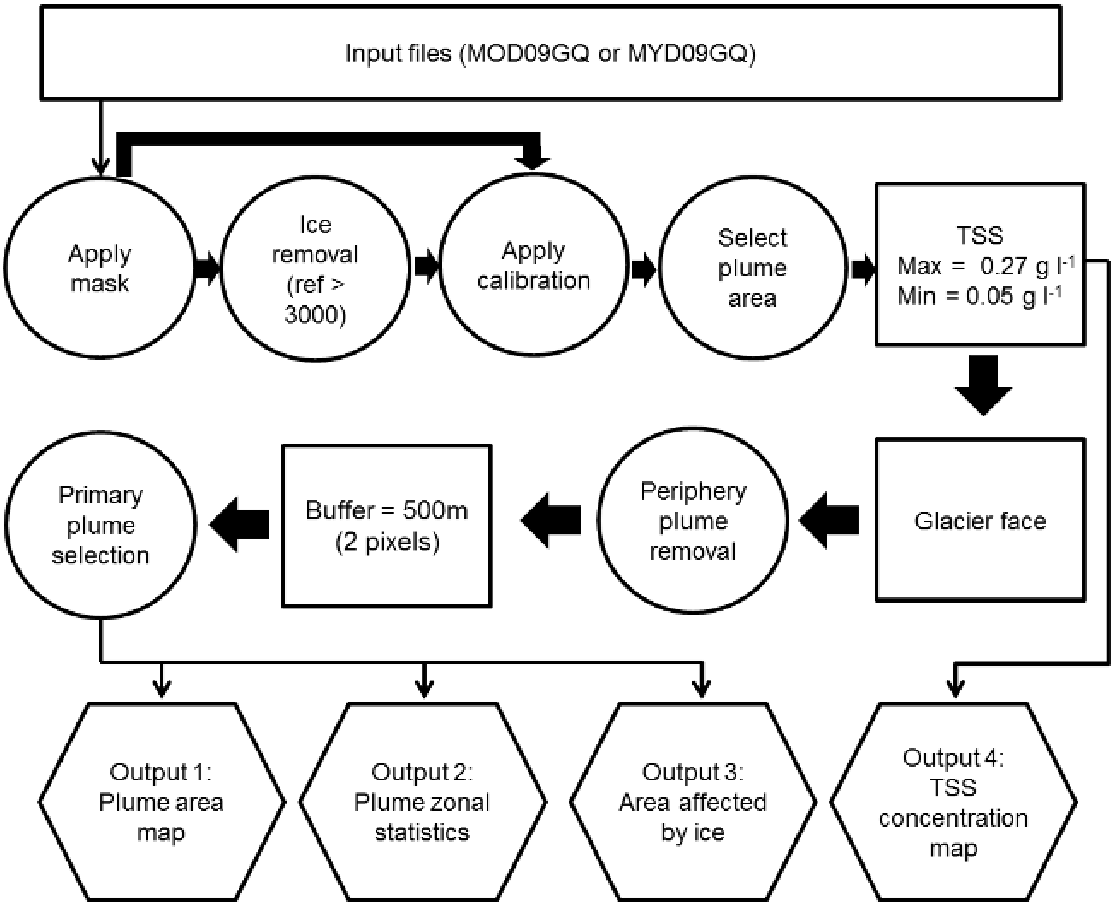

Figure 4.10: Schematic detailing the processes undertaken by the sediment plume model, and the corresponding result outputs

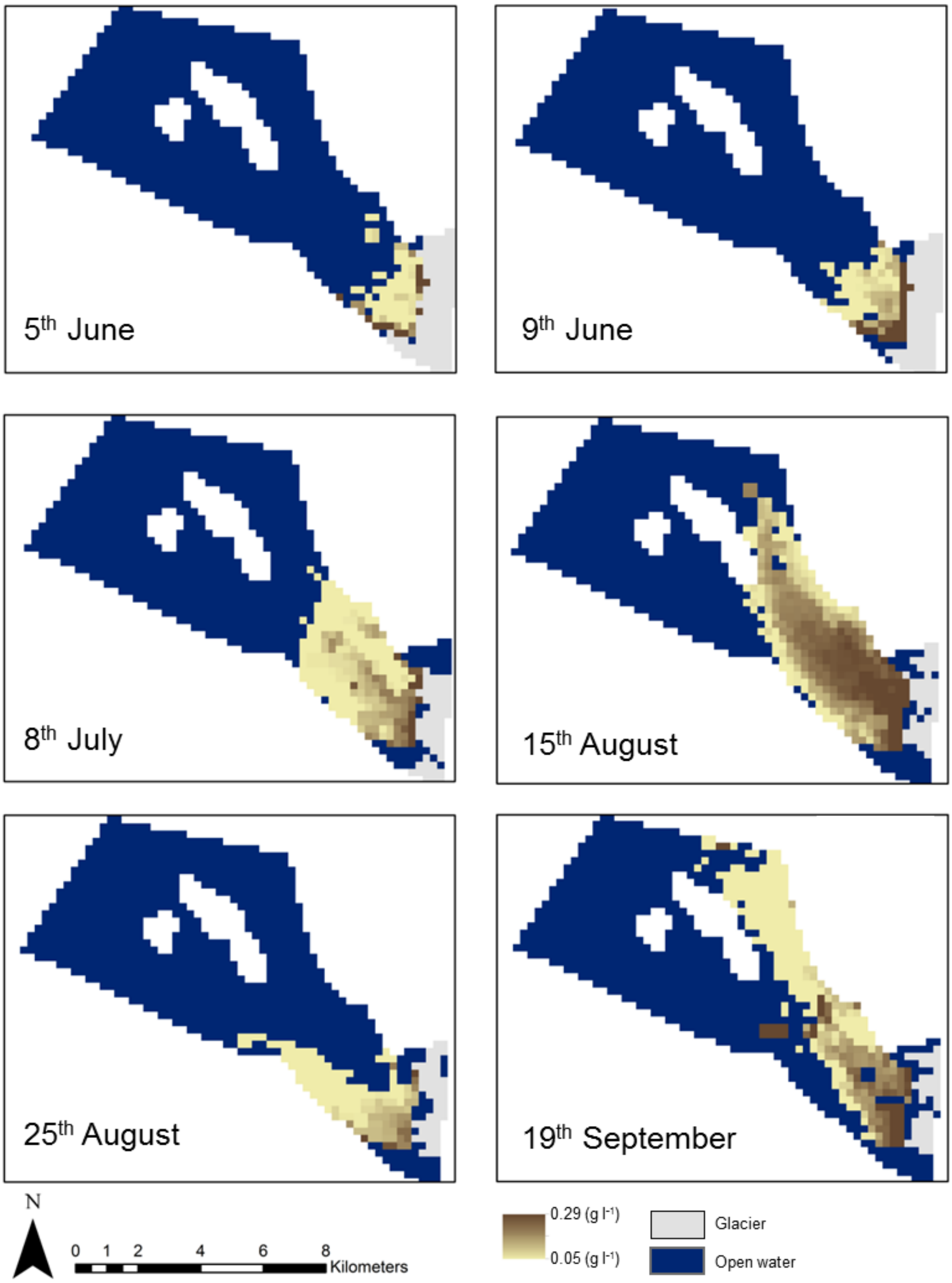

Figure 4.11: Temporal and spatial variability of TSS during 2012 from the plume detection model.

4.3.2 Sediment plume area and ice cover 2002 – 2013

Plume area has been quantified for the 234 cloud free days between June - September from 2002 – 2013 (Figure 4.12). In addition, the area of ice within the masked area at Kronebreen's terminus has been revealed. Plume area is variable at short time scales, ranging from 1 – 58 km^2. Early season plume areas are generally small (<10 km^2), apart from in 2006, where they appear to be in the region of 20 km^2. Due to the frequency of MODIS retrievals, determining seasonality is difficult when assessing individual years.

Ice area decreased throughout the season, which is particularly prominent in 2008 and 2009. Early season glacier extent in the region of interest was >6 km^2 from 2002 – 2012, whereas the glacier front retreated in 2013, exhibiting an area of <5 km^2.

4.3.3 Temporal variability of sediment plume area and total suspended solids

Seasonal

The modelled results of plume area and TSS in Kongsfjorden illustrate a seasonal pattern of plume development, in addition to interannual variability (Figure 4.12). The trends and variability of TSS and plume area is apparent at monthly, 10 - day, and daily time scales. Plume area ranges from 1.0 km^2 to 50.8 km^2, with an overall mean of 14.2 km^2.

To assess the monthly to seasonal variability in both plume area and TSS, the results for the 12 year sampling period have been combined. June exhibits a mean plume area of 9.8 km^2, which increases to 16.8 and 17.6 km^2 respectively for July and August (Table 4.3). Mean plume area decreases in September to 12.6 km^2, but remains above the mean plume are for June. The minimum plume area is smallest during June (1.0 km^2) and increases to its maximum in July (6.3 km^2). The minimum plume area in September, which represents the end of the ablation season, was 3.6 km^2. This is greater than the early season minimum in June. The maximum plume area is greatest in June and July, 55.5 and 52.8 km^2 respectively. July exhibits the smallest standard deviation from the monthly mean of 7.9 km^2 whilst the largest of 10.5 km^2 occurs in August.

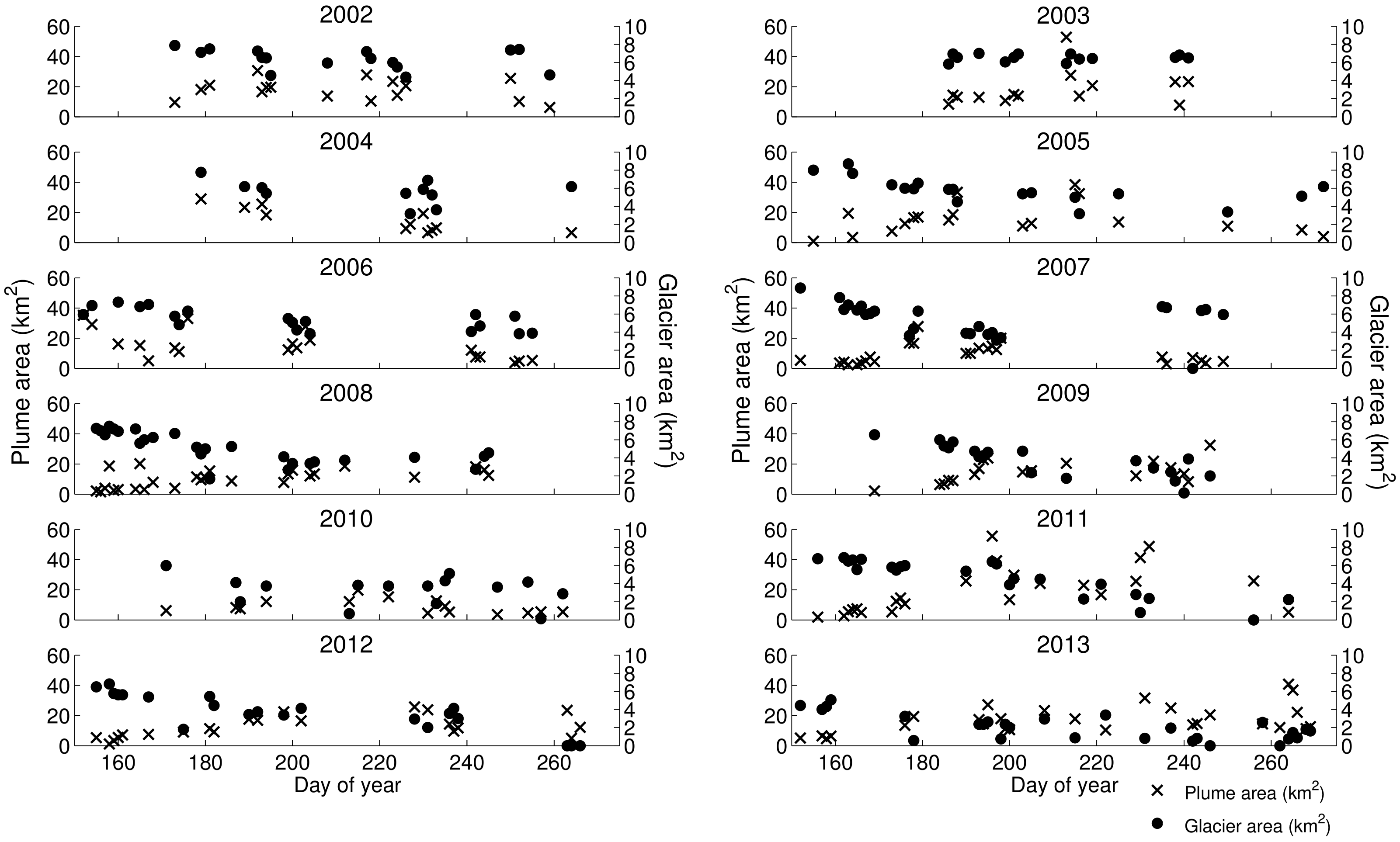

Figure 4.12: Sediment plume area (km^2; black crosses) and area of glacier terminus ice (km^2; black dots) at Kronebreen's calving front for each cloud free day from 2002 – 2013.

	June	July	August	September	Mean June - Sept
Mean	9.8	16.8	17.6	12.6	14.2
Min	1.0	6.3	2.9	3.6	3.5
Max	35.1	55.5	52.8	40.8	46.0
Range	34.1	50.8	49.2	35.2	48.5
Sd	7.9	8.1	10.5	9.9	9.1

Table 4.3: Mean monthly characteristics of plume area (km^2) 2002 – 2013

Unlike plume area, there is little seasonality observed in TSS when analysing monthly means (Table 4.4). TSS$_{mean}$ is 0.01 g l^{-1} greater in July and August, whilst the maximum and minimum remain the same throughout.

	June	July	August	September	Mean June - Sept
Mean	0.15	0.16	0.16	0.15	0.15
Min	0.05	0.05	0.05	0.05	0.05
Max	0.21	0.21	0.21	0.21	0.21
Range	0.16	0.15	0.15	0.16	0.16

Table 4.4: Mean monthly characteristics of TSS (g l^{-1}) 2002 – 2013

A seasonal trend is observed in monthly means for plume area, but there doesn't appear to be a defined seasonal trend for TSS. By increasing the temporal resolution from monthly means to 10 day means, a more detailed analysis of seasonal variability has been achieved. The plume area and TSS$_{mean}$ values for 10 days prior to the marker were averaged (Figure 4.13).

Plume area is low at the beginning of the season extending 7.2 km^2 on average between 1st - 18th June (day 152 – 169). As the season evolves, plume area increases until 29th July - 7th August (day 210 – 219), where the mean plume area peaks at 23.9 km^2. From the peak of the season, the plume area decreases steadily, until reaching 5 – 10 km^2 at the end of September, which is similar to the extent during the early season plumes. This seasonal evolution of plume area is similar to what was revealed in the monthly analysis.

Analysis of the 10 day mean reveals that TSS$_{mean}$ is the highest of the season, 0.10 g l^{-1}, between 1st - 18th June (day 152 – 169) (Figure 4.14). This corresponds with a small mean plume area. TSS$_{mean}$ declines from 19th June (day 170), remaining steady at approximately 0.09 g l^{-1} until the end of September. Standard deviation from the mean was greatest between 1st - 18th June and 18th August -

30th September at >0.01 g l^{-1}. Comparably it was much smaller during the peak of the melt season between 19th June - 17th August, ranging between 0.006 – 0.008 g l^{-1}.

Interannual variability of plume area and total suspended solids

The results for both plume area and TSS indicate interannual variability (Table 4.5). The maximum plume extent during the 12 year period was 55.5 km^2, measured on the 15th July 2011. The minimum extent was <1% (0.4 km^2), which was found on multiple occasions. The 12 year mean plume area was 14.2 km^2. The mean plume length of 5.25 km is 30% of the overall length of the study region. There is a positive relationship (R^2 = 0.90 p <0.001) between plume area and plume length. The two largest mean annual plume areas were in 2003 and 2011, 18.3 and 19.4 km^2, respectively. The smallest was 8.7 km^2 in 2010 (Figure 4.15). The mean annual plume area displays no particular temporal trend, over the twelve years.

Annual TSS$_{mean}$ displays a contrasting picture in which larger plume area corresponds to lower TSS$_{mean}$ (R^2 -0.63, p <0.05, n = 12). The highest TSS$_{mean}$ of 0.10 g l^{-1}) was found in 2010, whilst the lowest was 0.08 g l^{-1} in 2003 (Table 4.6).

During the 12 year period, TSS$_{mean}$ of the sediment plumes is 0.15 g l^{-1}, maximum concentration was recorded to be 0.21 g l^{-1} and the minimum 0.05 g l^{-1}. The upper TSS boundary (0.27 g l^{-1}), formed from *in situ* measurements was never met. In contrast, the TSS minimum boundary value of 0.05 g l^{-1} has been met on multiple occasions, acting as a minimum cut-off point; only 13% of the minimum individual TSS concentrations were 0.051 g l^{-1} or above. Interannual variability of both plume area and TSS is present, however, there is no persistent trend of increase or decline, from 2002 – 2013.

The TSS detection model has also produced the area of ice coverage at Kronebreen's terminus. This occurred because the ice was omitted, when determining the extent of the sediment plumes. Although ice area does show a decline during the season (Figure 4.6), the year to year mean annual variability provides information on the stability of the ice front. The maximum annual mean ice area was in 2009, 1.95 km^2, and the smallest was 2013 at 0.14 km^2. From 2007 onwards, mean annual ice area was 1.0 km^2 or less. Three years, 2007, 2012 and 2013 all displayed 0 km^2 as the minimum ice area. This is because the end of season ice front retreated beyond the masked region.

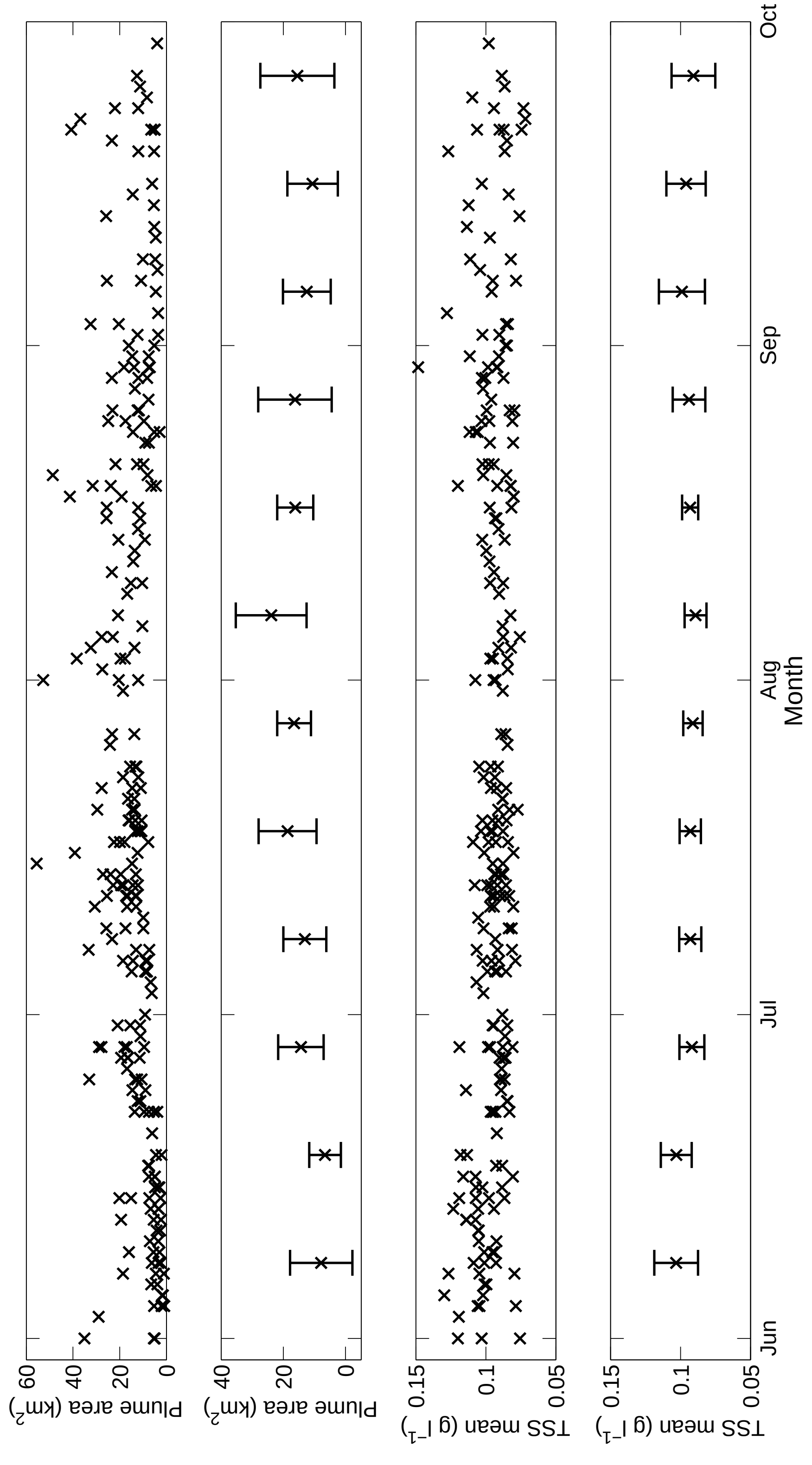

Figure 4.13: Plume area (km^2) and TSS (g l^{-1}) for each cloud free day from 2002 – 2013, and also displayed in 10 - day means with bars representing standard deviation from the mean.

	Sediment plume area (km^2)				Sediment plume length (km).			
Year	Min	Max	Range	Mean	Min	Max	Range	Mean
2002	4.19	29.94	25.75	17.90	0.75	10.99	10.24	6.53
2003	6.63	50.80	44.19	18.31	2.39	13.49	11.10	6.74
2004	5.06	27.88	22.81	15.23	1.82	10.50	8.68	5.28
2005	0.50	36.19	35.69	15.29	1.27	12.63	11.36	5.65
2006	2.13	33.31	31.19	15.12	1.58	10.52	8.94	5.80
2007	1.44	26.75	25.31	8.94	1.18	10.95	9.77	3.83
2008	1.31	18.50	17.19	10.17	1.57	10.03	8.46	4.06
2009	1.44	28.25	26.81	14.66	1.19	9.31	8.12	5.38
2010	0.94	59.38	58.44	8.74	0.25	11.91	11.66	3.62
2011	1.31	54.50	53.19	19.37	1.41	13.68	12.27	6.04
2012	0.38	22.63	22.25	12.30	0.25	11.88	11.63	4.65
2013	2.56	35.88	33.31	17.06	2.08	12.35	10.27	5.67

Table 4.5: Annual mean results for sediment plume area (km^2) and plume length (km)

	Total suspended solids (g l^{-1})				Ice coverage (km^2).				
Year	TSS_{min}	TSS_{max}	TSS_{mean}	Std. Dev	Min	Max	Range	Mean	Std. Dev
2002	0.051	0.209	0.089	0.029	0.938	2.500	0.938	1.712	0.493
2003	0.050	0.208	0.087	0.027	1.313	1.313	1.313	1.696	0.203
2004	0.050	0.209	0.096	0.032	0.625	4.563	3.938	1.688	1.035
2005	0.052	0.209	0.095	0.032	0.688	9.875	9.188	1.959	2.066
2006	0.051	0.209	0.096	0.034	0.563	4.000	3.438	1.382	0.776
2007	0.050	0.209	0.101	0.037	0.000	2.188	2.188	1.029	0.394
2008	0.051	0.209	0.096	0.035	0.375	2.125	1.750	0.921	0.454
2009	0.050	0.209	0.098	0.033	0.313	1.500	1.188	0.776	0.776
2010	0.051	0.209	0.104	0.035	0.063	4.438	4.375	0.798	0.798
2011	0.050	0.209	0.092	0.028	0.250	2.313	2.063	0.924	0.464
2012	0.051	0.209	0.091	0.027	0.000	3.000	3.000	0.440	0.698
2013	0.050	0.209	0.091	0.022	0.000	2.000	2.000	0.140	0.399

Table 4.6: Annual mean results for total suspended solids (g l^{-1}) and glacier terminus ice coverage (km^2)

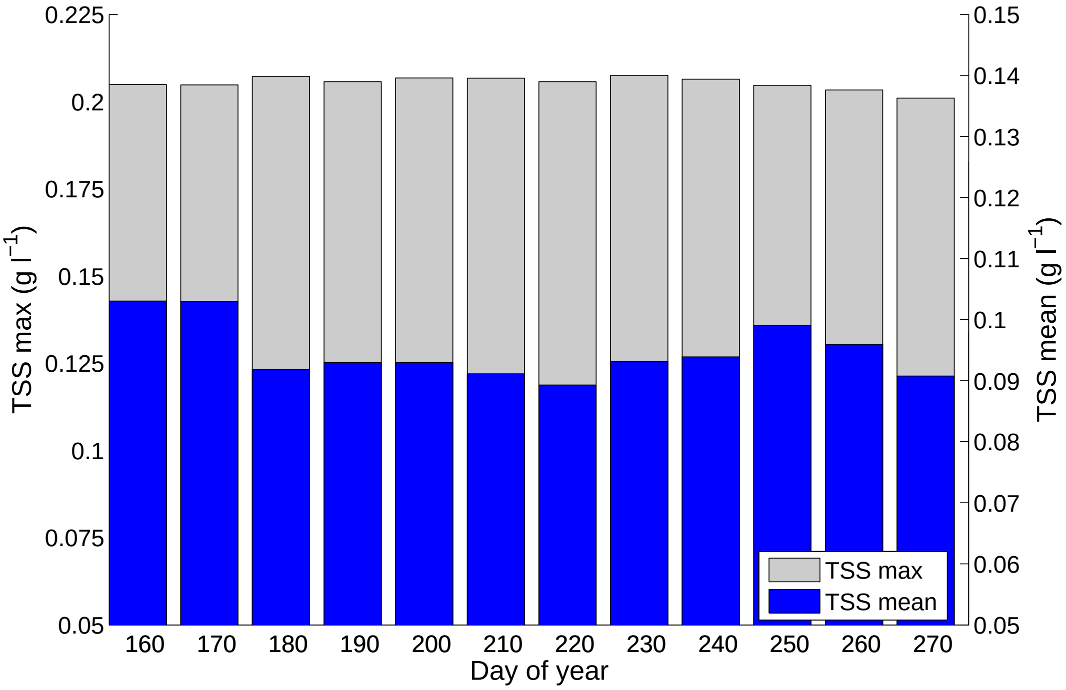

Figure 4.14: Ten day binned TSS_{max} and TSS_{mean}, from 2002 – 2013.

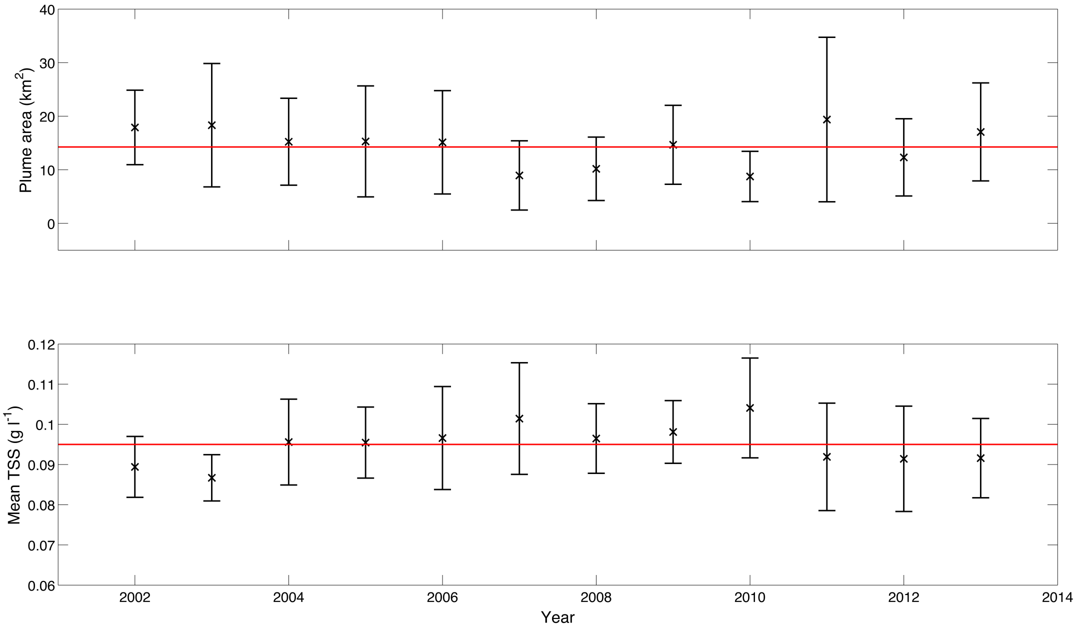

Figure 4.15: Annual mean variability of plume area, TSS_{mean} and TSS_{sum} from 2002 – 2013, displayed with bars of standard deviation. Red line indicates 12 year mean.

4.4 Discussion

This chapter has presented TSS concentration for each of the 234 cloud free days between June - September from 2002 – 2013. Calibrating MODIS band 1 satellite spectral reflectance data with *in situ* measurements of TSS has enabled the quantification of meltwater delivery from the Kronebreen - Kongsvegen system. The approach of empirical modelling has facilitated the upscaling of point *in situ* measurements, to an area of 65 km^2. The seasonal and interannual variability of TSS and plume area have been determined, which would have previously required intensive *in situ* sampling (Collins, 1990). Whilst hydrological data from the Arctic remains sparse, this study presents an effective method to further understand the TSS and meltwater delivery from a fast flowing tidewater glacier.

4.4.1 Total suspended solids model

Building on previous work, this model has used an empirical relationship between *in situ* TSS and spectral reflectance (Chu et al., 2009; 2012; Tedstone and Arnold, 2012), to calibrate MODIS band 1 images. This has provided the TSS and plume extent, of freshwater discharge from Kronebreen, on cloud free days. Tedstone and Arnold (2012) indicated that detecting sediment plumes discharged from tidewater glaciers is more difficult than terrestrial runoff, due to the presence of ice melange and bergy bits. However, these were rarely present in Kongsfjorden, and was therefore not such a problem. Areas of bergy, floating ice were identified and removed, but this did not hinder obtaining plume extents. At its minimum width of 4 km, there was a minimum of 16, 250 m pixels, across the ice front. Studies in Greenland, revealed that fjords with a width of 2 km or less were not suitable for plume identification (Tedstone and Arnold, 2012). Quantification of plume area is constrained by the 250 x 250 m resolution of MODIS. Landsat 8 offers a much higher spatial resolution of up to 15 m, but only offers a 16 day repeat cycle. Such a constraint on temporal sampling would hinder the ability for Landsat 8 to be used effectively as a monitoring tool at seasonal time scales.

The fast flowing nature of Kronebreen meant that the TSS model required adjustment to account for the changing location of the calving face. This enabled the plume area from 2012 and 2013 to not be underestimated by being cut off by the requirement of the plume to interact with the glacier front. However, the TSS$_{max}$ and TSS$_{min}$ values, 0.05 and 0.27 g l^{-1} respectively, appear to act as cut off boundaries for the plume. This is particularly apparent for TSS$_{max}$ concentrations, in which no TSS was detected closest to the ice front during 2012 and 2013 where TSS is most likely to be highest (Figure 4.11). The main outlet from Kronebreen is in the centre of the calving front, which also displays some open water pixels. Therefore open water pixels in direct contact with Kronebreen are likely to have exceeded the TSS_{max} value that was put in place. The region not captured by the model is closest to the ice front, which was not sampled due to safety concerns. *In situ* samples could only be taken 250 m from the glacier front, which is the same as the pixel resolution of MODIS band 1. Using both band 1 and band 2 of MODIS did offer a slight improvement on the retrieval. A method combining the these bands has been applied in Greenland (Hudson et al., 2014), which enabled the detection of high TSS, which was was curtailed in a previous plume detection study (Chu et al., 2009). However, owing to the terrestrial nature of these studies, TSS_{max} is higher than in Kongsfjorden. Therefore, increasing the *in situ* samples to accommodate the full range of TSS, would strengthen the model (Klemas, 2011). The lower plume boundary of TSS_{min} also represents the level at which copepods are affected by surface sedimentation, providing a measure of the area of the fjord that will be inhibiting for primary productivity (Arendt et al., 2011).

Remote sensing does not allow for the relative sources of freshwater to be determined. But, the change in plume extent does give insight to the amount of freshwater entering the system, with greater spatial accuracy and temporal resolution than *in situ* sampling alone. Therefore, *in situ* hydrographic measurements, as presented in Chapter 3, form a valuable compliment to remotely sensing sediment plumes.

Detection of the glacier ice at Kronebreen's terminus was not the primary goal when building the TSS detection model. It has however, provided an insight to seasonal degradation of the glacier front, and interannual variability in terminus positions. The terminus positions, however, are not as accurate as when using Landsat (Figure 1.7). For the model to be used more extensively for terminus positions, the region of interest mask needs to cover a greater proportion of the lower extent of Kronebreen. This would avoid the minimum cut off as seen in 2007, 2012 and 2013. Extraction of the terminus positions would be a valuable addition, particularly for detecting terminus position change within an ablation season.

4.4.2 Seasonal evolution of meltwater and total suspended solids delivery from Kronebreen to Kongsfjorden

A daily snapshot of TSS and plume area has proved adequate to resolve the variability in meltwater delivery from the tidewater glacier, Kronebreen, at daily (where images permit) to interannual intervals. The extent of the plume Arctic fjords, has been found to change in response to meltwater forcing, which changes during the ablation season (McGrath et al., 2010; Chu et al., 2009; Hudson et al., 2014). Contrasting previous studies, this research has focussed solely on a tidewater glacier. Therefore, the TSS detected is representative of the sediment discharged from subglacial conduits to the fjord, since the meltwater has not been transported through terrestrial streams for mixing of sediments to take place (Gurnell, 1982). As a polythermal glacier, the variability of TSS transport by glacial meltwater is largely expected to be dictated by the rate of meltwater production at the surface of Kronebreen, and the subsequent routing through the glacier (Collins, 1979; Gurnell et al., 1992b; Clifford et al., 1995). Determining changes in sediment plume area provides a method to remotely detect meltwater delivery to the marine environment. Given the frequency of MODIS image acquisition, seasonal and interannual trends have been identified in this chapter. This provides an insight into Kronebreen's glacial architecture and hydrological processes, in addition to providing an indicator of changing ablation patterns.

These results have highlighted three distinctive periods within the season: 1st June - 18th, 19th June - 17th August, and 18th August - 30th September. As such, the following discussion addresses each of these time periods separately to discern the seasonal properties in TSS and plume area.

Early season: 1st June - 18th June (Day 152 – 180)

Meltwater release from Kronebreen persists throughout the year due to the polythermal properties of the glacier (Irvine-Fynn et al., 2011). The contribution of freshwater to the marine system increases with the onset of snow ablation in late April, followed by glacial ablation, which begins in June in Svalbard (Hanssen-Bauer et al., 1990). In addition, the early season marks the beginning of the englacial and subglacial drainage systems beneath Kronebreen becoming re-established after winter (Collins, 1990).

Plume area is predominantly <10 km^2 during this period, indicative of low meltwater discharge. Meltwater delivery from Kronebreen early in the ablation season appears to be characterised by high TSS_{mean} relative to plume area. This relationship has been noted in many other glacial environments including alpine glaciers (Collins, 1989; 1990) and high Arctic glaciers (Hodgkins et al., 2003; Hodson et al., 1996), but has not previously been characterised in the sediment plumes emerging from tidewater glaciers. Sediment is mobilised throughout the year by glacial sliding, leading to high sediment concentrations at the base of the glacier (Collins, 1979). Eroded sediment remains at the base of the glacier, having been isolated from hydrologic controls during the winter months (Collins, 1990).

Hydraulic instabilities enable meltwater to access the glacier bed, promoting the sediment rich meltwater to be flushed from the system (Collins, 1988; 1989). This occurrence of high TSS_{mean} at the beginning of the ablation season (Figure 4.14), before 19th June, is in conjunction with the maximum extent of the distributed system (Willis et al., 1996). High TSS_{mean} could be a result of winter erosion products being flushed from the system(Østrem, 1975). Large quantities of TSS in meltwater release can also be caused by glacial advance (Humphrey and Raymond, 1994; Iken and Truffer, 1997); this has been discounted here as Kronebreen has been in retreat during the study period (Figure 1.7).

In contrast to TSS_{mean}, sediment plume area is at its smallest of the ablation season (Figure 4.13). Plume area is predominantly below 10 km^2, with only 7 events reaching above 18 km^2. The area of the sediment plume is heavily reliant on meltwater contributions to the marine system. Meltwater originating at the surface of Kronebreen must navigate through the snow pack and the internal glacier drainage system to reach the glacier bed, in order to be expelled into Kongsfjorden. The supraglacial drainage of polythermal glaciers does not facilitate efficient drainage from the glacier surface to the glacier bed early in the ablation season (Hodgkins, 2001). Superimposed ice, formed by meltwater freezing at the base and within snow pack (Müller and Keeler, 1969; Wakahama et al., 1976) inhibits the permeability of the glacier. The snow pack can become interspersed with ice layers, restricting percolation of surface melt (Wadham et al., 2000). Approximately 35% of the surface of Kongsvegen is covered by superimposed ice, which is comparable to the area of bare ice (36%) (Obleitner and Lehning, 2004; König et al., 2002). Restricted flow through the snow pack leads to accumulation of meltwater in ponds at the glacier surface early in the ablation season (Hodgkins, 2001; Obleitner and Lehning, 2004). Early season internal glacier dynamics prevent the vertical percolation of snow melt and encourage lateral flow instead (Fountain, 1996). As such, hydraulic inefficiencies of the snow pack and englacial drainage system could be responsible for the constraint upon meltwater discharge from Kronebreen during the early season, as has been found at warm based glaciers (Willis et al., 1996).

The area of ice detected at Kronebreen's terminus is greatest during the early season, at approximately 9 km^2. It is variable, but remains fairly constant. Because of the speed of Kronebreen, its area appears to increase slightly from day to day. Due to the resolution of MODIS, it is difficult to get an accurate representation of the location of the ice front.

Mid season: 19th June - 17th August (Day 181 – 230)

Following the early season flushing, the TSS$_{mean}$ declines to approximately 0.09 g l^{-1}, whilst TSS$_{max}$ remain at approximately 0.21 g l^{-1}. Throughout the rest of the season, both TSS$_{mean}$ and TSS$_{max}$ do not substantially change (Figure 4.14). Alpine glaciers have exhibited this trend of constant sediment supply, after the initial hydraulic engagement of the bed (Collins, 1990). Increased sediment load during the ablation season has been observed at other polthermal glaciers, thought to be caused by increased meltwater reaching the subglacial environment (Vatne, 1992; Vatne et al., 1995; Hodson and Ferguson, 1999).

TSS delivery has been linked with the evolution of subglacial drainage, in which meltwater is constrained to the area of the bed from where sediment has already been flushed (Collins, 1990). Basal erosion is reduced as a channelized systems develop, which constrains meltwater to the area of the bed from where sediment has already been flushed (Willis et al., 1996). Increased englacial hydraulic efficiency has been observed at Finsterwalderbreen, Svalbard, through the monitoring of dissolved solutes (Wadham et al., 1998). However, in Kongsfjorden the size of the sediment plume expelled from Kronebreen typically increases from the 19th June; as such the lower TSS$_{mean}$ in comparison to 1st – 19th June, could be a result of the same quantity of TSS entering Kongsfjorden, but being spread over a greater area, therefore reducing the concentration of TSS$_{mean}$. The high discharge velocity associated with large meltwater discharge events, forces the sediment further across the fjord surface. This can have negative connotations for primary productivity due to greater limitation of light (Piwosz et al., 2009).

Glacial ablation commences before the peak of the melt season (19th July - 8th August) (Hanssen-Bauer et al., 1990), leading to greater meltwater availability. As a result, increased water pressure at the base of Kronebreen exerts greater meltwater release into Kongsfjorden (Gurnell et al., 1992a; Clifford et al., 1995). During this period, plume area ranges from 10 – 56 km^2. The change from restricted flow to more variable meltwater delivery is illustrated by the variability of plume area during the mid season, compared to the early season (Figure 4.13). Whether the hydrological system of Kronebreen evolves during the ablation season, moving from a distributed system to a channelized configuration (Hodson and Ferguson, 1999), cannot be discerned from these TSS and plume size results alone. The plume extent does not give any insight to glacier hydrology, since the timing between melt production and the surface, and discharge as a plume, cannot be determined. The mid-season is characterised by an ice face area of approximately 4 km^2, which marks the largest seasonal change. This is indicative of calving events once the ablation season has begun (Benn et al., 2007).

Late season: 18th August - 30th September (Day 231 – 270)

The latter part of the ablation season is characterised by the same TSS values as during the peak of the melt season from the 19th June, but plume areas are generally below 20 km^2. Sediment exhaustion is not explicitly apparent from Kronebreen. This lies in agreement with studies of other Arctic polythermal glaciers, which have not revealed seasonal sediment exhaustion (Hodson and Ferguson, 1999; Irvine-Fynn et al., 2005). However, seasonal TSS exhaustion has been widely documented at multiple time scales in proglacial streams (Hodgkins et al., 2003) and is a notable signature of warm based glaciers (Østrem, 1975; Hodson and Ferguson, 1999).

The intra-seasonal pattern of meltwater delivery from Kronebreen to Kongsfjorden aligns with observations from studies of other Arctic tidewater glaciers (Vieli et al., 2004; Andersen et al., 2010). Small plume size is prevalent the early in the season, increasing at the peak of ablation when there is greater meltwater availability, and decreases at the end of the season as meltwater production decreases. In comparison to the early season, plume area is larger and more variable at the end of the season (Figure 4.13). It is possible that glacial efficiency of meltwater transport, from the supraglacial to the subglacial, improves during the ablation season. The results from TSS and plume area present the intra-seasonal development of meltwater discharge, but do not offer any indication on the temporal variability in timing, between melt production and discharge. Knowledge of supraglacial processes, such as atmospheric temperature and runoff production, would provide information on the production of melt. The timing between meltwater production and discharge as a sediment plume, could provide an insight to the seasonal development of englacial hydrological efficiency. The terminus of Kronebreen remains with an ice area similar to the mid-season, indicating that calving has not continued to accelerate.

4.4.3 Interannual variability

The onset of seasonal melt can lead to more surface meltwater reaching the basal surface, acting as lubricant and increasing glacier velocity (Dunse et al., 2012). The rapid decrease in SMB of Kronebreen - Kongsvegen from 1995 – 2007 has been highlighted as a factor leading to greater meltwater flux, which has the potential to alter subglacial hydrology (Nuth et al., 2012). Increased surface melt can induce high rates of calving (Zwally et al., 2002) and increase glacier velocity (Schoof, 2010). However, over the 12 year period, there has been no sustained pattern of increased mean annual plume extent. It remains variable, responding to meltwater fluxes. Chu et al. (2012) found that mean annual plume extent correlated with PDD. Therefore, under scenarios of enhanced Arctic warming (IPCC, 2013), increased discharge of meltwater and sediment to Arctic fjords would occur. Sediment transport to fjords, from tidewater glaciers, leads to the formation of grounding line fans, which can act to stabilise the glacier and even allow for glacier advance (Stearns et al., 2015). This however is dependent on the rate of retreat, because sediment transported to the fjord during rapid retreat is spread out, rather than becoming built up (Dowdeswell et al., 2015).

During the course of an ablation season, there was a general decline in glacier ice coverage at Kronebreen's terminus. Over the 12 year period, there has been a decline at the terminus, which corroborates with the terminus retreat in Figure 1.7. The marked retreat from 2011 to 2013 is apparent as mean annual ice area declines from 0.9 – 0.1 km^2. The ice area provides a measure of retreat, but area alone does not indicate which region has undergone retreat. For instance, Kongsvegen underwent a marked retreat in 2013; using annual mean area alone does not give any spatial representation of the location of retreat.

4.5 Conclusions

This study has identified the seasonality within meltwater delivery from the tidewater glacier Kronebreen, into Kongsfjorden. Quantification of plume area and TSS is feasible in Kongsfjorden, using an automated model to calibrate MODIS satellite images with *in situ* measurements. A total of 234 cloud free days were available for analysis between June and September, from 2002 – 2013, from the Terra and Aqua satellites. This expands upon previous studies which have used remote sensing to determine meltwater delivery from terrestrial glacial rivers (Chu et al., 2009; 2012; Tedstone and Arnold, 2012). The seasonal development of meltwater discharge has been captured in plume extent, as well as TSS delivery. Interannual variability is apparent, but the drivers behind this have not been addressed in this Chapter.

These results have revealed a seasonal trend in both plume area, a proxy for meltwater delivery, and TSS. Plume area is typically <10 km^2 before 19th June, and increases to range between 10 – 58 km^2 at the peak of the melt season from 19th July – 18th August. The availability of meltwater decreases at the end of the season, characterised by plume areas <20 km^2. Evaluation of plume area together with TSS indicates early season flushing of sediment from 1st - 19th June, with a seasonal maximum for TSS_{mean} (>0.1 g l^{-1}), despite the smallest mean plume area of the season. Whilst this process has been documented in alpine and terrestrial Arctic glaciers, this is the first indication of this process in a tidewater glacier environment. Despite more meltwater reaching the base of the glacier, seasonally there was no increase in TSS_{mean}, indicative of constant TSS availability for transportation to Kongsfjorden. This study did not discern any significant signs of sediment exhaustion at the end of the season. Constrained by daylight availability for adequate MODIS image retrieval, the sampling period ended on 30^{th} September, before the onset of the Polar night. As such sediment exhaustion may occur beyond this time frame. Development of glacier drainage systems, from supraglacial to subglacial, and the transport time of meltwater cannot be discerned from these data alone.

The year to year variability of both TSS and mean plume extent is apparent. High melt years, indicated by large mean plume area, transport a greater sediment flux to Kongsfjorden. Studies in Greenland have also found this both through direct observations, (Hasholt et al., 2013) and by remote sensing of sediment plumes (Chu et al., 2009; Hudson et al., 2014). Whilst the TSS_{sum} maintains a close relationship with plume area, TSS_{mean} has little relationship. The increased velocity of larger meltwater discharge is able to transport the sediment further, creating a larger plume, resulting in lower TSS_{mean}. In this instance, TSS_{mean} is not representative of the total flux of sediment to the fjord. There is no trend of increase or decline during the 12 year period. Further work is required to determine what controls the annual contributions of TSS and freshwater discharge. Glacier ice was identified through the process of exclusion when determining TSS. Although a proportional area of glacier ice at Kronebreen's terminus was established, the resolution for an accurate assessment of the terminus is difficult using MODIS. The annual change of Kronebreen's terminus position is much better addressed using Landsat 8 (Figure 1.7). However these results do reveal the dramatic ice front retreat in 2013.

Despite Tedstone and Arnold (2012) suggesting that remote sensing of sediment plumes from tidewater glaciers is not appropriate for quantifying meltwater discharge, the ice melange free environment of Kongsfjorden has suggested otherwise. Calibration with MODIS band 1 has been appropriate for the quantity of TSS in Kongsfjorden, despite other studies using a multi-band approach (Hudson et al., 2014). For a specific site, this method has provided a novel insight to both the temporal, and spatial variability of meltwater and sediment transport, from a tidewater glacier. The TSS detection model was modified to account for the retreating position of Kronebreen's terminus. With this in mind, synoptic scale use of sediment plume detection from tidewater glaciers may not be appropriate. Instead, it is a viable tool for site specific investigations.

Following the call from Chu (2014), to better understand tidewater glacier hydrology, further work could be undertaken to extend this study. Sediment plumes provide a proxy for meltwater discharge, and surface melt production is obtain-able from surface mass balance models (Aas, 2015). Therefore, determining if there are links between the two would offer information on the amount of meltwater that actually enters the fjord, and the time scales involved between surface melt production and subglacial discharge.

Chapter 5

Seasonal and interannual evolution of meltwater production, storage and release from Kronebreen

5.1 Introduction

Polythermal glaciers follow a pattern of meltwater storage and release, which controls the seasonal discharge regime (Hodgkins, 1997). Meteorological factors play a crucial role in meltwater production, with glacier hydrology modulating meltwater storage and drainage (Irvine-Fynn et al., 2011). A solid understanding of the connections between the supraglacial and subglacial environments is required to determine the rate that meltwater can reach the glacier bed, where it can impact velocity and frontal calving (e.g. Vieli et al., 2004; Andersen et al., 2010). Quantifying supraglacial melt alone is not enough to determine how much meltwater reaches the ocean, since glaciers can store water both intra-seasonally, and from year to year (Hooke, 2005). Retention of meltwater within glaciers, is causing large uncertainties in sea level rise forecasts (Harper et al., 2012).

Determining the drivers of meltwater production is important to accurately forecast future inputs to the marine environment. As such, the climate forcing on meltwater delivery and the time scale between meltwater production and discharge is to be examined, together with investigation into the seasonal glacial hydrology. To achieve this, the following research questions have been addressed:

i How does sediment plume area compare with runoff from the WRF - CMB model?

ii What is the role of atmospheric temperature on meltwater delivery at daily, seasonal and interannual time scales?

iii Are there intra-seasonal and interannual differences in meltwater delivery?

iv Does precipitation make a significant contribution to the sediment plumes?

Glacier hydrology plays an important role in determining flow velocity, which can influence calving rates at the terminus of tidewater glaciers and their overall mass balance. Comparable to their temperate counterparts, the drainage of polythermal glaciers is complex, yet they remain less well studied (Hodgkins et al., 2013). This study utilises sediment plume extent, as determined in Chapter 4, which revealed seasonal and interannual variability in meltwater delivery to Kongsfjorden. To determine if sediment plume extent is a suitable proxy for runoff, a comparison will be made with runoff results from the WRF-CMB model (Aas, K 2015, pers. comm., 30 Jan).

A long time series of SMB studies from Kronebreen and Kongsvegen exist from the 1950s (Hagen and Liestøl, 1990) and continues to the present day (Karner et al., 2013). The SMB of Kronebreen and Kongsvegen was near zero until the late 1990s, at which point it became negative until 2007, stabilising thereafter (Nuth et al., 2012). The relative stability of Kongsvegen in comparison to other smaller glaciers such as Brøggerbreen has been attributed to its greater size and higher mean altitude (Hagen, 1988). Although relatively stable, the south-south-westerly atmospheric flow of 2013 broke the summer melt record for Svalbard, displaying a negative SMB of -20.4 Gt yr^{-1} (Lang et al., 2015). Recent research has focussed on Kronebreen's velocity (Figure 1.6) and calving regime (Figure 1.7) (Rolstad and Norland, 2009; Sund et al., 2011).

Despite this, the connection with discharge to Kongsfjorden has not previously been investigated. A time series of discharge has also been found to be an effective method of discerning the seasonal and interannual development of glacial drainage (Hodgkins et al., 2013). However, an *in situ* gauging station at the grounding line of Kronebreen, where meltwater is discharged into Kongsfjorden, is not currently feasible. Therefore a remote detection method, determining the size of suspended sediment plumes, has been employed to determine meltwater delivery (Chapter 4).

Plume extent, determined by calibrating MODIS band 1 imagery with *in situ* TSS and spectral reflectance, has been found to be a good indicator of meltwater discharge (Chapter 4). However, obtaining plume extent from MODIS satellite images is reliant on cloud free days (Table 4.1), meaning there is not a continuous seasonal record, as with a gauging station. Therefore plume extent is compared with modelled surface runoff from the WRF-CMB model, to determine if it is a suitable proxy for meltwater discharge. Focus is placed on the relationship between meteorology and discharge, both intraseasonally and annually. The time between meltwater runoff formation, and sediment plume formation, provides an indicator for the seasonal evolution of meltwater production, storage and discharge. Owing to the duration of this study, from 2002 – 2013, interannual variability and winter controls on meltwater storage are revealed. Consideration is also placed upon annual changes to the NAO and the Arctic oscillation (AO), which affect Arctic temperatures.

5.2 Methodology

The temporal variability of the extent of sediment plume area and TSS concentration, as determined in Chapter 4, will be analysed with both meteorological and modelled runoff data. A series of regression and statistical analyses will examine the effect of atmospheric temperature on plume formation, from daily to interannual time scales, from 2002 – 2013. The interactions between plume area and runoff, produced by the WRF-CMB model, will be examined from 2004 – 2013; modelled runoff data are only available from 2004.

5.2.1 Meteorological data

Hourly meteorological data are available from the weather station based at Ny-Ålesund research station which is 14 km away, south-west of Kronebreen (eKlima, 2014). This study focusses on mean, maximum and minimum daily temperature and daily mean precipitation.

Atmospheric temperature is strongly seasonal, with large interannual variability. A ten day running average has been applied to reduce the daily noise in these data (Figure 5.1). A daily climatological mean has been calculated for the 12 year period, taking the average of the same day each year, in order to determine the overall seasonal trend, whilst dampening interannual variability. This will provide a basis to highlight annual anomalies and deviation from the climatological seasonal trends due to the passage of air masses (Nesje et al., 2000).

Assessing the 2002 – 2013 average daily temperature, the range of temperature differs throughout the year. The winter months (December, January, and February) display the greatest standard deviation from the mean, ± 4.5 °C. This is much reduced in June, July and August at ± 1.1 °C (Figure 5.1). The temperature rises above zero from approximately 1st June until 30th September. However, the annual mean remained negative at -4.0 °C. The maximum mean temperature was 6.3°C, occurring on 2nd August, whilst the minimum of -13.5 °C occurred on 3rd March. Atmospheric temperature is negative for the majority of the year, consequently during periods of positive temperatures the glaciers will be prone to melt. Snow ablation generally starts at the end of April, in coordination with the surface energy balance (Hinzman and Kane, 1992).

The coldest year was 2003, which exhibited an annual mean temperature of -5.8 °C and the warmest was 2012 with a mean annual temperature of -2.5 °C. The maximum and minimum daily mean temperatures from 2002 – 2013 are displayed in Figure 5.1. The overall coldest day was the 23rd January 2004 which exhibited a mean temperature of -21.9 °C, whilst the warmest daily mean temperature was 13.4 °C on 7th July 2005.

In this study the PDD is the cumulative sum of daily mean temperature above zero, from 1st January – 30th September. Typically positive temperatures do not occur until May. The PDD season was curtailed at the 30th September due to the polar night limiting suitable MODIS retrievals beyond this time. The length of the melt season has been determined by how many PDDs there are in a season. Two measures have been used: 1) the total number of days above zero from 1st January – 30th September and 2) the number of continuous positive days, in which there can only be a one day break into negative temperatures. This second measure provides the continuous melt season length.

Mean and cumulative snow depth have been calculated from 2009 – 2013; data are not available before this period. Data from 1st October to 31st May have been used to determine the annual values.

5.2.2 Runoff data from the Weather Research and Forecasting - Surface Energy Balance model

Modelled results for runoff from Kronebreen and Kongsvegen, in addition to the Infantfonna ice field, are available at hourly resolution from 2004 – 2013 from WRF-CMB model. The WRF model has been used in many surface - boundary layer process studies in Svalbard (e.g. Kilpeläinen et al., 2012; Mayer et al., 2012). The set up of the WRF model has used version 3.4.1 (Skamarock et al., 2008) and the full set up is described in (Aas et al., 2015). Comparison of observed energy balance with modelled surface energy balance using the WRF model have reproduced monthly to seasonal mean temperatures across Svalbard very well (Aas et al., 2015). To link with the cryosphere, the WRF model has been coupled with a physically-based CMB model to form WRF-CMB. This incorporates a coupled high-resolution mesoscale atmospheric component to link glacier CMB feedbacks with the atmosphere as described in Collier et al. (2013). The full model simulation

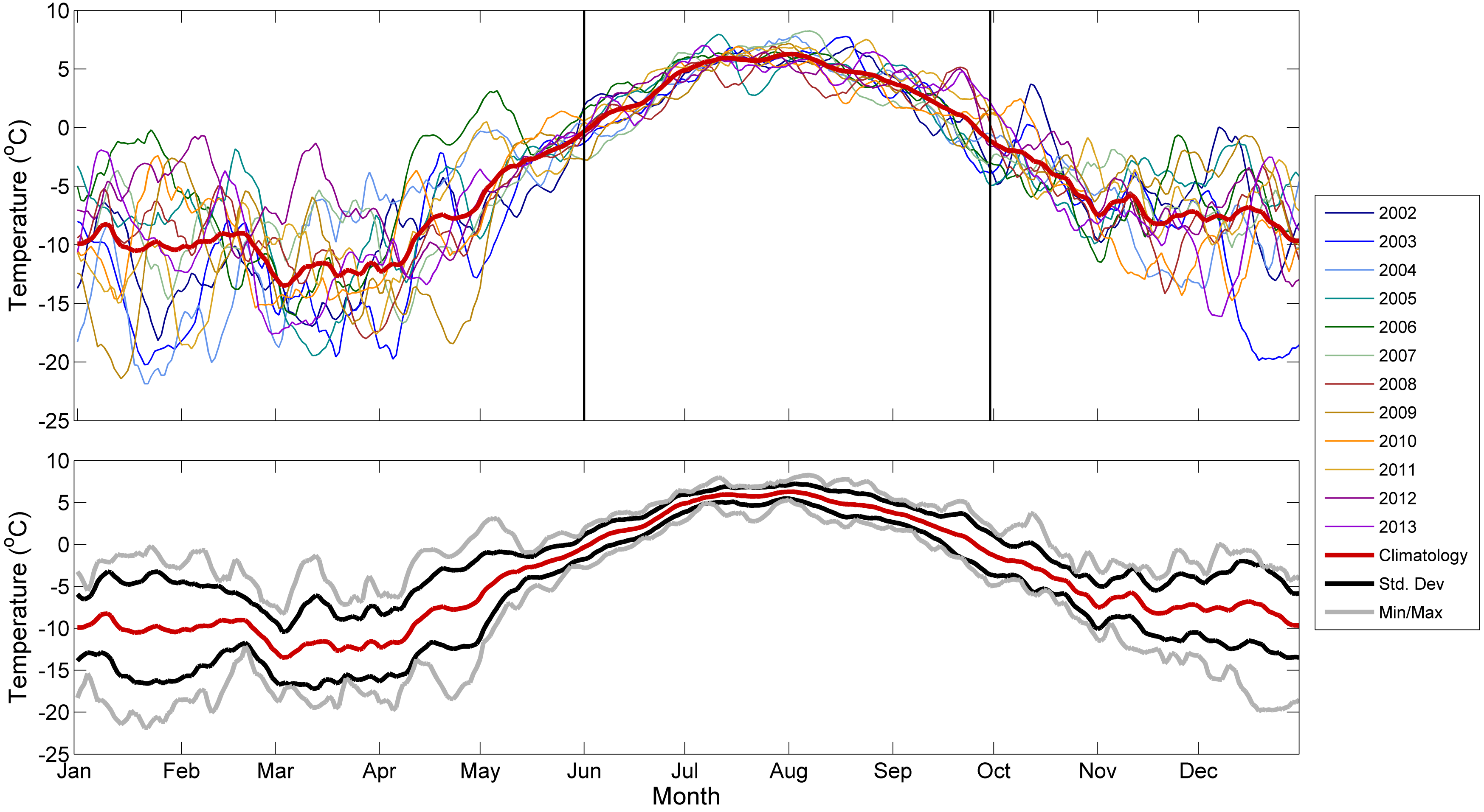

Figure 5.1: Upper: Ten day running average of seasonal temperature from 2002 – 2013, sourced from the Ny-Ålesund weather station. The twelve year mean is displayed (red line), together with the period of satellite image (vertical black lines). Lower: The mean atmospheric temperature climatology for the 12 years is displayed in red, the standard deviation from the mean is in black, and the climatologies for minimum and maximum temperatures are displayed in grey. There is much greater temperature variability between October and May, than between June and September.

setup is documented by Aas (2015, in press) and mean daily runoff ($m^3\ s^{-1}$) results were contributed to this study by personal communication.

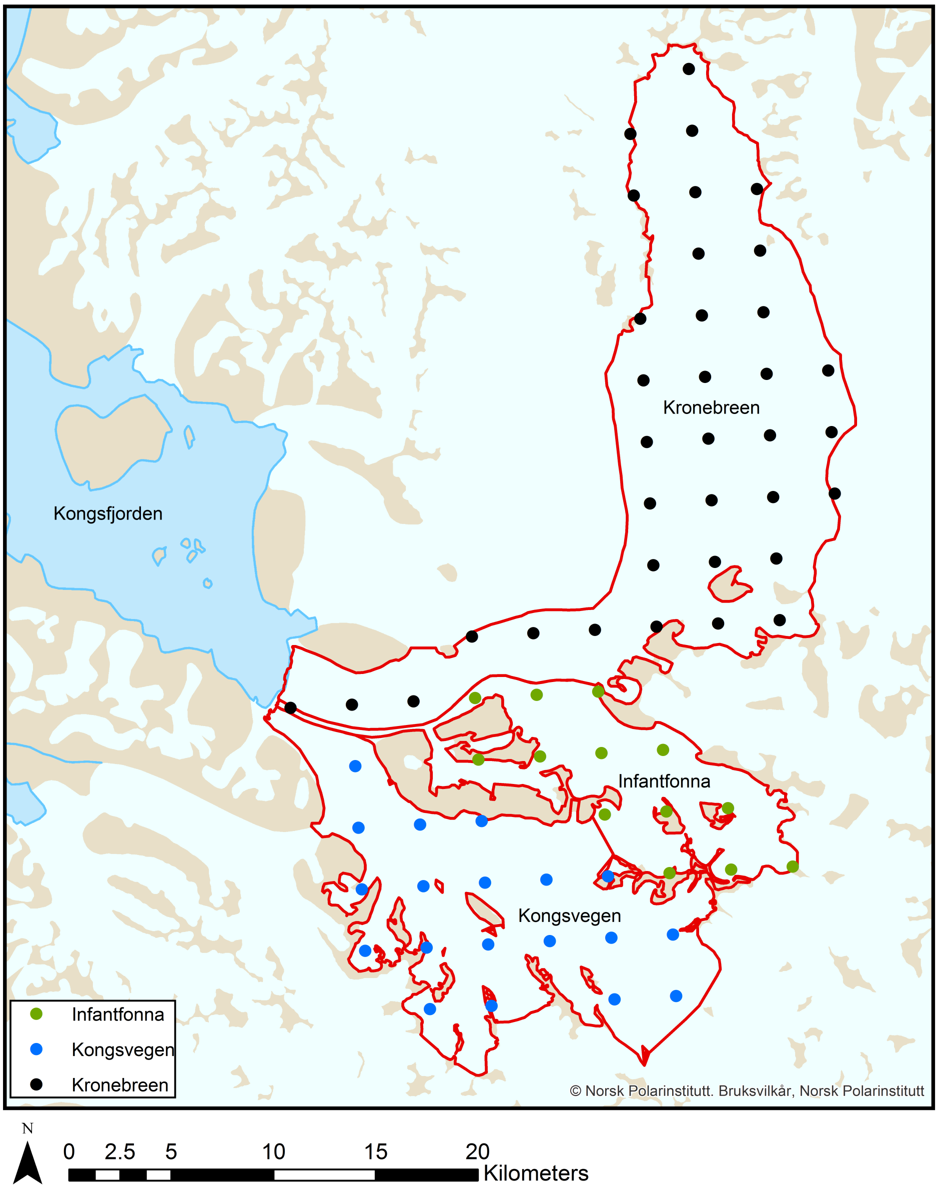

Figure 5.2: Map illustrating grid points included from the WRF - CMB runoff model for Kronebreen (black), Infantfonna ice field (green) and Kongsvegen (blue).

5.3 Results

5.3.1 Relationship between plume area and WRF - CMB runoff

Results from the WRF-CMB model indicate that daily mean runoff from 1st June – 30th September from 2004 – 2013 was 31 m^3 s^{-1}, whilst the maximum was 484 m^3 s^{-1}. Runoff is variable from daily to interannual time scales (Figure 5.3). To assess the seasonal evolution of runoff, a mean for the same day from 2004 – 2013 has been taken to provide a 10 year daily mean. Seasonally there is an association between plume area and runoff, despite the comparatively limited plume area measurements (Figure 5.4). Runoff is near zero in the early season from 1st June to 18th June, whereas plume area is approximately 10 km^2. From 19th June both runoff and plume area increase displaying a good relationship; 2005 is a good example of this. Runoff increases between 28th June and 17th August ranging from 27 – 184 m^3 s^{-1}. A maximum peak in runoff occurs around day 31st July, coinciding with several large plume events (area >25 km^2). From 18th August onwards, runoff remains variable, but the outputs are largely <60 m^3 s^{-1}. Runoff only reaches zero at the end of September. The end of season pattern in similar to mean plume area in which it decreases, remaining variable, but doesn't stop altogether.

The seasonal correlation between plume area and runoff is r = 0.56, p <0.001, with plume area lagging behind runoff by two days. During June, the correlation is lower than for the overall season (r = 0.42, p <0.001); there are not many occurrences of runoff from the WRF-CMB model during this time (Figure 5.5). July exhibits a lag of 6 days with the maximum correlation of r = 0.52, p <0.001. Response between runoff and plume area increases in August illustrated by a higher correlation than the seasonal average (r = 0.70 p <0.001) and no lag. The correlation increases again in September, but with a two day lag (r = 0.82, p 0.001).

Regression analysis reveals a relationship between runoff and plume area, which increases in strength throughout the ablation season (Figure 5.6). June and July exhibit significant association despite being moderate. The relationship strengthens with less lag time in August and September. Runoff in September can account for 71% of the sediment plume size, which is greater than 50% in August.

From 2004 – 2013 there is a relationship between mean annual plume area and total runoff (Figure 5.7). This is despite plume area being determined from only the cloud free days, rather than runoff which is available at a daily time scale. Runoff can explain 41% of the variance in mean plume area over the 10 year study

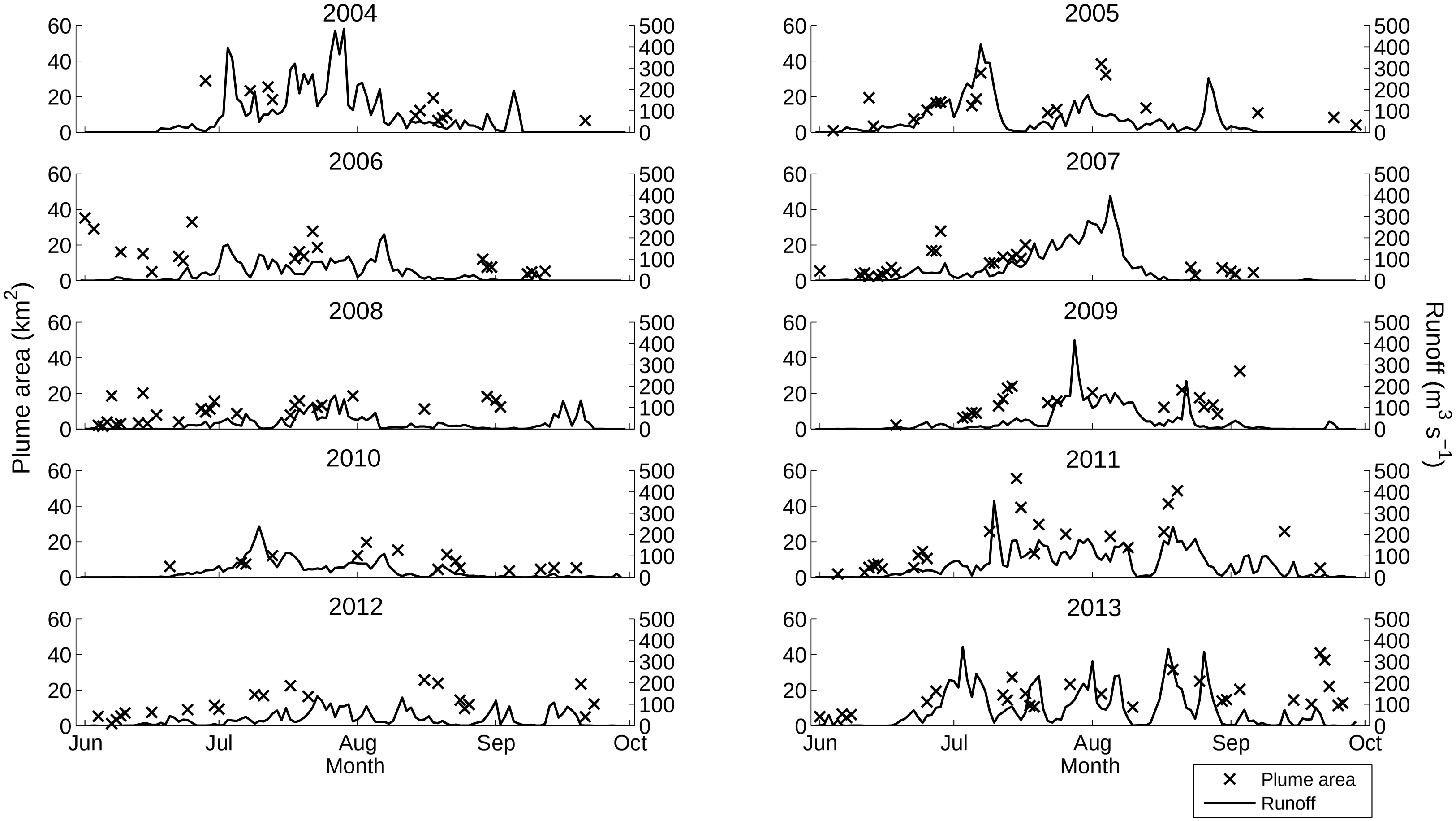

Figure 5.3: Mean daily runoff (m^3 s^{-1}) from the WRF - CMB model (black line), with plume area (km^2; black crosses) for every cloud free day from 2004 – 2013.

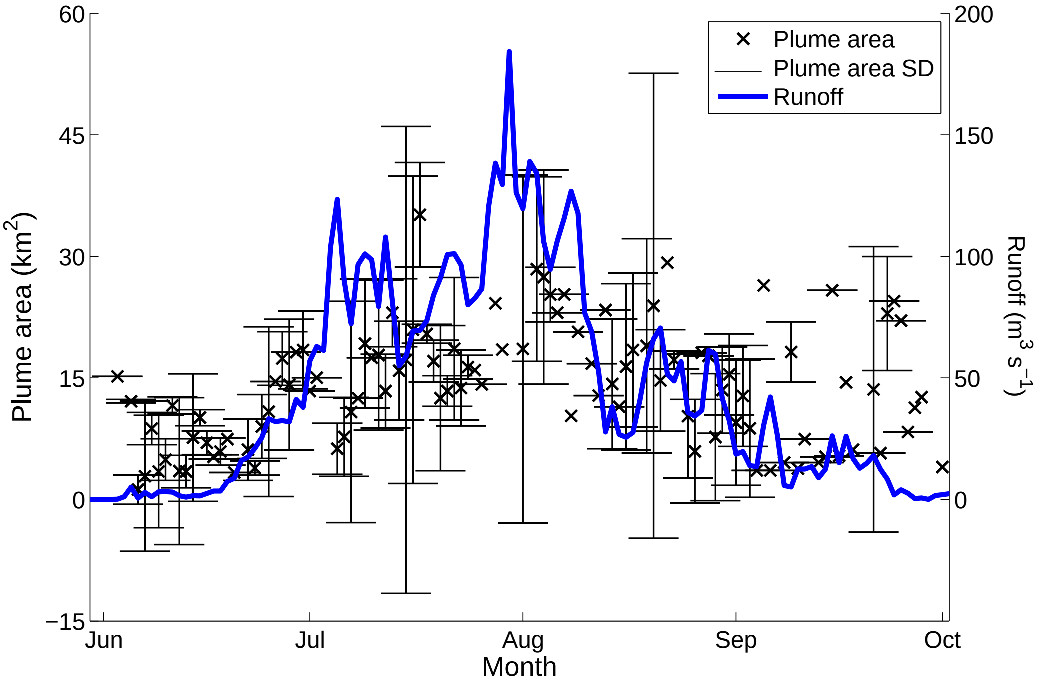

Figure 5.4: Daily mean runoff (m^3 s^{-1}) from the WRF - CMB model. Each day is averaged from 2004 – 2013 (blue line), with plume area (km^2; black crosses) for every cloud free day from 2002 – 2013. Standard deviation from the mean is represented by the black bars.

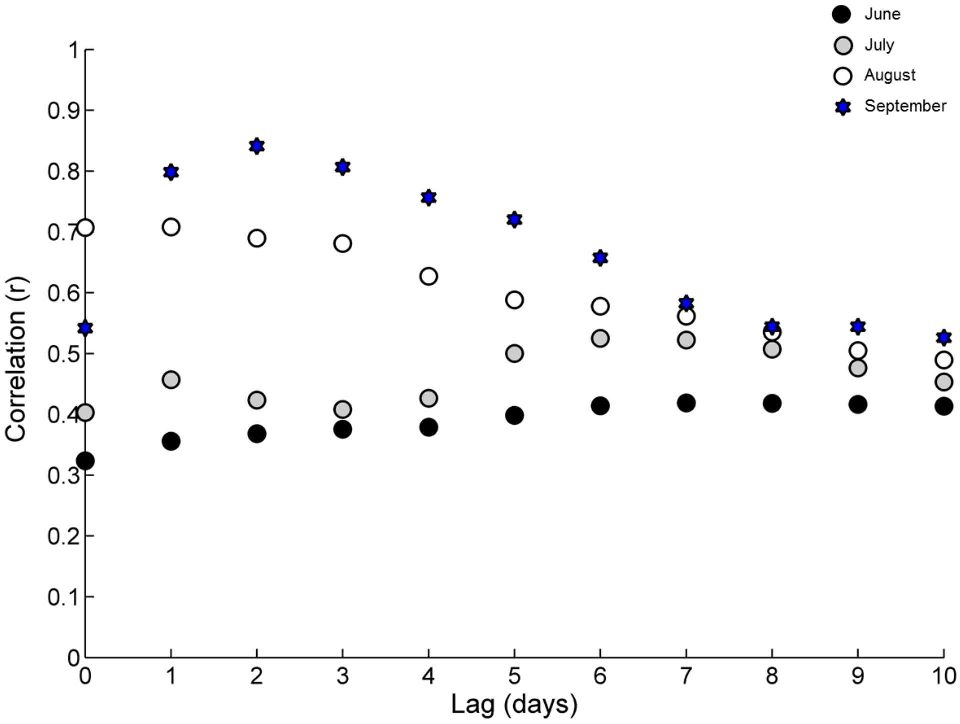

Figure 5.5: Correlation coefficients between daily mean plume area (km^2) and runoff (m^3 s^{-1}) from the WRF - CMB model, for June, July, August and September, with a 0 –25 day lag applied for monthly, from 2004 – 2013.

period ($R^2 = 0.41$, $p < 0.05$). Only in 2004 and 2007 does the trend reverse, in which plume area decreases but total runoff increases (Figure 5.4).

5.3.2 Seasonal plume response to atmospheric temperature

Association between atmospheric temperature and plume area is not clear when addressing each year individually (Figure 5.8). Years such as 2007 and 2009 display an increase in plume area from 29th June to 19th July identifiable due to several consecutive cloud-free MODIS retrievals. In contrast, years such as 2004 and 2010 exhibit a relative data sparsity in successful, successive, MODIS retrievals and therefore do not display any particular trends.

Taking the mean plume area for each day over the 12 year period reveals a seasonal evolution, which follows a similar composition to the seasonal climatology of atmospheric temperature (Figure 5.9). Greatest plume area occurs at the peak of the melt season in July. A moderate correlation is present between the seasonal atmospheric temperature climatology and plume area ($r = 0.49$, $p < 0.01$, $n = 105$), implying that there is a seasonal association in that atmospheric temperature is a driving mechanism for plume area.

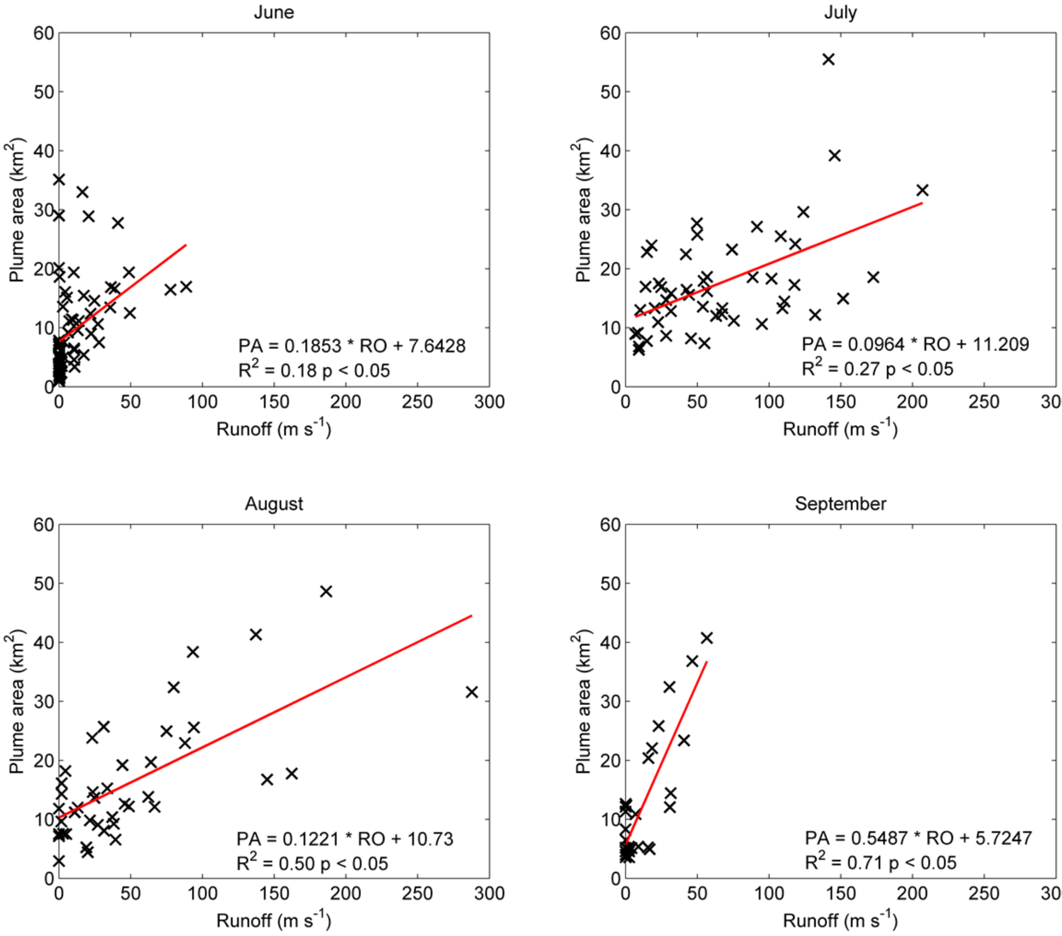

Figure 5.6: Regression between runoff (m s^{-1}) and plume area (km^2) for the lag day with highest association as displayed in Figure 5.5: June 7 day, July 6 day, August 1 day and September 2 day lag.

Month	Mean	Min	Max	Std
June	2.8	-2.4	8.2	2.23
July	5.9	0.7	13.4	1.59
August	4.89	-0.1	10.9	1.96
September	1.1	-8.4	7.7	3.2

Table 5.1: Mean monthly characteristics in atmospheric temperature (°C) from 2002 – 2013.

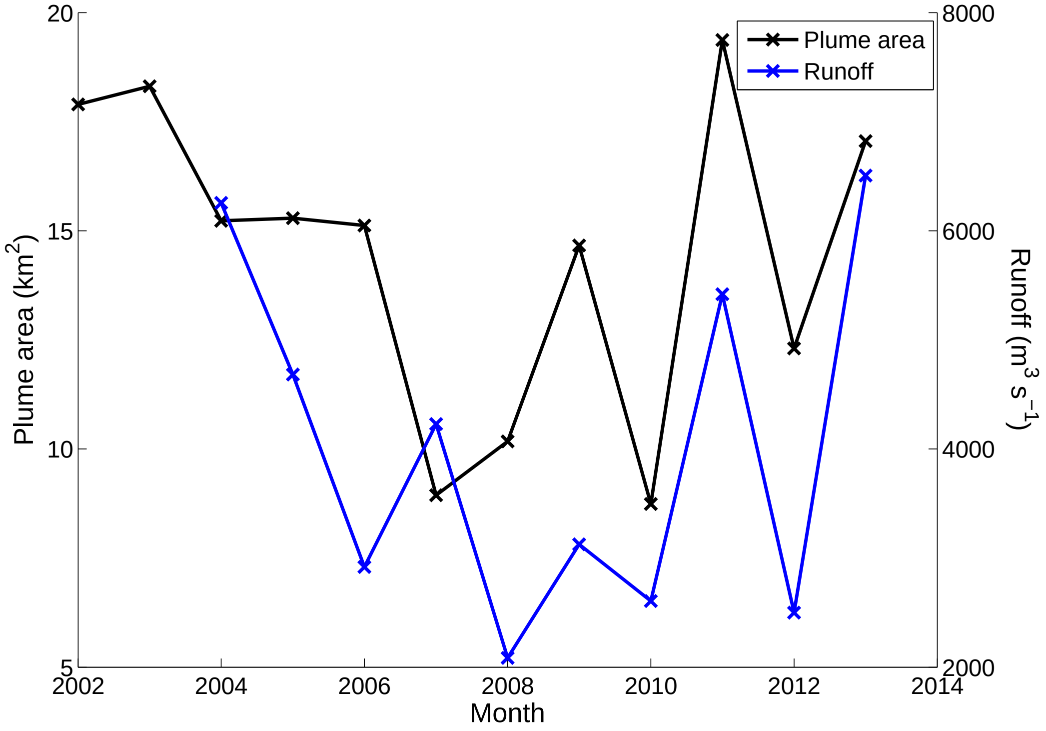

Figure 5.7: Mean annual plume area (km^2) from 2002 – 2013 (black line) and total annual runoff (m^3 s^{-1}; blue line).

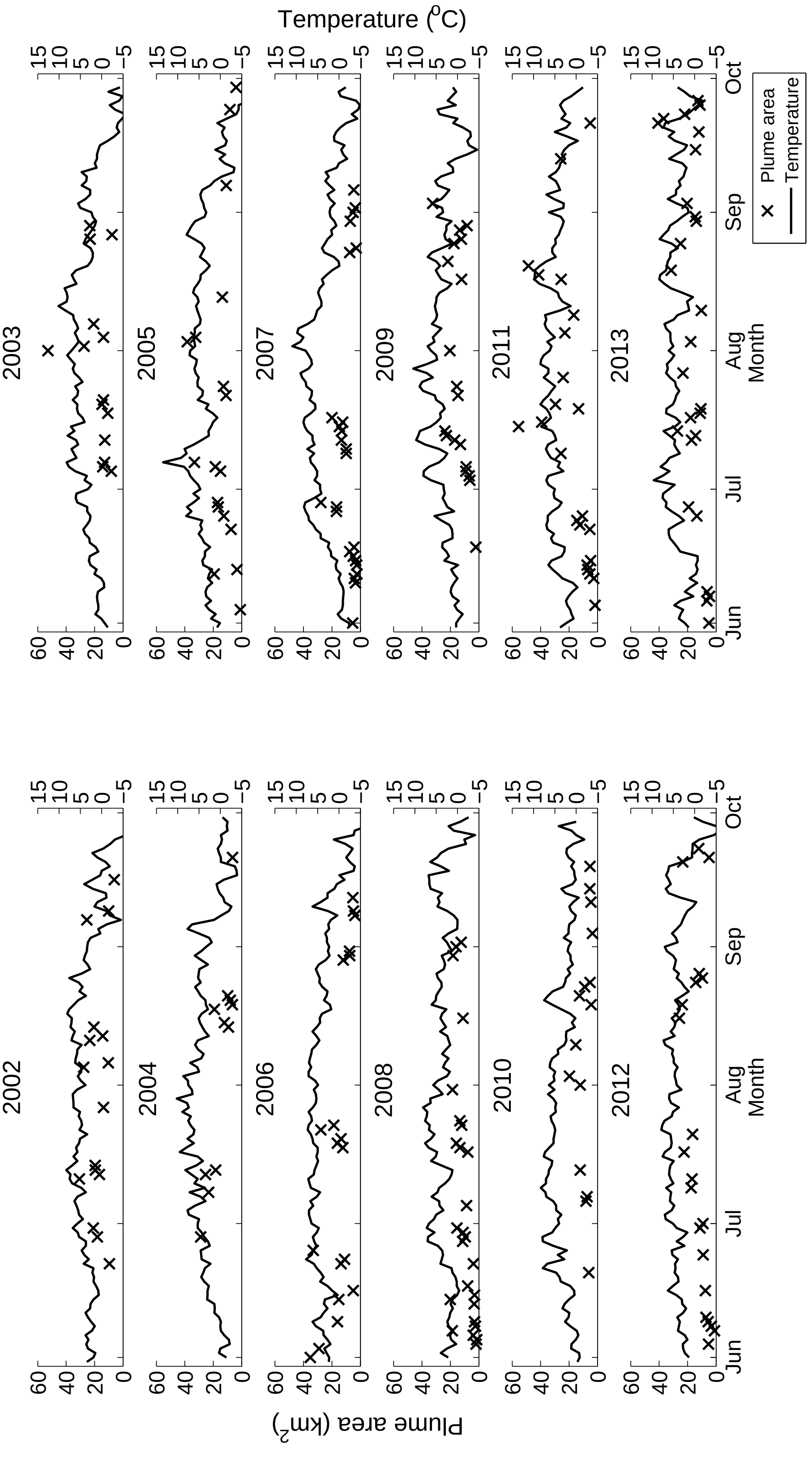

Figure 5.8: Interannual variation of sediment plume area (km^2; black crosses), with atmospheric temperature (°C; black line) sourced from Ny-Ålesund.

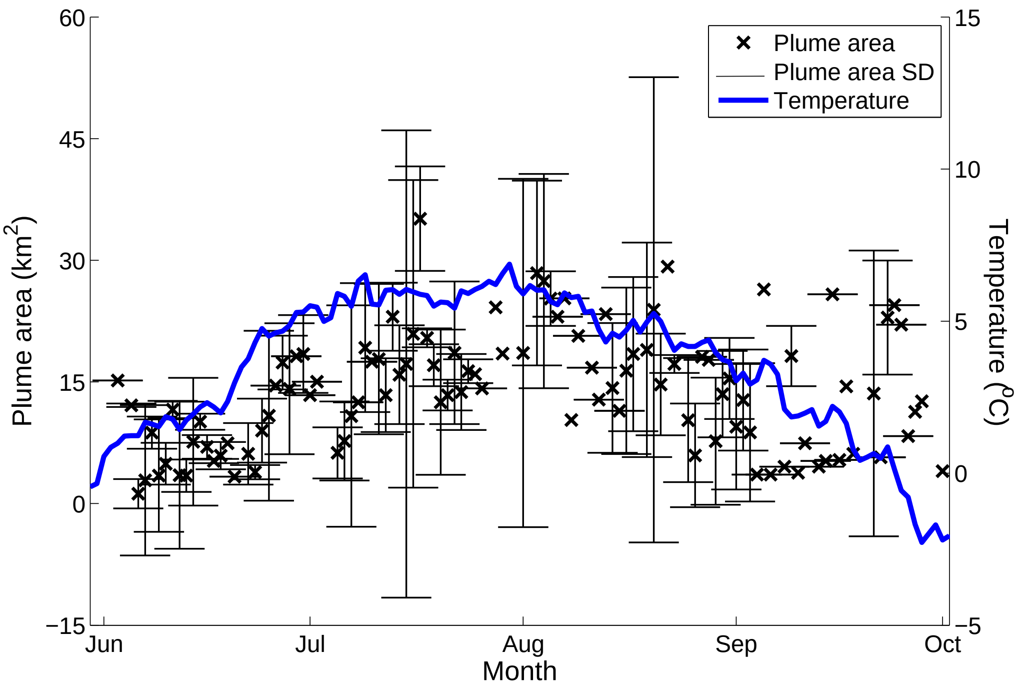

Figure 5.9: Plume area (km^2) from 2002 – 2013 (black crosses) with daily climatology of mean atmospheric temperature (°C) (blue line). Standard deviation of mean plume area is displayed as black lines.

Considering all of the data available, correlating daily mean atmospheric temperature with plume area reveals that plume area does not respond instantaneously to atmospheric temperature. Plume area lags behind atmospheric temperature (Figure 5.10). The mean temperature has the greatest influence on plume area seasonally, with the greatest response to temperature from 4 – 13 days prior to the day of plume formation ($r = 0.55 \pm 0.001$, $p < 0.05$). Maximum and minimum temperatures follow a similar pattern to the mean temperature, with the response to temperature increased from lag day 4; at this point minimum temperature exerts greater control than the maximum temperature. These converge and peak at lag days 12 – 13. From lag day 14 onwards, the response of plume area to mean, maximum and minimum temperature decreases. However, the seasonal influence of temperature on plume area masks any variability which may be taking place during the melt season.

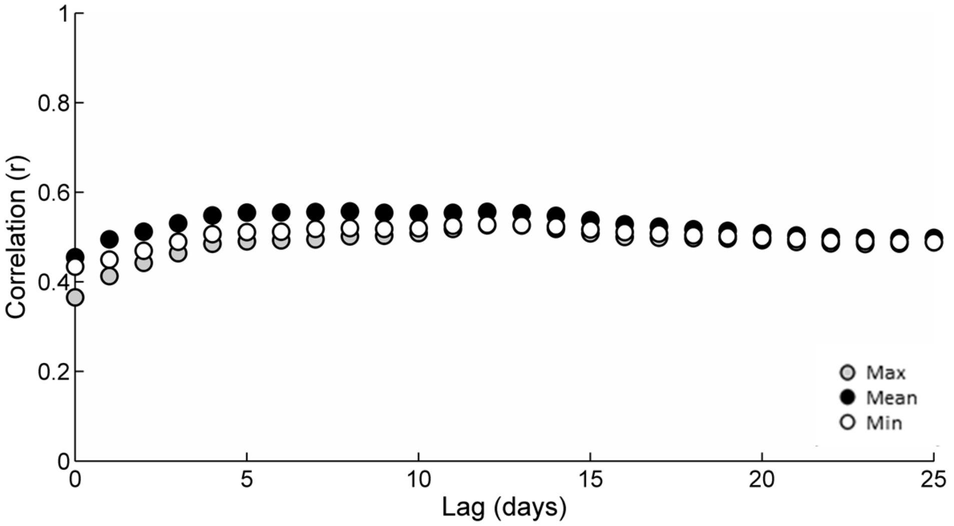

Figure 5.10: Correlation coefficients between daily plume area (km^2) and mean, maximum and minimum temperatures (°C), seasonal mean from 2002 – 2013, with 0 – 25 day lag applied.

A monthly outlook breaks down the seasonal means, illustrating the influence of atmospheric temperature on plume area throughout the melt season. During June, mean and minimum temperatures exert almost the same control over plume area, whereas the effect of maximum temperature is on average 35% less (Figure 5.11). The greatest effect of mean temperature on plume area is from lag day 7 – 9 (r = 0.53, $p = 0.001$). From lag day 10, the effect of mean and minimum temperature decreases. July presents a different outlook with mean, maximum and minimum temperatures all exerting similar control until lag day 14. The degree of correlation increases with lag time, presenting two peaks during July. The first on lag day 7 (r = 0.48, $p < 0.01$) and the second between lag days 12 – 14 (r = 0.48 ± 0.005, $p < 0.001$). From lag day 14 the degree of association decreases, as was observed in the seasonal trend. The fastest plume area response to temperature occurs during August, illustrated by the highest correlation coefficient of the season, r = 0.70, $p < 0.001$, at lag day 2. A steady decrease in association between mean temperature and plume area occurs until lag days 11 – 13 (r = 0.59 ± 0.004, $p < 0.001$), which corresponds in timing to a similar secondary peak in July. From lag day 14, once again the degree of association decreases. September exhibits the second highest correlation coefficient. Plume area responds to the maximum temperature 4 days prior (r = 0.57, $p < 0.001$), which is a greater response than for both the mean and minimum temperatures. From lag day four onwards the plume response to temperature is relatively uniform, with the secondary peaks no longer apparent. During September the maximum temperature appears to be the dominant driver of plume formation, which opposes the trend of June which saw the minimum and mean temperatures exerting greatest control.

Correlation analysis reveals that plume area responds to atmospheric temperature at different time scales throughout the ablation season. August responded not only the fastest, but with the highest correlation. Regression analysis indicates that the temperature two days prior to plume formation it responsible for almost 50% (R^2 0.49) of the plume area.

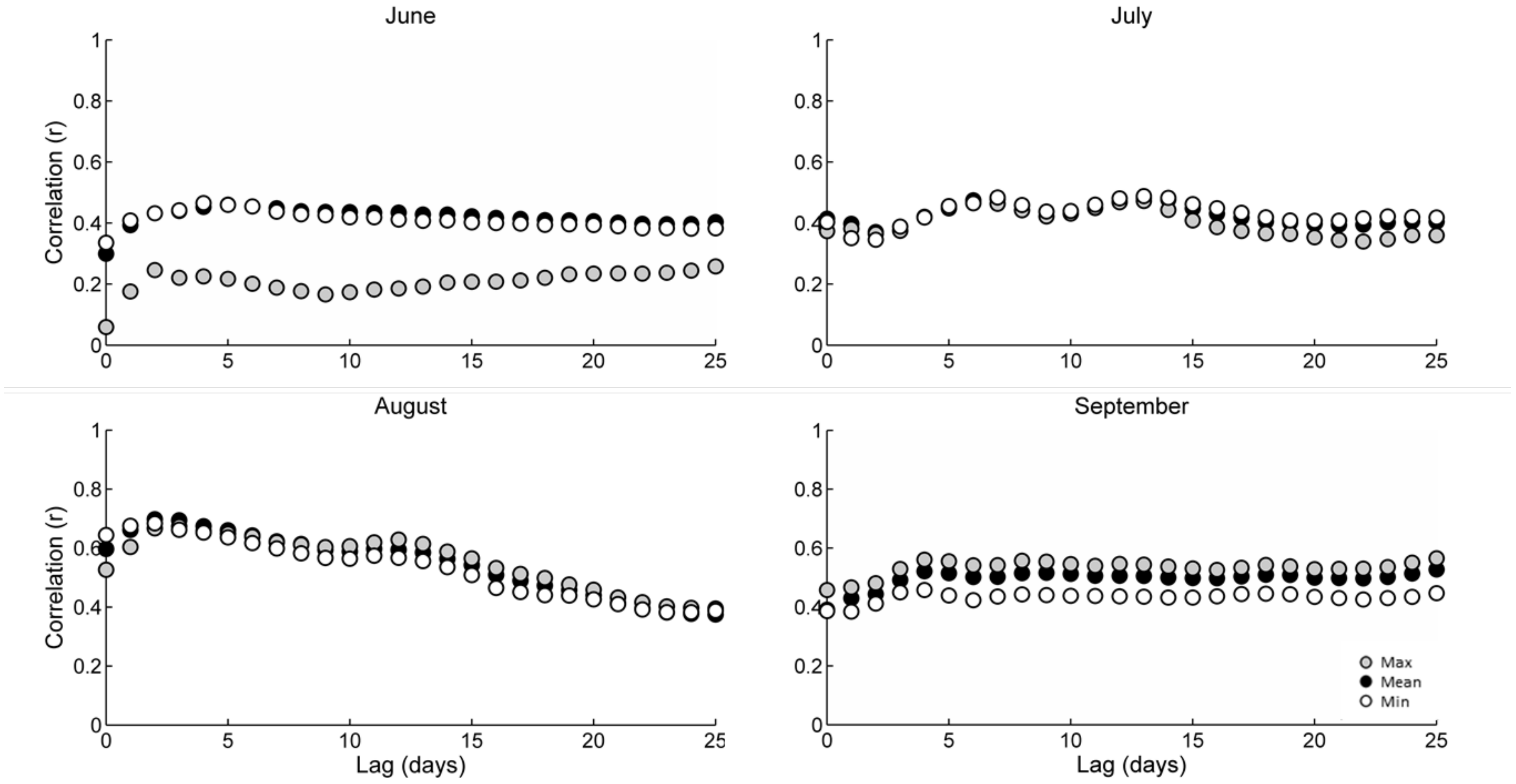

Figure 5.11: Correlation coefficients between daily plume area (km^2) and mean, maximum and minimum temperatures (°C), from June - September, with 0 – 25 day lag applied.

5.3.3 Effects of rainfall during the summer melt season

For all months during 2002 – 2013 the mean rainfall was 1.2 mm day^{-1}, with a maximum of 98.0 mm occurring on 30th January 2012. The seasonal mean, from June - September was slightly less at 1.0 mm day^{-1}, whilst the maximum is approximately one third of the annual maximum precipitation measured at 36.1 mm on 22nd July 2002. There is no defined seasonality to precipitation from rainfall between 2002 – 2013 (Figure 5.12). Mean monthly rainfall exhibits a range of only 0.9 mm from June – September (Table 5.2). Interannually there is a 1.6 mm range in mean precipitation. The wettest summer was in 2013 with an average daily rainfall of 1.9 mm day^{-1}, and the driest year was 2010 with an average daily rainfall of 0.4 mm day^{-1}. Total rainfall in summer 2013 was 243 mm compared with only 40 mm in 2010.

Correlation analysis reveals that rainfall has little, if any impact on the area of sediment plumes; this is true both with the seasonal daily mean from 2002 – 2013, and daily influence. Precipitation occurring on the day of plume formation has no significant impact upon the plume area (r = 0.005, p >0.90, n 235). There is no significant relationship between plume area and rainfall within 7 days of plume formation. With a lag of 11 days applied, there is a slight, significant correlation (r = 0.192, p <0.05, n 235). This increase could be seen as a random artefact due to the time between rainfall events.

Month	Mean	Max	Sd
June	0.4	15.2	1.4
July	1.1	36.1	3.4
August	1.2	24.0	3.1
September	1.3	18.2	2.9

Table 5.2: Mean monthly characteristics in rainfall (mm) from 2002 – 2013.

5.3.4 Interannual variability of plume formation

Meltwater delivery from Kronebreen is influenced on a seasonal time scale by atmospheric temperature. Understanding the interannual drivers of meltwater delivery is important to quantify how freshwater inputs to Kongsfjorden may change in the future. Mean plume area was 14.4 km^2 for the 12 year period. During this time, four years presented with below average plume area: 2007, 2008, 2010 and 2012, whilst the other 8 years were above average.

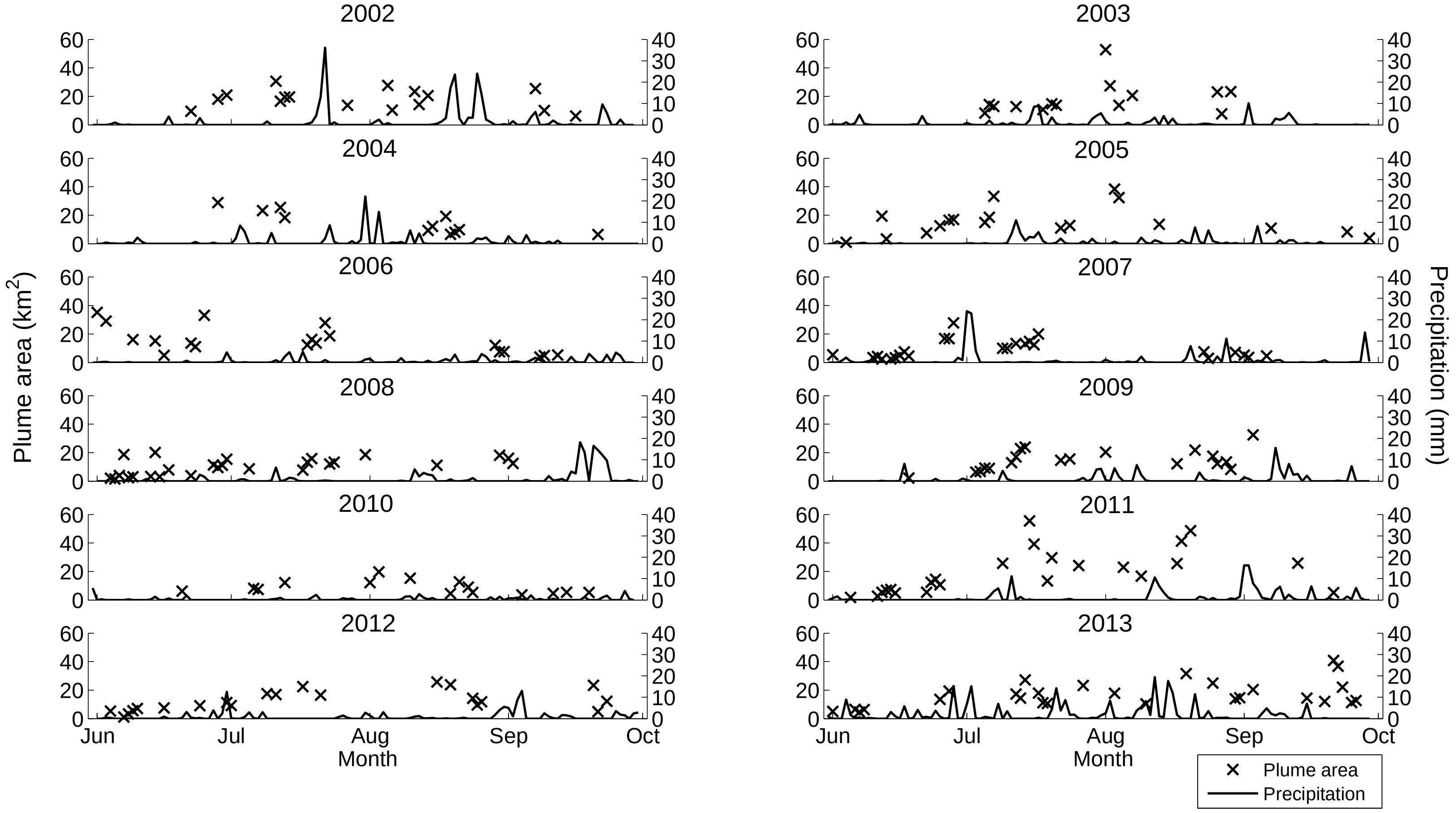

Figure 5.12: Interannual variation of sediment plume area (km^2) with precipitation. Daily mean precipitation (mm).

Year	Plume area (km^2)	Temperature DJFM (°C)	Mean TSS_{sum} ($g\ l^{-1}$)	PDD (°C)	Melt Length (days)	Continuous melt length (days)	Mean snow depth (cm)	Cumulative snow depth (cm)	Total rainfall (mm)
2002	17.9	-11.73	21.6	485.1	115	104	-	-	202
2003	18.3	-12.79	22.5	461.8	114	97	-	-	101
2004	15.2	-12.79	19.0	470.2	109	89	-	-	116
2005	15.3	-13.99	18.4	489.6	115	101	-	-	86
2006	15.1	-7.71	18.1	568.9	144	115	-	-	72
2007	8.9	-8.12	10.1	446.6	100	90	-	-	115
2008	10.2	-9.24	11.1	433.3	118	97	-	-	139
2009	14.6	-10.55	16.2	440.9	126	101	36.5	8878	107
2010	8.7	-9.04	13.0	433.1	137	108	9.1	2218	40
2011	19.4	-11.99	22.8	606.4	131	122	35.7	8674	138
2012	12.3	-5.73	12.1	536.5	133	115	14.7	3572	105
2013	17.0	-9.95	16.6	548.5	126	99	17.2	4177	245
Mean	14.4	-10.3	16.8	493.4	122.3	103.2	22.6	5504	123

Table 5.3: Annual mean values for plume area, winter temperature, TSS_{sum}, PDD, melt season length, winter snow depth and summer rainfall from 2002 – 2013.

Influence of summer meteorological parameters

PDD varied from the annual maximum of 606 °C in 2011 to the minimum of 433 °C in 2010, whilst the 12 year mean was 493 °C (Figure 5.13). The annual PDD has been variable throughout the study period but has not significantly changed ($R^2 = 0.16$ $p = 0.2$ n 12; Figure 5.13). Plume area is positively influenced by PDD ($R^2 = 0.33$, $p < 0.05$, $n = 12$); larger plume areas form with higher PDD (Figure 5.14). This analysis indicates that 33% of plume size can be attributed to PDD at an annual time scale. The maximum PDD coincides with the largest mean plume area in 2011, whilst the minimum PDD is the same year as the smallest mean plume area in 2010. The total amount of TSS brought to the marine environment is also controlled by PDD, with 18% of TSS_{sum} dependant on PDD ($R^2 = 0.18$, $p < 0.05$, $n = 12$).

The mean length of the melt season was 122 days, the longest melt season was in 2006 totalling 144 days, and the shortest was 2007 with only 100 days (Table 5.3). The longest continuous melt was in 2011 with 122 melt days, over a month longer than the continuous melt of 2004 which was only 89 days. Unlike PDD, the duration of the melt season has no significant impact on plume area (Figure 5.14).

Annual summer rainfall ranges from 40 mm in 2010 to 245 mm in 2013. The 12 year summer mean was 122 mm yr^{-1}. Although a source of freshwater, rainfall does not play a significant role in determining the size of sediment plumes at an annual time scale (Figure 5.14).

Influence of winter meteorological parameters

Mean annual winter temperatures (December, January, February, March) range from -14.0 °C in 2005 to -5.7 °C in 2012. The 12 year mean was -10.3 °C (Table 5.3). When snow data were available (2008 – 2013), the annual mean snow depth was 22.6 cm. The winters of 2009 and 2011 displayed the greatest mean snow depths, 36.5 and 35.7 cm respectively. These coincided the coldest winters, exhibiting mean winter temperatures of -10.6 °C in 2009 and -12.0 °C in 2011. Winter temperature was above average, -9.0 °C whist mean snow depth was below average, 9.1 cm, preceding the 12 year minimum mean plume area of 2010.

Linear regression has identified that colder winters promote larger plume areas in the following ablation season (Figure 5.15). Mean temperature during DJFM accounts for 36% of plume area in the summer ($R^2 = 0.36$, $p < 0.5$, $n = 12$). Winter temperatures exert even greater control, 52%, on sediment availability during the ablation season ($R^2 = 0.52$, $p < 0.5$, $n = 12$). With only 5 years of snow data, its relationship with plume area cannot be determined with any significance.

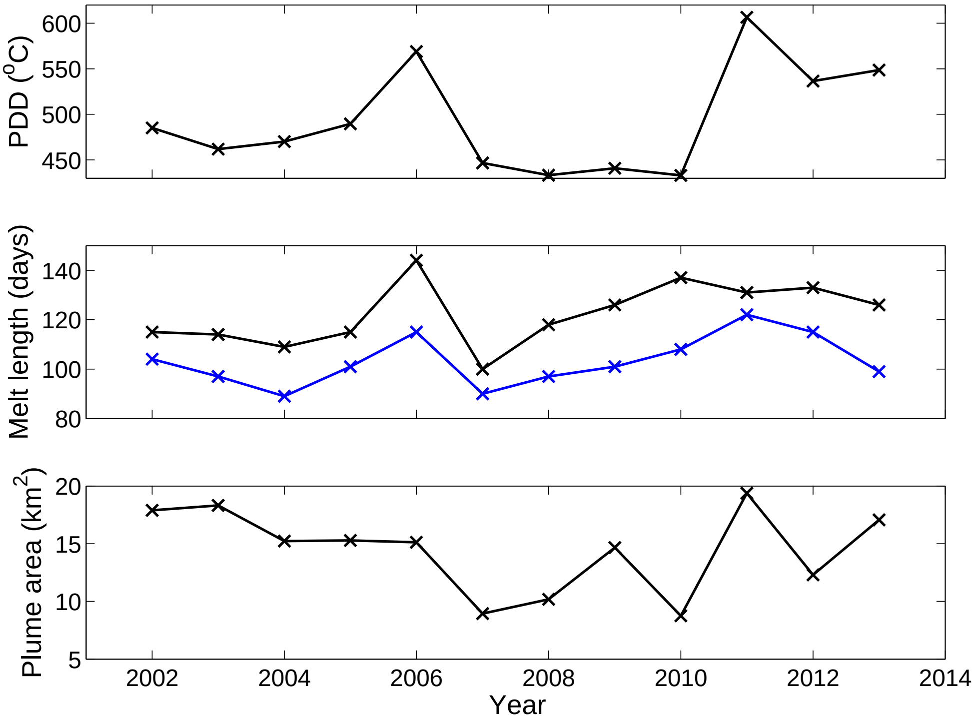

Figure 5.13: (A) Annual PDD (°C), (B) black line represents the total annual melt season length, and the blue line shows the annual consecutive melt season length (days), (C) Mean annual plume area (km^2).

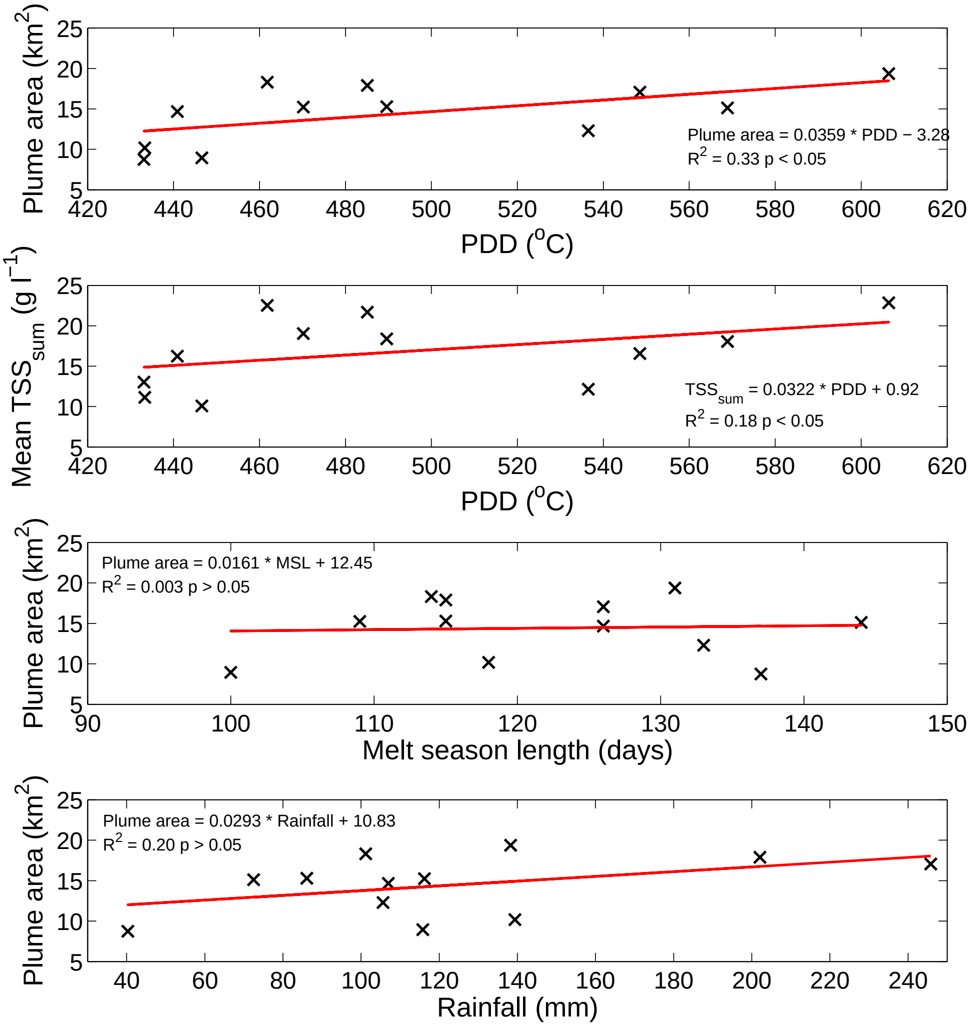

Figure 5.14: Influence of PDD (°C) and melt length (days) on sediment plume area (km^2) from 2002 – 2013. (A) Positive trend between PDD and plume area. (B) Relationship between total melt season length and plume area. (C) Relationship of the period of continuous melt on plume area.

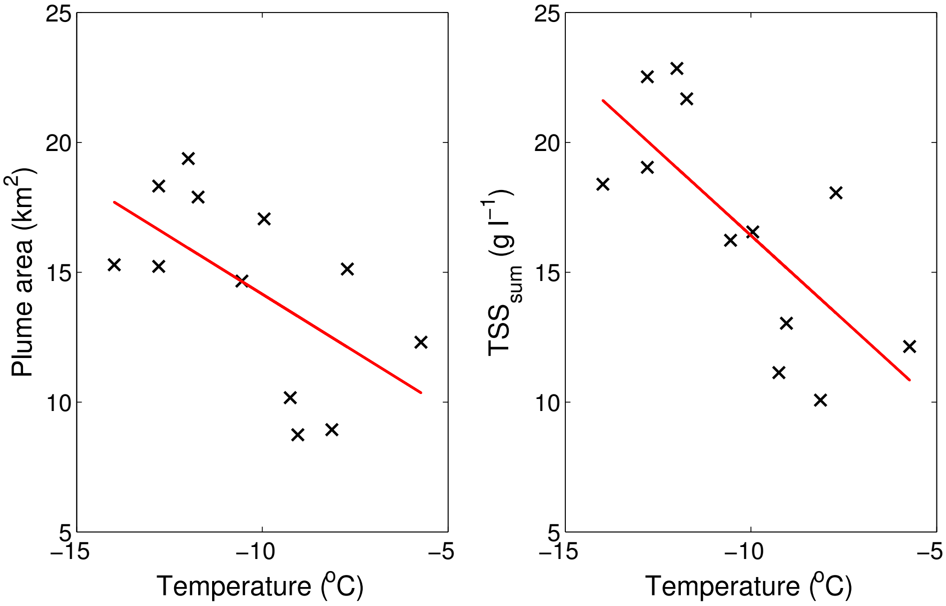

Figure 5.15: Influence of mean winter (DJFM) temperature (°C) on mean plume area and mean TSS$_{sum}$.

Influence of the NAO and AO on interannual freshwater production

The NAO brings basin wide change of the location of the North Atlantic jet stream, influencing modulation in meridional and zonal transport of heat and moisture. During its positive phase northern Europe experiences above average temperatures, with increased precipitation. In contrast, Greenland experiences below normal temperatures and less precipitation. The AO also modulates atmospheric circulation, with winds constrained in counter-clockwise circulation around the North Pole during positive AO phases. This circulation relaxes during negative phases allowing cold winds to penetrate further south.

The summer (June, July August, September; JJAS) NAO index was negative from 2006 – 2012, whilst the AO index was also negative from 2007 – 2011. The largest mean plume area was 19.4 km^2 in 2012, which occurred with the second greatest snowfall the preceding winter, and the highest PDD that summer. Both the NAO and AO were negative, with normally means colder temperatures for northern Europe. Greenland had record surface melt in 2010 and 2012 (Box et al., 2010; 2012), however plume discharge from Kronebreen and rainfall were below average for both of these years. Linear regression indicates that there is no significant relationship between either the summer NAO or the AO with plume size. The same relationship is apparent with PDD.

Increased snow cover in the Autumn can lead to a negative phase of the AO in the winter (Cohen et al., 2012). With limited snow data, this pattern has not been apparent. Both 2009 and 2011 exhibited cumulative snow depths greater than the mean (5504 cm) of >8500 cm from October - May (Table 5.3). However, the mean annual AO index for both these years differs, being negative (-0.33) in 2009 yet positive (0.53) in 2011. The NAO indexes for each of these years exhibits the same pattern as the AO, negative in 2009 (-0.24) and positive in 2011 (0.29).

5.4 Discussion

Satellite remote sensing together with *in situ* measurements, addresses the temporal and spatial limitations associated with *in situ* sampling alone (Klemas, 2011). The extent of sediment plumes, reflects the changes in meltwater discharge, corroborating with sediment plume detection studies in Greenland (McGrath et al., 2010; Chu et al., 2009; 2012; Tedstone and Arnold, 2012). This is the first study to focus on the intraseasonal and interannual variability of meltwater discharge from a tidewater glacier, using this method.

Unlike with terrestrially terminating glaciers, discharge cannot be measured at a gauging station. Instead, runoff, as determined by the WRF-CMB model, has been used as a measure of subaerial melt production. A good correlation exists between surface runoff and plume extent. This strengthens during the ablation season, indicating production and delivery become better connected.

As a glacerised basin, Kronebreen supports energy dominated meltwater production, rather than precipitation driven, as found in glacier-free catchments (Lang, 1986; Chen and Ohmura, 1990). Rainfall does not play a significant role in the transport of TSS to Kongsfjorden (Figure 5.2). The glacierised rather than non-glacierised catchment of Kronebreen maintains ice melt as the primary producer of meltwater which transports sediment during the ablation season (Hodgkins et al., 2009). Atmospheric temperature has been identified as the primary driving mechanism of freshwater production during the ablation season, with PDD responsible for 33% of plume size each year. This corroborates with Chu et al. (2012), who ascertained a good relationship between annual PDD and mean annual plume extent. Winter meteorological conditions play a significant role in determining TSS availability during the summer, as well as meltwater availability (Figure 5.15).

The following discussion focusses on the relationship between plume area with runoff and atmospheric temperature, and explores the evolution of meltwater and TSS discharge throughout the year from Kronebreen into the head of Kongsfjorden.

5.4.1 Seasonal evolution of meltwater production, storage and discharge during summer from Kronebreen

Stimulating surface melt, atmospheric temperature drives meltwater production during the ablation season, indicated by the positive correlation between plume area and PDD. The time at which plume formation responds to atmospheric temperature is variable during the ablation season (Figure 5.11), indicating that there are other elements of the glacial system controlling the travel time of meltwater. If the seasonal correlation between plume area and atmospheric temperature is used alone, the shorter term variability is masked out (Figure 5.11), making the correlation appear weaker than it is. This is same pattern as with the correlation between plume extent and surface runoff; the correlation of both temperature and surface runoff, increases during the melt season. Bartholomew et al. (2010) found that the same is true when analysing seasonal ablation rates with velocity of Greenland glaciers; seasonal correlations masked the variability within a season. Polythermal glaciers, such as Kronebreen, have typically cold ice surfaces which are largely impermeable, restricting the flow of surface melt to the basal regions (Hodgkins, 1997). This leads to intermediate-term storage of snow and water, which is a notable characteristic of polythermal glaciers (Jansson et al., 2003). Insights to the evolution of meltwater production, storage and transport at a seasonal scale for the Kronebreen - Kongsvegen system are discussed. The lag between plume area and glacial runoff and PDD indicates that the snow pack and glacial reservoirs serve as temporary storage locations for meltwater (Kjell, 1988; Vatne et al., 1996; Hodgkins, 2001; Hodson et al., 2005a).

Onset of the ablation season starts in June when atmospheric temperatures become positive (Hanssen-Bauer et al., 1990). The mean and minimum temperature during June holds most control over plume area (Figure 5.11). During this period temperatures are not yet constantly above zero (Figure 5.1), and minimum temperatures control surface melt. This is because ME can be both positive or negative while the mean temperature can fluctuate around zero. Meltwater can be refrozen within or at the base of the snow pack, forming layers of superimposed ice (Müller and Keeler, 1969; Wakahama et al., 1976). Interspersion of ice layers in the snow inhibits meltwater percolating through the glacier, leading to storage of early season snow melt at the surface in supraglacial ponds (Hodgkins, 1997). With low glacier cover of 0 – 7%, water can be stored for up to a month (Fountain and Walder, 1998). As the cover of exposed glacier increases, the storage time decreases. Early in the ablation season, 36% of Kongsvegen's surface is bare ice, and 35% superimposed ice (Obleitner and Lehning, 2004; König et al., 2002). Surface melt from Kronebreen - Kongsvegen takes approximately 4 – 9 days to reach

Kongsfjorden as a sediment plume, as determined by correlation with PDD and runoff. This is the mean of the maximum influence across June.

During July the correlation coefficient remains the same as June, but the lag time changes to 6 – 7 days between runoff, PDD and plume formation (Figure 5.11). This is indicative of continued water storage within the glacier system. Ground penetrating radar surveys of Stagnation Glacier, Canada, revealed noise in the surface from the storage of water, and a strong reflectance from the temperature ice below (Irvine-Fynn et al., 2006). Later in the season, there was less water storage present. Similar seasonal storage has been observed at Haut Glacier d'Arolla, Switzerland (Richards et al., 1996) and Mikkaglaciären, Sweden (Stenborg, 1970), in which discharge at each location occurred in the latter part of the season. The lagged response of plume formation, or a discharge upwelling, to the onset of glacier melt has been documented in at Austre Brøggerbreen and Midtre Lovénbreen, Svalbard (Irvine-Fynn et al., 2005; Hodson et al., 2005a) and at John Evans Glacier, Canada (Skidmore and Sharp, 1999), among others.

The rapid reduction in time lag from 7 days in July to 1 day in August indicates that the critical water pressure has been met, forcing the development of drainage by reopening englacial conduits or overcoming ice damming at the glacier margin (Bingham et al., 2005; Skidmore and Sharp, 1999; Wadham et al., 2001). The surface of Kronebreen is heavily crevassed, providing a means of rapid meltwater transport from surface to bed (Benn et al., 2009). Surface meltwater can pond in crevasses, which forms a hydrological driving mechanism propagating from the surface to the bed (Boon and Sharp, 2003; Bingham et al., 2005). The larger the surface melt accumulation, the greater the pressure acting upon the crevasse, which increases the likelihood of extension to the glacier bed (Van der Veen, 1998). Owing to the cold nature of non-temperate glaciers, refreezing of propagating meltwater can occur, obstructing drainage along fractures (Boon and Sharp, 2003).

The correlation coefficient between plume area and atmospheric temperature is highest in August (r = 0.7, p <0.05), indicating a stronger response to surface processes. This implies that flow is less restricted than in June and July, likely because the subglacial drainage has developed by this point. At Haut Glacier d'Arolla, channelised drainage systems develop during the ablation season, increasing hydraulic efficiency (Nienow et al., 1998). This decreases the residence time of meltwater as observed at Finterwalderbreen, Svalbard, by dissolved solute analysis over the duration of an ablation season (Wadham et al., 1998). The effect of cooling can be identified in the lag between atmospheric temperature and plume extent; in contrast to June, the highest correlation is with the minimum temperature (r = 0.6, p <0.05). ME is decreasing as $SW \downarrow$ and $LW \downarrow$ decrease, with the onset of the Polar night. However, September exhibits the highest correlation coefficient of the season between plume area and runoff (r = 0.82, $p < 0.05$), presenting with a 2 day lag. By this point in the season the subglacial system will be at its seasonal maximum, allowing for rapid transport of surface runoff through en/subglacial channels to be released into Kongsfjorden. Continued flow of meltwater to the glacier bed increases the subglacial water pressure, reduces friction and increases Kronebreen's sliding velocity (Kääb et al., 2005). These results reveal the seasonal change in drainage efficiency, but cannot illuminate drainage pathways as can be achieved with dye tracing experiments (Vatne et al., 1995).

By mid-October temperatures remain consistently below zero and darkness sets in (Hanssen-Bauer et al., 1990). As winter sets in, the hydrological regime is anticipated to become largely dormant as the subglacial drainage starts to freeze (Hodgkins et al., 2009). Englacial conduits can store water (Benn et al., 2009), the volume of which is dependent on the size of the channels and glacier, and the rate of hydrologic shut down after summer (Irvine-Fynn et al., 2011).

5.4.2 Controls on interannual variability of plume formation

Atmospheric temperature plays a significant role on meltwater delivery to Kongsfjorden. Years with higher PDD typically have the largest mean plume areas, placing this study in agreement with Chu et al. (2012). Increased energy from the atmosphere is driving meltwater production, leads to increased meltwater delivery in Kongsfjorden.

No significant increase in meltwater delivery with time has been found in this study; a longer temporal series would be needed to determine if there were longer term trends. The recent extensive melt patterns occurring in Greenland have not been mirrored in Svalbard. In 2010, Greenland underwent record temperatures during winter, spring and summer together with record surface melt (Box et al., 2010; Cappelen et al., 2011), while Svalbard displayed below average PDD and plume area (Table 5.3). Melt in Greenland started two weeks earlier than normal in 2012, setting new melt record (Box et al., 2012), while plume size in Kongsfjorden was again, below average.

Extensive Greenland melt has in part been attributed to the negative NAO, which brings mild, southerly airflows to the ice sheet (Hanna et al., 2012). However, under these conditions, the European sector is colder and typically receives less precipitation. This is reflected in the meteorological conditions imposed upon Svalbard. Both 2010 and 2012 exhibited below average plume area, snow depth and rainfall. Despite this, there was no significant relationship between either the

NAO or AO with plume area during the study period. However, other studies have found that indices of the NAO and AO for both the current and previous hydrological years can partly explain the length of accumulation and ablation, in addition to snow depth (Luks et al., 2011). A negative winter AO phase can in part be instigated by greater snow cover in the autumn, indicating that the relationship between the AO and snow is not simplistic (Cohen et al., 2012).

5.4.3 Winter controls on sediment availability and meltwater production

The controls of winter temperatures on the delivery of meltwater from the cryospheric hydrological system to the Kongsfjorden have been revealed by regression analysis of mean winter temperature (DJFM) and mean plume area. The winter temperature accounts for 36% of plume formation, and therefore meltwater delivery, during the following summer. For discharge to occur, there must be hydrologic pressure in the glacier. The retention of meltwater during the winter allows for a rapid regeneration of discharge in the following ablation season (Hodson et al., 2005a). Winter meltwater storage has also been identified at Scotts Turnerbreen glacier, Svalbard, in which ice marginal channel ice over, because the drainage cannot adjust to the end of season melt contributions (Hodgkins, 1997). There have been very few studies which address winter storage, and even less so in tidewater glaciers, yet it plays a crucial role in determining mass balance and glacier flow dynamics (Rennermalm et al., 2013). Cryospheric hydrological storage is deemed to be responsible for a large part of the uncertainties when predicting sea level rise from the Greenland ice sheet (Harper et al., 2012). As such, understanding the seasonal and interannual controls which determine meltwater delivery is imperative.

Winter storage, but also drainage, is apparent in the Greenland ice sheet, with meltwater delivery even during the cold season (Harper et al., 2012). Signals of such processes can now be discerned in Kronebreen. The coldest winters, 2009 and 2011, also had the greatest snow cover. Snow cover not only contributes to potential meltwater, but it also acts as an insulator. Therefore, a greater extent and depth of snow cover can increase the insulation provided to the glacier, reducing ablation (Boike et al., 2003). However, these results indicate that during colder winters, less meltwater can escape during the cold period, which leads to increased meltwater delivery in the following summer season. This is despite the increased snow depth. In contrast, milder winters do not have the capacity to retain so much meltwater, and subsequently it can be released during the cold months.

The winter freeze-up not only retains meltwater, but also traps basal sediment, increasing availability for the following summer. Up to 56% of summer sediment availability can be explained by winter temperatures, with higher TSS_{sum} after the coldest winters. This can have implications for primary productivity and the marine ecosystem (Hop et al., 2002). The phenomenon of melt storage has previously been observable in ice cores (Harper et al., 2012) and river discharge data (Rennermalm et al., 2013). This study highlights that these retention processes take place in fast flowing tidewater glaciers, as well as terrestrially terminating. It is also novel to be able to detect these signals using plume size, determined from remotely sensed data, giving further value to such plume detection studies.

5.5 Conclusions

As meltwater production increases in a warming climate (IPCC, 2013), more is expected to reach the subglacial environment which leads to increased glacier velocities (Kääb et al., 2005). As such, studies of englacial routing of have become increasingly important (Parizek and Alley, 2004). This chapter has presented the added value to which sediment plume studies hold. It is the first study to have revealed the seasonal evolution of tidewater glacier meltwater production, storage and delivery using remotely sensed data. Valuable information about tidewater glacier hydrology can be drawn from these results. In addition, these methods offers a novel way to detect winter storage of meltwater, which has been at the focus of recent studies (Harper et al., 2012).

Plume extent is representative of surface meltwater runoff production, as determined by correlation with results from the WRF - CMB model. Meltwater production at Kronebreen - Kongsvegen is produced by atmospheric temperature driving glacial ablation. June and July are characterised by plume formation in Kongsfjorden, 6 – 10 days after surface runoff. This decreases to 1 – 2 days during August and September. The same pattern occurred between surface runoff and plume extent. These time lags highlight the meltwater storage in the early part of the season, likely in part by retention in firn (Christianson et al., 2015). Saturation of firn and the evolution of subglacial drainage reduces storage, driving an efficient flow of meltwater through the englacial system. The response of plume area to PDD and runoff is almost twice as great in August and September, compared to June and July, supporting the notion of increased glacier efficiency throughout the ablation season.

With only 12 years of data from this study, it is difficult to determine the factors controlling plume size beyond interannual, since interdecadal patterns cannot be discerned. Whilst other studies have highlighted the effects of the NAO and AO on snowpack in Svalbard (Luks et al., 2011; Cohen et al., 2012), further investigation is required to see if they do impact plume size, and therefore meltwater delivery to Kongsfjorden.

This chapter has presented the drivers of meltwater production and seasonal storage at Kronebreen - Kongsvegen. However, if suspended sediment is to be used as a proxy for meltwater delivery, it is critical to understand the other factors than can effect plume size and the concentration of TSS once in Kongsfjorden. Effects of wind and tide have been observed to alter plume size in other locations (Castaing and Allen, 1981). As such, analysis to determine if and how wind and tides effect sediment plume size in Kongsfjorden are presented in Chapter 6.

Chapter 6

Spatial distribution of total suspended solids at the head of Kongsfjorden

6.1 Introduction

Throughout the summer months the head of Kongsfjorden is supplied with sediment from Kronebreen and Kongsvegen. Entering at the grounding line it rises in a buoyant plume, and spreads laterally across the surface of the fjord (Chapter 4). Plume extent has been successfully used as a proxy for meltwater discharge from Kronebreen. However, to ensure the plume size is representative of meltwater discharge, considerations must be paid to the effects of external forcing factors, such as winds and tides.

Using *in situ* measurements of TSS and particle size this, the spatial variability in surface sediment plume characteristics is assessed. To complement this, the temporally and spatially high resolution results of TSS from Chapter 4, together with daily wind speed and direction, and tide height, have enabled external forcing factors on plume size to be characterised. This chapter presents analysis on the spatial distribution of TSS, which has addressed the following questions:

i What is the concentration and size of the particles through the sediment plume?

ii Does wind speed and direction alter the extent of sediment plumes?

iii What role do tidal currents play in the distribution of TSS?

Tidewater glaciers lose mass through iceberg calving, which is reduced in the presence of shallower water depths because glacier buoyancy and thinning rates at the glacier terminus are reduced (Benn et al., 2007). High sedimentation rates at the glacier terminus can act to stabilise the glacier by reducing the water depth in front of the ice face. However, this is only the case if the terminus is in relative stability (Dowdeswell et al., 2015). Glacimarine sedimentation can also protect the glacier terminus from submarine melting (Powell, 1991). Whilst submarine melt has been a significant factor in the retreat of tidewater glaciers in Greenland (e.g. Rignot et al., 2010; Mortensen et al., 2011; Straneo et al., 2013) and Antarctica (Holland et al., 2008), only a small proportion of freshwater entering Kongsfjorden is from direct submarine melting of the glacier terminus (Chapter 3).

Changes in sediment plume area have been used to reveal the seasonal and interannual variability of freshwater inputs to Kongsfjorden (Chapter 4). However, suspended sediment plumes are not only controlled by meltwater inputs (Dowdeswell and Cromack, 1991), but also external forces such as wind and tidal currents (Castaing and Allen, 1981). Wind forcing can move well stratified plumes within the fjord, causing elongation or degradation (Buckley and Pond, 1976; Stumpf et al., 1993). The state of the tide, either flood or ebb, can impact the size of buoyant plumes: large plume area coincides with flood tides, and the smallest plume area is found at low tide (Dowdeswell and Cromack, 1991). In addition to the size of the plume, the tidal height (Castaing and Allen, 1981) and amplitude (Szczucinski and Zajaczkowski, 2012) can dictate how much sediment remains in suspension.

The fjord floor bathymetry is altered by the glacimarine sedimentation process; the relative water depth closest to the glacier terminus shallows with increased deposition (Powell, 1991). Near terminus sedimentation rates at the head of Kongsfjorden have previously been quantified by *in situ* sampling utilising sediment traps and bathymetric mapping (Trusel et al., 2010; Kehrl et al., 2011). Larger sediment grains typically fall out of suspension soon after being discharged, leaving a pattern of fining with distance from source (Dowdeswell and Cromack, 1991; Elverhøi et al., 1983). Therefore, understanding the spatial distribution and size of sediment particles, can provide further insights to glacimarine processes in the ice proximal zone of Kronebreen.

Freshwater inputs and light limitation from sediment load are limiting factors for phytoplankton in Kongsfjorden (Cui et al., 2006), providing further motivation to understand the spatial distribution of surface sediments. The diversity and composition of surface microbial communities are likely to change with the freshening of Arctic fjords (Piquet et al., 2010). During melt events, photosynthetic activity close to Kongsfjorden is reduced, as indicated by lower chlorophyll a concentrations, despite increased nutrient contributions (Cui et al., 2006). Strong winds, despite increasing vertical mixing can rapidly decrease surface phytoplankton biomass, contrasting lighter wind events which promote higher plankton biomass (Andersen and Prieur, 2000).

The premise for better understanding of sediment supply and deposition in Kongsfjorden is twofold: 1) increased sediment can act to stabilise or destabilise the calving front of Kronebreen and 2) freshwater, sediment and wind can all act to change phytoplankton communities and abundance, having a direct impact on the marine food web. While using sediment plume size as a proxy for meltwater discharge, it is important to determine the external forcing factors on plume size, as well as the consequences of the sediment load.

6.2 Methodology

6.2.1 *In situ* total suspended solid distribution and particle sizing

In situ TSS samples were taken from the head of Kongsfjorden as described in Chapter 4. Since the samples had been filtered, the sediment had to be returned to suspension for particle sizing analysis. The filter papers were placed in a beaker of deionised water in a sonic bath. When as much sediment as possible was removed from the filter papers, they were disposed of. The TSS samples were stored in plastic vials whilst they waited to be processed. Before processing, each sample was returned to the sonic bath for 15 minutes to break up the flocculated particles which formed during storage. Using a micro volume module, the samples were sized using a Beckman Coulter laser particle scanner. A one minute run time and six repeats was used for each sample. The mean of the six repeats has been used in this analysis.

6.2.2 Influence of the tide

The tidal amplitude outside of Kongsfjorden is 0.5 m, which propagates through the fjord as a Kelvin wave. This induces a semi-diurnal force upon the water masses in Kongsfjorden (Svendsen et al., 2002). Over the fortnightly spring-neap period, tidal amplitude varies between 1.5 – 2.0 m, with weak currents (Bluhm et al., 2001). During the flood tide, an intrusion of dense, coastal water enters Kongsfjorden, whilst an ebb tides sees this intrusion return to the shelf seas (Perkin and Lewis, 1978).

To determine the extent to which tides effect the sediment plumes in Kongsfjorden, two factors must be known: 1) the time of MODIS image acquisition, and 2) whether the tide was in an ebb or flood state at the time of image acquisition.

Using the frequency at which plumes of a particular size form, under which tidal state, will determine the influence of tides on plume extent.

Satellite overpass times were sourced from NASA's overpass prediction service (NASA, 2014b). This provides the time at which the satellite, either Terra or Aqua, passed over a particular latitude and longitude. Due to the high latitude of Kongsfjorden, the satellites pass over this location multiple times a day. Therefore, the images acquired were compared with the original swath images (NASA, 2014a). Image acquisition times have been obtained for Terra images from 2007 – 2013. When there have been multiple raw images, occasionally none of them could be exactly matched with the MOD09GQ plate, the image has been discarded from tide analysis. This is to ensure that all acquisition times used are as accurate as possible.

The height and state of the tide is measured and recorded at a tidal gauge at Ny-Ålesund. The observed tidal height data are available in 10 and 60 minute intervals from Vannstand (2014). In this study, ten minute data have been used; positive values denote a flood tide and negative values an ebb tide. The slack period of the tide has been identified by periods of small changes in tidal height; heights which change less than 2 cm in between the 10 minute samples has been classified as slack. Numerical indicators have been applied to the tidal state: flood = 1, ebb = -1 and slack = 0 (Figure 6.1). Both the tidal height and state were associated with the acquisition time of each MODIS image (NASA, 2014b), using the 10 minute data.

6.2.3 Wind speed and direction

Daily mean wind speed and direction have been sourced from the automatic weather station at Ny-Ålesund. These can be obtained from eKlima (2014). The weather station is located 14 km to the southwest of Kronebreen.

6.3 Results

6.3.1 *In situ* total suspended solids characteristics and spatial distribution

Total suspended solids spatial distribution

In situ measurements of TSS through the surface meltwater plume reveal a decrease in TSS with increasing distance from the ice front (Figure 6.2). The highest TSS is found closest to Kronebreen at the historical site of submarine discharge (1987 – 2001) (Trusel et al., 2010), and decreases with distance down Kongsfjorden.

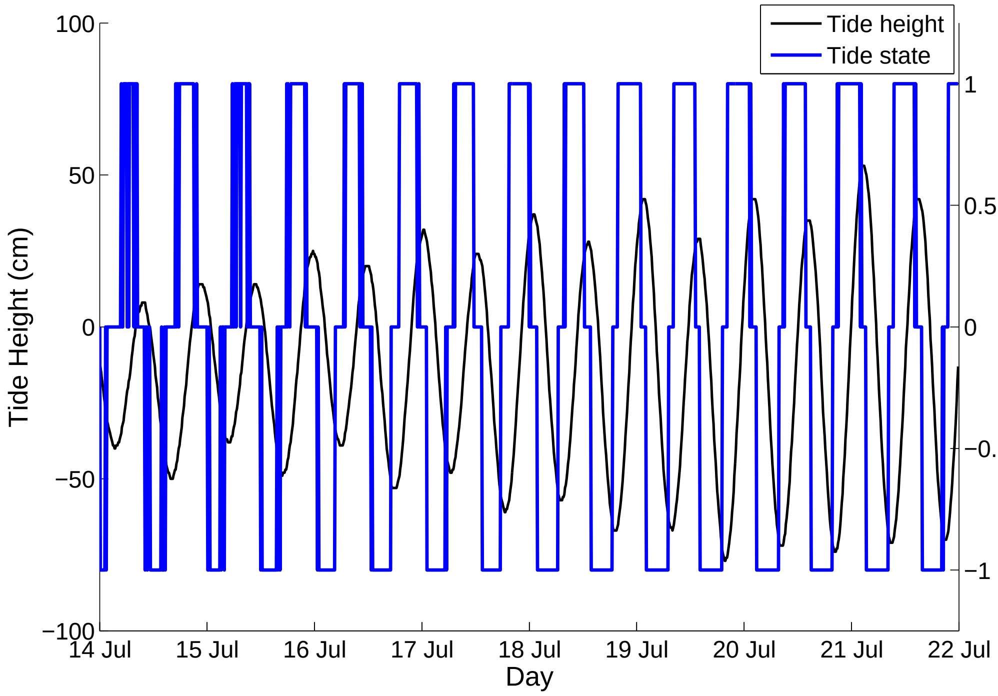

Figure 6.1: Example of semi-diurnal tidal height (cm; black) and tidal state (blue; flood = 1, ebb = 2, slack = 0) from 14th July to 21st July 2012. Tide data obtained from Vannstand (2014).

Due to large amounts of bergy bits in front of the modern location of submarine discharge, no TSS samples were taken at this location. High TSS is also found at the Kongsvegen upwelling located at the southern extent of the section (Figure 6.2).

The section across the ice front reveals variable TSS in front of Kronebreen (Figure 6.3). The lowest TSS, 0.11 g l^{-1} was located at the northernmost extent. TSS increases to 0.23 g l^{-1}, located 1.45 km south from the fist sampling station, in the centre of the transect. Continuing south along the transect, TSS declines up to a distance of 2 km. TSS increases to a maximum of 0.27 g l^{-1}, located at the southern most extent, 2.7 km along the transect. This is indicative of meltwater entering from the Kongsvegen upwelling, a second source of meltwater from the glacier system entering at the head of Kongsfjorden. With this variability of TSS along the ice face, there is no statistical significance between TSS and distance from the initial sampling station (one-sample t(5) = -9.06, p <2.02, at the 0.05 significance level).

In contrast, a more definitive pattern of TSS decline is observable through out the plume. The maximum of 0.27 g l^{-1} was located closest to the ice front, at 0 km on the section, decreasing to 0.14 g l^{-1} at 0.5 km away. This rate of decline is not sustained, as TSS only decreases 0.03 g l^{-1} from 0.5 – 2 km distance. Beyond 2 km the measured TSS is only 20% of that closest to the ice face, measuring 0.06 g l^{-1} (Figure 6.3). Repeat measurements at 1.25 km distance reveal a ± 0.04 g l^{-1} difference from the mean from over the 3 days of sampling. The reduction of TSS with distance from the ice face is statistically significant at the 0.05 significance level (one-sample $t(5) = 1.89$, $p < 3.83$).

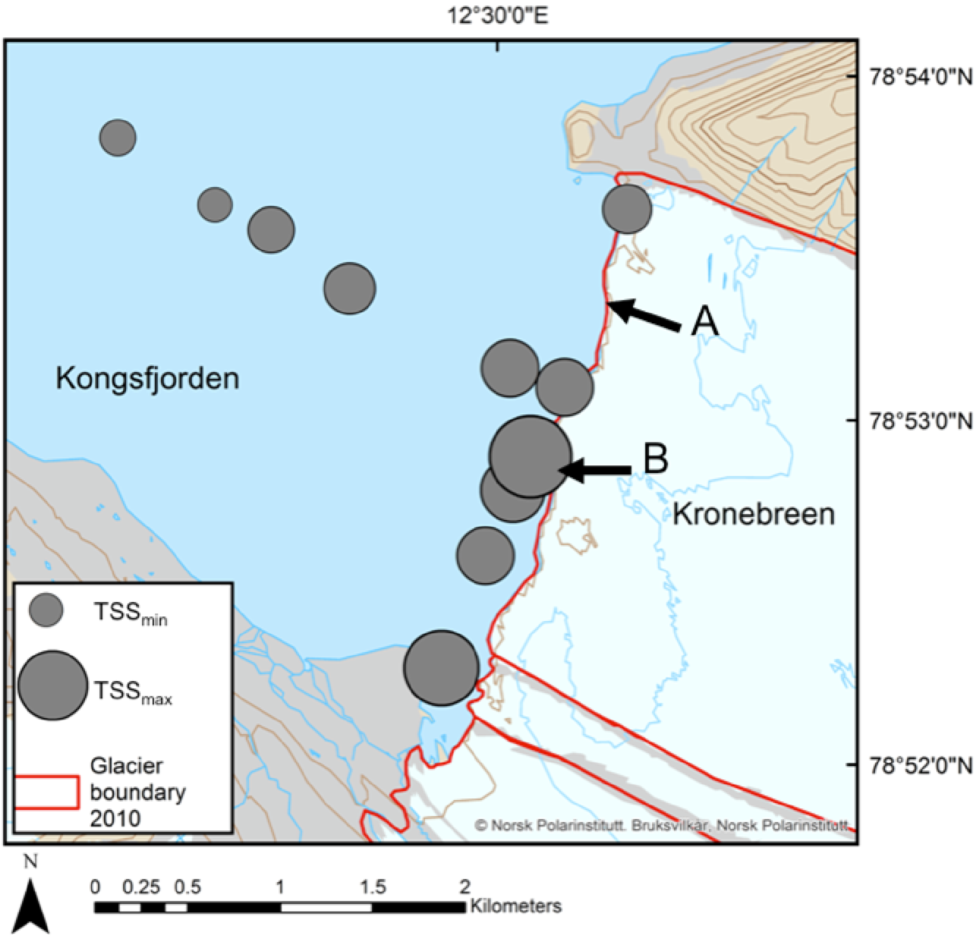

Figure 6.2: *In situ* measurements of TSS along Kronebreen's ice front and through the sediment plume extending down fjord. Symbols are proportionate to the weight of TSS, where TSS ranges between: $TSS_{min} = 0.05$ g l^{-1} and $TSS_{max} = 0.21$ g l^{-1}. Arrows denote current and historical upwelling zones as defined by Trusel et al. (2010): (A) modern submarine discharge and location of upwelling from Kronebreen (B) historical submarine discharge site from 1987 – 2001.

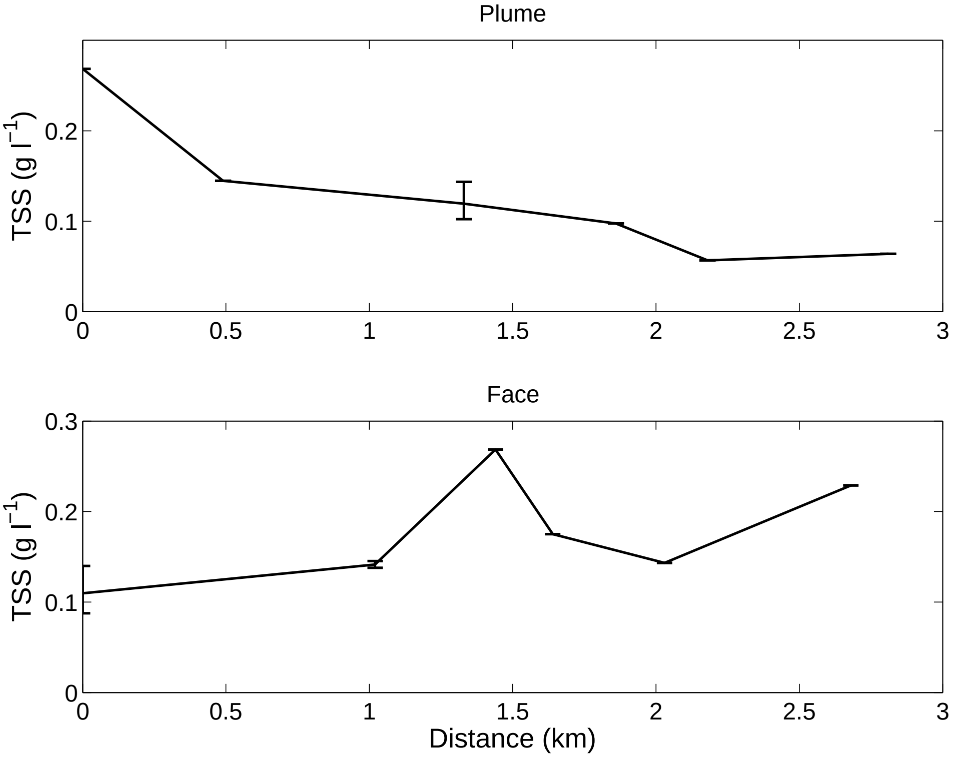

Figure 6.3: TSS declines with distance from the glacier, through the plume (0 km closest to Kronebreen; top) and is variable in front of the ice face (0 km is at the north of Kronebreen, with a transect south; bottom).

Particle size

The particle size of the sediment samples indicates a dominance of silt material, <63 μm (Wentworth, 1922). Mean particle size ranges from 8.66 μm to 24.69 μ m through the plume extending away from Kronebreen (Figure 6.4). The transect parallel to the ice front displays particle sizes ranging from 8.86 – 15.62 μm. In contrast to TSS there is no significant fining of sediment with distance from the ice face (one-sample t(6) = -7.25, p >0.05, at the 0.05 significance level. This applies to the samples across the ice front, one-sample t(5) = -7.17, p >0.05, at the 0.05 significance level (Figure 6.5).

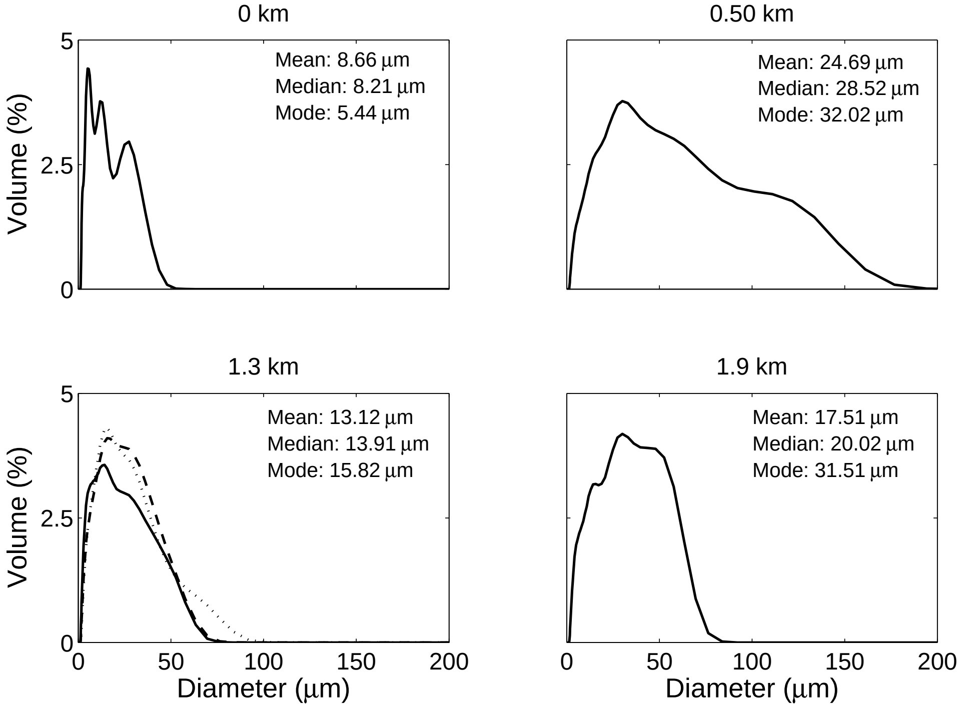

Figure 6.4: Particle size of surface suspended sediments through the plume, from point closest to Kronebreen (0 km) out to a distance of 1.9 km.

6.3.2 Tidal influence on plume formation

Results from Chapter 3 indicate that the state of the tide effects the surface waters. To determine if tidal currents play a role in determining the size of plumes, tidal gauge data has been analysed with plume area and TSS concentration results from Chapter 4.

The largest plume areas (mean 15.9 km^2) were found to form under the influence of a flood tide (Figure 6.6). In contrast, smaller plume areas (mean 10.8 km^2) were found during ebb tides (Table 6.1). There was little change in TSS$_{mean}$

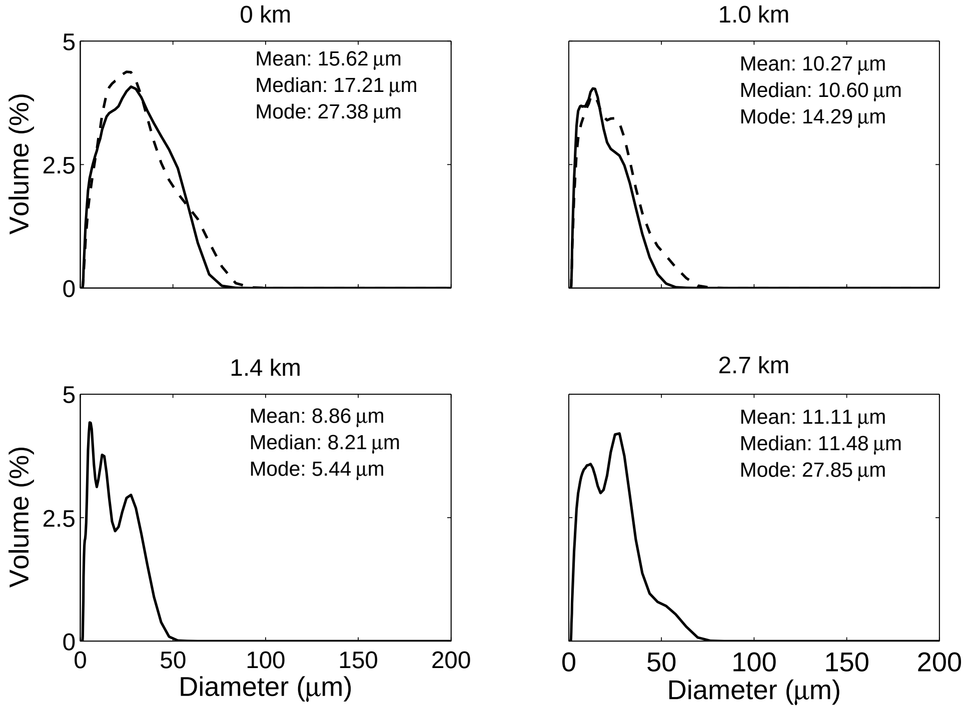

Figure 6.5: Particle size of surface suspended sediments in front of Kronebreen's calving face, starting at 0 km in the north, to 2.7 km south towards Kongsvegen glacier.

Tide state	Numerical indicator	Mean Plume area (km^2)	TSS$_{sum}$	n
Flood	1	15.9	22.3	32
Ebb	-1	10.8	16.24	24
Slack	0	12.5	18.6	47

Table 6.1: Mean plume area and TSS$_{sum}$ under the influence of flood, ebb and slack tides.

however, TSS_{sum} was higher during flood tides than ebb. One tailed t-tests have revealed a significant relationship between plume size and tide height: t(102) = 9.04, p <0.05. TSS_{sum} is also significantly related to the tide height: t(102) = 10.7, p <0.05.

6.3.3 Wind speed and direction

The wind direction in Kongsfjorden is predominantly northwest or southeast, with winds being channelled along the fjord axis (Figure 6.7). Kongsfjorden is subjected to persistent katabatic winds throughout the year, with varying strength. The most dominant wind direction is south-easterly, channelled down fjord driven by mechanical wind channelling from topographic features, and the thermally driven land-sea breeze (Esau and Repina, 2012). The second most dominant wind direction is northwesterly, channelled up fjord (Svendsen et al., 2002). The fastest wind speeds occur down fjord, forced by katabatic winds and are most dominant in the winter months (Esau and Repina, 2012).

Over the 12 year period, the winter (October, November, December, January; ONDJ) displayed the fastest mean wind speed of 4.6 m s^{-1}, followed by spring (February, March, April, May; FMAM) at 4.1 m s^{-1}. Summer (JJAS) displayed the slowest mean wind speed, 2.9 m s^{-1}. The overall maximum wind speed of 25.4 m s^{-1} occurred during summer. Maximum wind speeds for winter and spring were 19.5 and 17.7 m s^{-1}, respectively.

Although wind direction is variable throughout the year (Figure 6.7) there is little seasonal difference. South-easterlies dominate, with mean wind directions for spring, summer, and winter as 158, 161 and 163°, respectively. The overall mean wind direction from 2002 – 2013 was 161°. This indicative of wind being funnelled either up or down fjord.

For days of successful MODIS image retrieval, wind speeds averaged 2.8 m s^{-1}, with a maximum speed of 8.8 m s^{-1}. The mean wind direction was 149° indicating the dominance of south south-easterly winds. Division by quadrants, using the mean wind direction as the mid-point of one of these, reveals that detection of sediment plumes is infrequent under up fjord winds. Only 6% of plumes detected were formed under north-westerly winds (285 – 14°), whilst 50% were formed under south-easterly wind conditions (105 – 194°) (Table 6.2). Plume length is greater between 14 – 104° and 105 – 194°, 5.9 and 5.4 km, respectively. The same is true for plume area (Table 6.2). Wind direction plays a significant role in determining plume length, in which longer plumes are formed under south-easterly winds, as indicated by a one-tailed t-test: $t(231) = 35.0$, p <0.05.

Plume length is typically longer with faster wind speeds (Table 6.3). Mean

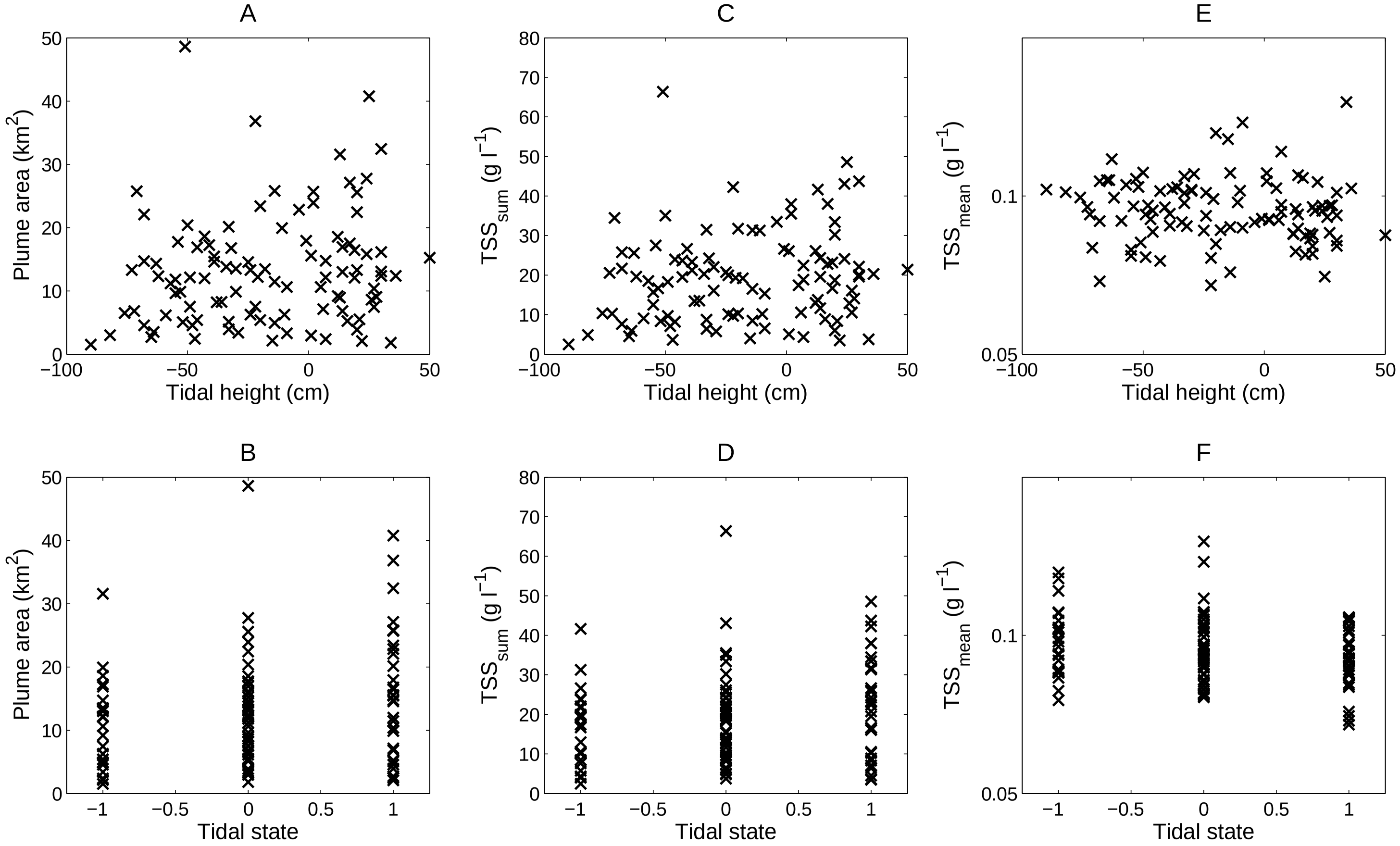

Figure 6.6: Plume area (A), TSS$_{sum}$ (C) and TSS$_{mean}$ (E) with respect to tidal height (cm). Plume area (A), TSS$_{sum}$ (B) and TSS$_{mean}$ (C) as a function of tide state (B, D, E).

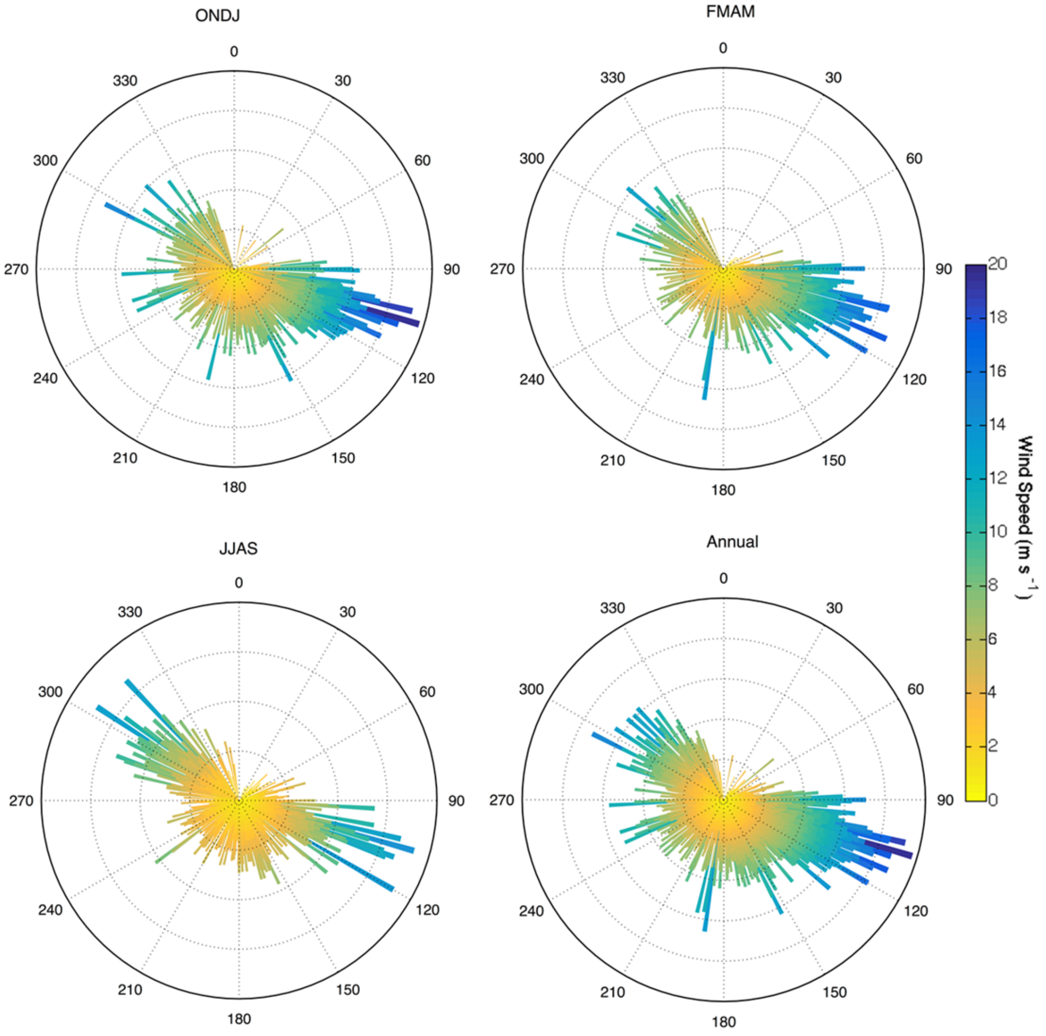

Figure 6.7: Seasonal and annual wind speed and direction measured at Ny-Ålesund research station, from 2002 – 2013.

Quad	Wind direction (°)	Plume length (km)			Plume area (km^2)			n
		mean	max	min	mean	max	min	
1	15 – 104	5.9	12.6	1.8	16.8	55.5	4.6	51
2	105 – 194	5.4	13.7	0.3	15.2	52.3	1.8	115
3	195 – 284	4.5	11.9	0.3	11.4	35.1	0.9	52
4	285 – 14	3.6	8.7	1.6	7.8	20.1	2.0	13

Table 6.2: Influence of wind direction (°) on mean wind speed (m s^{-1}), mean plume length (km) and mean plume area (km^2).

plume length on days with wind speeds <2 m s^{-1} was 4.4 km, increasing to 6.9 km when winds were >6 m s^{-1}. The relationship between wind speed and plume length is significant, with longer plumes formed under faster wind speeds, as indicated by a one-tailed t-test: $t(231) = 12.2$, $p < 0.05$. The minimum plume length was 0.3 km when winds were <4 m s^{-1}. Once >4 m s^{-1}, the minimum plume length increased to 1.6 km. Plume area did not display these characteristics however, the smallest minimum plume area was formed under winds <2 m s^{-1}, while the largest minimum plume area was formed when winds were >6 m s^{-1} (Table 6.3). The effect of wind speed and direction is depicted in Figure 6.8. Note that the bars depicting wind direction have been reversed, so that the length of bar representing sediment plume length is orientated down fjord.

Wind speed (m s^{-1})	Plume length (km)			Plume area (km^2)			n
	mean	max	min	mean	max	min	
0 – 2.0	4.4	11.8	0.3	11.5	32.1	0.9	92
2.1 – 4.0	5.2	13.5	0.3	14.2	52.8	2.4	94
4.1 – 6.0	6.6	12.7	1.6	19.9	55.5	2.0	31
>6.0	6.9	13.7	1.6	21.5	48.6	3.0	14

Table 6.3: Influence of wind speed (m s^{-1}) on mean, minimum and maximum plume length (km) and mean, maximum and minimum plume area (km^2).

6.4 Discussion

6.4.1 Spatial distribution of total suspended solids

In situ measurements taken in July 2012 reveal a significant decrease in TSS with distance away from Kronebreen (Figure 6.2). This is a common observation of *in situ* sediment plume characteristics (Syvitski, 1989; Cowan and Powell, 1991). This implies that sedimentation is greater closer to the ice front leading to accumulation and shallower water depths, as seen in the CTD profiles (Figure 3.8). The reported rates of sedimentation at the ice front is variable; Elverhøi et al. (1980) report rates of >0.10 m a^{-1}, Trusel et al. (2010) of >0.06 m a^{-1} (within 500 m of the point of meltwater delivery) and the greatest sedimentation rate of 1.0 m a^{-1} from Kehrl et al. (2011). Sedimentation results in raised grounding line fans are found to be present at each of locations A and B, with A still being built and B eroded away (Kehrl et al., 2011).

Surface TSS declined with distance whilst water depth increased; the majority of sedimentation appears to take place within 500 m of the transect, approximately 800 m from the ice front of Kronebreen (Figure 6.3). Zajaczkowski (2008) detailed

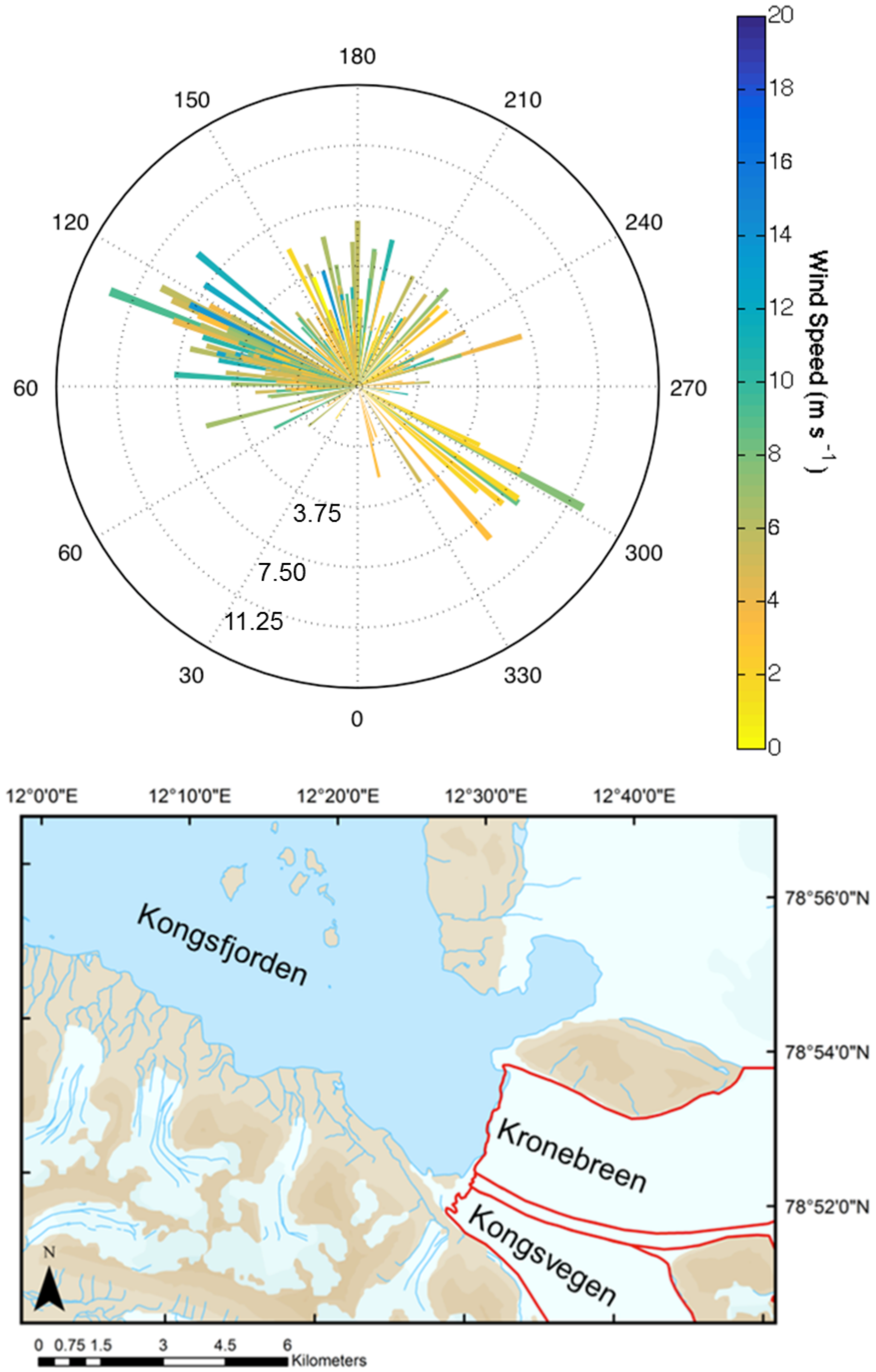

Figure 6.8: Distribution of plume length (length of bar) with wind speed (colour of bar) and reversed direction (orientation of bar). Wind direction reversed to highlight plume formation down fjord. The map of the study area is for reference.

a three stage sedimentation regime in front of Kronebreen: high, constant TSS concentrations from 0 – 1 km, decreasing surface TSS from 1 – 3 km, and a low, constant TSS concentrations from 3 – 7 km. The *in situ* measurements of TSS presented in this study fit within the regime of Zajaczkowski (2008). Unfortunately no *in situ* measurements were taken beyond 3 km from Kronebreen.

Across the ice front TSS is greatest in the centre, 1.5 km along the transect. It is anticipated that this is the point closest to the source of sediment supply (Cowan and Powell, 1990). However, the maximum TSS at the ice front coincides with the historical location of submarine discharge and upwelling, rather than the modern location as identified by Trusel et al. (2010). The location of upwelling from 1987 – 2001 was at site B. It moved in 2002 where it is believed to have remained stable since (Trusel et al., 2010; Kehrl et al., 2011). Bergy bits restricted sampling in the modern upwelling zone. Therefore, it is not possible to determine the exact location of entry of submarine meltwater delivery from these *in situ* TSS measurements alone. High TSS was also present at the southernmost extent, near the Kongsvegen outflow.

The contribution of sediment from tidewater glaciers to glacial fjords plays an important role on stabilising the glacier front (Meier and Post, 1987). If sedimentation is high near the glacier terminus, a grounding line fan can form. This is reliant on the marine terminus remaining stable; large periods of retreat will cause the sediment to be spread over a wider area, and will not be able to build up much vertical height (Dowdeswell et al., 2015). Grounding line fans can protect parts of the glacier from submarine melt, in addition to enabling advance of the glacier terminus (Powell and Alley, 1997; Alley et al., 2007). It has been estimated that a grounding line fan could emerge at the surface of Kongsfjorden, in front of Kronebreen within two decades, should the glacier terminus remain stable (Trusel et al., 2010). However, with the large retreat of 2013 (Figure 1.7), using this method of remote sensing of TSS, offers a mean to monitor both sediment discharge, and the rate of retreat of the glacier front.

Despite the expectation of coarser particles settling faster due to lateral mixing between the plume and surface waters causing deceleration in the plume (McClimans, 1978), particle size in Kongsfjorden did not show any significant relationship between size and proximity to the source. This contrasts other studies which have revealed a fining of sediments with increased distance down fjord (e.g. Dowdeswell and Cromack, 1991; Elverhøi et al., 1983). However, these results of fining have been determined from core samples, which was not possible in this study. To make a valid comparison of methods, more surface samples are required, and a faster analysis of them would be preferential.

The temporal and spatial variability of TSS has been quantified by calibrating

MODIS band 1 satellite images with *in situ* TSS and spectral reflectance, which is a beneficial advance on *in situ* measurements alone (Dowdeswell and Cromack, 1991). It is assumed that all TSS has originated from the submarine plume from Kronebreen since there has been no transport through streams for mixing of sediments to take place (Gurnell, 1982). However, sediment is also transported into Kongsfjorden by icebergs (Dowdeswell and Dowdeswell, 1989), which has not been considered here. The highest TSS concentrations are always closest to Kronebreen and decrease with distance as per the *in situ* measurements. High TSS reduces light availability for primary productivity in Kongsfjorden (Cui et al., 2006). Enhanced TSS supply and plume extent will increase the area of the fjord surface that inhibits light; as a result ecosystems will have to adapt, and marine diversity may decrease as a response (Lydersen et al., 2014).

6.4.2 Tidal influence on sedimentation

The relationship between tidal height and both plume size and TSS_{sum} is significant. Previous studies have revealed two controls that tides exert on buoyant sediment plumes: i) by affecting the rate of sedimentation and ii) by damming freshwater against the ice face during flood tides reducing the area of the sediment plume (Cowan and Powell, 1990). During flood tides turbidity is high and the velocity of surface water increases as the thickness decreases, maintaining sediment in suspension. During ebb tides surface plume velocity decreases with the thickening of the surface waters. This decrease in turbidity releases sediment from suspension, decreasing the amount detectable at the surface. This corroborates with findings from McBride Inlet, Alaska, in which flood tides were found to keep fine grained material in suspension due to the high current velocities (Cowan and Powell, 1990). Vertical settling of particulate matter is expected during the slack tides as a result of reduced current velocities, with deposition of both fine and course material at low tide (Ó Cofaigh and Dowdeswell, 2001). The majority of sedimentation occurs within 5 km of Kronebreen's ice front, with sedimentation further down fjord being reliant on redeposition and resuspension (Zajaczkowski, 2008). Previously, semi-diurnal sedimentation patterns have been determined by sediment traps and cores in Arctic fjords (Cowan and Powell, 1990; Hill et al., 1998; Ó Cofaigh and Dowdeswell, 2001; Zajaczkowski, 2008).

Sediment remains in suspension for longer during spring tides, whereas rapid deposition takes place during neap tides (Szczucinski and Zajaczkowski, 2012). Sediment trap experiments have found that the highest measured sedimentation fluxes are found in the traps closest to the sea floor (Szczucinski and Zajaczkowski, 2012) which has been attributed to bottom resuspension of sediments (Wassmann et al., 1996; Zajaczkowski, 2002).

6.4.3 Wind forcing on sediment plumes

Arctic fjords differ to estuarine and coastal environments by having steep walls and a relatively narrow channel, exhibiting comparably different flow regimes for both wind and ocean currents (Cushman-Roisin et al., 1994). Kongsfjorden's wind flow is modulated by mechanical wind channelling from topographic features and the thermally driven land-sea breeze originating from Kronebreen (Esau and Repina, 2012). The mean wind direction on days with detectable plume formation was 149°, which supports down fjord wind channelling. These south south-easterly winds increase the size of sediment plumes down Kongsfjorden. Up fjord winds reduce plume size by pushing the surface water towards Kronebreen, instigating downwelling and mixing of surface water deeper into the water column (Table 6.2). Wind speed also plays a role in determining plume size, significant at the 0.05 level as indicated by a one-tailed t-test. Faster winds channelled down Kongsfjorden push surface waters further away from Kronebreen, initiating upwelling of cold, deep water to the fjord surface. As the surface plume spreads it thins and wind mixing reduces its overall buoyancy (Whitney and Garvine, 2005). When wind speeds are >4 m s^{-1} the minimum plume length increases from 0.3 km to 1.6 km. This could imply a point at which wind driven flow takes over from buoyancy driven flow as has been found in the Delaware Coastal Current (Whitney and Garvine, 2005).

6.5 Conclusions

The size of sediment plumes found at the head of Kongsfjorden provide a metric for quantifying freshwater contributions from Kronebreen (Chapter 5). However this chapter has revealed that plume size is not only dictated by freshwater availability, but is also significantly impacted by wind and tide forcing. These are important findings, which must be considered when using sediment plume area as a proxy for meltwater discharge. As such, the methods employed in this study have enabled the glacimarine sedimentation regime at the head of Kongsfjorden to be assessed over several years, which has previously not been achieved.

TSS declined significantly with distance away from Kronebreen, with the greatest sedimentation occurring at the glacier terminus. Across Kronebreen's ice front TSS was greatest at points of submarine discharge, building grounding line fans. There was no significant change in particle size throughout the sections, despite this having been observed in other Arctic fjord environments (Dowdeswell and

Cromack, 1991; Elverhøi et al., 1983).

South south-easterly winds prevailed, which increased the length of sediment plumes down fjord. Up fjord winds dammed sediment plumes in front of Kronebreen, resulting in smaller plume size. Plumes were also extended under faster wind speeds, causing spreading and thinning of the surface layer across the fjord. Minimum plume length increased from 0.3 to 1.6 km under wind speeds >4 m s^{-1}. This indicates a possible threshold in which wind forcing overrides buoyancy forcing.

Flood tides maintain sediment in suspension, as displayed by larger plume areas and higher TSS_{sum} than during ebb tides. Smaller plume areas and lower TSS_{sum} are a significant indicator of sedimentation taking place during ebb tides when turbulence is low. This study has not found a direct correlation between the height of the tide and plume size, despite height of tide. Damming of plumes against Kronebreen's ice front has not been apparent in flood tides.

Winds and tides play a significant role on modulating the suspension of sediments in surface waters. However, this study has not been able to draw a direct correlation between winds and tide on plume size. In order to fully establish this relationship, more images of the plume extent are required. This could be achieved using a time lapse camera, together with data from a weather stations on Kronebreen, or closer to the terminus than the station at Ny-Ålesund. Such additional work to determine the thickness and velocity of the surface plume under different wind speeds and tide conditions would be beneficial. The impacts of wind and tides on the water column in Kongsfjorden, and subsequent drivers behind changes in primary productivity, would be better understood.

Chapter 7

Synthesis

This thesis illustrates that meltwater discharge from tidewater glaciers can be monitored by remote detection of sediment plumes. This is the first comprehensive study of discharge variability from daily to interannual timescales. The combination of *in situ* hydrographic measurements, TSS and spectral reflectance, together with remotely sensed imagery, has provided key findings regarding ice - ocean interactions, and the circulation processes taking place at the head of Kongsfjorden. Thus study has furthered the understanding of tidewater glacier hydrology, addressing the some of the uncertainties which surround meltwater export from marine terminating glaciers, as presented by Chu (2014).

This chapter provides a synthesis of discussions and conclusions from earlier chapters, placing this study contextually with the wider literature. An overview of the research aims that were presented in Section 1.3, together with how each has been addressed is detailed in Section 7.1. A holistic review of meltwater production, storage and delivery is presented in Section 7.2, and potential avenues for future research are explored in Section 7.4. The concluding remarks are presented in Section 7.5.

7.1 Realisation of research aims

Each chapter has addressed one of the four primary aims of this thesis as detailed in Section 1.3. Here a brief synthesis is provided, describing how each was achieved.

In Chapter 3, temperature and salinity profiles were used to separate the freshwater fractions, SgFW and GiFW, from ambient water (Figure 3.3). A water mass mixing model drew upon differing potential temperatures of each freshwater source, revealing SgFW as the dominant freshwater source at the head of Kongsfjorden. The volume of freshwater from the tidewater glacier, Kronebreen, was determined by using geostrophic current velocities. This provided an estimation of freshwater volume which was comparable to other oceanographic studies as well as runoff data from the WRF-CMB model. It also illustrated the two layer circulation, with a strong outflow of SW, and an inflow of AW at depth (Figure 3.15).

Chapter 4 utilised spot, *in situ* measurements, of TSS and spectral reflectance to calibrate MODIS band 1 spectral reflectance. This was possible for 234 cloud free images during the ablation season (June - September), from 2002 – 2013. This allowed the area of buoyant sediment plumes, emerging from Kronebreen's grounding line, to be quantified, providing a measure of discharge (Figure 4.11). The seasonal development of meltwater and TSS delivery to Kongsfjorden from Kronebreen has been revealed, in addition to the interannual variability. Small plume area and high TSS_{mean} dominates the early season, followed by large plume areas in the middle of the ablation season with comparatively less TSS_{mean} (Figure 4.13). The end of the ablation season presents smaller, but variable plumes with TSS_{mean} remaining the same as the mid-season.

Plume extent was found to be responsive to changes in subaerial meltwater production, as revealed by correlation analysis between plume area and runoff results from the WRF-CMB model in Chapter 5. Determining the lag between meltwater production and plume formation was achieved by correlating atmospheric temperature and plume area. Seasonal storage was found to play a key role in the early season, illustrated by the 7 – 9 day lag between production and discharge during June and July, which decreased substantially by the end of the ablation season (Figure 5.6). It has been proposed that this is due to intermediate term storage and the evolution of an efficient hydrological drainage system. Interannually, low winter temperatures impose a deep freeze on meltwater and TSS englacially, creating greater availability for release in the following ablation season (Figure 5.15).

The seasonal pattern of meltwater delivery is present in plume area, despite it being affected by external forcing factors once in the fjord, as presented in Chapter 6. Wind speed and direction both play a role in extending plumes down fjord, which occur under faster and down fjord winds (Table 6.2). Tides have an impact on how much sediment remains in suspension, with more TSS under the influence of flood tides, rather than ebb tides (Figure 6.6). TSS declines with distance from the ice front, corroborating with other glacimarine sedimentation studies.

This thesis has highlighted the wealth of research possibilities associated with sediment plume detection studies. Together with *in situ* hydrographic measurements, and meteorological data, a deeper understanding of the source to sea development of meltwater production, storage and discharge has been presented. It is the first study to use remote sensing to determine the intra-seasonal development and interannual variability in meltwater discharge, from a tidewater glacier. This method has explored the viability of sediment plume detection for use as a site specific tool, with tidewater glaciers. The results have linked meltwater delivery with glacier hydrology, providing insights to the supra and englacial processes of meltwater production, storage and transport, exemplifying the value of sediment plume detection studies. Both the summer and winter meteorological controls on plume formation are clear, despite wind and tidal forcing impacting plume size. Therefore, it is a valuable tool to remotely monitor largely inaccessible glaciers, both seasonally and interannually.

7.2 Results

The results presented in this thesis provide insights to meltwater delivery and the glacier hydrology of the Kronebreen - Kongsvegen complex. As such, the following discussion focusses on these results with a source to sea approach: meltwater production, storage and transport, and finally, the plume and sedimentary characteristics once in the fjord.

7.2.1 Meltwater production

Supraglacial meltwater production is dictated by atmospheric influence on the glacier surface. For tidewater glaciers, this melt is transported to the marine terminus where it is discharge subglacially, dispelling freshwater to the marine environment. However, the importance of submarine melting at marine terminating glaciers was highlighted at LeConte glacier, Alaska by Motyka et al. (2003). As such, quantifying the proportions of each of submarine melt and glacial runoff has become the focus of much research (Mortensen et al., 2011; Sutherland and Straneo, 2012; Sciascia et al., 2013; Mortensen et al., 2014).

At the head of Kongsfjorden, up to 30% of the surface water was SgFW and only 3% GiFW. At an order of magnitude greater than direct submarine melt production, SgFW from Kronebreen is the dominant freshwater type found at the head of Kongsfjorden (Chapter 3). The emerging buoyant plume is sediment laden, which has enabled it to be detected remotely. By detecting TSS, plume size provides a tool to quantify meltwater discharge (Chu et al., 2009; 2012), furthering the understanding of the quantity and timing of freshwater delivery to the marine environment. Since freshwater inputs vary both seasonally and interannually, water column stratification (Mortensen et al., 2013) and fjord circulation are affected (Mortensen et al., 2014).

Supraglacial meltwater production

Meltwater contributions entering at the head of Kongsfjorden have been quantified by sediment plume area in Chapter 4. Rising from the northern section of Kronebreen's ice front, the buoyant freshwater plumes are sediment laden. *In situ* measurements determined surface sediment loading to be between 0.05 – 0.27 g l^{-1}, which has been used to determine the area of the sediment plumes. Plume extent increases in response to increased meltwater production, as determined by correlation with runoff from the WRF-CMB model (Aas. 2015. Pers. Comms). This exemplifies that plume extent provides a representative proxy for melt production. The extent of plumes has revealed seasonality in discharge, which can be attributed to seasonal evolution of atmospheric temperature which drives production of surface runoff. The lag between production and discharge reveals the seasonal storage of meltwater (Chapter 5).

Correlation analysis revealed that atmospheric temperature is the significant driver of meltwater production, with plume extent reflecting the amount discharged into Kongsfjorden. Rainfall does does significantly contribute to the freshwater discharge, as discerned by plume extent (Chapter 5). Solar radiation increases at Ny-Ålesund at the beginning of February, peaking in June at approximately 600 W m^{-2}. Temperatures start to rise above 0°C in late April and early May. It is at this point in late May when snow albedo starts to rapidly decrease from its winter reflectivity of $\sim$80% (Winther et al., 1999). It is the minimum daily temperature that holds the greatest control on meltwater production during the early season, rather than the mean. This is because ME can be both positive and negative, dependent on early season temperatures (Hock, 2003). Typical precipitation in Svalbard, between September and May, is 400 mm; this mainly falls as snow (Førland et al., 1997). Snow depth is at its annual maximum during April, 0.8 – 1.0 m in 1999 and 2000, and rapidly melts during the latter part of May and early June, until there is none left by late June (Boike et al., 2003). Small plume size, typically $<$10 km^2, has been detected between 1st – 18th June, supporting the notion that this is predominantly snow melt, with limited supply. Snow has an approximate density of 350 kg m^{-3}, whilst ice has a much greater density of 850 kg m^{-3} (Shumskiy, 1960). Prior to melting, the high albedo of snow enables it to act as an insulator of the glacier ice below (Boike et al., 2003). Once removed, the lower albedo of glacier ice makes it more susceptible to melt, whilst the higher density of ice means that there is more volume available.

During the middle of the ablation season, 19th June – 17th August, the increased availability and variability of meltwater production is emphasised by larger plume areas, which range from 10 – 56 km^2. Temperatures are constantly above 0°C, but radiation starts to decline from its peak in July (Boike et al., 2003). During this time, there is a stronger correlation between plume area and atmospheric temperature, than in the early season, indicating that meltwater production is more responsive to changes in temperature (Chapter 5). This has an impact on glacier albedo, which changes both spatially and temporally during an ablation season, dictating the amount of energy the glacier absorbs (Hock, 2005). Albedo decreases throughout the season as the area of exposed bare ice increases, which can be determined visually by oblique photography (Huss et al., 2013), and MODIS imagery (Dumont et al., 2012). Decreased albedo causes Kronebreen and Kongsvegen to absorb more energy, driving increased surface melt, which leads to the larger sediment plumes, which have been detected in Kongsfjorden. Larger sediment plumes reflect the increase in surface melt production, as per previous glacial sediment plume studies (Chu et al., 2009; McGrath et al., 2010; Chu et al., 2012; Hudson et al., 2014).

The end of the melt season, 18th August – 30th September, exhibits plume sizes <20 km^2, but they are much more variable in size than during the early season. By this point, temperatures can start to dip below 0 °C and radiative forcing declines, as the polar night set in at the end of September (Boike et al., 2003). This causes the mean maximum temperature to hold greatest control on plume formation, the reverse of the early season. The snow line will be at its highest elevation of the season, leaving the greatest area of bare ice exposed. Plume area detected in September exhibited the highest correlation with both temperature and runoff, of the season. As such, the variability in the latter part of the season comes from temperature conditions, which control whether supraglacial melt takes place. This will be limited during periods when temperatures are below 0 °C, allowing freezing to occur.

Over the 12 year study period, 33% of mean annual plume extent can be attributed to the PDD of the corresponding year, as determined by interannual analysis (Chapter 5). There was no significant trend of increasing mean annual plume extent during the study period. This relationship with mean annual plume extent and PDD has also been observed in Greenland (Chu et al., 2009). However, it also indicates that temperate alone is not the only factor which controls plume size. Although the climate of Svalbard has been relatively stable over the last ~30 years (Lang et al., 2015), the glaciers on the west coast have been in retreat (Kohler et al., 2007). The extreme melt event of Greenland in the summer of 2010 has been attributed to above average temperatures, which led to increased surface ablation which reduced the albedo over much of the ice surface (As et al., 2012). With increasing temperatures forecast for the duration of this century (IPCC, 2013), Svalbard's glaciers will likely decrease in size, following trends presented by Nuth et al. (2010), discharging more meltwater to the ocean. There has been no significant influence of either the NAO or AO on plume extent. These are interdecadal trends, and therefore unlikely to be detectable in a 12 year study. However, the NAO/AO is forecast to become persistently positive this century (Serreze et al., 1997). Shifts in the location of the Icelandic low can have large scale impacts upon Kongsfjorden, making it susceptible in synoptic scale changes in climate (Cottier et al., 2007).

Being able to detect the meltwater through sediment plume detection, provides a method of remotely monitoring meltwater discharge, at both intraseasonal and interannual time scales. Variability of meltwater discharge from the grounding line of Kronebreen can greatly enhance the ice-ocean heat transfer (Jenkins, 2011; Kimura et al., 2014), which leads to differing rates of submarine melt. This exemplifies the key role that atmospheric temperature has on the production of supraglacial melt, and the effect it has on albedo.

Submarine melt

Meltwater produced by submarine melt processes is an order of magnitude smaller than supraglacial meltwater production (Chapter 3). However, understanding the processes attributed to submarine melt is important for assessing what changes could occur in the future. Increased submarine melt of Greenland's tidewater glaciers has been attributed to the influence of warmer AW entering the fjords (Straneo et al., 2012). Given the strong influence the WSC holds on determining the ocean temperatures in Kongsfjorden (Cottier et al., 2007), warming of northward flowing AW has the potential to affect Svalbard's marine termini (Pavlov et al., 2013). As Motyka et al. (2003) detailed, it is not only the effect of warm ocean waters melting tidewater glacier termini that contributes to submarine melt rates, but the entrainment of warm, ambient water, with the rising buoyant plume which drives melt. Convective melt, driven by rising buoyant plumes, is another driver of ice melt at marine terminating termini (Jenkins, 2011; Kimura et al., 2014; Slater et al., 2015).

Emerging from Kronebreen's grounding line is one dominant buoyancy driven plume, as determined by outflow velocities and remote sensing of plume area. This SgFW is produced supraglacially and routed through the glacier to subglacial conduits. This meltwater exits Kronebreen as a submarine jet, forming a buoyant vertical plume which spreads horizontally across the fjord surface. Modelling studies indicate that the buoyancy flux of the plume is the most important for driving the lateral spread of the plume, because momentum from the jet is soon lost (Salcedo-Castro et al., 2011). The buoyant plume rises vertically from the grounding line, remaining connected with the ice face, regardless of the velocity (Salcedo-Castro et al., 2011). Earlier observational studies, proposed that under low velocity conditions plumes would remain connected to the ice face (Syvitski, 1989), but that high velocity conditions would cause the plume to detach and be pushed down fjord, emerging at the surface (Syvitski, 1989; Cowan and Powell, 1990).

The buoyancy driving force for the plume comes from the SgFW, since the proportion of GiFW is small. GiFW is predominantly found where the plume is located, indicative of convection driven melt, rather than heat driven (Jenkins, 2011). In the region of plume upwelling, convection drives ice melt whilst the ambient ocean temperature plays a negligible role. However, the proportion of the ice face not affected by convective melt will be more prone to changes in ambient water temperature (Jenkins, 2011). This indicates that the southern extent of Kronebreen, which receives a stronger inflow of AW than the northern extent, could be more prone to changing AW temperatures. Therefore, monitoring the inflow at the mouth of Kongsfjorden would further illuminate the circulation within the fjord (Cottier et al., 2007). A mooring would be ideal, which presents changes in water column properties for prolonged periods of time (Figure 2.5). However, to obtain the transport of water, a mooring array would be required.

The melt rate to form GiFW is related to the freshwater flux; the melt rate is dependant on the cube root of the freshwater flux, in which doubling the melt rate will produce an order of magnitude increase in the flux (Jenkins, 2011). Such an increase in SgFW will lead to an increase in GiFW, because the plume will have greater acceleration, therefore increasing the transfer of heat by turbulent mixing at the ice - ocean boundary (Kimura et al., 2014). At present, convective driven melt at Kronebreen forms a small proportion of the freshwater flux to Kronebreen, but under scenarios with larger GiFW inputs it has the potential to substantially increase. Increases in surface melt with drive a positive feedback, resulting in greater submarine melt.

As well as the volume of freshwater, the number of submarine outlets also affects the rate of submarine melt. Convective driven melt of the ice face is less with one plume than several plumes along the ice front (Slater et al., 2015). Therefore, it is anticipated that the melt emerging from multiple plumes would create greater frontal melt than the one which is currently present at Kronebreen. If englacial conduits were to move, creating more than one submarine outlet, an increase in submarine melt would be expected (Slater et al., 2015). It is possible to determine the locations of submarine meltwater delivery by detection of TSS, which highlights another value of this remote sensing method.

7.2.2 Meltwater storage and drainage

Storage of meltwater in glacier systems varies temporally and spatially, modulating the amount discharged from the glacier. Meltwater can be stored supraglacially, englacially and subglacially, with intr-aseasonal and interannual variability, (Chu, 2014). Retention of meltwater in the glacial hydrologic system remains at the centre of current research (Rennermalm et al., 2013), since it is partly responsible for the discrepancies in sea level rise predictions (Harper et al., 2012). The lagged relationship that both runoff and atmospheric temperature have with plume area, provides a novel insight to the intraseasonal and interannual storage of meltwater and drainage development in the Kronebreen-Kongsvegen system.

The restricted size of sediment plumes during the early season (1st - 18th June), has been attributed to the limited runoff supply, due to melting snow rather than ice (Boike et al., 2003). Snow is much less dense that ice, therefore less meltwater is produced, attributing to small, constrained plume sizes (Shumskiy, 1960). In addition, energy availability to drive melt is also limited. During this period, it was found that the maximum atmospheric temperature holds greatest control over plume formation, since temperatures can still return to <0 °C. Surface albedo is high early in the summer owing to perennial snow cover, meaning that upward shortwave radiation is high. Incoming shortwave radiation must be able to provide enough energy to instigate melting, which supports the findings that its the maximum temperatures early in the season, that are most important for the onset of melt (Broeke et al., 2008).

The largest variability in plume size (10 – 58 km^2) was found during the peak of the ablation season, from 19th June - 17th August. From 18th August - 30th September plume area was generally <20 km^2. Net radiation drives surface melt in the ablation zone, leading to higher production during the peak of the melt season (Broeke et al., 2008). Melt at higher elevations, in the percolation zone, is driven by both temperature, and the decreasing albedo of the glacier surface as the melt season progresses (As et al., 2012). Melt is enhanced with the increasing exposure of bare ice. Lower elevation melt production is driven by temperature alone (As et al., 2012). During September, plume formation was most responsive to minimum temperatures; as atmospheric cooling takes place, the minimum temperature now needs to be >0 °C, the reverse of June. This supports the temperature driven melt regime (As et al., 2012). These results affirm that the intraseasonal and interannual hydrologic response of sediment plumes to supraglacial melt can be observed at the tidewater glacier Kronebreen, as has been found in proglacial rivers (Chu et al., 2009; McGrath et al., 2010).

Seasonal storage of meltwater within the Kronebreen - Kongsvegen glacier system is notable in this study from the lag time between plume formation with both runoff and atmospheric temperature. This supports the idea of englacial storage (Humphrey et al., 2012), which prevents rapid discharge to the fjord. Hydrological connections need to be established over time, presenting a seasonal signature in meltwater discharge, as discussed by Irvine-Fynn et al. (2006). During June and July sediment plumes form 7 – 9 days after the most influential atmospheric temperature, which is within the time frame of 1 month proposed by Fountain and Walder (1998). This is the first study to have identified meltwater retention, as detected by sediment plumes. Plume studies in Greenland revealed rapid linkage between supraglacial and subglacial hydrology (Chu et al., 2009). However, the growing body of literature supporting englacial storage of meltwater retention (Humphrey et al., 2012; Rennermalm et al., 2013), supports the idea that there is a delay in discharge, which varies during a season. Aerial photographs illustrate supraglacial melt storage is present in ponds, as well as in crevasses. Recent research has revealed that the upper extent of Kronebreen has PFAs (Christianson et al., 2015), further supporting the idea of meltwater storage.

Supraglacial melt driven by atmospheric temperature will percolate through the snow pack, where if temperatures permit, it becomes refrozen. This forms layers of superimposed ice, which can be within or at the base of the snow pack (Müller and Keeler, 1969; Wakahama et al., 1976). The melt and refreeze process of firn is important for the intraseasonal storage of meltwater, and modulating its release as runoff (Fountain and Walder, 1998). Firn becomes ice through metamorphic processes which close the void spaces, increasing its density. Meltwater can become trapped within a matrix of refrozen vertical flow and superimposed ice, providing storage (Humphrey et al., 2012). The Holtedalfonna ice field, which drains into Kronebreen, has a notable PFA, in which the upper ∼10 m of firn is dry, whilst saturated firn is present from ∼10 – 35 m depth (Christianson et al., 2015). Meltwater percolates through the firn, when temperature conditions allow, until it reaches glacial ice, where it is driven to the firn line by gravity (Christianson et al., 2015).

The presence of superimposed ice can lead to supraglacial water storage in the form of melt ponds early in the melt season (Hodgkins, 1997). Superimposed ice, which covers approximately 35% of the surface of Kongsvegen (Obleitner and Lehning, 2004), restricts meltwater flow through the snow pack, causing it to accumulate in surface ponds (Hodgkins, 2001). The presence of meltwater ponds reduces the surface albedo, enhancing radiative-driven melt, forming a positive feedback mechanism, driving further melt (Lüthje et al., 2005). Supraglacial streams provide a surface transport mechanism for meltwater; these form by thermal and radiative processes excavating incisions in the surface of the glacier (McGrath et al., 2011). These streams transport volumes of water down glacier to the crevassed zone. The crevasses provide a subglacial reservoir for meltwater (Skidmore and Sharp, 1999), which dampens the diurnal cycle of meltwater delivery (McGrath et al., 2011). Crevasses are found from Kronebreen's terminus to 12 km back (Sund et al., 2011); approximately one fifth of Kronebreen's surface is crevassed, forming a large reservoir for meltwater storage at lower elevations. Supraglacial lake drainage events were identifiable in sediment plume formation in Kangerlussuaq fjord (Chu et al., 2009), but this process is not applicable to Kronebreen. The fast velocity of Kronebreen likely inhibits the formation of moulins, therefore making crevasse drainage the primary linkage between supraglacial and subglacial environments, which supports Benn et al. (2009).

Plume formation only lagged atmospheric temperature and runoff by 1 – 2 days in August and September. This reveals the strong seasonal signature of meltwater retention, agreeing with Irvine-Fynn et al. (2006), who details greater meltwater storage earlier in the melt season, than at the end. Meltwater travels through polythermal glaciers via a network of englacial fractures, which form an internal hydrological system, providing connections between the surface and the bed of the glacier (Fountain et al., 2005). However, englacial crevassing has been suggested as a primary mechanism for firn aquifer drainage (Fountain et al., 2005). Surface melt that forms ponds in crevasses (Figure 2.13), increases the hydraulic pressure (Boon and Sharp, 2003; Bingham et al., 2005), which drives surface meltwater through the englacial fractures (Fountain et al., 2005). This can lead to hydro-fracturing, in which high rates of summer meltwater can cause crevasses to propagate to the glacier bed, intersecting with subglacial drainage channels (Benn et al., 2009). Meltwater transported through crevasses, rather than moulins, means that discharge is slower and steady, rather than rapid evacuation (McGrath et al., 2011). This discharge route also dampens the diurnal cycle of meltwater input (McGrath et al., 2011). However, this engagement between the surface and subglacial channels allows for rapid delivery of meltwater, which is supported by the short lag times between runoff and temperature, with plume formation. It is likely that a move from a distributed drainage system to a channelised system would account for the increased englacial drainage efficiency, as has been documented at Haut Glacier d'Arolla, Switzerland (Nienow et al., 1998). Smaller channels and cavities will become dormant, with larger channels growing into a simpler, more efficient network (Hock and Hooke, 1993; Walder, 2010). Cavities in the upper extent of the glacier are particularly prone to becoming isolated (Fountain et al., 2005).

The large variability in plume size from July onwards is likely to be due to the establishment of the englacial drainage system. As the season progresses, an efficient connection between the supraglacial and subglacial has been formed

(McGrath et al., 2011). Meltwater discharge can respond rapidly to changes in surface meltwater production (Broeke et al., 2008), which is reflected in the size of the sediment plumes at the head of Kongsfjorden. Plume size at the end of the season remains larger than at the beginning of the season, probably because the glacier is already saturated with meltwater. The pressure within the glacial system has been formed, so discharge will continue until freezing takes place (Boon and Sharp, 2003).

Feasibility for observations during the winter months means that the hydrological system remains poorly understood (Chu, 2014). This study has provided further insights to winter processes regarding melt discharge and storage. Colder winter temperatures have been found to play a significant role in increasing meltwater availability for the following summer (Chapter 5). In addition, the mean temperature of DJFM plays a significant role in sediment availability. Extremely cold winters cause a deep freeze, in which meltwater is not able to slowly discharge. As a result, increased meltwater delivery occurred in the following ablation season, because winter storage was released. This lies in agreement with (Hodson et al., 2005a), who suggest that when there is greater storage of meltwater over winter, its easier to re-energise the hydrological system the following season. The winter freeze also traps basal sediment, which is flushed from the subglacial conduits when melt discharge is instigated at the onset of the melt season. Other studies have revealed stored winter water exhibits geochemical properties which are resultant of storage in an anoxic, geochemically reactive sedimentary environment (Hodson et al., 2005b). If temperatures are mild enough, the pressure remaining in the system can enable melt to slowly discharge (Irvine-Fynn et al., 2011).

7.2.3 Delivery of meltwater and total suspended solids to Kongsfjorden

A net influx of meltwater is delivered at the head of Kongsfjorden, from the ice-ocean interface, as determined by geostrophic current velocities on the two days of CTD profiling (Chapter 3). The fastest outflow from Kronebreen was observed in the SW, north of the bathymetric high. This corroborates with Trusel et al. (2010), who documented that the location of submarine discharge moved northwards from its historical, more southerly location, which was occupied between 1987 – 2001. Entering at the grounding line, the plume is buoyancy driven by the flux of supraglacially produced meltwater, causing it to rise vertically up the ice face and raise the sea surface at the ice-ocean interface (Salcedo-Castro et al., 2011). It then spreads horizontally across the fjord surface, transporting sediment, which provides a proxy for meltwater discharge (Chu et al., 2009; 2012; Tedstone and Arnold, 2012).

During the peak of the ablation season in 2012, meltwater delivery ranged between 3.6 – 4.4 x 10^6 m^3 d^{-1}, which equates to an annual influx of 4.4 – 5.3 x 10^8 m^3 yr^{-1}. Determined by geostrophic velocity, these measurements are an order of magnitude smaller than annual runoff for 2012, (Aas, K 2015, pers. comm., 30 Jan). The primary flow away from the ice face is at the surface, driving the two layer fjord circulation (Svendsen et al., 2002; Cottier et al., 2010). Plume velocity close to the location of discharge is dependent on the volume of discharge Syvitski et al. (1990), whereas further down the fjord the estuarine circulation of the fjord will dominate (Inall and Gillibrand, 2010). The surface water of the plume contains 30% SgFW, which has been discharged from the submarine conduit, entraining ambient AW at it rises to the fjord surface. The fraction of GiFW is an order of magnitude smaller, likely due to the velocity of discharge. The calculated discharge rates of 41 – 50 m^3 s^{-1}, are much smaller than the 100 m^3 s^{-1}, which is proposed by Bendtsen et al. (2015) to be the point at which direct melting of the ice face becomes an important producer of freshwater.

The maps of TSS coverage in the fjord, as well as *in situ* measurements indicate that TSS declines with distance away from the ice face. This corroborates with modelling studies, which found that progressive dilution by entrainment causes the spatial decline in surface TSS (Salcedo-Castro et al., 2013). This study revealed that fine sediment can be transported at least 13.5 km away from the ice face, with TSS decreasing with distance, lying in agreement with Zajaczkowski (2008). However, a fining of particles with increased distance has not been observed in TSS in Kongsfjorden, contrasting measurements from the inlet of Signehamma, Svalbard (Dowdeswell and Cromack, 1991) and Howe Sound, Canada (Syvitski and Murray, 1981). Sedimentation can be affected by the landward estuarine currents in the lower part of the water column, which transports sediment back towards the glacier (Salcedo-Castro et al., 2013). Estuarine circulation can affect the sediment, but the sediment can also impact estuarine circulation. Increased sediment loading in the buoyant plume can reduce the buoyancy of the plume (Salcedo-Castro et al., 2013). Early season flushing of sediment is present in Kongsfjorden, with increased TSS_{mean} in early June. Early season meltwater discharge was characterised by high TSS, and plume areas of <10 km^2, indicative of sediment flushing from the subglacial channels. This is the first study to have identified this in a tidewater glacier system, but it has been previously identified in discharge from high Arctic glaciers (Hodgkins et al., 2003; Hodson et al., 1996). Reduced buoyancy will decrease the plume velocity, which in turn will decrease the production of GiFW at the ice face (Kimura et al., 2014; Bendtsen et al., 2015).

Once in the fjord, the buoyant sediment plumes are affected by both wind and the tidal state, as revealed in Chapter 3. Despite this, the relationship with plume area and runoff remains clear, enabling plume area to be used as a proxy for meltwater discharge. A large tidal range enabled SW to extend further down fjord, with depth decreasing with distance. Such tidal straining is a common observation in estuarine environments, in which tides influence stratification (Simpson et al., 1990). Under a smaller tidal amplitude, the SW was disrupted, and no definitive trend was observed with distance. As well as stratification, tides employ control on surface TSS. This study reveals that under ebb tide conditions, TSS is less than during flood tides. This has been attributed to the reduced turbidity during ebb tides, which allows for sedimentation to take place (Szczucinski and Zajaczkowski, 2012). Previously, factors controlling sedimentation have been determined by sediment traps and cores (e.g. Dowdeswell and Cromack, 1991; Trusel et al., 2010). Quantifying TSS by calibrating *in situ* measurements with MODIS satellite imagery is a new and novel method, which can be used to address not only meltwater delivery, but factors affecting the distribution of TSS.

Wind is another factor which affects the size of buoyant sediment plumes; faster winds extend plumes further downstream (Whitney and Garvine, 2005). As such, it is important to consider the impacts of winds and tides as external forcing factors, which can alter the distribution of TSS. However, in this case, the seasonal and interannual patterns were clear, despite the plumes being affected by external forcing when in Kongsfjorden. This provides reassurance to the methods used, and prompts that sediment plumes provide a mean of remotely detecting not only meltwater delivery, but TSS distribution fjord environments.

Owing to light availability for MODIS satellite images, this study is constrained to the summer months. As such, processes which determine the timing and magnitude of meltwater delivery during the winter requires further investigation. Winter stratification of the water column will be different (Mortensen et al., 2013), in addition to the geochemical properties of the meltwater (Hodson et al., 2005b).

7.3 Wider implications of this research

Remote detection of sediment plumes at low latitudes, in coastal and estuarine environments, is well developed. For decades, researchers have been able to deduce rates of river discharge, identify pollutants, and ascertain the impacts of discharge variability on the environment. It remains a largely unexplored tool in the Polar Regions, despite having large potential (Chu, 2014). There remains a ±20% uncertainty in sea level rise contributions from glaciers and ice caps, (excluding the Greenland and Antarctic peripheral glacier and ice caps; Jacob et al., 2012). Therefore, understanding the linkages between surface melt and glacial discharge will make a valuable scientific contribution, leading to better accuracies when forecasting sea level rise (Church et al., 2013). The combination of *in situ* and remotely sensed data used in this study has provided insights to glacier hydrology, with benefits for a range of research. It has also provided a foundation for future remote sensing studies, particularly regarding tidewater glaciers, to further explore the potential of such work.

The Arctic is undergoing a period of amplified warming; land surface temperature has increased by approximately 2 °C since the 1960s, with positive anomalies persisting in the 21st century (Overalnd et al., 2014). The declining albedo, among other things, has forged several positive feedback mechanisms leading to accelerated change to the atmosphere, cryosphere, land and oceans in the Arctic (Hodgkins, 2014). The increased thinning of Svalbard's glaciers is producing larger meltwater contributions (Kohler et al., 2007). Increased meltwater contributions can lead to Arctic freshening, prompting changes in both local (Shadwick et al., 2013) and large scale circulation (Morison et al., 2012). *In situ* measurements are needed to determine the water masses, but changes to meltwater delivery can be tracked by sediment plume development in both land (Chu et al., 2009; 2012) and marine terminating glaciers. By using this methodology, meltwater delivery can be monitored, and reveal interannual variability, which is advantageous when annual measurements are not able to be taken. Monitoring annual discharge plume by remote sensing also provides an indicator as to when direct glacier melt might be increasing. Larger rates of SgFW discharge are more likely to produce GiFW, forging a positive feedback in freshwater contributions (Slater et al., 2015; Bendtsen et al., 2015). Enhanced plume discharge increases entrainment, thus heat transfer at the ice-ocean interface also increases (Kimura et al., 2014).

A sea ice free Arctic is predicted by 2040 – 2060 (Overland and Wang, 2013), which will cause many more tidewater glaciers to have an open connection with the ocean. Almost 40% of the total global glacerised area is formed of tidewater glaciers (Arendt et al., 2012), which are currently thinning at a faster rate than their terrestrial counterparts in Alaska and Greenland (Arendt et al., 2006; Sole et al., 2008). However this has not yet been observable in the Canadian Arctic Archipelago (Gardner et al., 2011). Northerly flows of water entering the Arctic, in both the Atlantic (Pavlov et al., 2013) and Pacific (Woodgate et al., 2012) sectors, is warming. This increases the need for methods to remotely monitor how these glaciers are effected by both ocean and atmosphere, and to quantify how much freshwater they are contributing to the marine system.

A wider implication of increased freshening is ocean acidification. Fjords can change from a CO_2 source to a CO_2 sink, driving another positive feedback leading to increased ocean acidification, which will change the living conditions of marine calcifying organisms (Fransson et al., 2015). This has been found in regions of the Antarctic, with glacier calving enhancing CO_2 saturation (Shadwick et al., 2013). Freshening of the surface waters also leads to higher zooplankton mortality rates, closest to the point of meltwater discharge, despite increased nutrient input; this already been observed in Kongsfjorden (Cui et al., 2006), and in other glacial environments (Weslawski and Legezynska, 1998). The transport of sediment via turbid meltwater discharge, reduces the extent of the euphotic zone (Svendsen et al., 2002), reducing rates of photosynthesis and primary production, determined by lower chlorophyll-*a* concentrations (Piwosz et al., 2009). Transport of sediment to fjord environments imposes light limitation, which restricts phytoplankton production (Cui et al., 2006). Meltwater discharge also changes the temperature of the water column, which can have impacts for the marine biodiversity (Svendsen et al., 2002; Slemmons et al., 2013). Variability of glacier hydrology has direct impacts on the marine food web, which has implications from planktonic species to mammals (Lydersen et al., 2014). As glaciers continue to melt and retreat, contributing large amount of freshwater to the marine environment, the effects of interseasonal and interannual variability in hydrology require better understanding (Sommaruga, 2015).

Transportation of sediment, by glacial discharge, leads to higher sedimentation rates closest to the glacier, which decrease with distance. If sedimentation rates are high, there is potential that the deposits could act as a stabilising mechanism, reducing iceberg calving (Meier and Post, 1987), and influencing rates of retreat or advance (Alley, 1991; Powell and Alley, 1997; Alley et al., 2007; Dowdeswell et al., 2015). The current rate of infill of the Kongsfjorden basin implies that a grounding line fan could emerge from the fjord within two decades, if Kronebreen's terminus remains stable (Trusel et al., 2010). This has previously taken place for Kongsvegen, which was once the dominant sediment source for Kongsfjorden. Sediment plume studies at Austfonna, Svalbard, revealed that if the glacier terminus is unstable, with fast retreat, the ice-proximal sediment deposits cannot form enough of a stabilising fan; tidewater glacier termini need to be stable for periods of years to decades (Dowdeswell et al., 2015). Therefore, monitoring of both the terminus and sediment contributions to glacial fjords is required to ascertain if a pronounced grounding line fan will form, facilitating the re-advance of the terminus in the future (Trusel et al., 2010).

7.4 Recommendations for future work

This thesis has opened several avenues for further investigation. It has built upon previous studies using remote sensing of sediment plumes (Chu et al., 2009; McGrath et al., 2010; Chu et al., 2012; Tedstone and Arnold, 2012; Hudson et al., 2014), by extending into a tidewater glacier system, quantifying TSS and has the added value of being accompanied by oceanographic measurements. Recommendations for future work is divided into: improvements to the methods for future work, extending the reach of this study and suggestions for new research directions as a result of this work.

This study would benefit from measurements of velocity, using an ADCP. This would directly measure the transport velocities flowing towards and away from the ice front, enabling the volume of meltwater to be more accurately quantified. A repeat survey adopting this method would enable the results to be compared with those calculated by geostrophic velocity in this study. This has been undertaken at Pine Island Glacier, Antarctica, with the results revealing the temporal change in circulation between the two field studies (Jacobs et al., 2011). This study was unable to determine the seasonal variability of meltwater production and subsequent fjord stratification, because hydrographic sections were only sampled in July. Sampling several times a year, in both winter and summer, gives greater insights to meltwater discharge and the impacts on fjord circulation (Mortensen et al., 2013; 2014). Melt water fractions were derived from temperature and salinity, which has been used in numerous other studies. However, the addition of oxygen strengthen this method (Jenkins and Jacobs, 2008) and would provide greater insights to the origin of melt (Meredith et al., 2008; Brown et al., 2014). Regarding *in situ* TSS sampling, this could be extended further down the fjord to obtain lower TSS values. Connected with this, obtaining high TSS samples from close to the ice front would mean the extremely high TSS values are included by the sediment plume model, thus not underestimating plume area. These however, are constrained by working at a safe distance from the calving regions of the glacier. Plume detection could be achieved at a finer resolution by using images from Landsat. This could be used to validate the MODIS images, when image pairs are available, to discern if MODIS over, or under estimates plume size, due to the resolution. The use of Landsat alone would not allow for the seasonal evolution of melt to be documented, because of the 16 day return interval on images, and cloud cover, which restricts image retrieval.

The sediment plume maps hold a wealth on information which could be used to extend the breadth of this study further. Mapping the seasonal change in the ice front, rather than just calculating the area of ice coverage, would present the degradation of the front with time, both during a season, and year to year. The resolution will not be a great as what can be achieved with Landsat (Figure 1.7), but it would ensure an annual estimate of frontal change. The plumes themselves provide key information for sedimentary processes. To take sections along the plume, would provide both temporal and spatial change in the concentration of TSS as in Zajaczkowski (2008). This would offer greater temporal and spatial details, than *in situ* sampling alone. This would allow for further work to investigate the removal rate of sediment, and better assess factors controlling sediment fluxes in glacial fjords (Szczucinski and Zajaczkowski, 2012). It also enables a tool to remotely monitor TSS contributions to Kongsfjorden, together with ice front positions, which can provide insights to the stability of the marine terminus, and whether advance may occur in the future (Dowdeswell et al., 2015). For the marine biology community, the TSS maps could be utilised to better understand the spatial impacts of sediment plumes on zooplankton diversity. Arendt et al. (2011) detailed that zooplankton communities are less diverse when TSS is >0.05 g l^{-1}, which is the lower boundary of what has been classified as "plume" in this study. As such, there is potential that the plume outlines could be associated with marine productivity.

Sustained hydrographic observations would make a valuable addition to knowledge, allowing the assessment of the oceanic heat flux entering Kongsfjorden. If these were located at the mouth of Kongsfjorden, and at the head in the ice proximal zone, the transport of both AW and SW through the fjord could be identified. Kongsfjorden has in the past been largely affected by changes in coastal waters during the winter (Cottier et al., 2007), which strengthens the need for year round monitoring to determine changes in circulation (Mortensen et al., 2013). This oceanographic work could be further developed by linking to the biogeochemical cycles. *In situ* measurements of nutrients and chlorophyll-*a* offers a mechanism to trace meltwater pathways (Torres-Valdés et al., 2013) and link with ecosystem development (Hodson et al., 2005b). *In situ* chlorophyll-*a* measurements can be used to calibrate remotely sensed images, which has been achieved in Kongsfjorden using Landsat 8 (Kim et al., 2014). This produces a simultaneous comparison between primary productivity and TSS. However, monitoring seasonal phytoplankton plume development with Landsat is less purposeful, because of the temporal sparsity of suitable images.

To further address the timing regarding the temporary storage of meltwater, a multispectral analysis of glacier facies could be implemented. Pope and Rees (2014) found that Landsat 8 is suitable for classifying glacier surfaces, whilst the 250 m resolution of MODIS was too coarse. Application of photogrammetry from UAV would give high resolution images, enabling identification of meltponds on

Kronebreen's surface. However, this would require a full summer field season to be able to determine seasonal change in supraglacial meltwater storage. Summer surveys UAV surveys have been undertaken, focussed on elevation change (Solbø and Storvold, 2013). Terrestrial time lapse photography has been documented as being an effective method to determine the relationship between supraglacial meltwater ponds and glacier velocity (Danielson and Sharp, 2013).

7.5 Concluding remarks

The research presented here has provided insights into meltwater production, storage and delivery, for the fast flowing tidewater glacier, Kronebreen, at seasonal and interannual time scales. It has revealed the complex interactions between climate, glacier hydrology, fjord circulation and glacimarine sedimentary processes. The multi-method approach has surmounted the temporal and spatial caveats associated with *in situ* observations alone. As a result, a detailed dataset of meltwater and TSS discharge is presented for a 12 year period. This is the first study to have applied this remote sensing method to a tidewater glacier, with a source to sea approach, resolving seasonal meltwater transport and revealing the effects of winter meltwater storage. The methods employed for this study in Kongsfjorden can be applied to similar glacial fjord environments (e.g. Greenland), providing knowledge regarding the glacial hydrological system, and the impacts placed upon Arctic fjords. Such expansions would enhance quantifications of glacial meltwater discharge, allowing for more accurate SLR estimates to be formulated.

This works highlights the value gained by exploring ways in which sediment plumes can be used, which extends beyond quantifying meltwater and sediment delivery. The plume detection model, together with a local automatic weather station, forms a cost and time effective way to monitor meltwater production, storage and discharge of both meltwater and sediment from tidewater glaciers to glacial fjords, over sustained periods of time to capture intraseasonal and interannual variability.

References

Aagaard, K., Greisman, P., 1975. Toward new mass and heat budgets for the Arctic Ocean. Journal of Geophysical Research 80 (27), 3821–3827.

Aas, K., 2015. Runoff data for Kronebreen, Kongsvegen and Infantfona from 2004 – 2013 produced by the WRF-CMB modelPersonal communication.

Aas, K., Berntsen, T., Boike, J., Etzelmüller, B., Kristjánsson, J. E., Maturilli, M., Schuler, T. V., Stordal, F., Westermann, S., 2015. A comparison between simulated and observed surface energy balance at the Svalbard archipelago. Journal of Applied Meteorology and Climatology 54 (5), 1102–1119.

Abdalati, W., Krabill, W., Frederick, E., Manizade, S., Martin, C., Sonntag, J., Swift, R., Thomas, R., Yungel, J., Koerner, R., 2004. Elevation changes of ice caps in the Canadian Arctic Archipelago. Journal of Geophysical Research: Earth Surface (2003–2012) 109 (F4).

Aliani, S., Bartholini, G., Deglinnocenti, F., Delfanti, R., Galli, C., Lazzoni, E., Lorenzelli, R., Malaguti, A., Meloni, R., Papucci, C., Salvi, S., Zaborska, A., 2004. Multidisciplinary investigations in the marine environment of the inner Kongsfiord, Svalbard islands (September 2000 and 2001). Chemistry and Ecology 20 (Supplement 1), S19–S28.

Alley, R., 1991. Sedimentary processes may cause fluctuations of tidewater glaciers. Annals of Glaciology 15, 119–124.

Alley, R., Anandakrishnan, S., Dupont, T., Parizek, B., Pollard, D., 2007. Effect of sedimentation on ice-sheet grounding-line stability. Science 315 (5820), 1838–1841.

Andersen, M., Larsen, T., Nettles, M., Elosegui, P., van As, D., Hamilton, G., Stearns, L., Davis, J., Ahlstrøm, A., de Juan, J., Ekström, G., Stenseng, L., Khan, S., Forsberg, R., Dahl-Jensen, D., 2010. Spatial and temporal melt variability at Helheim Glacier, East Greenland, and its effect on ice dynamics. Journal of Geophysical Research: Earth Surface (2003–2012) 115 (F4).

Andersen, V., Prieur, L., 2000. One-month study in the open NW Mediterranean Sea (DYNAPROC experiment, may 1995): overview of the hydrobiogeochemical structures and effects of wind events. Deep Sea Research Part I: Oceanographic Research Papers 47 (3), 397–422.

Andrews, L., Catania, G., Hoffman, M., Gulley, J., Lüthi, M., Ryser, C., Hawley, R., Neumann, T., 2014. Direct observations of evolving subglacial drainage beneath the Greenland Ice Sheet. Nature 514 (7520), 80–83.

Arendt, A., Bolch, T., Cogley, J., Gardner, A., Hagen, J., Hock, R., Kaser, G., Pfeffer, W., Moholdt, G., Paul, F., Radic, V., Andreassen, L., Bajracharya, S., Beedle, M., Berthier, E., Bhambri, R., Bliss, A., Brown, I., Burgess, E., Burgess, D., Cawkwell, T., Copland, L., Davies, B., De Angelis, H., Dolgova, E., Filbert, K., Forester, R., Fountain, A., Frey, H., Giffen, B., Glasser, N., Gurney, S., Hagg, W., Hall, D., Haritashya, U., Hartman, G., Helm, C., Herreid, S., Howat, I., Kapustin, G., Khromova, T., Kienholz, C., Koenig, M., Kohler, J., Kriegel, D., Kutuzov, S., Lavrentiev, I., LeBris, R., Lund, J., Manley, W., Mayer, C., Miles, E., Li, X., Menounos, B., Mercer, A., Moelg, N., Mool, P., Nosenko, G., Negrete, A., Nuth, C., Pettersson, R., Racoviteanu, A., Ranzi, R., Rastner, P., Rau, F., Rich, J., Rott, H., Schneider, C., Seliverstov, Y., Sharp, M., Sigurosson, O., Stokes, C., Wheate, R., Winsvold, S., Wolken, G., Wyatt, F., Zheltyhina, N., 2012. Randolph Glacier Inventory [v1. 0]: A dataset of global glacier outlines. Global land ice measurements from space, Boulder Colorado, USA. Digital Media.

Arendt, A., Echelmeyer, K., Harrison, W., Lingle, C., Zirnheld, S., Valentine, V., Ritchie, B., Druckenmiller, M., 2006. Updated estimates of glacier volume changes in the western Chugach Mountains, Alaska, and a comparison of regional extrapolation methods. Journal of Geophysical Research: Earth Surface (2003–2012) 111 (F3).

Arendt, K., Dutz, J., Jónasdóttir, S. H., Jung-Madsen, S., Mortensen, J., Møller, E., Nielsen, T., 2011. Effects of suspended sediments on copepods feeding in a glacial influenced sub-Arctic fjord. Journal of Plankton Research 33 (10), 1526–1537.

As, D. v., Hubbard, A., Hasholt, B., Mikkelsen, A., Van den Broeke, M., Fausto, R., 2012. Large surface meltwater discharge from the Kangerlussuaq sector of the Greenland ice sheet during the record-warm year 2010 explained by detailed energy balance observations. The Cryosphere 6 (1), 199–209.

Azetsu-Scott, K., Tan, F., 1997. Oxygen isotope studies from iceland to an East Greenland fjord: Behaviour of glacial meltwater plume. Marine Chemistry 56 (3), 239–251.

Bamber, J., 1989. Ice/bed interface and englacial properties of Svalbard ice masses deduced from airborne radio echo-sounding data. Journal of Glaciology 35 (119), 30–37.

Barry, R., 2006. The status of research on glaciers and global glacier recession: a review. Progress in Physical Geography 30 (3), 285–306.

Bartholomaus, T., Larsen, C., ONeel, S., 2013. Does calving matter? Evidence for significant submarine melt. Earth and Planetary Science Letters 380, 21–30.

Bartholomew, I., Nienow, P., Mair, D., Hubbard, A., King, M., Sole, A., 2010. Seasonal evolution of subglacial drainage and acceleration in a Greenland outlet glacier. Nature Geoscience 3 (6), 408–411.

Bartholomew, I., Nienow, P., Sole, A., Mair, D., Cowton, T., King, M., 2012. Short-term variability in Greenland Ice Sheet motion forced by time-varying meltwater drainage: Implications for the relationship between subglacial drainage system behavior and ice velocity. Journal of Geophysical Research: Earth Surface (2003–2012) 117 (F3).

Baumberger, A., 2007. Massebalanse på Kronebreen/Holtedahlfonna, Svalbard-kontrollerende faktorer: En studie av romlige og temporale variasjoner i massebalanse og de mekanismer som styrer endringene. Sammenlikning med Kongsvegen. Masters thesis, University of Oslo.

Bendtsen, J., Mortensen, J., Lennert, K., Rysgaard, S., 2015. Heat sources for glacial ice melt in a West Greenland tidewater outlet glacier fjord: The role of subglacial freshwater discharge. Geophysical Research Letters 42 (10).

Benn, D., Gulley, J., Luckman, A., Adamek, A., Glowacki, P., 2009. Englacial drainage systems formed by hydrologically driven crevasse propagation. Journal of Glaciology 55 (191), 513–523.

Benn, D., Warren, C., Mottram, R., 2007. Calving processes and the dynamics of calving glaciers. Earth-Science Reviews 82 (3), 143–179.

Bennett, M., Hambrey, M., Huddart, D., Glasser, N., Crawford, K., 1999. The landform and sediment assemblage produced by a tidewater glacier surge in Kongsfjorden, Svalbard. Quaternary Science Reviews 18 (10), 1213–1246.

Benson, C., 1961. Stratigraphic studies in the snow and firn of the Greenland ice sheet. Folia Geographica Danica 9, 13 – 37.

Beszczynska-Moller, A., Walczowski, W., Weslawski, J., Zajaczkowski, M., 1997. Estimation of glacial meltwater discharge into Svalbard coastal waters. Oceanologia 39, 289–298.

Bhatia, M., Das, S., Kujawinski, E., Henderson, P., Burke, A., Charette, M., 2011. Seasonal evolution of water contributions to discharge from a Greenland outlet glacier: insight from a new isotope-mixing model. Journal of Glaciology 57 (205), 929–941.

Bhatia, M., Kujawinski, E., Das, S., Breier, C., Henderson, P., Charette, M., 2013. Greenland meltwater as a significant and potentially bioavailable source of iron to the ocean. Nature Geoscience 6 (4), 274–278.

Bingham, R., Nienow, P., Sharp, M., Boon, S., 2005. Subglacial drainage processes at a high Arctic polythermal valley glacier. Journal of Glaciology 51 (172), 15–24.

Björnsson, H., Gjessing, Y., Hamran, S.-E., Hagen, J., Liestøl, O., Pálsson, F., Erlingsson, B., 1996. The thermal regime of sub-polar glaciers mapped by multi-frequency radio-echo sounding. Journal of Glaciology 42 (140), 23–32.

Błaszczyk, M., Jania, J., Hagen, J., 2009. Tidewater glaciers of Svalbard: Recent changes and estimates of calving fluxes. Polish Polar Research 30 (2), 85–142.

Bluhm, B., Iken, K., Laudien, J., Lippert, H., 2001. German activity in cold water scientific diving.

Boike, J., Roth, K., Ippisch, O., 2003. Seasonal snow cover on frozen ground: Energy balance calculations of a permafrost site near Ny-ålesund, spitsbergen. Journal of geophysical research-atmospheres, 108 (D2) 8163 4, 1–11.

Boon, S., Sharp, M., 2003. The role of hydrologically-driven ice fracture in drainage system evolution on an Arctic glacier. Geophysical Research Letters 30 (18).

Box, J., Cappelen, J., Chen, C., Decker, D., Fettweis, X., Mote, T., Tedesco, M., van de Wal, R., Wahr, J., 2012. Greenland [in Arctic report card 2012]`http://www.arctic.noaa.gov/report12/greenland_ice_sheet.html`.

Box, J., Cappelen, J., Decker, D., Fettweis, X., Mote, T., Tedesco, M., van de Wal, R., 2010. Greenland [in Arctic report card 2010]`http://www.arctic.noaa.gov/reportcard/`.

Braithwaite, R., 2002. Glacier mass balance: the first 50 years of international monitoring. Progress in Physical Geography 26 (1), 76–95.

Brandt, O., Kohler, J., Lüthje, M., 2008. Spatial mapping of multi-year superimposed ice on the glacier Kongsvegen, Svalbard. Journal of Glaciology 54 (184), 73–80.

Brodie, J., Schroeder, T., Rohde, K., Faithful, J., Masters, B., Dekker, A., Brando, V., Maughan, M., 2010. Dispersal of suspended sediments and nutrients in the Great Barrier Reef lagoon during river-discharge events: conclusions from satellite remote sensing and concurrent flood-plume sampling. Marine and Freshwater Research 61 (6), 651–664.

Broeke, M., Smeets, P., Ettema, J., Veen, C., Wal, R., Oerlemans, J., 2008. Partitioning of melt energy and meltwater fluxes in the ablation zone of the west Greenland ice sheet. The Cryosphere 2 (2), 179–189.

Brown, P., Meredith, M., Jullion, L., Garabato-Naveira, A., Torres-Valdés, S., Holland, P., Leng, M., Venables, H., 2014. Freshwater fluxes in the Weddell Gyre: results from δ18o. Philosophical Transactions of the Royal Society of London A: Mathematical, Physical and Engineering Sciences 372 (2019), 20130298.

Buckley, J., Pond, S., 1976. Wind and the surface circulation of a fjord. Journal of the Fisheries Board of Canada 33 (10), 2265–2271.

Burko, D., 2015. Polar Investigations: Arctic - Svalbard. `http://www.dianeburkophotography.com/polar-investigations-north`; accessed May 15, 2015.

Campbell, J., 2006. Introduction to remote sensing. CRC Press.

Cappelen, J., Laursen, E. V., Jørgensen, P. V., Kern-Hansen, C., 2011. DMI monthly climate data collection 1768–2010, Denmark, the Faroe Islands and Greenland. Technical Report 05-05`http://www.dmi.dk/fileadmin/Rapporter/TR/tr11-05.pdf`.

Castaing, P., Allen, G., 1981. Mechanisms controlling seaward escape of suspended sediment from the Gironde: a macrotidal estuary in France. Marine Geology 40 (1), 101–118.

Cavalieri, D., Parkinson, C., 2012. Arctic sea ice variability and trends, 1979–2010. The Cryosphere 6 (4), 881–889.

Chandler, D., Wadham, J., Lis, G., Cowton, T., Sole, A., Bartholomew, I., Telling, J., Nienow, P., Bagshaw, E., Mair, D., Vinen, S., Hubbard, A., 2013. Evolution of the subglacial drainage system beneath the Greenland ice sheet revealed by tracers. Nature Geoscience 6 (3), 195–198.

Chapuis, A., 2011. What controls the calving of glaciers? From observations to predictions. Ph.D. thesis, PhD thesis, Norwegian University of Life Sciences, Norway, 1–104.

Chen, J., Ohmura, A., 1990. On the influence of Alpine glaciers on runoff. In: Hydrology in Mountainous Regions I. Hydrological Measurements; The Water Cycle. Lausanne Symposia. Vol. 193. IAHS Publication, pp. 117–125.

Chen, S., Han, L., Chen, X., Li, D., Sun, L., Li, Y., 2015. Estimating wide range Total Suspended Solids concentrations from MODIS 250 m imageries: An improved method. ISPRS Journal of Photogrammetry and Remote Sensing 99, 58–69.

Christianson, K., Kohler, J., Alley, R. B., Nuth, C., Pelt, W. J., 2015. Dynamic perennial firn aquifer on an Arctic glacier. Geophysical Research Letters 42 (5), 1418–1426.

Chu, V., 2014. Greenland ice sheet hydrology: A review. Progress in Physical Geography 38 (1), 19–54.

Chu, V., Smith, L., Rennermalm, A., Forster, R., Box, J., 2012. Hydrologic controls on coastal suspended sediment plumes around the Greenland Ice Sheet. The Cryosphere 6 (1), 1–19.

Chu, V., Smith, L., Rennermalm, A., Forster, R., Box, J., Reehy, N., 2009. Sediment plume response to surface melting and supraglacial lake drainages on the Greenland ice sheet. Journal of Glaciology 55 (194), 1072–1082.

Church, J., Clark, P., Cazenave, A., Gregory, J., Jevrejeva, S., Levermann, A., Merrifield, M., Milne, G., Nerem, R., Nunn, P., 2013. Sea level change. Climate Change 2013: The Physical Science Basis. Contribution of Working Group I to the Fifth Assessment Report of the Intergovernmental Panel on Climate Change.

Chylek, P., Folland, C., Lesins, G., Dubey, M., Wang, M., 2009. Arctic air temperature change amplification and the Atlantic Multidecadal Oscillation. Geophysical Research Letters 36 (L14801).

Cisewski, B., Budéus, G., Krause, G., 2003. Absolute transport estimates of total and individual water masses in the northern Greenland Sea derived from hydrographic and acoustic Doppler current profiler measurements. Journal of Geophysical Research: Oceans (1978–2012) 108 (C9).

Clark, C., 1993. Satellite remote sensing of marine pollution. International Journal of Remote Sensing 14 (16), 2985–3004.

Clifford, N., Richards, K., Brown, R., Lane, S., 1995. Scales of variation of suspended sediment concentration and turbidity in a glacial meltwater stream. Geografiska Annaler. Series A. Physical Geography, 45–65.

Cohen, J., Furtado, J., Barlow, M., Alexeev, V., Cherry, J., 2012. Arctic warming, increasing snow cover and widespread boreal winter cooling. Environmental Research Letters 7 (1), 014007.

Collier, E., Mölg, T., Maussion, F., Scherer, D., Mayer, C., Bush, A., 2013. High-resolution interactive modelling of the mountain glacier–atmosphere interface: an application over the Karakoram. The Cryosphere 7 (3), 779–795.

Collins, D., 1979. Sediment concentration in melt waters as an indicator of erosion processes beneath an alpine glacier. Journal of Glaciology 23, 247–257.

Collins, D., 1988. Suspended sediment and solute delivery to meltwaters beneath an Alpine glacier. Mitteilungen der Versuchsanstalt fur Wasserbau, Hydrologie und Glaziologie an der Eidgenossischen Technischen Hochschule Zurich (94), 147–161.

Collins, D., 1989. Seasonal development of subglacial drainage and suspended sediment delievery to meltwaters beneath an Alpine glacier. Annals of Glaciology 13, 45–50.

Collins, D., 1990. Seasonal and annual variations of suspended sediment transport in meltwaters draining from an Alpine glacier. Hydrology in Mountainous Regions 1, 439–446.

Copland, L., Sharp, M. J., Nienow, P. W., 2003. Links between short-term velocity variations and the subglacial hydrology of a predominantly cold polythermal glacier. Journal of Glaciology 49 (166), 337–348.

Cottier, F., Nilsen, F., Inall, M., Gerland, S., Tverberg, V., Svendsen, H., 2007. Wintertime warming of an Arctic shelf in response to large-scale atmospheric circulation. Geophysical Research Letters 34 (10), L10607.

Cottier, F., Nilsen, F., Skogseth, R., Tverberg, V., Skarhamar, J., Svendsen, H., 2010. Arctic fjords: a review of the oceanographic environment and dominant physical processes. Geological Society, London, Special Publications 344 (1), 35–50.

Cottier, F., Tverberg, V., Inall, M., Svendsen, H., Nilsen, F., Griffiths, C., 2005. Water mass modification in an Arctic fjord through cross-shelf exchange: The seasonal hydrography of Kongsfjorden, Svalbard. Journal of Geophysical Research: Oceans (1978–2012) 110 (C12).

Cowan, E., 1992. Meltwater and tidal currents: controls on circulation in a small glacial fjord. Estuarine, Coastal and Shelf Science 34 (4), 381–392.

Cowan, E., Powell, R., 1990. Suspended sediment transport and deposition of cyclically interlaminated sediment in a temperate glacial fjord, Alaska, USA. Geological Society, London, Special Publications 53 (1), 75–89.

Cowan, E., Powell, R., 1991. Ice-proximal sediment accumulation rates in a temperate glacial fjord, southeastern Alaska. Geological Society of America Special Papers 261, 61–74.

Cowan, E., Powell, R., 2004. High frequency climate signals in fjord sediments of Glacier Bay National Park, Alaska. In: Proceedings of the Fourth Glacier Bay Science Symposium. Citeseer, pp. 46–49.

Cowan, E., Seramur, K., Powell, R., Willems, B., Gulick, S., Jaeger, J., 2010. Fjords as temporary sediment traps: History of glacial erosion and deposition in Muir inlet, Glacier Bay National park, southeastern Alaska. Geological Society of America Bulletin 122 (7-8), 1067–1080.

Cowton, T., Nienow, P., Sole, A., Wadham, J., Lis, G., Bartholomew, I., Mair, D., Chandler, D., 2013. Evolution of drainage system morphology at a land-terminating Greenlandic outlet glacier. Journal of Geophysical Research: Earth Surface 118 (1), 29–41.

Cuffey, K., Paterson, W., 2010. The physics of glaciers. Academic Press.

Cui, S., He, J., He, P., Zhang, F., Lin, L., Ma, Y., 2006. The adaptation of Arctic phytoplankton to low light and salinity in Kongsfjorden (Spitsbergen). Advances in Polar Science 71, 182–231.

Curran, P., Hansom, J., Plummer, S., Pedley, M., 1987. Multispectral remote sensing of nearshore suspended sediments: a pilot study. International Journal of Remote Sensing 8 (1), 103–112.

Curran, P., Novo, E., 1988. The relationship between suspended sediment concentration and remotely sensed spectral radiance: a review. Journal of Coastal Research, 351–368.

Cushman-Roisin, B., Asplin, L., Svendsen, H., 1994. Upwelling in broad fjords. Continental shelf research 14 (15), 1701–1721.

Danielson, B., Sharp, M., 2013. Development and application of a time-lapse photograph analysis method to investigate the link between tidewater glacier flow variations and supraglacial lake drainage events. Journal of Glaciology 59 (214), 287–302.

Defant, A., 1961. Physical Oceanography. New York: Macmillan Company.

Dowdeswell, J., Cromack, M., 1991. Behaviour of a glacier-derived suspended sediment plume in a small Arctic inlet. The Journal of Geology, 111–123.

Dowdeswell, J., Dowdeswell, E., 1989. Debris in icebergs and rates of glaci-marine sedimentation: observations from Spitsbergen and a simple model. The Journal of Geology, 221–231.

Dowdeswell, J., Forsberg, C., 1992. The size and frequency of icebergs and bergy bits derived from tidewater glaciers in Kongsfjorden, northwest Spitsbergen. Polar Research 11 (2), 81–91.

Dowdeswell, J., Hamilton, G., Hagen, J., 1991. The duration of the active phase on surge-type glaciers: contrasts between svalbard and other regions. Journal of Glaciology 37 (127), 388–400.

Dowdeswell, J., Hogan, K., Arnold, N., Mugford, R., Wells, M., Hirst, J. P., Decalf, C., 2015. Sediment-rich meltwater plumes and ice-proximal fans at the margins of modern and ancient tidewater glaciers: Observations and modelling. Sedimentology.

Dumont, M., Gardelle, J., Sirguey, P., Guillot, A., Six, D., Rabatel, A., Arnaud, Y., 2012. Linking glacier annual mass balance and glacier albedo retrieved from MODIS data. The Cryosphere 6, 1527–1539.

Dunse, T., Schuler, T., Hagen, J., Reijmer, C., 2012. Seasonal speed-up of two outlet glaciers of Austfonna, Svalbard, inferred from continuous GPS measurements. The Cryosphere 6 (2), 453–466.

eKlima, N. M. I., 2014. eKlima data series. Norwegian meterological data service. `http://www.eklima.no`; accessed November 21, 2014.

Elverhøi, A., Liestøl, O., Nagy, J., 1980. Glacial erosion, sedimentation and microfauna in the inner part of Kongsfjorden, Spitsbergen. Norsk Polarinstitutt Skrifter 172, 33–58.

Elverhøi, A., Lønne, Ø., Seland, R., 1983. Glaciomarine sedimentation in a modern fjord environment, Spitsbergen. Polar Research 1 (2), 127–150.

Enderlin, E., Howat, I., 2013. Submarine melt rate estimates for floating termini of Greenland outlet glaciers (2000–2010). Journal of Glaciology 59 (213), 67–75.

Esau, I., Repina, I., 2012. Wind climate in Kongsfjorden, Svalbard, and attribution of leading wind driving mechanisms through turbulence-resolving simulations. Advances in Meteorology 2012, 1–16.

Fer, I., Widell, K., 2007. Early spring turbulent mixing in an ice-covered Arctic fjord during transition to melting. Continental Shelf Research 27 (15), 1980–1999.

Ferguson, R., 1973. Sinuosity of supraglacial streams. Geological Society of America Bulletin 84 (1), 251–256.

Fettweis, X., Hanna, E., Lang, C., Belleflamme, A., Erpicum, M., Gallée, H., 2013. Important role of the mid-tropospheric atmospheric circulation in the recent surface melt increase over the Greenland ice sheet. The Cryosphere 7, 241–248.

Førland, E., Hansen-Bauer, I., Nordli, P., 1997. Orographic precipitation at the glacier Austre Brøggerbreen. DNMI Rep. 2/97 Klima.

Forster, R., van den Broeke, M., Miège, C., Burgess, E., van Angelen, J., Lenaerts, J., Koenig, L., Paden, J., Lewis, C., Gogineni, S. P., 2014. Extensive liquid meltwater storage in firn within the greenland ice sheet. Nature Geoscience 7 (2), 95–98.

Fountain, A., 1989. The storage of water in, and hydraulic characteristics of, the firn of South Cascade Glacier, Washington State, USA. Annals of Glaciology 13, 69–75.

Fountain, A., 1996. Effect of snow and firn hydrology on the physical and chemical characteristics of glacial runoff. Hydrological Processes 10 (4), 509–521.

Fountain, A., Jacobel, R., Schlichting, R., Jansson, P., 2005. Fractures as the main pathways of water flow in temperate glaciers. Nature 433 (7026), 618–621.

Fountain, A., Tangborn, W., 1985. The effect of glaciers on streamflow variations. Water Resources Research 21 (4), 579–586.

Fountain, A., Walder, J., 1998. Water flow through temperate glaciers. Reviews of Geophysics 36 (3), 299–328.

Fransson, A., Chierici, M., Nomura, D., Granskog, M., Kristiansen, S., Martma, T., Nehrke, G., 2015. Effect of glacial drainage water on the CO2 system and ocean acidification state in an Arctic tidewater-glacier fjord during two contrasting years. Journal of Geophysical Research: Oceans 120 (4), 2413–2429.

Gade, H., 1979. Melting of ice in sea water: A primitive model with application to the Antarctic ice shelf and icebergs. Journal of Physical Oceanography 9 (1), 189–198.

Gardner, A., Moholdt, G., Cogley, G., Wouters, B., Arendt, A., Wahr, J., Berthier, E., Hock, R., Pfeffer, W., Kaser, G., Ligtenberg, S., Bolch, T., Sharp, M., Hagen, J., van den Broeke, M., Paul, F., 2013. A reconciled estimate of glacier contributions to sea level rise: 2003 to 2009. Science 340 (6134), 852–857.

Gardner, A., Moholdt, G., Wouters, B., Wolken, G., Burgess, D., Sharp, M., Cogley, G., Braun, C., Labine, C., 2011. Sharply increased mass loss from glaciers and ice caps in the Canadian Arctic Archipelago. Nature 473 (7347), 357–360.

Gerland, S., Renner, A., 2007. Sea-ice mass-balance monitoring in an Arctic fjord. Annals of Glaciology 46 (1), 435–442.

Gjevik, B., Straume, T., 1989. Model simulations of the M2 and the K1 tide in the Nordic Seas and the Arctic Ocean. Tellus A 41 (1), 73–96.

Glazovsky, A., Macheret, Y., Vasilenko, E., 2006. Calving glaciers of Novaya Zemblya and Franz Joseph land. The Mass Budget of Arctic Glaciers, 43.

Gordon, S., Sharp, M., Hubbard, B., Smart, C., Ketterling, B., Willis, I., 1998. Seasonal reorganization of subglacial drainage inferred from measurements in boreholes. Hydrological Processes 12 (1), 105–133.

Gray, D., 1973. Handbook on the principles of hydrology.

Gulley, J., Benn, D., 2007. Structural control of englacial drainage systems in Himalayan debris-covered glaciers. Journal of Glaciology 53 (182), 399–412.

Gulley, J., Benn, D., Müller, D., Luckman, A., 2009. A cut-and-closure origin for englacial conduits in uncrevassed regions of polythermal glaciers. Journal of Glaciology 55 (189), 66–80.

Gurnell, A., 1982. The dynamics of suspended sediment concentration in an Alpine pro-glacial stream network. Hydrological Aspects of Alpine and High Mountain Areas, 319–330.

Gurnell, A., Clark, M., Hill, C., 1992a. Analysis and interpretation of patterns within and between hydroclimatological time series in an Alpine glacier basin. Earth Surface Processes and Landforms 17 (8), 821–839.

Gurnell, A., Clark, M., Hill, C., Greenhalgh, J., Bogen, J., Walling, D., Day, T., 1992b. Reliability and representativeness of a suspended sediment concentration monitoring programme for a remote alpine proglacial river. Vol. 24. IAHS Press Wallingford, Oxfordshire, UK, p. 28.

Hagen, J., 1988. Glacier mass balance investigations in the balance year 1986 – 87. Polar Research 6 (2), 205–209.

Hagen, J., Kohler, J., Melvold, K., Winther, J.-G., 2003a. Glaciers in Svalbard: mass balance, runoff and freshwater flux. Polar Research 22 (2), 145–159.

Hagen, J., Liestøl, O., 1990. Long-term glacier mass-balance investigations in Svalbard. Annals of Glaciology 14, 102–106.

Hagen, J., Melvold, K., Pinglot, F., Dowdeswell, J., 2003b. On the net mass balance of the glaciers and ice caps in Svalbard, Norwegian Arctic. Arctic, Antarctica, and Alpine Research 35 (2), 264–270.

Hall, D., Riggs, G., Salomonson, V., 1995. Development of methods for mapping global snow cover using moderate resolution imaging spectroradiometer data. Remote sensing of Environment 54 (2), 127–140.

Hallet, B., Hunter, L., Bogen, J., 1996. Rates of erosion and sediment evacuation by glaciers: A review of field data and their implications. Global and Planetary Change 12 (1), 213–235.

Hambrey, M., 1977. Supraglacial drainage and its relationship to structure, with particular reference to Charles Rabots Bre, Okstindan, Norway.

Han, L., Rundquist, D., 1994. The response of both surface reflectance and the underwater light field to various levels of suspended sediments: preliminary results. Photogrammetric Engineering and Remote Sensing 60 (12), 1463–1471.

Hanna, E., Mernild, S., Cappelen, J., Steffen, K., 2012. Recent warming in greenland in a long-term instrumental (1881–2012) climatic context: I. Evaluation of surface air temperature records. Environmental Research Letters 7 (4), 045404.

Hanna, E., Navarro, F., Pattyn, F., Domingues, C., Fettweis, X., Ivins, E., Nicholls, R., Ritz, C., Smith, B., Tulaczyk, S., Whitehouse, P., Zwally, H., 2013. Ice-sheet mass balance and climate change. Nature 498 (7452), 51–59.

Hanssen-Bauer, I., Solås, M. K., Steffensen, E., 1990. Climate of Spitsbergen. DNMI.

Harland, W., 1997. Central western Spitsbergen. Geological Society, London, Memoirs 17 (1), 154–178.

Harper, J., Humphrey, N., Pfeffer, W., Brown, J., Fettweis, X., 2012. Greenland ice-sheet contribution to sea-level rise buffered by meltwater storage in firn. Nature 491 (7423), 240–243.

Hasholt, B., Bech Mikkelsen, A., Holtegaard Nielsen, M., Andreas Dahl Larsen, M., 2013. Observations of runoff and sediment and dissolved loads from the Greenland ice sheet at Kangerlussuaq, west Greenland, 2007 to 2010. Zeitschrift für Geomorphologie, Supplementary Issues 57 (2), 3–27.

Hawkings, J., Wadham, J., Tranter, M., Raiswell, R., Benning, L., Statham, P., Tedstone, A., Nienow, P., Lee, K., Telling, J., 2014. Ice sheets as a significant source of highly reactive nanoparticulate iron to the oceans. Nature communications 5, 3929.

Hill, P., Syvitski, J., Cowan, E., Powell, R., 1998. In situ observations of floc settling velocities in Glacier Bay, Alaska. Marine Geology 145 (1), 85–94.

Hinzman, L., Kane, D., 1992. Potential response of an Arctic watershed during a period of global warming. Journal of Geophysical Research: Atmospheres (1984–2012) 97 (D3), 2811–2820.

Hock, R., 2003. Temperature index melt modelling in mountain areas. Journal of Hydrology 282 (1), 104–115.

Hock, R., 2005. Glacier melt: a review of processes and their modelling. Progress in physical geography 29 (3), 362–391.

Hock, R., Hooke, R. L., 1993. Evolution of the internal drainage system in the lower part of the ablation area of Storglaciären, Sweden. Geological Society of America Bulletin 105 (4), 537–546.

Hock, R., Iken, A., Wangler, A., 1999. Tracer experiments and borehole observations in the overdeepening of Aletschgletscher, Switzerland. Annals of Glaciology 28 (1), 253–260.

Hodgkins, R., 1997. Glacier hydrology in Svalbard, Norwegian high Arctic. Quaternary Science Reviews 16 (9), 957–973.

Hodgkins, R., 2001. Seasonal evolution of meltwater generation, storage and discharge at a non-temperate glacier in Svalbard. Hydrological Processes 15 (3), 441–460.

Hodgkins, R., 2014. The twenty-first-century Arctic environment: accelerating change in the atmospheric, oceanic and terrestrial spheres. The Geographical Journal 180 (4), 429–436.

Hodgkins, R., Cooper, R., Tranter, M., Wadham, J., 2013. Drainage-system development in consecutive melt seasons at a polythermal, Arctic glacier, evaluated by flow-recession analysis and linear-reservoir simulation. Water Resources Research 49 (7), 4230–4243.

Hodgkins, R., Cooper, R., Wadham, J., Tranter, M., 2003. Suspended sediment fluxes in a high-Arctic glacierised catchment: implications for fluvial sediment storage. Sedimentary Geology 162 (1), 105–117.

Hodgkins, R., Cooper, R., Wadham, J., Tranter, M., 2009. The hydrology of the proglacial zone of a high-Arctic glacier (Finsterwalderbreen, Svalbard): atmospheric and surface water fluxes. Journal of hydrology 378 (1), 150–160.

Hodgkins, R., Tranter, M., Dowdeswell, J. A., 1998. The hydrochemistry of runoff from a cold-basedglacier in the High Arctic (Scott Turnerbreen, Svalbard). Hydrological Processes 12 (1), 87–103.

Hodson, A., Anesio, A., Tranter, M., Fountain, A., Osborn, M., Priscu, J., Laybourn-Parry, J., Sattler, B., 2008. Glacial ecosystems. Ecological Monographs 78 (1), 41–67.

Hodson, A., Ferguson, R., 1999. Fluvial suspended sediment transport from cold and warm-based glaciers in Svalbard. Earth Surface Processes and Landforms 24 (11), 957–974.

Hodson, A., Kohler, J., Brinkhaus, M., Wynn, P., 2005a. Multi-year water and surface energy budget of a high-latitude polythermal glacier: evidence for overwinter water storage in a dynamic subglacial reservoir. Annals of Glaciology 42 (1), 42–46.

Hodson, A., Mumford, P., Kohler, J., Wynn, P., 2005b. The High Arctic glacial ecosystem: new insights from nutrient budgets. Biogeochemistry 72 (2), 233–256.

Hodson, A., Tranter, M., Dowdeswell, J., Gurnell, A., Hagen, J., 1996. Glacier thermal regime and suspended-sediment yield: a comparison of two high-Arctic glaciers. Annals of Glaciology 24, 32–37.

Holland, P., Jenkins, A., Holland, D., 2008. The response of ice shelf basal melting to variations in ocean temperature. Journal of Climate 21 (11), 2558–2572.

Hooke, R. L., 2005. Principles of glacier mechanics. Cambridge university press.

Hop, H., Borgå, K., Gabrielsen, G. W., Kleivane, L., Skaare, J. U., 2002. Food web magnification of persistent organic pollutants in poikilotherms and homeotherms from the Barents Sea. Environmental Science & Technology 36 (12), 2589–2597.

Hoskin, C., Burrell, D., 1972. Sediment transport and accumulation in a fjord basin, Glacier Bay, Alaska. The Journal of Geology, 539–551.

Howe, J., Moreton, S., Morri, C., Morris, P., 2003. Multibeam bathymetry and the depositional environments of Kongsfjorden and Krossfjorden, western Spitsbergen, Svalbard. Polar Research 22 (2), 301–316.

Hubbard, B., Nienow, P., 1997. Alpine subglacial hydrology. Quaternary Science Reviews 16 (9), 939–955.

Hubbard, B., Sharp, M., Willis, I., Nielson, M., Smart, C., 1995. Borehole water-level variations and the structure of the subglacial hydrological system of Haut Glacier dArolla, Valais, Switzerland. Journal of Glaciology 41 (139), 572–583.

Hudson, B., Overeem, I., McGrath, D., Syvitski, J., Mikkelsen, A., Hasholt, B., 2014. MODIS observed increase in duration and spatial extent of sediment plumes in Greenland fjords. The Cryosphere 8 (4), 1161–1176.

Humphrey, N., Raymond, C., 1994. Hydrology, erosion and sediment production in a surging glacier: Variegated Glacier, Alaska, 1982-83. Journal of Glaciology 40 (136), 539–552.

Humphrey, N. F., Harper, J. T., Pfeffer, W. T., 2012. Thermal tracking of meltwater retention in Greenland's accumulation area. Journal of Geophysical Research: Earth Surface (2003–2012) 117 (F1).

Huss, M., Sold, L., Hoelzle, M., Stokvis, M., Salzmann, N., Farinotti, D., Zemp, M., 2013. Towards remote monitoring of sub-seasonal glacier mass balance. Annals of Glaciology 54 (63), 75–83.

Iken, A., Truffer, M., 1997. The relationship between subglacial water pressure and velocity of Findelengletscher, Switzerland, during its advance and retreat. Journal of Glaciology 43, 328–338.

Inall, M., Gillibrand, P., 2010. The physics of mid-latitude fjords: a review. Geological Society, London, Special Publications 344 (1), 17–33.

Ingvaldsen, R., Reitan, M. B., Svendsen, H., Asplin, L., 2001. The upper layer circulation in Kongsfjorden and Krossfjorden-a complex fjord system on the west coast of Spitsbergen (scientific paper). Memoirs of National Institute of Polar Research. Special issue 54, 393–407.

IPCC, 2013. Climate Change 2013: The Physical Science Basis: Working Group I Contribution to the Fifth Assessment Report of the Intergovernmental Panel on Climate Change. Cambridge University Press.

Irvine-Fynn, T., Hodson, A., Moorman, B., Vatne, G., Hubbard, A., 2011. Polythermal glacier hydrology: a review. Reviews of Geophysics 49 (4), 2010RG000350.

Irvine-Fynn, T., Moorman, B., Williams, J., Walter, F., 2006. Seasonal changes in ground-penetrating radar signature observed at a polythermal glacier, Bylot Island, Canada. Earth Surface Processes and Landforms 31 (7), 892–909.

Irvine-Fynn, T., Moorman, B., Willis, I., Sjogren, D., Hodson, A., Mumford, P., Walter, F., Williams, J., 2005. Geocryological processes linked to high Arctic proglacial stream suspended sediment dynamics: examples from Bylot Island, Nunavut, and Spitsbergen, Svalbard. Hydrological Processes 19 (1), 115–135.

Jacob, T., Wahr, J., Pfeffer, W., Swenson, S., 2012. Recent contributions of glaciers and ice caps to sea level rise. Nature 482 (7386), 514–518.

Jacobs, S., Jenkins, A., Giulivi, C., Dutrieux, P., 2011. Stronger ocean circulation and increased melting under Pine Island Glacier ice shelf. Nature Geoscience 4 (8), 519–523.

Jansson, P., Hock, R., Schneider, T., 2003. The concept of glacier storage: a review. Journal of Hydrology 282 (1), 116–129.

Jenkins, A., 1999. The impact of melting ice on ocean waters. Journal of physical oceanography 29 (9), 2370–2381.

Jenkins, A., 2011. Convection-driven melting near the grounding lines of ice shelves and tidewater glaciers. Journal of Physical Oceanography 41 (12), 2279–2294.

Jenkins, A., Jacobs, S., 2008. Circulation and melting beneath George VI ice shelf, Antarctica. Journal of Geophysical Research: Oceans (1978–2012) 113 (C4).

Jo, Y.-H., Yan, X.-H., Dzwonkowski, B., Liu, W. T., 2005. A study of the freshwater discharge from the Amazon River into the tropical Atlantic using multisensor data. Geophysical Research Letters 32 (2).

Jonsell, U., Hock, R., Holmgren, B., 2003. Spatial and temporal variations in albedo on Storglaciä ren, Sweden. Journal of Glaciology 49 (164), 59–68.

Jónsson, S., Foldvik, A., Aagaard, K., 1992. The structure and atmospheric forcing of the mesoscale velocity field in Fram Strait. Journal of Geophysical Research: Oceans (1978–2012) 97 (C8), 12585–12600.

Kääb, A., Lefauconnier, B., Melvold, K., 2005. Flow field of Kronebreen, Svalbard, using repeated Landsat 7 and ASTER data. Annals of Glaciology 42 (1), 7–13.

Karner, F., Obleitner, F., Krismer, T., Kohler, J., Greuell, W., 2013. A decade of energy and mass balance investigations on the glacier Kongsvegen, Svalbard. Journal of Geophysical Research: Atmospheres 118 (10), 3986–4000.

Kaser, G., Cogley, J., Dyurgerov, M., Meier, M., Ohmura, A., 2006. Mass balance of glaciers and ice caps: consensus estimates for 1961–2004. Geophysical Research Letters 33 (19).

Kaser, G., Großhauser, M., Marzeion, B., 2010. Contribution potential of glaciers to water availability in different climate regimes. Proceedings of the National Academy of Sciences 107 (47), 20223–20227.

Kehrl, L., Hawley, R., Powell, R., Julie, B., 2011. Glacimarine sedimentation processes at Kronebreen and Kongsvegen, Svalbard. Journal of Glaciology 57 (205), 841–847.

Killingtveit, Å., Pettersson, L.-E., Sand, K., 2003. Water balance investigations in Svalbard. Polar Research 22 (2), 161–174.

Kilpeläinen, T., Vihma, T., Manninen, M., Sjöblom, A., Jakobson, E., Palo, T., Maturilli, M., 2012. Modelling the vertical structure of the atmospheric boundary layer over Arctic fjords in Svalbard. Quarterly Journal of the Royal Meteorological Society 138 (668), 1867–1883.

Kim, S.-i., Kim, H.-c., Shin, J.-i., Park, S.-y., Park, K.-s., 2014. High resolution ocean color products estimation in fjord of Svalbard, Arctic Sea. EARSeL 34th Symposium Proceedings, 16–20 June 2014 10, 6–10.

Kimura, S., Holland, P., Jenkins, A., Piggott, M., 2014. The effect of meltwater plumes on the melting of a vertical glacier face. Journal of Physical Oceanography 44 (12), 3099–3117.

Kjell, R., 1988. The hydrology of Bayelva, Spitsbergen. Nordic hydrology 19 (4), 259–268.

Klemas, V., 2011. Remote sensing of coastal plumes and ocean fronts: overview and case study. Journal of Coastal Research 28 (1A), 1–7.

Klinck, J., O'Brien, J., Svendsen, H., 1981. A simple model of fjord and coastal circulation interaction. Journal of Physical Oceanography 11 (12), 1612–1626.

Koenig, L., Miège, C., Forster, R., Brucker, L., 2014. Initial in situ measurements of perennial meltwater storage in the Greenland firn aquifer. Geophysical Research Letters 41 (1), 81–85.

Kohler, J., James, T., Murray, T., Nuth, C., Brandt, O., Barrand, N., Aas, H., Luckman, A., 2007. Acceleration in thinning rate on western Svalbard glaciers. Geophysical Research Letters 34 (18).

König, M., Wadham, J., Winther, J.-G., Kohler, J., Nuttall, A.-M., 2002. Detection of superimposed ice on the glaciers Kongsvegen and midre Love
nbreen, Svalbard, using SAR satellite imagery. Annals of Glaciology 34 (1), 335–342.

Koppes, M., Hallet, B., 2002. Influence of rapid glacial retreat on the rate of erosion by tidewater glaciers. Geology 30 (1), 47–50.

Lamont, J., 1876. Yachting in the Arctic seas. Chatto and Windus.

Lang, C., Fettweis, X., Erpicum, M., 2015. Stable climate and surface mass balance in Svalbard over 1979–2013 despite the Arctic warming. The Cryosphere 9 (1), 83–101.

Lang, H., 1986. Forecasting meltwater runoff from snow-covered areas and from glacier basins. In: River flow modelling and forecasting. Springer, pp. 99–127.

Lefauconnier, B., 1987. Fluctuations glaciaires dans le Kongsfjord, (baie du roi), 79°N, Spitsbergen, analyses et conseqences (Glacier fluctuations in Kongsfjorden, 79°N, Spitsbergen, analyses and consequences). Unpublished thesis. Université de Grenoble.

Lefauconnier, B., Hagen, J., Rudant, J., 1994. Flow speed and calving rate of Kongsbreen glacier, Svalbard, using SPOT images. Polar Research 13 (1), 59–65.

Liestøl, O., 1988. The glaciers in the Kongsfjorden area, Spitsbergen. Norsk Geografisk Tidsskrift - Norwegian Journal of Geography 42.

Liestøl, O., Repp, K., Wold, B., 1980. Supra-glacial lakes in Spitsbergen. Nor. Geogr. Tidsskr 34 (2), 89–92.

Lindsay, R., Schweiger, A., 2015. Arctic sea ice thickness loss determined using subsurface, aircraft, and satellite observations. The Cryosphere 9 (1), 269–283.

Loveland, T., Dwyer, J., 2012. Landsat: Building a strong future. Remote Sensing of Environment 122, 22–29.

Luks, B., Osuch, M., Romanowicz, R., 2011. The relationship between snowpack dynamics and NAO/AO indices in SW Spitsbergen. Physics and Chemistry of the Earth, Parts A/B/C 36 (13), 646–654.

Lüthje, M., Pedersen, L., Reeh, N., 2005. Modelling drainage processes, a numerical and remote sensing investigation of pond formation on ice surfaces. Technical University of DenmarkDanmarks Tekniske Universitet, Department of Civil EngineeringInstitut for Byggeri og Anlæg.

Lydersen, C., Assmy, P., Falk-Petersen, S., Kohler, J., Kovacs, K., Reigstad, M., Steen, H., Strøm, H., Sundfjord, A., Varpe, Ø., Waldek, W., Jan Marcin, W., Zajaczkowski, M., 2014. The importance of tidewater glaciers for marine mammals and seabirds in Svalbard, Norway. Journal of Marine Systems 129, 452–471.

Lydersen, C., Gjertz, I., 1986. Studies of the ringed seal (Phoca hispida Schreber 1775) in its breeding habitat in Kongsfjorden, Svalbard. Polar Research 4 (1), 57–63.

MacArthur, A., MacLellan, C., Malthus, T., 2012. The fields of view and directional response functions of two field spectroradiometers. Geoscience and Remote Sensing, IEEE Transactions on 50 (10), 3892–3907.

Mair, D., Willis, I., Fischer, U., Hubbard, B., Nienow, P., Hubbard, A., 2003. Hydrological controls on patterns of surface, internal and basal motion during three spring "events": Haut Glacier dArolla, Switzerland. Journal of Glaciology 49 (167), 555–567.

Marston, R., 1983. Supraglacial stream dynamics on the Juneau Icefield. Annals of the Association of American Geographers 73 (4), 597–608.

Matthews, J., 1981. The seasonal circulation of the Glacier Bay, Alaska fjord system. Estuarine, Coastal and Shelf Science 12 (6), 679–700.

Mayer, S., Jonassen, M., Sandvik, A., Reuder, J., 2012. Profiling the Arctic stable boundary layer in Advent Valley, Svalbard: Measurements and simulations. Boundary-layer meteorology 143 (3), 507–526.

McClimans, T., 1978. Fronts in fjords. Geophysical & Astrophysical Fluid Dynamics 11 (1), 23–34.

McGrath, D., Colgan, W., Steffen, K., Lauffenburger, P., Balog, J., 2011. Assessing the summer water budget of a moulin basin in the Sermeq Avannarleq ablation region, Greenland Ice Sheet. Journal of Glaciology 57 (205), 954–964.

McGrath, D., Steffen, K., Overeem, I., Mernild, S., Hasholt, B., van den Broeke, M., 2010. Sediment plumes as a proxy for local ice-sheet runoff in Kangerlussuaq Fjord, West Greenland. Journal of glaciology 56 (199), 813–821.

Mehlum, F., 1991. Breeding population size of the common eider Somateria mollissima in Kongsfjorden, Svalbard, 1981–1987. Skrifter-Norsk Polarinstitutt (195), 21–29.

Meier, M., Dyurgerov, M., Rick, U., O'Neel, S., Pfeffer, T., Anderson, R., Anderson, S., Glazovsky, A., 2007. Glaciers dominate eustatic sea-level rise in the 21st century. Science 317 (5841), 1064–1067.

Meier, M., Post, A., 1987. Fast tidewater glaciers. Journal of Geophysical Research: Solid Earth (1978–2012) 92 (B9), 9051–9058.

Melvold, K., 1992. Studie av brebevegelse på Kongsvegen og Kronebreen, Svalbard. A study of glacier movement on Kongsvegen and Kronebreen, Svalbard.) Rapportserie i Naturgeografi 1.

Melvold, K., Hagen, J., 1998. Evolution of a surge-type glacier in its quiescent phase: Kongsvegen, Spitsbergen, 1964-95. Journal of Glaciology 44 (147), 394–404.

Meredith, M., Brandon, M., Wallace, M., Clarke, A., Leng, M., Renfrew, I., Van Lipzig, N., King, J., 2008. Variability in the freshwater balance of northern Marguerite Bay, Antarctic Peninsula: Results from δ18o. Deep Sea Research Part II: Topical Studies in Oceanography 55 (3), 309–322.

Miller, R., McKee, B., 2004. Using MODIS Terra 250 m imagery to map concentrations of total suspended matter in coastal waters. Remote Sensing of Environment 93 (1), 259–266.

Moholdt, G., Nuth, C., Hagen, J., Kohler, J., 2010. Recent elevation changes of Svalbard glaciers derived from ICESat laser altimetry. Remote Sensing of Environment 114 (11), 2756–2767.

Moore, G., 1977. Satellite surveillance of physical water-quality characteristics. In: Proceedings of the Twelfth International Symposium on Remote Sensing of Environment Ann Arbor, Michigan April 20-26.

Morison, J., Kwok, R., Peralta-Ferriz, C., Alkire, M., Rigor, I., Andersen, R., Steele, M., 2012. Changing Arctic Ocean freshwater pathways. Nature 481 (7379), 66–70.

Mortensen, J., Bendtsen, J., Lennert, K., Rysgaard, S., 2014. Seasonal variability of the circulation system in a west Greenland tidewater outlet glacier fjord, Godthåbsfjord (64 N). Journal of Geophysical Research: Earth Surface 119 (12), 2591–2603.

Mortensen, J., Bendtsen, J., Motyka, R., Lennert, K., Truffer, M., Fahnestock, M., Rysgaard, S., 2013. On the seasonal freshwater stratification in the proximity of fast-flowing tidewater outlet glaciers in a sub-Arctic sill fjord. Journal of Geophysical Research: Oceans 118 (3), 1382–1395.

Mortensen, J., Lennert, K., Bendtsen, J., Rysgaard, S., 2011. Heat sources for glacial melt in a sub-Arctic fjord (Godthåbsfjord) in contact with the Greenland Ice Sheet. Journal of Geophysical Research: Oceans (1978–2012) 116 (C1).

Motyka, R., Dryer, W., Amundson, J., Truffer, M., Fahnestock, M., 2013. Rapid submarine melting driven by subglacial discharge, LeConte Glacier, Alaska. Geophysical Research Letters 40 (19), 5153–5158.

Motyka, R., Hunter, L., Echelmeyer, K., Connor, C., 2003. Submarine melting at the terminus of a temperate tidewater glacier, LeConte Glacier, Alaska, USA. Annals of Glaciology 36 (1), 57–65.

Müller, F., 1962. Zonation in the accumulation area of the glaciers of Axel Heiberg Island, NWT, Canada. Journal of Glaciology 4, 302–311.

Müller, F., Keeler, C., 1969. Errors in short-term ablation measurements on melting ice surfaces. Journal of Glaciology 8 (52), 91–105.

Nahrgang, J., Varpe, Ø., Korshunova, E., Murzina, S., Hallanger, I. G., Vieweg, I., Berge, J., 2014. Gender specific reproductive strategies of an Arctic key species (Boreogadus saida) and implications of climate change. PloS one 9 (5), e98452.

Nakayama, Y., Schröder, M., Hellmer, H., 2013. From circumpolar deep water to the glacial meltwater plume on the eastern Amundsen Shelf. Deep Sea Research Part I: Oceanographic Research Papers 77, 50–62.

NASA, 2012a. MODIS Specifications. `http://modis.gsfc.nasa.gov/about/specifications.php`; accessed 29th October 2012.

NASA, 2012b. NASA Arctic Subset Images. `http://lance-modis.eosdis.nasa.gov/imagery/subsets/?subset=Arctic_r02c04.2012153.terra.250m`; accessed 2nd October 2013.

NASA, 2012c. NASA Reverb Portal. `http://reverb.echo.nasa.gov/reverb`; accessed 6th July, 2014.

NASA, 2014a. MODIS real time swath images. `http://rapidfire.sci.gsfc.nasa.gov/cgi-bin/imagery/realtime.cgi`; accessed 31st March, 2014.

NASA, 2014b. NASA satellite overpass prediction service. `http://www-air.larc.nasa.gov.tools/predict.htm`; accessed February 15th, 2014.

Nesje, A., Lie, Ø., Dahl, S., 2000. Is the North Atlantic Oscillation reflected in Scandinavian glacier mass balance records? Journal of quaternary Science 15 (6), 587–601.

Nghiem, S., Hall, D., Mote, T., Tedesco, M., Albert, M., Keegan, K., Shuman, C., DiGirolamo, N., Neumann, G., 2012. The extreme melt across the Greenland ice sheet in 2012. Geophysical Research Letters 39 (20).

Nienow, P., Sharp, M., Willis, I., 1998. Seasonal changes in the morphology of the subglacial drainage system, Haut Glacier d'Arolla, Switzerland. Earth Surface Processes and Landforms 23 (9), 825–843.

Nilsen, F., 2011. Warm water reappears in Spitsbergen fjords. `http://www.unis.no/60_NEWS/6070_Archive_2011/n_11_11_04_spitsbergen_fjords/warm_water_reappears_news_04112011.htm`; accessed May 5th 2014.

Nilsen, F., Cottier, F., Skogseth, R., Mattsson, S., 2008. Fjord–shelf exchanges controlled by ice and brine production: the interannual variation of Atlantic water in Isfjorden, Svalbard. Continental Shelf Research 28 (14), 1838–1853.

Nilsen, F., Gjevik, B., Schauer, U., 2006. Cooling of the West Spitsbergen Current: isopycnal diffusion by topographic vorticity waves. Journal of Geophysical Research: Oceans (1978–2012) 111 (C8).

NOAA, 2015. AVHRR Specifications. `http://noaasis.noaa.gov/NOAASIS/ml/avhrr.html`; accessed 15th May 2015.

Nuth, C., Kohler, J., König, M., Deschwanden, A. v., Hagen, J., Kääb, A., Moholdt, G., Pettersson, R., 2013. Decadal changes from a multi-temporal glacier inventory of Svalbard. The Cryosphere 7 (5), 1603–1621.

Nuth, C., Moholdt, G., Kohler, J., Hagen, J., Kääb, A., 2010. Svalbard glacier elevation changes and contribution to sea level rise. Journal of Geophysical Research: Earth Surface (2003–2012) 115 (F1).

Nuth, C., Schuler, T. V., Kohler, J., Altena, B., Hagen, J., 2012. Estimating the long-term calving flux of Kronebreen, Svalbard, from geodetic elevation changes and mass-balance modelling. Journal of Glaciology 58 (207), 119–133.

Ó Cofaigh, C., Dowdeswell, J., 2001. Laminated sediments in glacimarine environments: diagnostic criteria for their interpretation. Quaternary Science Reviews 20 (13), 1411–1436.

Obleitner, F., Lehning, M., 2004. Measurement and simulation of snow and superimposed ice at the Kongsvegen glacier, Svalbard (Spitzbergen). Journal of Geophysical Research: Atmospheres (1984–2012) 109 (D4).

Oerlemans, J., 2001. Glaciers and climate change. Balkema.

Oerlemans, J., 2005. Extracting a climate signal from 169 glacier records. Science 308 (5722), 675–677.

Onarheim, I., Smedsrud, L., Ingvaldsen, R., Nilsen, F., 2014. Loss of sea ice during winter north of Svalbard. Tellus A 66.

Østrem, G., 1975. Sediment transport in glacial meltwater streams. Glaciofluvial and Glaciolacustrine Sedimentation 23, 101–122.

Overalnd, J., Hanna, E., Hanssen-Bauer, I., Kim, S.-J., Walsh, J., Wang, M., Bhatt, U., 2014. Air temperature, atmospheric circulation and clouds. `http://www.arctic.noaa.gov/reportcard/air_temperature.html`; accessed April 02, 2015.

Overland, J. E., Wang, M., 2013. When will the summer Arctic be nearly sea ice free? Geophysical Research Letters 40 (10), 2097–2101.

Parizek, B., Alley, R., 2004. Implications of increased Greenland surface melt under global-warming scenarios: ice-sheet simulations. Quaternary Science Reviews 23 (9), 1013–1027.

Paterson, W., 2001. The physics of glaciers. Butterworth-Heinemann.

Pavlov, A., Tverberg, V., Ivanov, B., Nilsen, F., Falk-Petersen, S., Granskog, M., 2013. Warming of Atlantic Water in two west Spitsbergen fjords over the last century (1912-2009). Polar Research 32.

Perkin, R., Lewis, L., 1978. Mixing in an Arctic fjord. Journal of Physical Oceanography 8 (5), 873–880.

Perovich, D., Gerland, S., Hendricks, S., Meier, W., Nicolaus, M., Richter-Menge, J., Tschudi, M., 2013. Sea ice [in Arctic report card 2013]`http://www.arctic.noaa.gov/report13/sea_ice.html`.

Pfeffer, W., Arendt, A., Bliss, A., Bolch, T., Cogley, J., Gardner, A., Hagen, J., Hock, R., Kaser, G., Kienholz, C., Miles, E., Moholdt, G., Mölg, N., Paul, F., Radiac, V., Rastner, P., Raup, B., Rich, J., Sharp, M., 2014. The Randolph Glacier Inventory: a globally complete inventory of glaciers. Journal of Glaciology 60 (221), 537.

Piquet, A., Scheepens, J., Bolhuis, H., Wiencke, C., Buma, A., 2010. Variability of protistan and bacterial communities in two Arctic fjords (Spitsbergen). Polar biology 33 (11), 1521–1536.

Piwosz, K., Walkusz, W., Hapter, R., Wieczorek, P., Hop, H., Wiktor, J., 2009. Comparison of productivity and phytoplankton in a warm (Kongsfjorden) and a cold (hornsund) Spitsbergen fjord in mid-summer 2002. Polar Biology 32 (4), 549–559.

Pope, A., Rees, W. G., 2014. Impact of spatial, spectral, and radiometric properties of multispectral imagers on glacier surface classification. Remote Sensing of Environment 141, 1–13.

Powell, R., 1991. Grounding-line systems as second-order controls on fluctuations of tidewater termini of temperate glaciers. Geological Society of America Special Papers 261, 75–94.

Powell, R., Alley, R., 1997. Grounding-line systems: Processes, glaciological inferences and the stratigraphic record. Geology and seismic stratigraphy of the Antarctic Margin, 2, 169–187.

Powell, R., Molnia, B., 1989. Glacimarine sedimentary processes, facies and morphology of the south-southeast Alaska shelf and fjords. Marine Geology 85 (2), 359–390.

Purkis, S., Klemas, V., 2011. Remote sensing and global environmental change. John Wiley & Sons.

Rennermalm, A., Smith, L., Chu, V., Box, J., Forster, R., Van den Broeke, M., As, D. V., Moustafa, S., 2013. Evidence of meltwater retention within the Greenland ice sheet. The Cryosphere 7, 1433–1445.

Richards, K., Sharp, M., Arnold, N., Gurnell, A., Clark, M., Tranter, M., Nienow, P., Brown, G., Willis, I., Lawson, W., 1996. An integrated approach to modelling hydrology and water quality in glacierized catchments. Hydrological Processes 10 (4), 479–508.

Rignot, E., Koppes, M., Velicogna, I., 2010. Rapid submarine melting of the calving faces of West Greenland glaciers. Nature Geoscience 3 (3), 187–191.

Rignot, E., Steffen, K., 2008. Channelized bottom melting and stability of floating ice shelves. Geophysical Research Letters 35 (2).

Robinson, I., 1995. Satellite oceanography: an introduction for oceanographers and remote-sensing scientists. Wiley.

Rogers, J., Yang, L., Li, L., 2005. The role of Fram Strait winter cyclones on sea ice flux and on Spitsbergen air temperatures. Geophysical Research Letters 32 (6).

Rolstad, C., Norland, R., 2009. Ground-based interferometric radar for velocity and calving-rate measurements of the tidewater glacier at Kronebreen, Svalbard. Annals of Glaciology 50 (50), 47–54.

Röthlisberger, H., 1972. Water pressure in intra- and subglacial channels. Journal of Glaciology 11, 177–203.

Ruhl, C., Schoellhamer, D., Stumpf, R., Lindsay, C., 2001. Combined use of remote sensing and continuous monitoring to analyse the variability of suspended-sediment concentrations in San Francisco Bay, California. Estuarine, Coastal and Shelf Science 53 (6), 801–812.

Rysgaard, S., Hansen, J., Sejr, M., Borum, J., Laursen, J., Ehlmé, G., Elander, M., Rasch, M., 1999a. Changes in Arctic marine production. Tech. rep., Danish Polar Center.

Rysgaard, S., Nielsen, T., Hansen, B., 1999b. Seasonal variation in nutrients, pelagic primary production and grazing in a high-Arctic coastal marine ecosystem, Young Sound, Northeast Greenland. Marine ecology. Progress series 179, 13–25.

Salcedo-Castro, J., Bourgault, D., Bentley, S., 2013. Non-hydrostatic modeling of cohesive sediment transport associated with a subglacial buoyant jet in glacial fjords: A process-oriented approach. Ocean Modelling 63, 30–39.

Salcedo-Castro, J., Bourgault, D., de Young, B., 2011. Circulation induced by subglacial discharge in glacial fjords: Results from idealized numerical simulations. Continental Shelf Research 31 (13), 1396–1406.

Saloranta, T., Haugan, P., 2004. Northward cooling and freshening of the warm core of the West Spitsbergen Current. Polar Research 23 (1), 79–88.

Saloranta, T., Svendsen, H., 2001. Across the Arctic front west of Spitsbergen: high-resolution CTD sections from 1998-2000. Polar Research 20 (2), 177–184.

Schauer, U., Beszczynska-Möller, A., Walczowski, W., Fahrbach, E., Piechura, J., Hansen, E., 2008. Variation of measured heat flow through the Fram Strait between 1997 and 2006. In: Arctic–Subarctic Ocean Fluxes. Springer, pp. 65–85.

Schauer, U., Fahrbach, E., Osterhus, S., Rohardt, G., 2004. Arctic warming through the Fram Strait: Oceanic heat transport from 3 years of measurements. Journal of Geophysical Research: Oceans (1978–2012) 109 (C6).

Schellenberger, T., Dunse, T., Kääb, A., Kohler, J., Reijmer, C., 2014. Surface speed and frontal ablation of kronebreen and kongsbreen, nw-svalbard, from sar offset tracking. The Cryosphere Discussions 8 (6), 6193–6233.

Schneider, T., 1999. Water movement in the firn of Storglaciaren, Sweden. Journal of Glaciology 45 (150), 286–294.

Schneider, T., 2000. Hydrological processes in the wet-snow zone of glaciers: A review. Zeitschrift fur Gletscherkunde und Glazialgeologie 36 (1), 89–105.

Schofield, O., Arnone, R., Bissett, W. P., Dickey, T., Davis, C., Finkel, Z., Oliver, M., Moline, M., 2004. Watercolors in the coastal zone: what can we see? Biological Sciences, 144.

Schoof, C., 2010. Ice-sheet acceleration driven by melt supply variability. Nature 468 (7325), 803–806.

Sciascia, R., Cenedese, C., Nicolì, D., Heimbach, P., Straneo, F., 2014. Impact of periodic intermediary flows on submarine melting of a Greenland glacier. Journal of Geophysical Research: Oceans 119 (10), 7078–7098.

Sciascia, R., Straneo, F., Cenedese, C., Heimbach, P., 2013. Seasonal variability of submarine melt rate and circulation in an East Greenland fjord. Journal of Geophysical Research: Oceans 118 (5), 2492–2506.

Serreze, M., Barrett, A., Stroeve, J., Kindig, D., Holland, M., 2009. The emergence of surface-based Arctic amplification. The Cryosphere 3 (1), 11–19.

Serreze, M., Carse, F., Barry, R., Rogers, J., 1997. Icelandic low cyclone activity: Climatological features, linkages with the nao, and relationships with recent changes in the northern hemisphere circulation. Journal of Climate 10 (3), 453–464.

Shadwick, E., Rintoul, S., Tilbrook, B., Williams, G., Young, N., Fraser, A., Marchant, H., Smith, J., Tamura, T., 2013. Glacier tongue calving reduced dense water formation and enhanced carbon uptake. Geophysical Research Letters 40 (5), 904–909.

Sharp, M., 2014. Glaciology news in brief. Environmental Earth Sciences 71 (6), 2973–2978.

Shevenell, A., Domack, E., Kernan, G., 1996. Record of Holocene palaeoclimate change along the Antarctic Peninsula: evidence from glacial marine sediments, lallemand fjord. In: Papers and Proceedings of the Royal Society of Tasmania. Vol. 130. pp. 55–64.

Shreve, R., 1972. Movement of water in glaciers. Journal of Glaciology 11, 205–214.

Shumskiy, P., 1960. Density of glacier ice. Journal of Glaciology 27, 568–573.

Simpson, J., Brown, J., Matthews, J., Allen, G., 1990. Tidal straining, density currents, and stirring in the control of estuarine stratification. Estuaries 13 (2), 125–132.

Skamarock, W., Klemp, J., Dudhia, J., Gill, D., Barker, D., Duda, M., Huang, X., Wang, W., Powers, J., 2008. A description of the advanced research WRF version 3. NCAR technical note NCAR/TN/u2013475.

Skarhamar, J., Svendsen, H., 2010. Short-term hydrographic variability in a stratified Arctic fjord. Geological Society, London, Special Publications 344 (1), 51–60.

Skidmore, M., Sharp, M., 1999. Drainage system behaviour of a High-Arctic polythermal glacier. Annals of Glaciology 28 (1), 209–215.

Skogseth, R., Fer, I., Haugan, P., 2005a. Dense-water production and overflow from an Arctic coastal polynya in Storfjorden. The Nordic Seas: An Integrated Perspective, 73–88.

Skogseth, R., Haugan, P., Jakobsson, M., 2005b. Watermass transformations in Storfjorden. Continental Shelf Research 25 (5), 667–695.

Slater, D., Nienow, P., Cowton, T., Goldberg, D., Sole, A., 2015. Effect of near-terminus subglacial hydrology on tidewater glacier submarine melt rates. Geophysical Research Letters.

Slemmons, K., Saros, J., Simon, K., 2013. The influence of glacial meltwater on alpine aquatic ecosystems: A review. Environmental Science: Processes & Impacts 15 (10), 1794–1806.

Sneed, W., Hamilton, G., 2007. Evolution of melt pond volume on the surface of the Greenland Ice Sheet. Geophysical Research Letters 34 (3).

Solbø, S., Storvold, R., 2013. Mapping svalbard glaciers with the cryowing UAS. ISPRS-International Archives of the Photogrammetry, Remote Sensing and Spatial Information Sciences XL-1 W 2, 373–377.

Sole, A., Mair, D., Nienow, P., Bartholomew, I., King, M., Burke, M., Joughin, I., 2011. Seasonal speedup of a Greenland marine-terminating outlet glacier forced by surface melt–induced changes in subglacial hydrology. Journal of Geophysical Research: Earth Surface (2003–2012) 116 (F3).

Sole, A., Payne, T., Bamber, J., Nienow, P., Krabill, W., 2008. Testing hypotheses of the cause of peripheral thinning of the Greenland Ice Sheet: is land-terminating ice thinning at anomalously high rates? The Cryosphere 2 (2), 205–218.

Sommaruga, R., 2015. When glaciers and ice sheets melt: consequences for planktonic organisms. Journal of Plankton Research, 1 – 10.

Spielhagen, R., Werner, K., Sørensen, S. A., Zamelczyk, K., Kandiano, E., Budeus, G., Husum, K., Marchitto, T., Hald, M., 2011. Enhanced modern heat transfer to the Arctic by warm Atlantic water. Science 331 (6016), 450–453.

Stearns, L., Hamilton, G., Veen, C., Finnegan, D., O'Neel, S., Scheick, J., Lawson, D., 2015. Glaciological and marine geological controls on terminus dynamics of Hubbard Glacier, southeast Alaska. Journal of Geophysical Research: Earth Surface 120 (6), 1065–1081.

Steele, M., Ermold, W., Zhang, J., 2008. Arctic Ocean surface warming trends over the past 100 years. Geophysical Research Letters 35 (2).

Stenborg, T., 1970. Delay of run-off from a glacier basin. Geografiska Annaler. Series A. Physical Geography, 1–30.

Storvold, R., 2012. Aerial uav image of the terminus of kongsvegen from july 2012Personal communication.

Straneo, F., Curry, R., Sutherland, D., Hamilton, G., Cenedese, C., Våge, K., Stearns, L., 2011. Impact of fjord dynamics and glacial runoff on the circulation near Helheim Glacier. Nature Geoscience 4 (5), 322–327.

Straneo, F., Heimbach, P., 2013. North Atlantic warming and the retreat of Greenland's outlet glaciers. Nature 504 (7478), 36–43.

Straneo, F., Heimbach, P., Sergienko, O., Hamilton, G., Catania, G., Griffies, S., Hallberg, R., Jenkins, A., Joughin, I., Motyka, R., Pfeffer, W. T., Price, S., Rignot, E., Scambos, T., Truffer, M., Vieli, A., 2013. Challenges to understanding the dynamic response of Greenland's marine terminating glaciers to oceanic and atmospheric forcing. Bulletin of the American Meteorological Society 94 (8), 1131–1144.

Straneo, F., Sutherland, D., Holland, D., Gladish, C., Hamilton, G., Johnson, H., Rignot, E., Xu, Y., Koppes, M., 2012. Characteristics of ocean waters reaching Greenland's glaciers. Annals of Glaciology 53 (60), 202–210.

Stronach, J., 1981. The Fraser River plume, Strait of Georgia. Ocean Management 6 (2), 201–221.

Stumpf, R., Gelfenbaum, G., Pennock, J., 1993. Wind and tidal forcing of a buoyant plume, Mobile Bay, Alabama. Continental Shelf Research 13 (11), 1281–1301.

Stumpf, R., Tyler, M., 1988. Satellite detection of bloom and pigment distributions in estuaries. Remote Sensing of Environment 24 (3), 385–404.

Sund, M., Eiken, T., Rolstad Denby, C., 2011. Velocity structure, front position changes and calving of the tidewater glacier Kronebreen, Svalbard. The Cryosphere Discussions 5 (1), 41–73.

Sutherland, D., Straneo, F., 2012. Estimating ocean heat transports and submarine melt rates in Sermilik Fjord, Greenland, using lowered acoustic Doppler current profiler (LADCP) velocity profiles. Annals of Glaciology 53 (60), 50–58.

Svanem, M., 2011. Terrestrial photogrammetry for velocity measurement of Kronebreen calving front. Masters thesis, The Norwegian University of Life science.

Svendsen, H., 1995. Physical oceanography of coupled fjord-coast systems in northern Norway with special focus on frontal dynamics and tides. Ecology of Fjords and Coastal Waters. Elsevier, New York, 149–164.

Svendsen, H., Beszczynska-Møller, A., Hagen, J., Lefauconnier, B., Tverberg, V., Gerland, S., Ørbøk, J. B., Bischof, K., Papucci, C., Zajaczkowski, M., , Azzolini, R., Bruland, O., Wiencke, C., Winther, J.-G., Dallmann, W., 2002. The physical environment of Kongsfjorden–Krossfjorden, an Arctic fjord system in Svalbard. Polar Research 21 (1), 133–166.

Swift, D., Nienow, P., Spedding, N., Hoey, T., 2002. Geomorphic implications of subglacial drainage configuration: rates of basal sediment evacuation controlled by seasonal drainage system evolution. Sedimentary Geology 149 (1), 5–19.

Syvitski, J., 1989. On the deposition of sediment within glacier-influenced fjords: oceanographic controls. Marine Geology 85 (2), 301–329.

Syvitski, J., Andrews, J., Dowdeswell, J., 1996. Sediment deposition in an iceberg-dominated glacimarine environment, East Greenland: basin fill implications. Global and Planetary Change 12 (1), 251–270.

Syvitski, J., LeBlanc, K. W., Cranston, R., 1990. The flux and preservation of organic carbon in Baffin island fjords. Geological Society, London, Special Publications 53 (1), 177–199.

Syvitski, J., Murray, J., 1981. Particle interaction in fjord suspended sediment. Marine Geology 39 (3), 215–242.

Szczucinski, W., Zajaczkowski, M., 2012. Factors controlling downward fluxes of particulate matter in glacier-contact and non-glacier contact settings in a subpolar fjord (Billefjorden, Svalbard). Sediments, Morphology and Sedimentary Processes on Continental Shelves: Advances in technologies, research and applications (Special Publication 44 of the IAS) 108, 369–386.

Tedstone, A., Arnold, N., 2012. Automated remote sensing of sediment plumes for identification of runoff from the Greenland ice sheet. Journal of Glaciology 58 (210), 699–712.

Teigen, S., Nilsen, F., Gjevik, B., 2010. Barotropic instability in the West Spitsbergen Current. Journal of Geophysical Research: Oceans (1978–2012) 115 (C7).

Tomczak, M., 1981. A multi-parameter extension of temperature/salinity diagram techniques for the analysis of non-isopycnal mixing. Progress in Oceanography 10 (3), 147–171.

Torres-Valdés, S., Tsubouchi, T., Bacon, S., Naveira-Garabato, A., Sanders, R., McLaughlin, F., Petrie, B., Kattner, G., Azetsu-Scott, K., Whitledge, T., 2013. Export of nutrients from the Arctic Ocean. Journal of Geophysical Research: Oceans 118 (4), 1625–1644.

Trusel, L., Powell, R., Cumpston, R., Brigham-Grette, J., 2010. Modern glacimarine processes and potential future behaviour of Kronebreen and Kongsvegen polythermal tidewater glaciers, Kongsfjorden, Svalbard. Geological Society, London, Special Publications 344 (1), 89–102.

Tverberg, V., Nøst, O., 2009. Eddy overturning across a shelf edge front: Kongsfjorden, west Spitsbergen. Journal of Geophysical Research: Oceans (1978–2012) 114 (C4).

USGS, 2015. Landsat missions information. `http://landsat.usgs.gov/band_designations_landsat_satellites.php`; accessed May 15, 2015.

Van der Veen, C., 1998. Fracture mechanics approach to penetration of surface crevasses on glaciers. Cold Regions Science and Technology 27 (1), 31–47.

Vannstand, 2014. Vannstand tide height prediction service. `http://vannstand.no/index.php/english-section/tide-table`; accessed February 15, 2014.

Vatne, G., 1992. Glaciofluvial sediment transfer of a subpolar glacier, Erikbreen, Svalbard. Im Selbstverlag des Geograhpischen Instituts der Universität Stuttgart.

Vatne, G., Etzelmüller, B., Ludvid Sollid, J., Ødegård, R. S., 1996. Meltwater routing in a high Arctic glacier, Hannabreen, northern Spitsbergen. Norsk Geografisk Tidsskrift-Norwegian Journal of Geography 50 (1), 66–74.

Vatne, G., Etzelmüller, B., Sollid, J., Strand, Ø., 1995. Hydrology of a polythermal glacier, Erikbreen, northern Spitsbergen. Nordic hydrology 26 (3), 169–190.

Vermote, E., Kotchenova, S., Ray, J., 2011. MODIS surface reflectance users guide., 2011.

Vieli, A., Jania, J., Blatter, H., Funk, M., 2004. Short-term velocity variations on Hansbreen, a tidewater glacier in Spitsbergen. Journal of Glaciology 50 (170), 389–398.

Vieli, A., Nick, F., 2011. Understanding and modelling rapid dynamic changes of tidewater outlet glaciers: issues and implications. Surveys in geophysics 32 (4-5), 437–458.

Vinje, T., 1982. The drift pattern of sea ice in the Arctic with particular reference to the Atlantic approach. L., Stonehouse, B.(Eds.), The Arctic Ocean. Macmillan, Indianapolis, IN, 83–96.

Voigt, U., 1966. The determination of the direction of movement on glacier surfaces by terrestrial photogrammetry. Journal of Glaciology 6, 359–367.

Voigt, U., 1967. Ergebnisse der Bewegungsmessungen an Kongsvegen und Kronebreen. Wissenschaftliche ergebnisse der deutschen Spitzbergenexpedition 1964-1965, geodät. Geophys. Veröff. (Berlin) 9 (3), 70 – 98.

Wadham, J., Hodgkins, R., Cooper, R., Tranter, M., 2001. Evidence for seasonal subglacial outburst events at a polythermal glacier, Finsterwalderbreen, Svalbard. Hydrological processes 15 (12), 2259–2280.

Wadham, J., Hodson, A., Tranter, M., Dowdeswell, J., 1998. The hydrochemistry of meltwaters draining a polythermal-based, high Arctic glacier, south Svalbard: I. the ablation season. Hydrological Processes 12 (12), 1825–1849.

Wadham, J., Tranter, M., Dowdeswell, J., 2000. Hydrochemistry of meltwaters draining a polythermal-based, high-Arctic glacier, south Svalbard: Ii. Winter and early Spring. Hydrological Processes 14 (10), 1767–1786.

Wakahama, G., Kuroiwa, D., Hasemi, T., Benson, C., 1976. Field observations and experimental and theoretical studies on the superimposed ice of McCall glacier, Alaska. Journal of Glaciology 16, 135–149.

Walczowski, W., Piechura, J., 2007. Pathways of the Greenland Sea warming. Geophysical Research Letters 34 (10).

Walczowski, W., Piechura, J., Osinski, R., Wieczorek, P., 2005. The West Spitsbergen Current volume and heat transport from synoptic observations in summer. Deep Sea Research Part I: Oceanographic Research Papers 52 (8), 1374–1391.

Walder, J., 2010. Röthlisberger channel theory: its origins and consequences. Journal of Glaciology 56 (200), 1079–1086.

Walker, G., 2006. Climate change: The tipping point of the iceberg. Nature 441 (7095), 802–805.

Walker, N., 1996. Satellite assessment of mississippi river plume variability: causes and predictability. Remote Sensing of Environment 58 (1), 21–35.

Wang, J.-J., Lu, X. X., Liew, S. C., Zhou, Y., 2010. Remote sensing of suspended sediment concentrations of large rivers using multi-temporal MODIS images: an example in the Middle and Lower Yangtze River, China. International Journal of Remote Sensing 31 (4), 1103–1111.

Warrick, J., Mertes, L., Washburn, L., Siegel, D., 2004. Dispersal forcing of southern California river plumes, based on field and remote sensing observations. Geo-Marine Letters 24 (1), 46–52.

Wassmann, P., Svendsen, H., Keck, A., Reigstad, M., 1996. Selected aspects of the physical oceanography and particle fluxes in fjords of northern Norway. Journal of Marine Systems 8 (1), 53–71.

Wentworth, C., 1922. A scale of grade and class terms for clastic sediments. The Journal of Geology, 377–392.

Weslawski, J., Gluchowska, M., Grzelak, K., 2015. Face2Face Project. `http://www.iopan.gda.pl/projects/Face2face/`; accessed March 5, 2015.

Weslawski, J., Legezynska, J., 1998. Glaciers caused zooplankton mortality? Journal of Plankton Research 20 (7), 1233–1240.

Whitney, M., Garvine, R., 2005. Wind influence on a coastal buoyant outflow. Journal of Geophysical Research: Oceans (1978–2012) 110 (C3).

Whittington, R., Forsberg, C., Dowdeswell, J., 1997. Seismic and side-scan sonar investigations of recent sedimentation in an ice-proximal glacimarine setting, Kongsfjorden, north-west Spitsbergen. In: Glaciated Continental Margins. Springer, pp. 175–178.

Willis, I., Richards, K., Sharp, M., 1996. Links between proglacial stream suspended sediment dynamics, glacier hydrology and glacier motion at Midtdalsbreen, Norway. Hydrological Processes 10 (4), 629–648.

Winther, J.-G., Gerland, S., Ørbæk, J., Ivanov, B., Blanco, A., Boike, J., 1999. Spectral reflectance of melting snow in a high arctic watershed on svalbard: some implications for optical satellite remote sensing studies. Hydrological Processes 13 (12-13), 2033–2049.

Winther, J.-G., Godtliebsen, F., Gerland, S., Isachsen, P. E., 2002. Surface albedo in Ny-ålesund Svalbard: variability and trends during 1981–1997. Global and Planetary Change 32 (2), 127–139.

Woodgate, R., Schauer, U., Fahrbach, E., 1998. Moored current meters in the Fram Strait at 79 N: preliminary results with special emphasis on the West Spitsbergen Current.

Woodgate, R., Weingartner, T., Lindsay, R., 2012. Observed increases in Bering Strait oceanic fluxes from the Pacific to the Arctic from 2001 to 2011 and their impacts on the Arctic Ocean water column. Geophysical Research Letters 39 (24).

Wright, L., Coleman, J., 1971. Effluent expansion and interfacial mixing in the presence of a salt wedge, Mississippi River delta. Journal of Geophysical Research 76 (36), 8649–8661.

Xu, Y., Rignot, E., Menemenlis, D., Koppes, M., 2012. Numerical experiments on subaqueous melting of Greenland tidewater glaciers in response to ocean warming and enhanced subglacial discharge. Annals of Glaciology 53 (60), 229–234.

Zajaczkowski, M., 2002. On the use of sediment traps in sedimentation measurements in glaciated fjords. Polish Polar Research 23 (2), 161–174.

Zajaczkowski, M., 2008. Sediment supply and fluxes in glacial and outwash fjords, Kongsfjorden and Adventfjorden, Svalbard. Polish Polar Research 29, 59–72.

Zajaczkowski, M., Legezynska, J., 2001. Estimation of zooplankton mortality caused by an Arctic glacier outflow. Oceanologia 43 (3), 341–351.

Zwally, H., Abdalati, W., Herring, T., Larson, K., Saba, J., Steffen, K., 2002. Surface melt-induced acceleration of Greenland ice-sheet flow. Science 297 (5579), 218–222.